

UNIVERSITY OF KENT

MASTERS THESIS

**The physical structure of
high-pressure supersonic gas jets
flowing from circular vents.**

Author:

Thomas Keogh

Supervisor:

Prof. Micheal Smith

*A thesis submitted in fulfillment of the requirements
for the degree of Masters of Science*

in the

Centre of Astrophysics and Planetary Science
School of Physics and Astronomy

October 20, 2022

Abstract

A puncture in the wall of a high pressure gas reservoir leads to a supersonic jet that is associated with many astrophysical, planetary and aerodynamical phenomena, from radio galaxies to volcanic plumes and rockets. We undertake a systematic numerical analysis of a range of different physical parameters focusing on jet pressures exceeding that of its surroundings. We take a particular interest in the first shock generated by the jet, known as the stand off shock, as these are the brightest and easiest to detect in observation. We have shown there is a relationship where the location of the stand off shock not only depends on the overpressure but also on density through a feedback process and we have defined laws for this. We conclude that even steady uniform outflows will rapidly evolve into one of three distinct flow patterns, taking the form of turbulent plumes at high over-pressures and regular oscillations at low over-pressures. We also explore how energy is transferred into the environment as over-pressured jets are thought to contribute to the regulation of star and galaxy formation through the generation of noise and screeching.

Acknowledgements

I would would like to thank my supervisor, Prof Michael Smith for the continued help and support throughout the project. I also wish to thank Tim Keneer and Mark Price for constantly fixing the temperamental super computer, without which the project would not have been possible.

Contents

Abstract	i
Acknowledgements	ii
1 Introduction	1
1.0.1 Shocks	2
1.0.2 Jet collimation	3
1.1 Jet Types	4
1.1.1 Radio sources	5
1.1.2 Protostellar jets	8
1.1.3 Planetary Nebula jets	9
1.1.4 Neutron stars	11
1.1.5 Comets	12
1.2 Overview	13
2 Theory and Methodology	16
2.1 The Code	16
2.2 The scaling	17
2.3 Mass, momentum and energy	21
2.4 Over-pressured flow types	24
3 Results	26
3.1 Analysis tools	26
3.2 Resolution	29

3.3	The high over-pressure regime	31
3.4	Dependence on density	35
3.5	Jet power	41
3.5.1	Energy change along the jet	41
3.5.2	Lateral energy dispersion	44
3.6	The stand off distance	47
3.7	Higher Mach numbers	53
4	Conclusions	57
A	Mach 2 Images	68
B	Mach 4 Images	87
C	Mach 6 Images	107
D	Mach 8 Images	126
E	Pluto.ini	151
F	init.c	154
G	Definitions.h	159

Chapter 1

Introduction

An astrophysical jet is a slender channel of high-speed gas propagating through a gaseous environment (Smith, 2012). They are linear structures associated with stars and galaxies that can span about seven orders of magnitude in size (Young, 1991). When resolved, bright compact knots can be seen in the jet, far away from the driving source (Buehrke, Mundt, and Ray, 1988; Derlopa et al., 2019; Massi et al., 2022). The knots are associated with shock waves, as shocks cause significant heating and compression of the material (Meyer et al., 2016). Knots are extremely luminous leading to them playing a key role in the detection of extragalactic jets.

It is extremely difficult to directly probe inside the engine that drives the jet, whether from rockets, planetary vents or astrophysical compact objects. This has led to numerous studies focussing on how the jet interacts and evolves through the ambient medium, and then working backwards to try and derive processes within the jet and information about the source.

Gas jets formed from high-pressure gas escaping through a circular vent have been thoroughly studied (Franquet et al., 2015). The early studies were limited in scope by their experimental nature. Some studies employed the method of characteristics to analyse the flow. However, the approximations required to cope with the flow after the shocks and the rotation introduced

are not sufficient (Palmer and Hanson, 1998). However, work still continues in primary areas of interest such as a jets ability to produce noise known as screeching. Numerical studies, such as Norman et al. (1982), were independently inspired by interferometric maps of radio galaxies and their modelling in terms of de Laval nozzles (Blandford and Rees, 1974). These simulations assume the jet pressure is matched to the ambient pressure, which is likely not the case in most scenarios.

Many other simulations of over-pressured jets have already been performed and analysed (e.g. Gómez et al., 1997; Martí, Perucho, and Gómez, 2016; Moya-Torregrosa et al., 2021). However, specific conditions were chosen and the parameter space was not explored. Jets in astronomy span across a vast range of initial conditions such as Mach number, density and pressure, in addition to a variety of physics such as adiabatic hydrodynamics. So here, through the use of computational simulations, we aim to explore a full range of parameter space to gain an insight into the behaviour of simple hydrodynamic jets to act as a building block for further study.

1.0.1 Shocks

Shocks can only exist in fluid jets when the flow is supersonic, flows with a Mach number greater than 1, with a non-zero opening angle. When material exits the nozzle, there is a pressure difference between the material in the jet and the ambient medium; we define this pressure ratio as K . For over-pressured jets ($K > 1$), material leaving the nozzle will begin to expand, lowering the pressure inside the jet. As the flow is supersonic, there is a delay in communication between the jet boundary and the axis leading the jet to over-expand, resulting in the pressure of the jet falling below that of the ambient medium. From the condition of constant pressure, the jet boundary must be inflected (Irie et al., 2003); therefore, the expansion waves are reflected off the

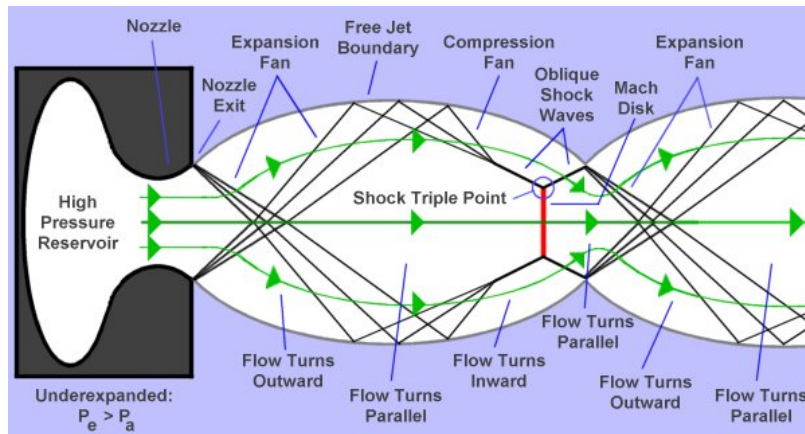


FIGURE 1.1: A sketch of the flow patterns in an under-expanded/over-pressured jet (Bashir et al., 2020).

jet boundary towards the axis (the centre of the jet). This causes compression of the material and is known as an oblique shock. Flow along the axis continues to fall with respect to the surface pressure, thus creating an inwards pressure gradient across the jet, causing the flow to converge. Shown in red in Fig. 1.1, a shock perpendicular to the axis is then required to increase the pressure. This shock is known as a Mach shock disk; flow that passes through the Mach shock disk will experience a significant pressure and temperature increase. The delay in communication can cause a hysteresis effect, causing oscillatory instabilities in the location of the shock.

1.0.2 Jet collimation

Collimation occurs when an outflow is narrow and the velocity is directed in its forward motion. It is defined where the length of a jet far exceeds its width (Waugh et al., 2009), thus, we observe jets as slender conduits of matter; appearing as a stream of particles (or light) aligned and projected in parallel into space (seen in Fig. 1.2). Observation tells us jets have a range in the magnitude of collimation, from highly collimated flows shown to be protruding from comets to jets of low collimation that originate from radio galaxies such as Fanaroff-Riley 1.

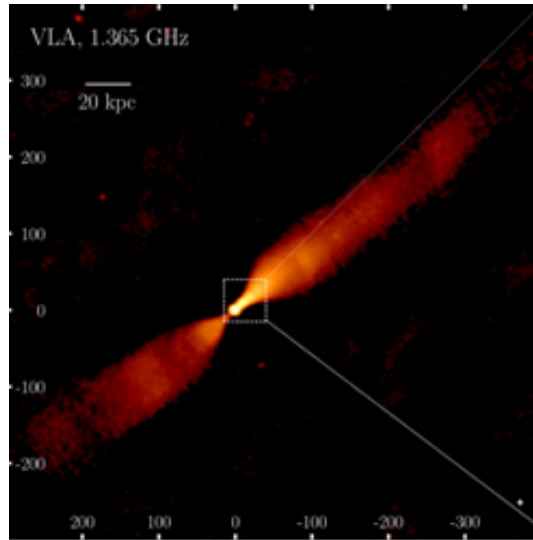


FIGURE 1.2: Images of the jets of NGC 315 reconstructed from archival VLA data at 1.365 GHz (Park et al., 2021).

Jets collimation can be described by the initial angle at which the jet opens; hydrodynamic principles tell us this angle is related to the Mach number of the jet. However, the full picture of collimation is not yet fully understood, it is thought that the decrease in internal pressure in the jet and the loss of thermal energy leads to collimation. When considering collimation in observation, you have to be careful in determining what is detected. The entire jet may not be visible. We may see just a narrow spine, an outer skin or embedded clumps. Perhaps we only see the outer sheath of entrained ambient material (Smith, 2012).

1.1 Jet Types

Gas is able to propagate away from a vast range of objects in astrophysics and space science in the form of collimated supersonic jets. We can see jets extending from relatively small objects inside our own solar system. Examples of this are the jet created by comet 67P as it approaches the inner solar system (Vincent et al., 2016) and the volcanic like plumes protruding from the moon Enceladus (Hansen et al., 2008). In contrast, the largest objects in

galaxies can also generate magnificent jets, we can see this from the bright stream of shocked particles launching from an object in the centre of the M87 galaxy; a supermassive black hole (Perlman et al., 2001). Due to the release of bottled-up pressures, jets are also studied for reasons of industrial and domestic safety e.g. Franquet et al. (2015) and Liger-Belair, Cordier, and Georges (2019).

1.1.1 Radio sources

Radio galaxies, like most other galaxies, are made up of stars, dark matter and interstellar medium. However, they are distinguished by the presence of a supermassive black hole at their core, which powers the emission of extensive radio jets (Begelman, Blandford, and Rees, 1984). These can be thought to be over-pressured jets as when material exits the core, there is a steep negative pressure gradient in the ambient medium, leaving the jet pressure to be relatively high on its exit from the core (Porth and Komissarov, 2015).

The launch of these relativistic jets is known to be the result of accretion processes onto extremely compact objects, such as black holes, in the presence of rotating accretion flows and magnetic fields (Mizuno, 2022). Various mechanisms have been suggested to explain the acceleration and collimation of the jet flow, including gas-pressure acceleration, radiation-driven acceleration, and processes grounded in magnetohydrodynamics (MHD). Within the framework of MHD, as matter falls towards the core it forms an accretion disk, the gravitational energy released in this process heats the gas to extremely high temperatures turning it into a plasma. As the plasma swirls around the black hole, the charged particles within it generate an electrical current and magnetic field. The varying rates of rotation in the disk induce twisting and torquing of magnetic field lines. As the magnetic field lines

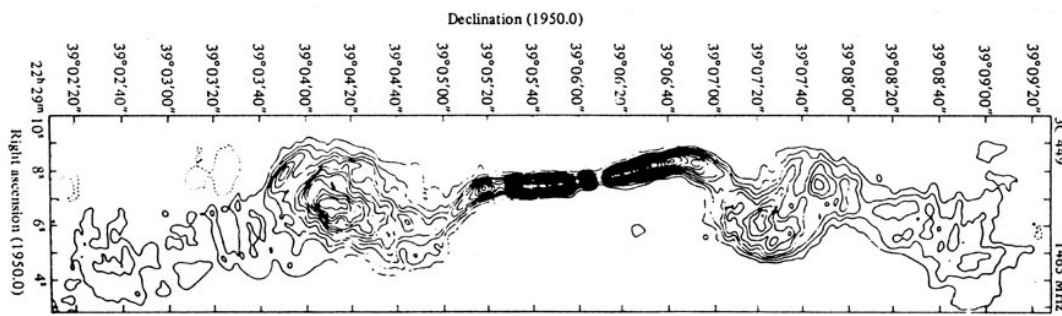


FIGURE 1.3: A VLA map of the FR-I galaxy 3C 449 made at 1465 MHz, with angular resolution 4.8×3.4 arcsec² (Perley, Willis, and Scott, 1979).

become more twisted, they store energy. Eventually, the stored magnetic energy becomes sufficient to overcome the gravitational pull of the black hole, resulting in the acceleration and launch of a collimated outflow (Chatterjee et al., 2019).

These galaxies are easily distinguished in observation due to long-lived radio emissions extending far beyond the visible structure. This radio emission is generated by synchrotron radiation. It is thought that on the launch of the jet and after interaction with the ambient medium, long-lived turbulent vortices are formed far from the source. Within this highly heated and pressurised setting, electrons within these vortices undergo ionisation, transitioning into a plasma state. Thus, synchrotron radiation is emitted as a consequence of concentrated pockets of ultra-relativistic electrons (Kellermann, 2002). Through the exchange of energy with the ambient medium, jets heat up gas in the interstellar medium creating a feedback loop between the AGNs and their environment. Therefore, AGN feedback can play a key role in regulating the growth of galaxies and star formation (Chatterjee et al., 2019).

Observations have shown that these jets have two distinct morphologies, leading to the classification of these jets falling into two types. The two types are called Fanaroff-Riley type 1 (FR1), also known as edge-darkened and Fanaroff-Riley type 2 (FR2), also known as edge-brightened (examples

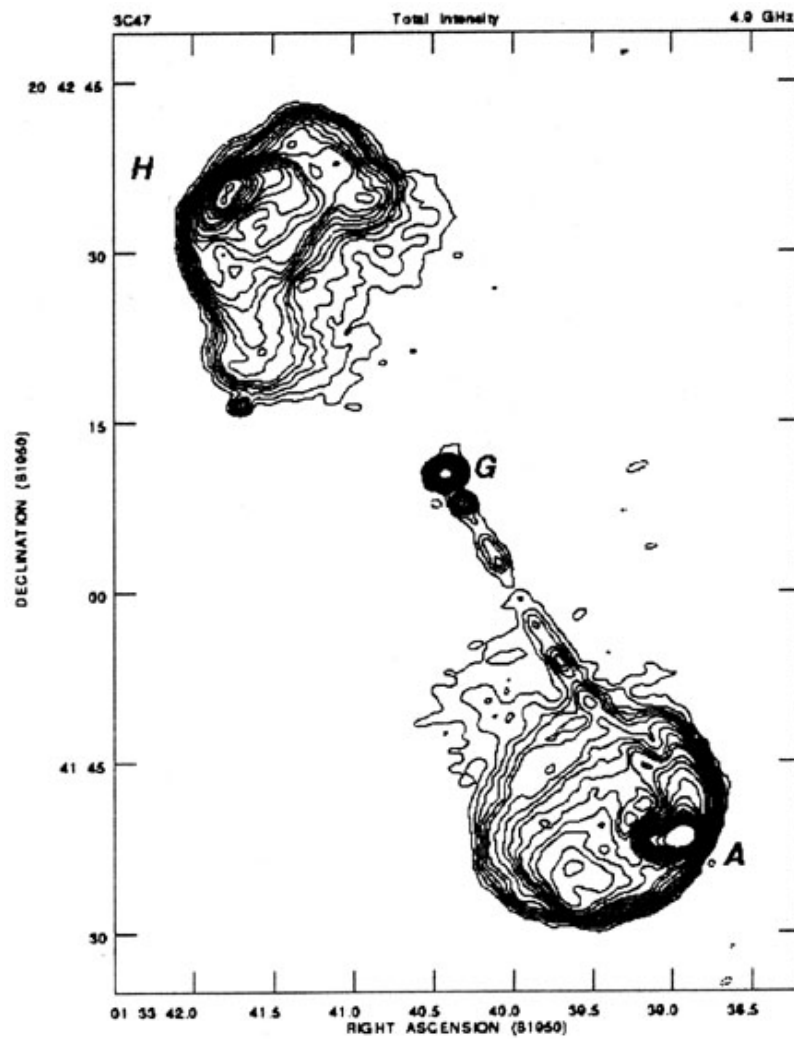


FIGURE 1.4: A VLA map of the FR-2 quasar 3C 47 made at 4.9 GHz with 1.45×1.13 arcsec² resolution (Bridle et al., 1994).



FIGURE 1.5: Two jets of material being emitted from HH-47, a protostar. The jets of material are half a light year long and emanate from the tiny bright dot at the centre of the image. However, this dot is not the star itself, but is rather a Solar System sized region of material surrounding it. Image credit: NASA. Link: <https://hubblesite.org/contents/media/images/1995/24/303-Image.html?keyword=hh-47>

are shown in Fig 1.3 and Fig 1.4 respectively). FR1 jets appear as weakly collimated turbulent plumes with a negative luminosity gradient spanning from the jet axis radially out. In contrast, FR2 jets are a highly collimated flow where extremely luminous hot spots are located at a distance far from the source. It is thought a super-massive black is responsible for the driving force for these huge jets spanning hundreds of kiloparsecs.

1.1.2 Protostellar jets

A protostar is an early stage in the process of star formation, where a dense region within a molecular cloud collapses under its own gravitational pull and begins to accumulate matter. The evolution of the star is dependent on its mass, the more massive a star, the shorter its lifespan. Larger, more massive stars have hotter cores that burn through their nuclear fuel more rapidly, leading to a lifespan measured in the millions of years, whereas smaller stars will last billions of years (Aithekar, 2019).

Observations of young stellar objects reveal the presence of directed outflows of atoms and molecules away from young stars (Zemskov et al., 2024). The launch process of jets in protostars involves similar physics principles to that of AGNs, but they occur on a vastly smaller scales. As ionised material accretes onto the forming protostar, it spirals inward due to the conservation of angular momentum, forming an accretion disk. This then creates an electric and magnetic field in the disk. Material accreting into the protostar can then transfer angular momentum to the magnetic field lines causing them to coil. This coiling leads to pockets of high magnetic pressure, causing the outflow of collimated material (shown in Fig.1.5). These jets, especially those from the earliest protostellar stage, can affect star evolution by carrying away significant amounts of mass and energy from the active central region and creating feedback in the surrounding medium (Rawlings and Jarvis, 2004).

1.1.3 Planetary Nebula jets

A planetary nebula is a luminous astronomical phenomenon that emerges during the later stages of a star's evolutionary journey. The process begins when a star, typically between 1 and 8 times the mass of our Sun, runs out of hydrogen in its core. The core contracts and heats up as the outer layers expand, creating a red giant. The outer layers eventually become unstable and material is ejected into the interstellar medium through stellar winds (Kwok, 1988). This material then forms a shell around the central core, which has now become a hot white dwarf. The hot white dwarf ionises the surrounding expelled material, causing it to fluoresce and emit light across a range of wavelengths.

Due to the complex nature of stellar winds, planetary nebula can take a range of morphologies. Not all planetary nebula have jets; about 13 percent of all planetary nebula have bipolar collimated outflows of material (Soker and



FIGURE 1.6: Two jets of material are emitted from the the central dying star of planetary nebula M2-9 at speeds of 300 km/sec. Image credit: NASA. Link: <https://hubblesite.org/contents/media/images/1997/38/563-Image.html?keyword=m2-9>

Livio, 1994), as illustrated in Fig.1.6 . The formation of jets in planetary nebulae is not as well understood as in other types of celestial objects like protostars or active galactic nuclei. The cause of this is thought to be the result of when a smaller jet from the star's core interacts with the stellar winds creating a much larger outflow (Livio, 2000).

The jets of planetary nebulae have similar speeds to the jets from protostars but are generally less well collimated. The expulsion of material through planetary nebula jets can significantly shape the surrounding interstellar medium, similar to protostar jets. Shocks are generated as the expelled material propagates through and interacts with the medium. This can be seen in Fig.1.6 as the two bright white dots away from the central source. These shocks heat and compress surrounding gas clouds changing the dynamics of the interstellar medium.

1.1.4 Neutron stars

A neutron star is an incredibly dense remnant that forms when a massive star undergoes a supernova explosion. During the explosion, the star's core collapses under its own gravity, resulting in the merging of protons and electrons to create neutrons. Since the neutron star must conserve the angular momentum of the original star, but is much smaller in size, its rotation rate increases significantly. They are characterised by extremely strong gravitational fields and intense magnetic fields, which can be billions of times stronger than those of typical stars.

A pulsar is a type of neutron star that emits beams of electromagnetic radiation from its magnetic poles. The formation of pulsars is contingent upon a specific combination of factors, rotation rate, magnetic field strength, and appropriate orientation. As the neutron star rotates, its magnetic field interacts with charged particles in the vicinity, accelerating them to high speeds along the field lines, emitting synchrotron radiation (H.E.S.S. Collaboration et al., 2018). Often, the magnetic field is not aligned with the spin axis, so those beams of particles and light are swept around as the star rotates. As the beam sweeps in and out of our line of sight from Earth, we see periodic pulses. Neutron stars that lack these conditions may not emit radiation in a pulsating manner observable from Earth and, therefore, are not classified as pulsars.

Other jets formed from pulsars are known as pulsar wind nebulae. As a pulsar rotates, it releases its rotational energy as a relativistic magnetised outflow called a pulsar wind. The pulsar wind collides with the surrounding supernova ejecta and creates complex flow patterns (Tanaka and Takahara, 2010). Similar to a planetary nebula, pulsar wind nebula have a range of morphologies but on a much larger scale. The pulsar wind creates shocks in the interstellar medium, shown in Fig.1.7 as the white areas away from the

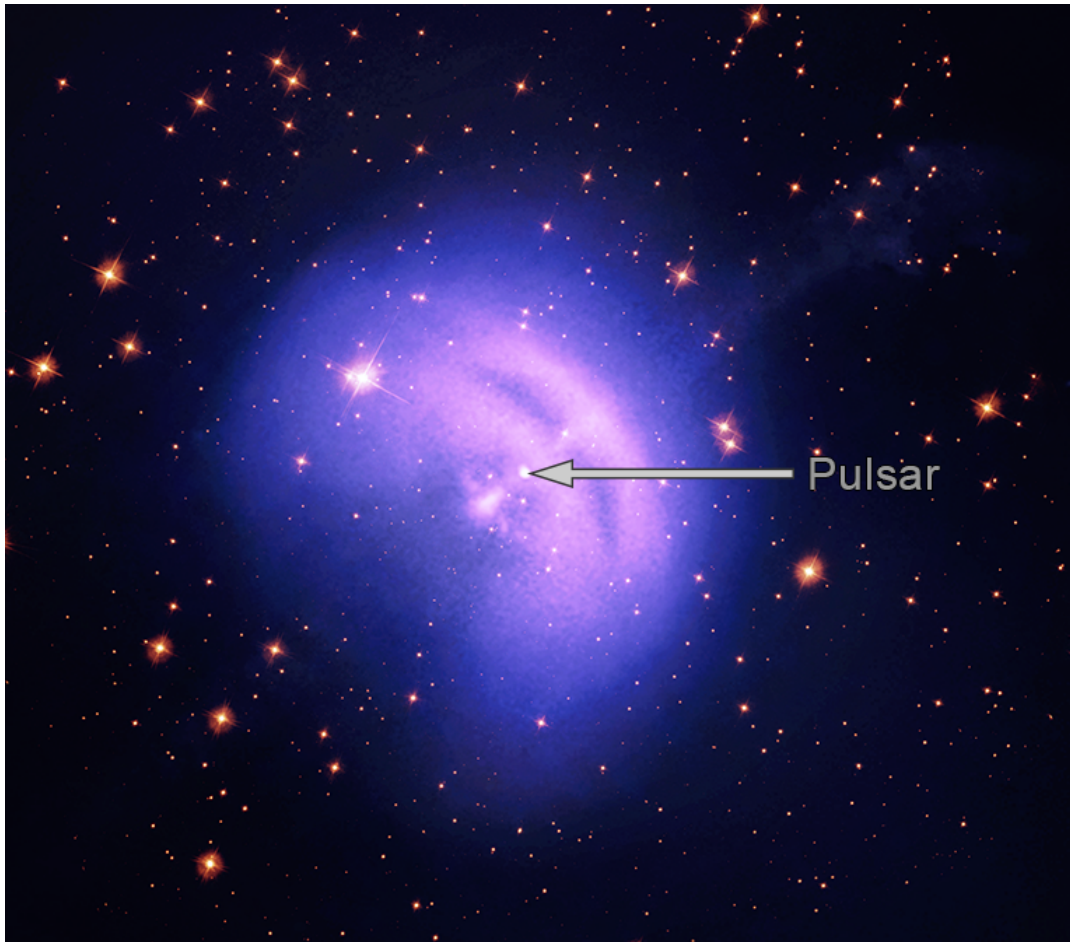


FIGURE 1.7: This is a X-ray image is of the Vela pulsar wind nebula published by Nasa. Image credit : NASA
Link: <https://www.nasa.gov/wp-content/uploads/2023/03/vela-pulsar-wind-nebulaixpe.jpg>

pulsar, heating and compressing the surrounding gas.

1.1.5 Comets

Comets are simply a mixture of dust, water and ice, with the ratio between these elements varying for each comet. As a comet like P67 moves through the solar system it is heated when coming within proximity to the sun or through interaction with solar wind. The water begins to evaporate, causing a release of gas and dust from the comet's surface opposing the direction of motion, known as a coma. This effect can be clearly seen when observing

the sun rise over a part of the comet; it becomes instantaneously active, leading to regular activity. In addition to this, sudden plumes can also be seen propagating away from comets. Study into these jets is limited; thus, our understanding of their dynamics is limited. Sudden plumes are thought to be attributed to a small pocket on the uneven surface of the comet. When the morphology of the surface changes, for example, due to a landslide, a pocket of ice can be exposed. The sudden heating of this ice can cause a plume. These jets may be subject to an adiabatic thermodynamic process as they are surrounded by the ISM, a low-pressure environment, implying cooling may be very slow. It is also thought that the gas can become magnetically driven as it passes its host star.

1.2 Overview

Astrophysical jets are a fascinating phenomenon. However, as beautiful and intriguing these dazzling displays of wonder may seem, their nature remains elusive and obscure (Smith, 2012). Each type of jet can provide unique insights into the processes and environments from which they originate, ranging from the early stages of star formation to the advanced phases of stellar evolution and the dynamics of active galactic nuclei. Despite this, a comprehensive investigation of under-expanded jets remains to be performed, as noted by Franquet et al. (2015). One motivation here is to determine how the details of the flow pattern can provide information on the driving source. A study has shown that the location of the first shock and its distance from the nozzle is a relationship based on the Mach number and the jets overpressure. Thus measuring this distance can give you information about the jet and characterise the flow e.g. Carlson and Lewis (1964) and Davidor and Penner (1971). This is extremely useful, as mentioned previously, shocks are extremely bright, therefore measuring the stand off distance is far easier than

trying to determine other physical parameters in the vicinity of the jet. However, this investigation was only interested in low Mach number and high-pressure jets. We aim to span a much larger region of parameter space and look to determine if this relationship can be shown as a general result.

A second motivation is to show the emission we detect from distant galaxies can be attributed to shocks from a gas jet. This analysis will not provide this answer as inclusion of advanced physics principles will need to be included and accounted for.

Besides the origin of the jet, we are also interested in how the jet interacts with the immediate surrounding environment to provide positive or negative feedback. This effect could be used to describe many evolutionary scenarios involving regulation and triggering that we do not currently understand (Rawlings and Jarvis, 2004). Therefore, we investigate the continuous energy transfer from the jet into its surroundings through noise, turbulence and heat.

We simulate here basic hydrodynamic supersonic jets into a uniform adiabatic medium. As each type of astrophysical jet will have a different environment and different external forces acting on it, such as gravity, chemistry or magnetic fields, we choose to ignore all external forces. This allows us to study the evolution of the jet and its effects on the ambient medium solely based on the initial conditions in the environment and basic hydrodynamics. Consequently, this thesis will act as a building block for further study as more research into each jet type is required to get a richer view on specific jet dynamics. We consider appropriate ranges in pressure and density ratios between the jet and its surrounding medium and test analytical approximations. Throughout the thesis, we will go on to show that not all flows reach a steady flow state and that the ambient density plays a key role in determining

the stability of the flow. This contrasts with the steady-state uniform pressure conditions in analytical solutions for which the ambient density plays no role. Although we do not drive pulses into the jet in this thesis, we do consider long-term variability leading to screeching and crackling noise as energy propagates out laterally from the jet into the ambient medium.

Chapter 2

Theory and Methodology

2.1 The Code

Fluid mechanics is the study of fluid behaviour (liquids, gases, blood, and plasmas) at rest and in motion (Ghassemi and Shahidian, 2017). This has strong implementations to astrophysics with many systems able to be described this way. Throughout this thesis we will model jets as a simple inviscid (has zero viscosity) and adiabatic (has no net heat transfer) hydrodynamic flow. We also do not consider any external forces such as gravity, chemistry or magnetic fields within the jet; this allows us to describe the jet through basic fluid mechanics principles (Chanson, 2004). These are the continuity equation (conservation of mass), the momentum principle (conservation of momentum) and the energy equation (conservation of energy).

The use of a solver is then required to build the computational simulations. Throughout this thesis all simulations were performed with *PLUTO*¹, a grid-based code, incorporating Godunov-type shock-capturing schemes, which is freely-distributed (Mignone et al., 2007). *PLUTO* is designed to integrate a general system of conservation laws that we write as:

$$\frac{\partial U}{\partial t} = -\nabla \cdot T(U) + S(U) \quad (2.1)$$

¹<http://plutocode.ph.unito.it/>

This means *PLUTO* has the capability of solving different systems of conservation laws, these being classical hydrodynamics (HD), magnetohydrodynamics (MHD), special relativistic hydrodynamics (RHD) and special relativistic MHD (RMHD). We chose classical hydrodynamics as discussed above.

To run the simulations three input files are needed: `definitions.h`, `init.c` and `pluto.ini` (examples of these files can be found in the appendix). The `definitions.h` file defines the jet setting; this includes user defined variables, such as the dimensions and geometry of the grid, and what physics to include, such as whether cooling is active in the jet. As discussed previously, we turn the additional physics effects off and chose to run the simulation on a 2-D cylindrical grid. This is also where we choose the MHD conservation laws. The `init.c` file contains algorithms and predefined comments that are specific to the Pluto code and not to be edited. The `pluto.ini` file defines all the jets properties that are needed for the numerical simulation. This is also the file where we change the initial conditions of the jet by modifying three parameters, the Mach number, M , the pressure ratio $\kappa = P_{\text{jet}}/P_{\text{amb}}$ and the density ratio $\eta = \rho_{\text{jet}}/\rho_{\text{amb}}$. This allows us to run the simulations over an array of different mach numbers, pressure ratios and density ratios.

2.2 The scaling

To make the results easier to interpret we normalise our unit scale. We do this by measuring distance in terms of the jet radius, which we set to $R_{\text{jet}} = 1$. We set our time unit to $R_{\text{jet}}/c_{\text{amb}}$, and by setting the speed of sound in the ambient medium to $c_{\text{amb}} = 1$, we now have our unit time also equal to 1. To finish we simply set the initial density in the ambient medium to $\rho_{\text{amb}} = 1$. It is now straightforward to manipulate already known physics equations to derive required quantities. We use the equation for the speed of sound (c) in an ideal gas, where γ represents the specific heat ratio:

$$c_{\text{amb}} = \sqrt{\frac{\gamma \cdot P_{\text{amb}}}{\rho_{\text{amb}}}} \quad (2.2)$$

After rearranging we see that the pressure in the ambient medium is given by:

$$P_{\text{amb}} = (\gamma - 1)u_{\text{amb}} \quad (2.3)$$

In our case, we can assume the specific heat ratio (γ) is 5/3, resulting in $P_{\text{amb}} = 0.6$. Next we obtain the internal energy per unit volume by the equation:

$$u_{\text{amb}} = (\gamma - 1)/P_{\text{amb}} \quad (2.4)$$

Using our previously found and assumed values it is clear $u_{\text{amb}} = 0.9$.

We assume an adiabatic media so that all quantities can be scaled. We can then look at what type of jets our simulation best represent. Table 2.1 shows how these dynamical scales vary between a supersonic jet formed by a rocket and a radio galaxy. The scale size between the two goes from centimetres to megaparsecs and the dynamical time goes between milliseconds to 100 Myr.

We are interested in jets that have already evolved and converged to a steady flow state. This means we are required to run the simulation over a long dynamical time, requiring a large reservoir of ambient medium for the jet to expand into without any side effects from boundary conditions. We set this up by first taking a uniform cylindrical grid of 200 by 200 x Mach number. We do this because, as the Mach number increases, we expect the jet to be stretched along the x-axis in proportion to the Mach number. In terms of jet radii, this corresponds to cylindrical grid of radius 15 jet radii and length 15 jet radii x Mach number. To ensure this is sufficient, we surround the grid with a large reservoir of ambient medium through the use of staggered

TABLE 2.1: The initial conditions for the non-dimensional parameters for both a light and heavy jet and their example scaled interpretations. Note that further physics is required for the astrophysical jets consistent. These will be added once the fundamental behaviour is rigorously established. The parameter $n_{p,amb}$ is the hydrogen nuclei (free proton) density in the ambient medium.

-	-	light jet	heavy jet		rocket	FR I radio
-	-	unit value	unit value		exhaust	galaxy
Jet radius	r_{jet}	1	1		13.5 cm	2.5 kpc
Simulated length	D	30	30		405 cm	75.0 kpc
Mach number	M_{jet}	2.0	2.0		2.0	2.0
Ambient density	ρ_{amb}	1	1	$1.1 \cdot 10^{-3} \text{ g cm}^{-3}$		$2.34 \cdot 10^{-26} \text{ g cm}^{-3}$
Sound speed	c_{amb}	1	1	$3.4 \cdot 10^4 \text{ cm s}^{-1}$		$6.72 \cdot 10^7 \text{ cm s}^{-1}$
Ambient parameters:						
Ambient temperature	T_{amb}	n/a	n/a		300 K	$2.0 \cdot 10^7 \text{ K}$
Internal energy	u_{amb}	0.9	0.9	$2.53 \cdot 10^6 \text{ erg cm}^{-3}$		$9.53 \cdot 10^{-11} \text{ erg cm}^{-3}$
Ambient pressure	P_{amb}	0.6	0.6	$1.01 \cdot 10^6 \text{ dyne cm}^{-2}$		$6.35 \cdot 10^{-11} \text{ dyne cm}^{-2}$
Pressure ratio	P_{jet}/P_{amb}	2.0	2.0		2.0	2.0
Density ratio	ρ_{jet}/ρ_{amb}	0.1	10		0.1	0.1
Jet speed	v_{jet}	8.94	0.89	$2.48 \cdot 10^5 \text{ cm s}^{-1}$		$4.03 \cdot 10^9 \text{ cm s}^{-1}$
Mass flux	\dot{M}_{jet}	2.81	28.1	$24.9 \cdot 10^3 \text{ gm s}^{-1}$		$2.80 M_{\odot} \text{ yr}^{-1}$
Thrust	P_{ram}	25.1	25.1	$6.40 \cdot 10^9 \text{ dyne}$		$7.12 \cdot 10^{35} \text{ dyne}$
Kinetic power	L_{jet}	112.4	11.2	$8.23 \cdot 10^{14} \text{ erg s}^{-1}$		$1.51 \cdot 10^{45} \text{ erg s}^{-1}$
Nozzle timescale	$t_o = r_{jet}/c_{amb}$	1	1	$0.4 \cdot 10^{-3} \text{ s}$		3.64 Myr
Dynamical time	D/v_{jet}	3.35	33.5	$1.57 \cdot 10^{-3} \text{ s}$		1.82 Myr

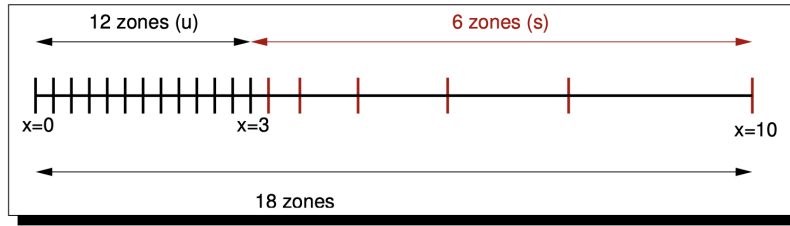


FIGURE 2.1: Example of staggered zones in a one-dimensional grid shown by a segment of 12 uniform zones and a segment of 6 stretched zones spanning an interval between 0 and 10. Image credit: *PLUTO* user guide. Link: <https://plutocode.ph.unito.it/files/userguide.pdf>

zones. This is where we add stretched zones onto our uniform grid, as shown in Fig.2.1. The stretched zones represent a larger spatial distance, allowing us to expand the domain by 65 jet radii radially and by $(15 + 100)$ M jet radii axially by only adding 100×200 zones. The use of staggered zones allows us to add a very large amount of ambient medium with the fraction of the computing power that would be required otherwise. We note that we have treated the y axis as an elastic wall to stop the jet material entering and immediately leaving the grid, this also better represents most astrophysical jets as the driving source would be located near the y axis and material would not immediately escape.

We aim to maintain an environment that is not immediately altered by the introduction of the jet and that is sufficiently large so that disturbances are not trapped close to the jet. Therefore, we must consider the speed of the jet when it initially enters the ambient material. Since our jets are supersonic and are moving very fast, they will cause great disturbance to the ambient medium. We aim to mitigate this affect by employing a ramp up time. We allow the initial jet speed to be zero and linearly accelerate it to the final speed over the course of 10 dynamical time steps.

Five properties are recorded for each zone across 1000 time dumps separated by 0.2 time units. The parameters are the density, ρ , pressure, p , two velocity

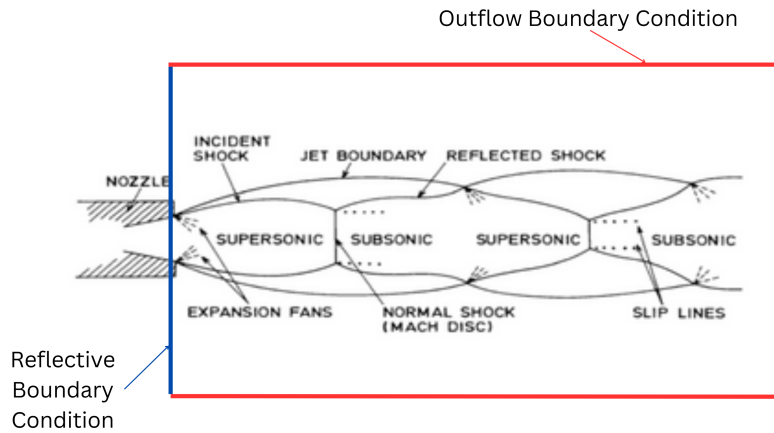


FIGURE 2.2: This shows the basic structure of over pressured jet with the reflective boundary condition marked with a blue line and the outflow boundary conditions marked with a red line.

Taken and modified from Adamson Jr and Nicholls (1959).

components, v_z and v_r , and a mass-weighted jet tracer, χ . The subsequent post-processing was performed with algorithms incorporated into *IDL* software.

2.3 Mass, momentum and energy

We earlier stated that the jet can be described through three different conservation quantities. To analyse the results, we must calculate these three quantities.

The first of which is the conservation of mass flux which is given by:

$$\dot{\mathcal{M}}_{\text{jet}} = \rho_{\text{jet}} \cdot v_{\text{jet}} \cdot A \quad (2.5)$$

where $A = (1 - \mu)\pi R_{\text{jet}}^2$ is the jet area and v is velocity. As we can only approximate the nozzle to a circular orifice in a grid based system, μ represents a small adjustment.

It is important to note the boundary conditions we are using; at the nozzle

exit we use a reflective boundary condition (shown in Fig.2.2 as the blue line). If we used an outflow boundary condition at the nozzle, as the flow first enters the medium, it would create a cocoon back flow removing mass from the grid; changing the initial conditions and effecting the jet evolution. As we want to control the initial conditions, we choose a reflective boundary at the nozzle. This means that there will be a linear increase in μ (Eq.2.5) over time for all the simulations with reflective outflow boundaries. This is because we are keeping the jet constant, thus there will always be a constant supply of mass flux being injected. We use outflow boundary conditions for above, below and at the far side of the jet (shown in Fig.2.2 by the red line). As we have used staggered zones, we have given the jet plenty of ambient medium to evolve, therefore we allow material to cross these boundaries to stop it becoming trapped and effecting the conditions of the medium.

The second conservation equation is the conservation of momentum flux that we will describe in terms of ram and thermal pressure:

$$\dot{P} = (\rho_{jet} \cdot v_{jet}^2 + P_{jet}) \cdot A \quad (2.6)$$

This can be written in the form:

$$\dot{P} = \pi\kappa(\gamma M^2 + 1) \quad (2.7)$$

Finally, the conservation of energy flux that we will describe in terms of enthalpy and kinetic energy. To describe enthalpy we must consider the internal energy and the work done, $p\mathcal{V}$, where $\mathcal{V} = 1/\rho$ is the specific volume.

We can then obtain Bernoulli's equation (with the Bernoulli constant being U) by dividing through by the equation for conservation of mass flux.

$$U^2 = v_{jet}^2 + \frac{2\gamma}{\gamma - 1} \frac{P_{jet}}{\rho_{jet}} \quad (2.8)$$

Therefore, the total available power entering the domain is $\dot{M}_{jet}U^2/2$. We can track these quantities to gain an understanding of the different ways the energy is exchanged.

If we assume the first bow shock tunnels through the ambient medium with a speed V , we know that a shock will occur, creating a high-pressure zone. This high-pressure zone will be approximately defined by the pressure of the shocked ambient medium. We then use the jump shock relationship that defines the pressure jump in the frame of the bow shock:

$$\frac{P_2}{P_1} = \frac{2\gamma}{\gamma + 1} (M_s^2 - 1) \quad (2.9)$$

As we are in the frame of the bow shock, the Mach number is represented slightly differently. It is now defined as the jet speed relative to the tunnelling speed, thus $M_s = v_{jet} - V$. We then substitute into the Bernoulli's equation to give:

$$\eta(v_{jet} - V)^2 - c_{jet}^2 = V^2 - c_{amb}^2 \quad (2.10)$$

Rearranging this gives:

$$V = v_{jet} \frac{\sqrt{\eta}}{1 + \sqrt{\eta}} \quad (2.11)$$

The equation in this form seems to imply the propagation of the bow shock is independent to over-pressure. However, if you hold the Mach number to a constant, you can again rearrange to obtain:

$$V = M \frac{\sqrt{\kappa}}{1 + \sqrt{\eta}} \quad (2.12)$$

2.4 Over-pressured flow types

The Mach angle is defined as $\sin^{-1}(1/M)$, this is the angle at which pressure waves will propagate into the jet from the nozzle. At very low over-pressures, sound waves propagate into and out of the jet, with a wavelength of $\sim MR_{jet}$ (Sanders, 1983).

At low over-pressures, a diamond chock pattern is formed (often referred to as regular reflection). We define the stand off distance as the location of the first shock and we will go on to show that this distance is proportional to the Mach number and a power of the pressure ratio:

$$D_1 = d_M \kappa \beta M R_{jet} \quad (2.13)$$

Here, the minimum distance, d_M , should be just beyond that given by the Mach angle: $d_M/R_{jet} \geq \arcsin 1/M$. The simulations below determine $\beta \sim 1.2$ for the particular range of conditions chosen here.

At high over-pressures, we do not see any type of repeating flow pattern. This is because the stand off shock is replaced with a Mach shock disk for high over-pressures. This Mach shock disk can reach a size in which it connects the oblique shocks together. This is known as a triple point.

Early experiments demonstrated that the stand off distance has a dependence on pressure and Mach number. This would require advanced 2-D integration to solve, the relationship has been calculated through experiments and a simple analytical formula was shown (Carlson and Lewis, 1964).

$$D_1 = 1.38 \gamma^{1/2} \kappa^{1/2} M \quad (2.14)$$

This formula was also found to be applicable when the ambient medium

flows over the nozzle by Buckley (1975), where a summary of the early experiments can be found.

The most recent comprehensive review by Franquet et al. (2015), upholds the above result. They note that the location of the Mach disk is the only reliable measure. This is due to the extreme turbulent nature of these flows.

The third flow pattern is considered as a transition state between the two. Oblique shocks follow the stand off shock, creating a complex array of oblique shocks. These are shown in the first case we go to discuss.

Chapter 3

Results

3.1 Analysis tools

To begin to analyse the simulations we have run, we will use two simple analysis tools to visualise the results. The first method is the four-panelled diagrams, with each panel showing the distribution of a different physical parameter in the z - r plane (using cylindrical coordinates). Fig.3.1 shows the density, axial velocity, jet tracer and pressure for the $M = 2$ and $\kappa = 2$ simulation. The jet tracer is simply mapping all ambient gas with a value of 0 and all material originating from the jet with a value of 1, allowing us to see the distribution of jet material in the ambient gas.

The pressure panel is particularly useful for identifying shock fronts. This comes from the nature of a shock being a sharp rise in pressure. This means that we see a sharp rise in the pressure gradient (where the graph transitions from dark red to white immediately), which will help us later determine the stand off distance (the location of the first shock front). Whereas the density panel is useful as it lets us observe the long lived vortices in the ambient medium created by the shearing motion of the jet.

In Table 3.1, we see that the entrance jet speed for Fig.3.1 is $\sqrt{20} = 8.944$. The speed downstream alternates between approximately 8 and 11 units.

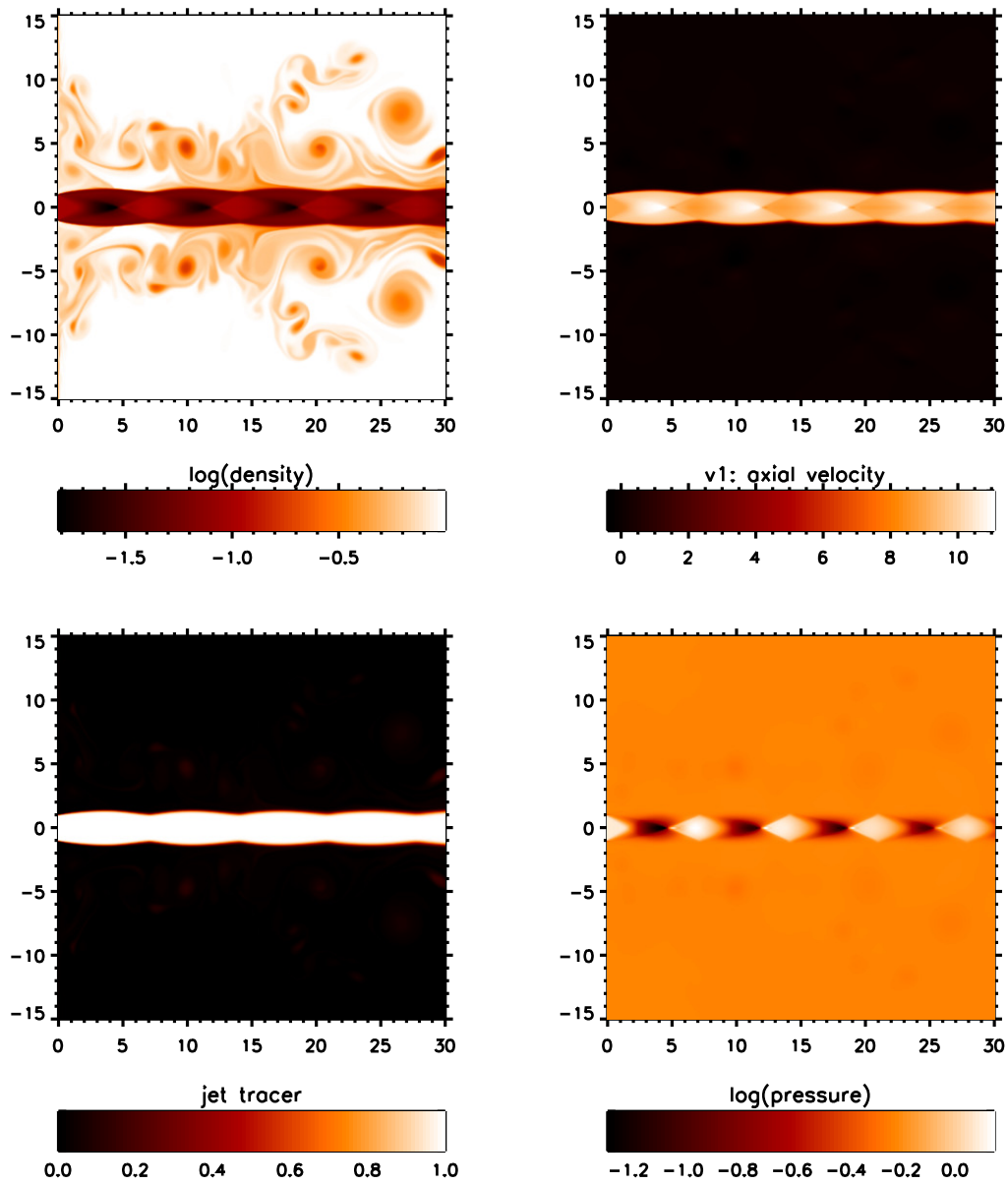


FIGURE 3.1: The distributions of physical parameters for a Mach 2 jet with over-pressure $\kappa = 2$ and density ratio $\eta = 0.1$. The time $t = 200$ corresponds to the end of the run. The length scale is in units of the jet radius. Upper-left panel: density, upper-right panel: axial velocity component, lower-left: tracer for jet gas, lower-right: pressure.

TABLE 3.1: Summary of parameters and figure numbers for the illustrated simulations.

Pressure ratio, κ	Density ratio, η	Derived jet speed	Resolution zones/ R_{jet}	Figure
2	0.1	8.944	13.33	3.1/3.2
2	0.1	8.944	53.33	3.3/3.4
4	0.1	12.65	13.33	3.5
16	0.1	25.30	13.33	3.6/3.7
2	10	0.894	13.33	3.8(a) /3.10(a)
2	10	2.530	13.33	3.8(b) /3.10(b)
1.2	0.1	6.928	13.33	3.11

The second analysis tool is a space-time diagram that shows the pressure along the axis of the jet, this is done for 1000 time dumps, all separated by a time of 0.2. Looking at Fig.3.2, we observe the initial bow shock (bottom right of the diagram) propagate through and disturb the ambient medium. Over time, we see the flow pattern converge and oscillate around a steady state. This allows us to see the full evolution of the jet and determine how quickly the jet can reach a steady state, if at all.

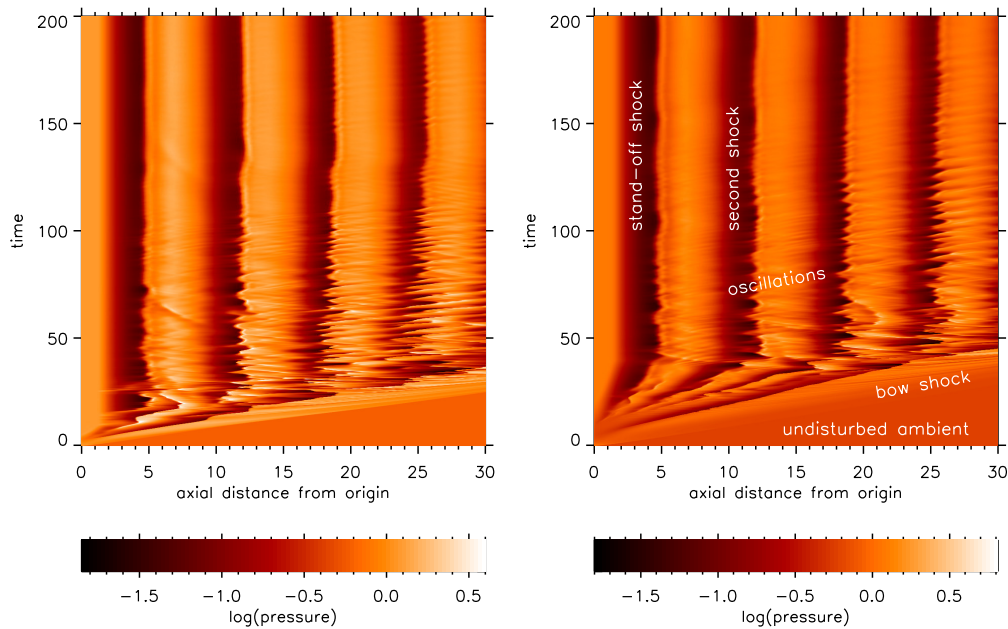


FIGURE 3.2: The distribution of the pressure along the jet axis as a function of the time for a Mach 2 jet with over-pressure $\kappa = 2$ and density ratio $\eta = 0.1$. Length scale is in units of the jet radius. The two panels differ only in the imposed initial ramp of jet speed up to the final values. Left panel: the jet speed increases linearly over the first ten time units. Right panel: the jet speed increases linearly over the first forty time units.

3.2 Resolution

We performed all the Mach 2 simulations with the same resolution, this being a grid of 200x400 zones. However, we have produced runs at two and four times this resolution for the jet with initial parameters of $M = 2$ and $\kappa = 2$. Both Fig.3.3 and Fig.3.4 have been run on a grid of 800x1600 zones with the same time of 200. A gas jet has a continuous density and pressure spectrum, therefore, fewer approximations are made with more zones. This increases the accuracy of the simulation and allows us to capture smaller-scale structures, features, and interactions in the flow that might be missed in lower resolution simulations. However, increasing the resolution drastically increases the computing power required, so we use the higher resolution runs to verify the accuracy of the larger structures seen in lower resolution runs.

Starting with the density panel (top left of Fig.3.3), we immediately see a significant increase in the amount of vortices created in the ambient medium and a reduction of the size when compared to Fig.3.2. The vortices in terms of density seem similar as by looking at the tracer panel (bottom right), we determine the vortex eyes are made of low density gas originating from the jet material.

Moving the attention to the top right panel (velocity panel), we notice the velocity has a steep negative gradient along the axis at roughly 25 jet radii from the origin. This is because the higher resolution is able to resolve the convergence of gas to the axis with a higher degree of accuracy. This allows us to see a small Mach disk that greatly reduces the velocity of the jet material that passes through it, which is why we see a channel of slow moving material.

The high resolution space time diagram (Fig.3.4) has greater detail in the oscillations of the shocks following the initial bow shock. We do note that while

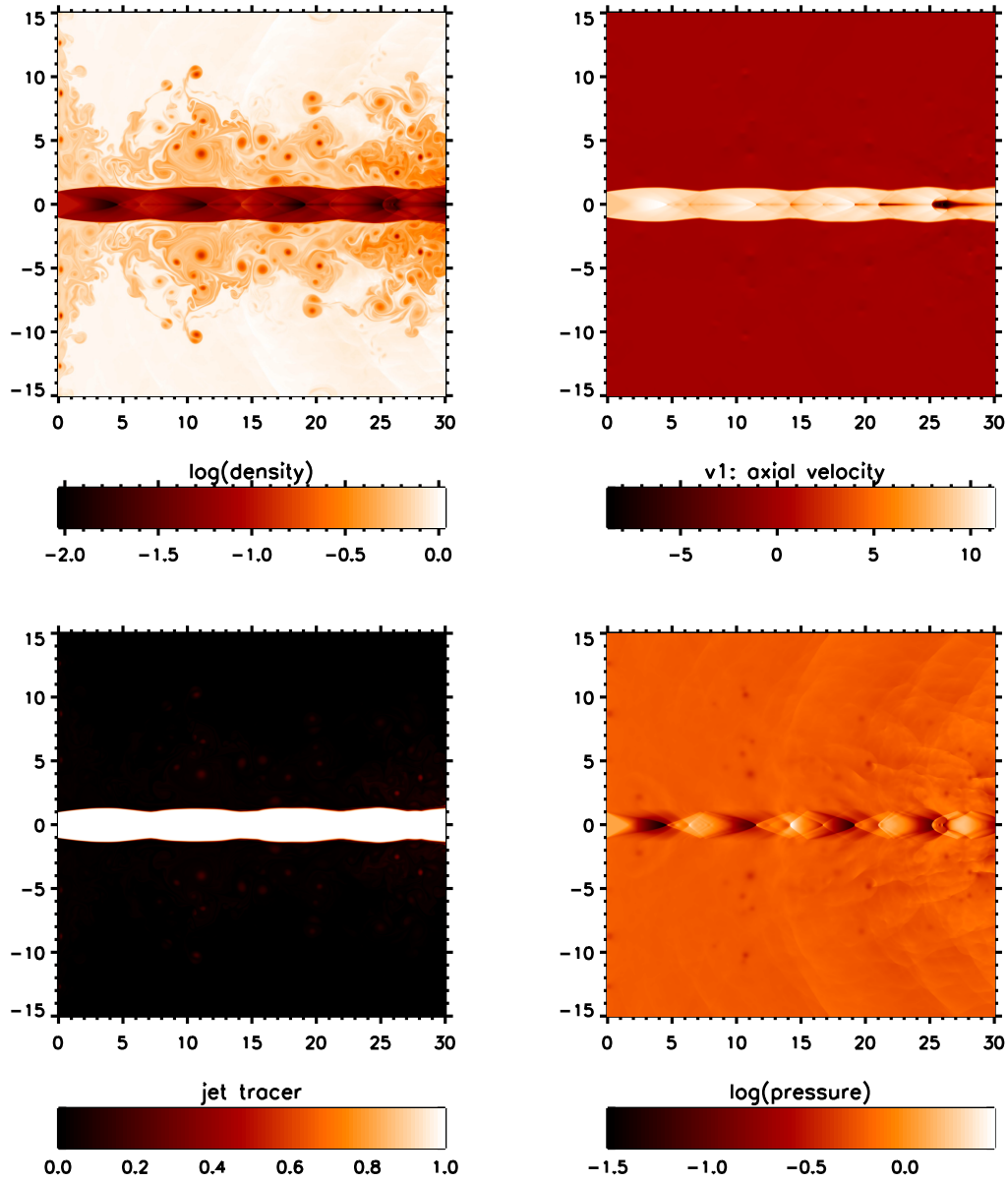


FIGURE 3.3: At the high resolution of $1,600^2$, distributions of physical parameters for a Mach 2 jet with over-pressure $\kappa = 2$ and density ratio $\eta = 0.1$. The time $t = 200$ corresponds to the end of the run. The length scale is in units of the jet radius. Upper-left panel: density, upper-right panel: axial velocity component, lower-left: tracer for jet gas, lower-right: pressure.

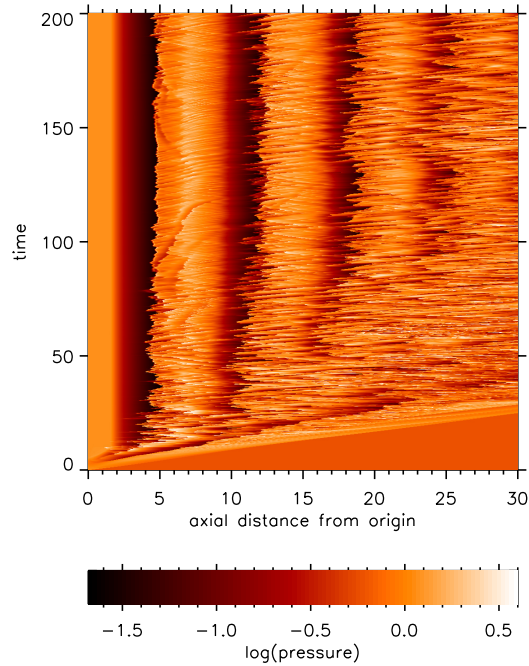


FIGURE 3.4: At high resolution, the distributions of the over-pressure along the jet axis as a function of the time for a Mach 2 jet with over-pressure $\kappa = 2$ and density ratio $\eta = 0.1$. Length scale is in units of the jet radius.

the oscillations are displayed much more clearly, they are of similar amplitude and frequency to that of the standard resolution run. The higher resolution run also converges to a steady state.

In the standard resolution run, the first stand off shock is still smudged at the end of the run due to its oscillations. In the higher resolution run, we can clearly identify defined oscillations of the stand off shock, however, they are still of a low amplitude.

3.3 The high over-pressure regime

For the Mach number of 2, we see distinct flow patterns forming depending on the initial pressure ratio. For low over-pressures of 2.5 and below, we see a repeated diamond shock pattern develop and the jet approaches a steady state. Then, for over-pressures between 2.5 - 4, we see the transition where the first shock transforms into a Mach shock disk. As shown in Fig.3.5, we

see the repeated shock pattern has been completely disturbed. This is because at high initial over-pressures, the pressure of the jet after exit falls too quickly, the first shock is then not enough to raise the pressure back to the high values thus it never recovers. However, we do still see the existence of a recollimation zone seen in the tracer panel (bottom left panel of Fig.3.5). We also note that because of the existence of a Mach shock disk, there is low density material with a high negative velocity along the axis.

When looking at the velocity panel (top right panel of Fig.3.5), we see the core of the jet is coated by high speed low density material. This sheath acts as a buffer zone between the jet core and the ambient medium. This observation was also seen by Ogden et al. (2008), who proposes a suitable model for volcanic gas eruptions through a vent.

We ran our simulations up to the extreme over-pressure of $\kappa = 16$ (see Fig.3.6). In this case, we see a very large Mach shock disk that almost completely cuts through the jet but we still see the existence of a narrow high speed sheath. There is also a considerably higher amount of turbulence in the ambient medium, especially in the downstream region of the jet. This turbulence is significant enough to raise the pressure of the ambient medium. This means that as the jet evolves, the 'effective pressure ratio' changes in correspondence to the ambient medium, this then causes the stand off shock to also evolve with time by moving further away from the origin.

Now looking at the space time diagram for $\kappa 16$ (see Fig.3.7), we can observe the difference in the evolution of the jet. We notice the initial bow shock propagates at a much greater speed; this is expected with the increase in pressure ratio. We also see oscillations of a huge amplitude at the location of the first shock, however, the time between these oscillations is roughly the same as in the low pressure ratios.

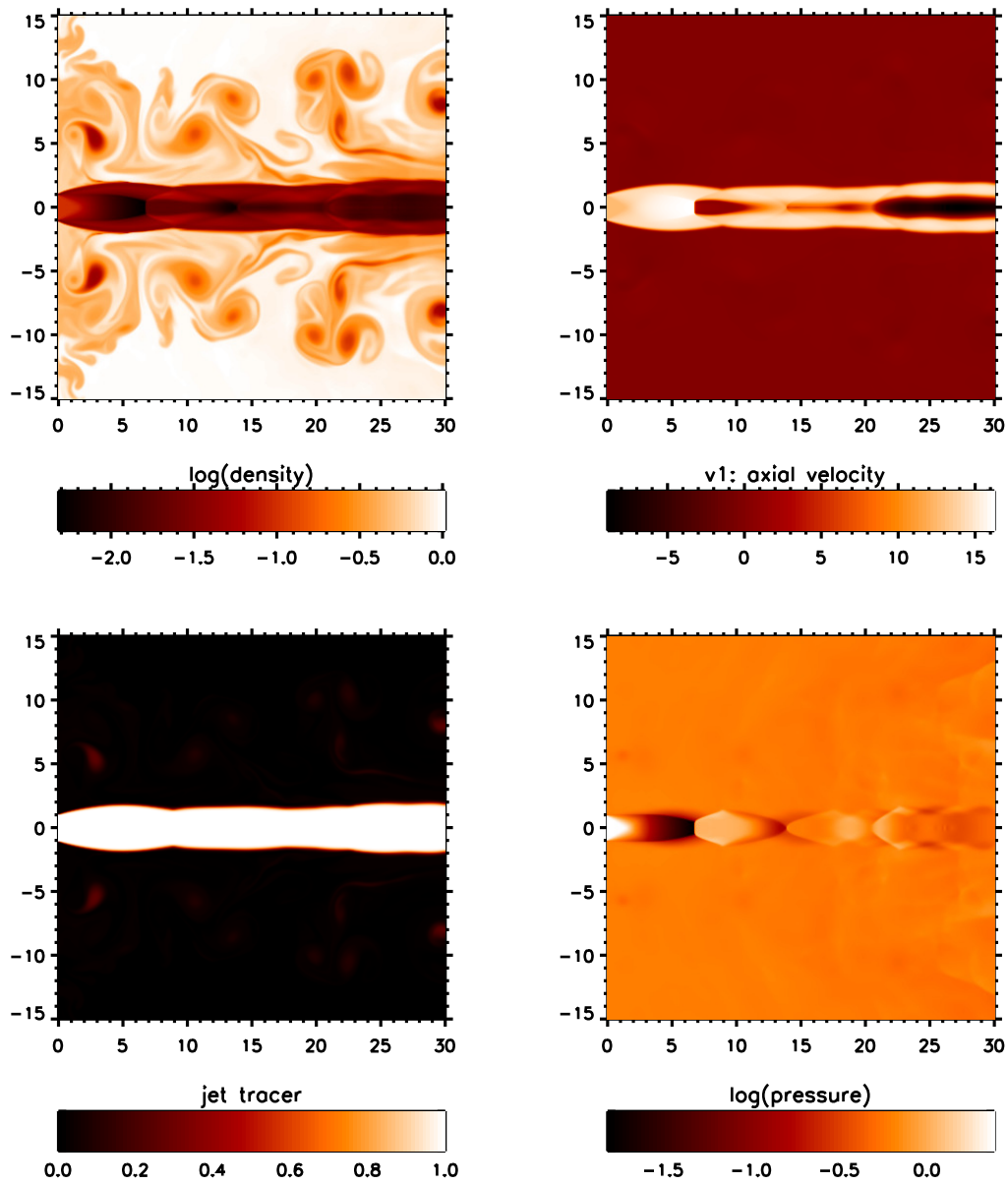


FIGURE 3.5: The distributions of physical parameters for a Mach 2 jet with over-pressure $\kappa = 4$ and density ratio $\eta = 0.1$. The time $t = 200$ corresponds to the end of the run. The length scale is in units of the jet radius. Upper-left panel: density, upper-right panel: axial velocity component, lower-left: tracer for jet gas, lower-right: pressure.

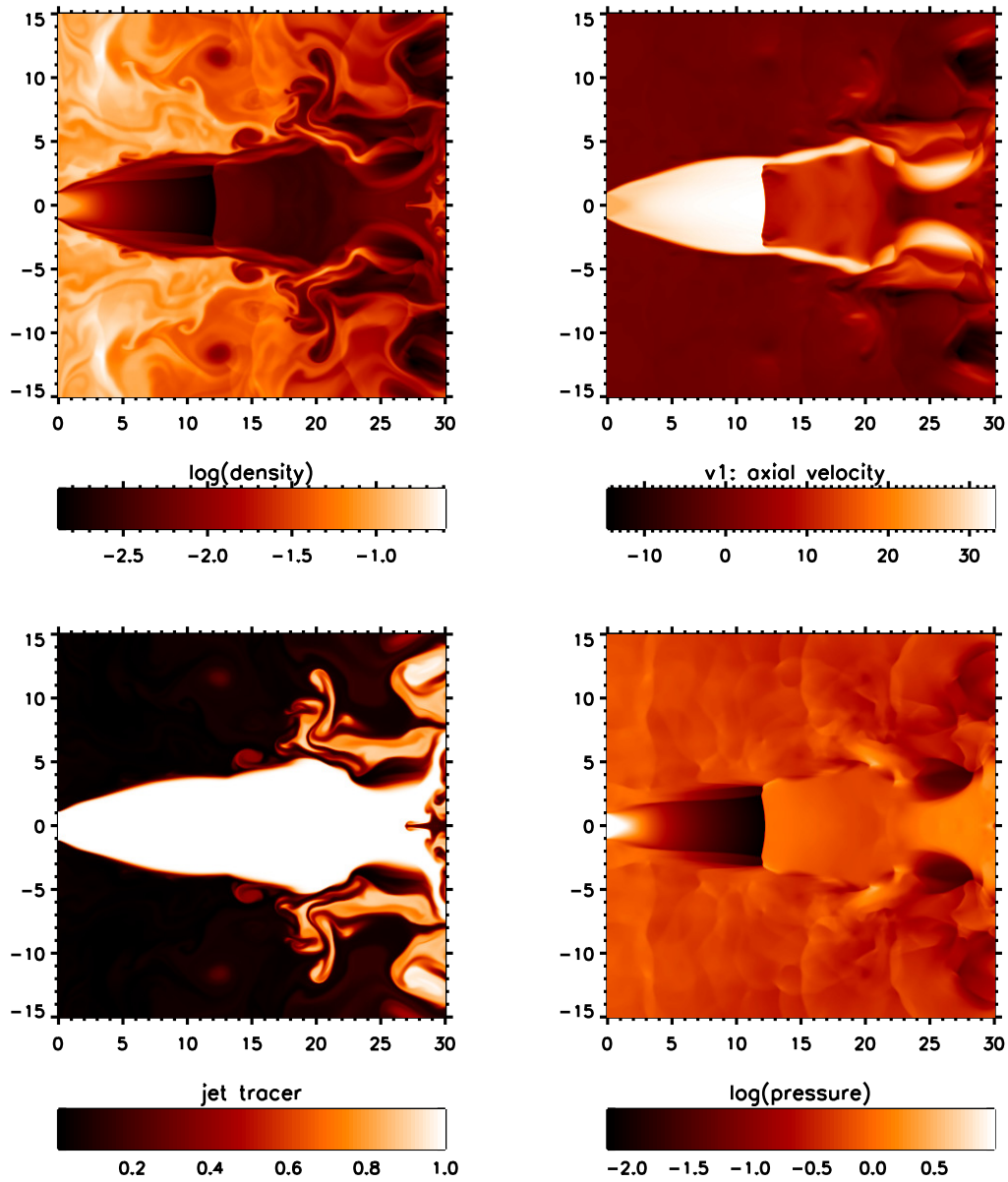


FIGURE 3.6: The distributions of physical parameters for a Mach 2 jet with over-pressure $\kappa = 16$ and density ratio $\eta = 0.1$. The time $t = 200$ corresponds to the end of the run. The length scale is in units of the jet radius. Upper-left panel: density, upper-right panel: axial velocity component, lower-left: tracer for jet gas, lower-right: pressure.

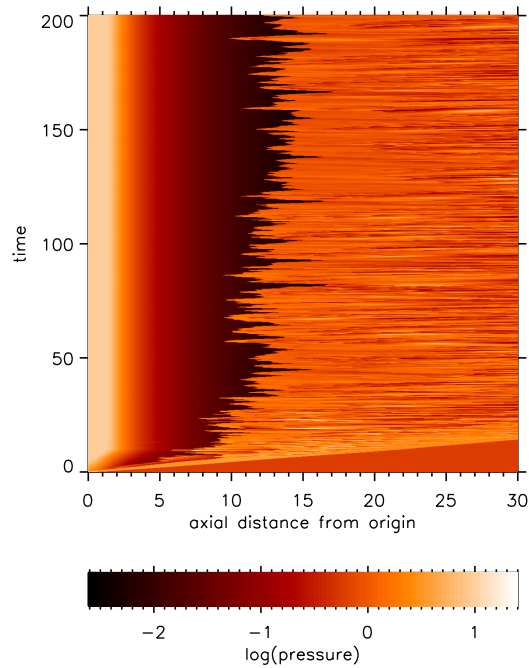


FIGURE 3.7: The distribution of the pressure along the jet axis as a function of the time for a Mach 2 jet with over-pressure $\kappa = 16$ and density ratio $\eta = 0.1$. Length scale is in units of the jet radius.

3.4 Dependence on density

In our simulations, we have included no additional forces such as chemistry or gravity and have focussed on modelling simple jets. This means we expect steady flow patterns that should only depend on the initial pressure ratio and Mach number. We do not expect density to have any effect, however, this is not the case as shown in Fig.3.8 and Fig.3.9 (for κ of 2 and 16 respectively). Flow patterns similar to the low density cases can be seen.

As the jets we have produced do not follow a steady flow pattern, it is likely the inertia of the higher density jet plays a role in supporting its stability. This can also be seen in Fig.3.10 where the oscillation pattern, although with the same amplitude, the time between them is much longer. This then causes less turbulence in the ambient medium so the 'effective pressure ratio' remains constant, meaning the stand off shock does not evolve away from the origin.

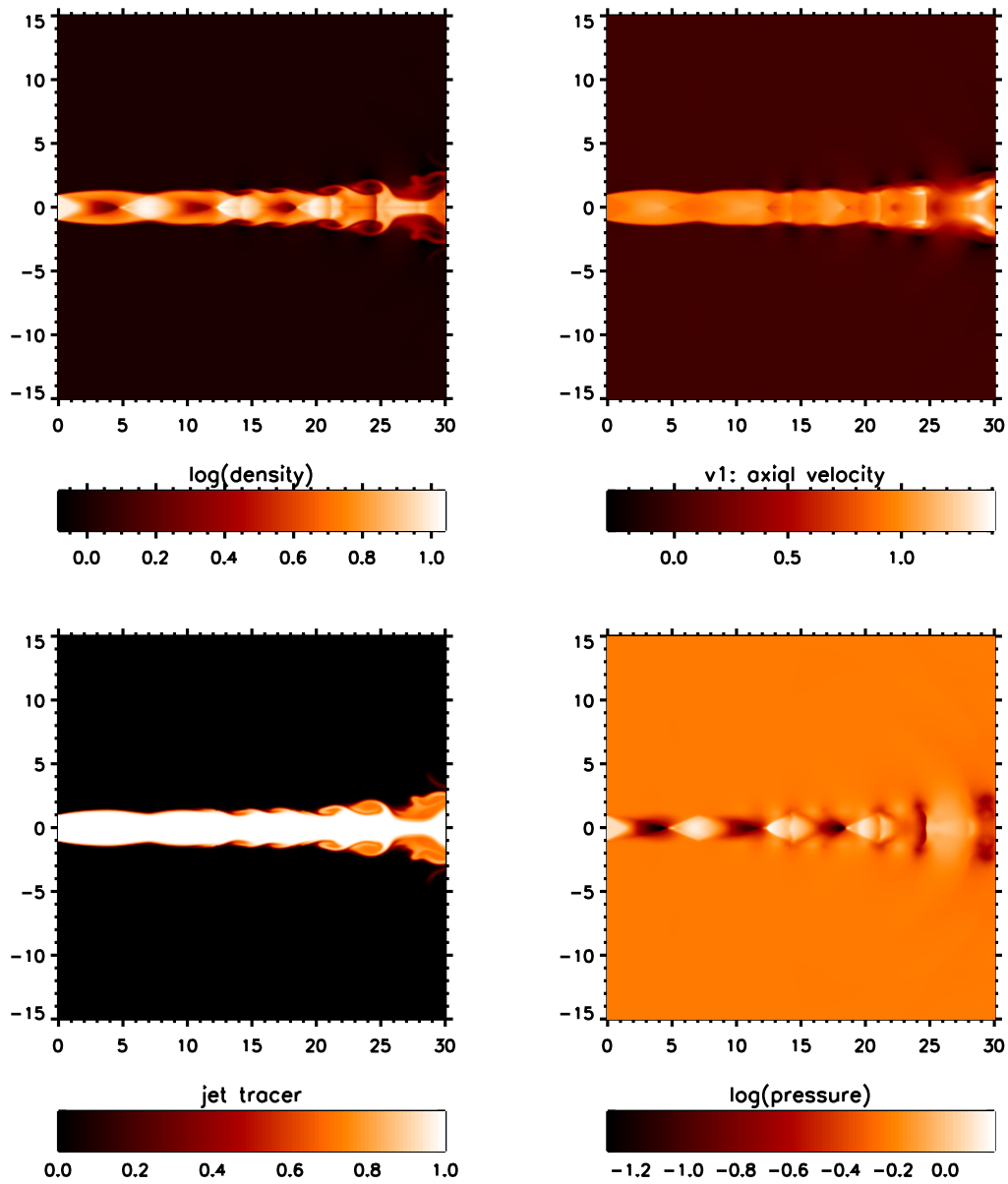


FIGURE 3.8: The distributions of physical parameters for a Mach 2 jet with over-pressure $\kappa = 2$ and density ratio $\eta = 10$. The time $t = 200$ corresponds to the end of the run. The length scale is in units of the jet radius. Upper-left panel: density, upper-right panel: axial velocity component, lower-left: tracer for jet gas, lower-right: pressure.

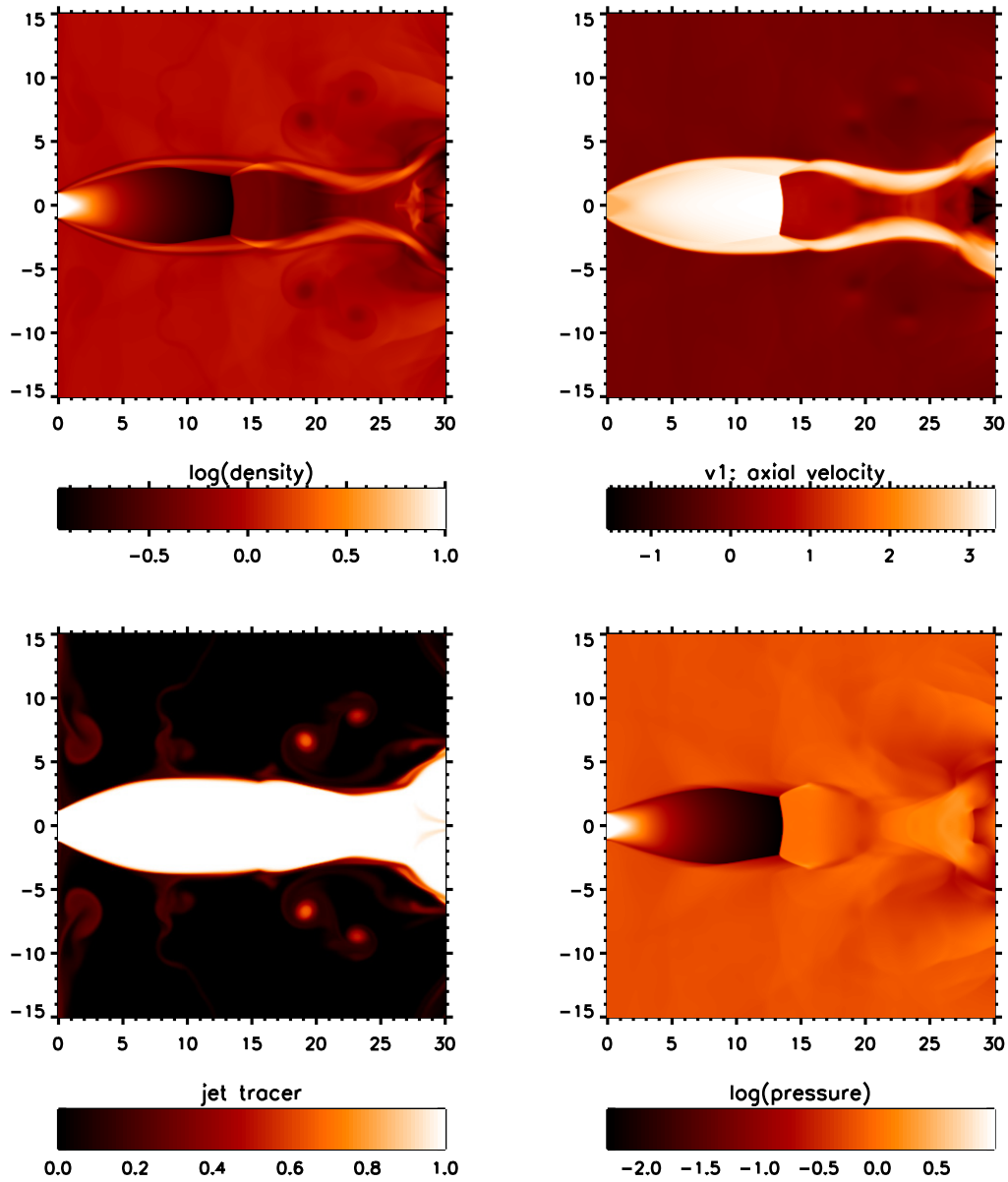


FIGURE 3.9: The distributions of physical parameters for a Mach 2 jet with over-pressure $\kappa = 16$ and density ratio $\eta = 10$. The time $t = 200$ corresponds to the end of the run. The length scale is in units of the jet radius. Upper-left panel: density, upper-right panel: axial velocity component, lower-left: tracer for jet gas, lower-right: pressure.

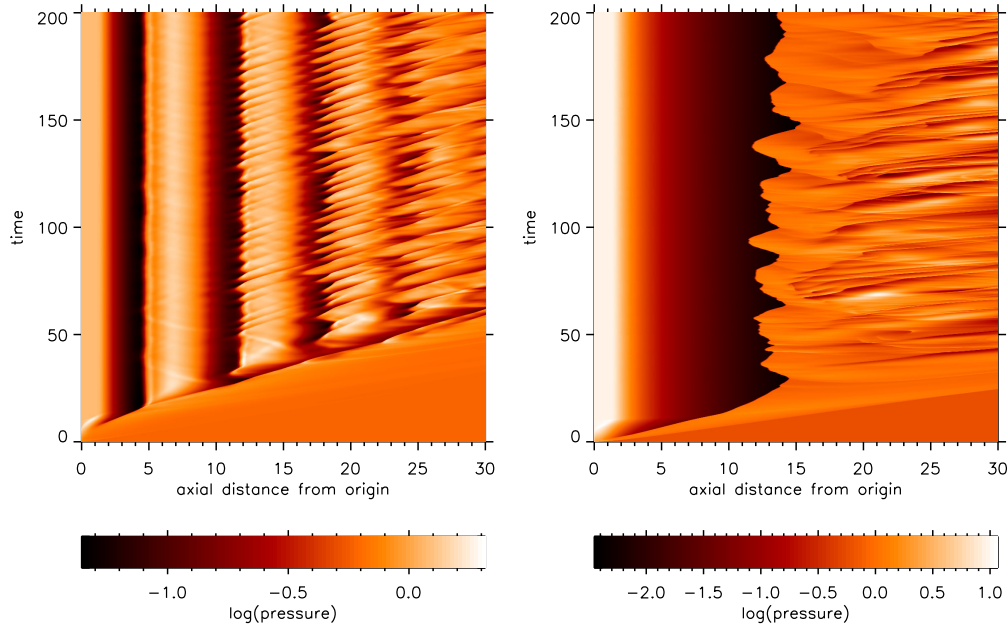


FIGURE 3.10: Space-time diagrams for a Mach 2 jet with a density ratio $\eta = 10$ and a over-pressure $\kappa = 2$ (left panel), $\kappa = 16$ (right panel). The time $t = 200$ corresponds to the end of the run. The length scale is in units of the jet radius.

As discussed, we know the shocks oscillate, causing pressure waves to propagate through the ambient medium. As we know, pressure waves are sound waves; therefore, these oscillations are responsible for the high-pitched jet screeching that emanates from the jet (Powell, 1953). The frequency of the screech will then be density and pressure dependent, and from the simulations, we can estimate the frequency of the screech. For $\kappa = 2$ we estimate $0.6c_{amb}/R_{jet}$ for $\eta = 0.1$ and $0.24c_{amb}/R_{jet}$ for $\eta = 10$. For $\kappa = 16$, we estimate $0.4c_{amb}/R_{jet}$ for $\eta = 0.1$ and $0.12c_{amb}/R_{jet}$ for $\eta = 10$.

As opposed to the regular oscillations of a stable flow that lead to high frequency screeching, at high over-pressures the whole flow becomes disrupted and turbulent. This produces sound with a broad range of frequencies that takes the form of noise (Tam, 1995).

The speed at which the jet interface traverses the grid is much slower at the high density (see Table 3.1). The speed is measured from the space-time diagrams to be ~ 0.5 for $\kappa = 2$ and 1.0 for $\kappa = 16$. We note that these values

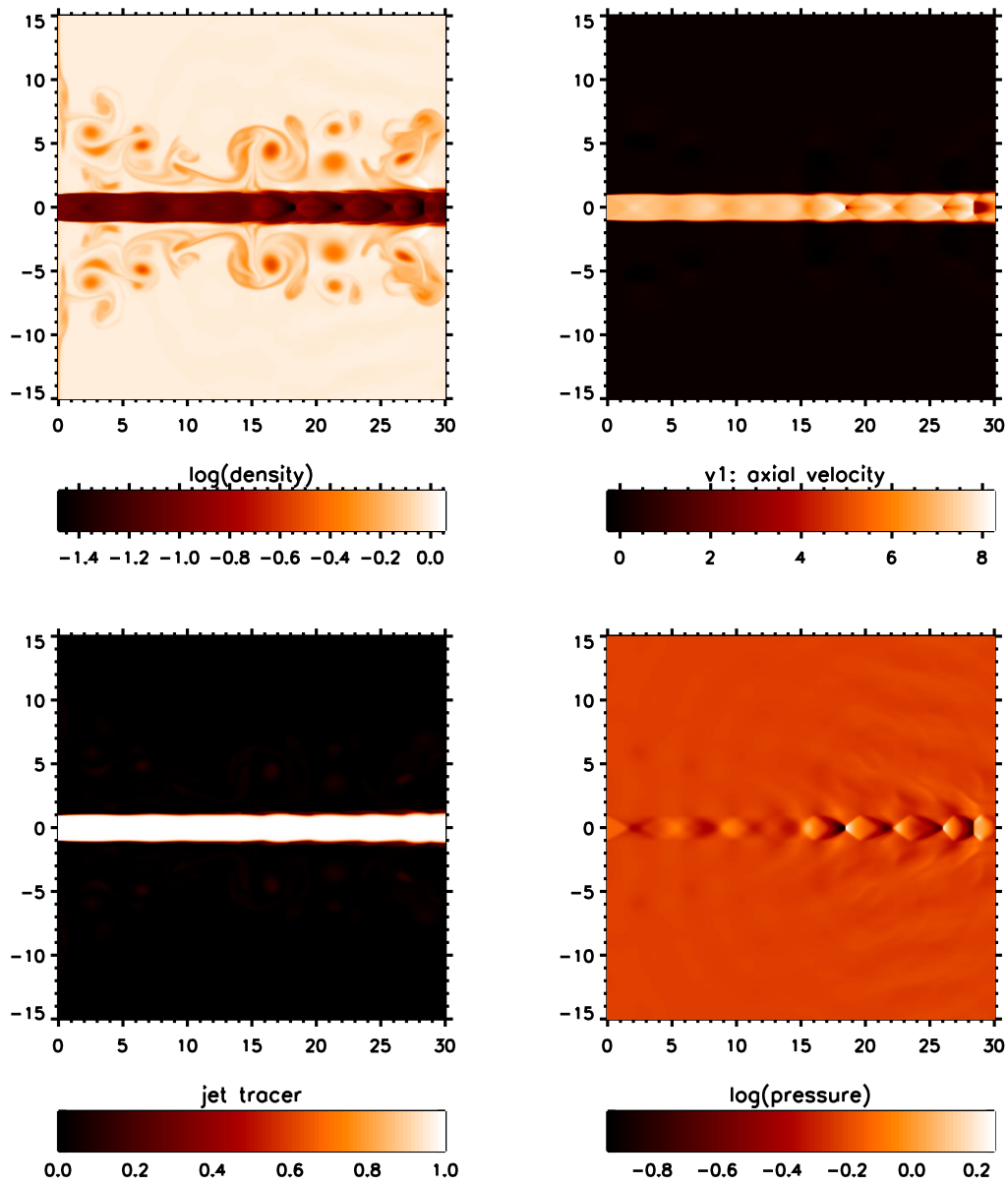


FIGURE 3.11: The distributions of physical parameters for a Mach 2 jet with over-pressure $\kappa = 1.2$ and density ratio $\eta = 0.1$. The time $t = 200$ corresponds to the end of the run. The length scale is in units of the jet radius. Upper-left panel: density, upper-right panel: axial velocity component, lower-left: tracer for jet gas, lower-right: pressure.

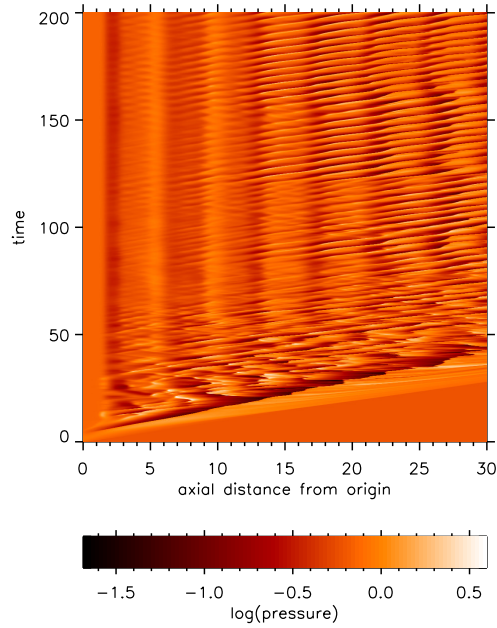


FIGURE 3.12: Space-time diagrams for a Mach 2 jet with a density ratio $\eta = 0.1$ and a over-pressure $\kappa = 1.2$. The time $t = 200$ corresponds to the end of the run. The length scale is in units of the jet radius

differ from what we can calculate using Eq.2.12. The actual speeds are lower than this due to the overall jet expansion and spreading of momentum over a larger area.

After the initial bow shock, a series of pressure waves will move through the diagram at the oblique angle. The speeds of these waves (V_{KH}) are related to a balance of the momentum, a diagnostic for Kelvin-Helmholtz fluid instabilities. These occur when two fluids with different densities are moving in contact with each other but with different velocities. A simple example of this is seen when wind moves in contact with the ocean and creates waves. In the surface mode, we expect disturbances to propagate at speed along a plane surface (Blake, 1972) as well as a pinched cylindrical jet (Hardee, 1979).

$$V_{KH} = v_{jet} \frac{\eta}{1 + \eta}. \quad (3.1)$$

Shown in Fig.3.8 we see instabilities in the jet of $\kappa = 2$ gradually grow until

finally creating a Mach shock disk. This is in complete contrast to the $\kappa = 1.2$ in Fig.3.11 where the dominant stable diamond shock pattern does not allow the instabilities to take effect. Fig.3.12 shows the spatial growth of the shock pattern for $\kappa = 1.2$, emphasising the advection of the non-linear waves across the grid at a speed consistent with that given by Eq.3.1.

3.5 Jet power

When studying jets, it is important to consider how the energy in the jet evolves over time. If the jet experiences a decrease in energy, it must release this energy into its surroundings, thereby impacting various physics concepts. For stellar jets, the level of support could restrict further star formation (Knee and Sandell, 2000; Dionatos and Güdel, 2017), while for extragalactic jets, the transfer of energy may regulate galaxy formation (Dubois et al., 2010). On the other hand, if the jet was to take in energy from the environment, it is possible that jets could provide support to the intergalactic medium, cutting off gas infall and quenching star formation (Dubois et al., 2010; Fabian, 2012; Ehlert et al., 2022).

3.5.1 Energy change along the jet

Here we look at how the energy in the jet is distributed after the effects from the propagation of the initial bow shock have settled. As our original expectation was for a steady flow pattern to form, we expected negligible energy transfer to the environment. As we saw from analysing density this is not the case, the jet is not steady and emitting energy into the environment in the form of sound waves. Understanding the rate of energy transfer will help us understand the contribution a jet has to the concepts mentioned above.

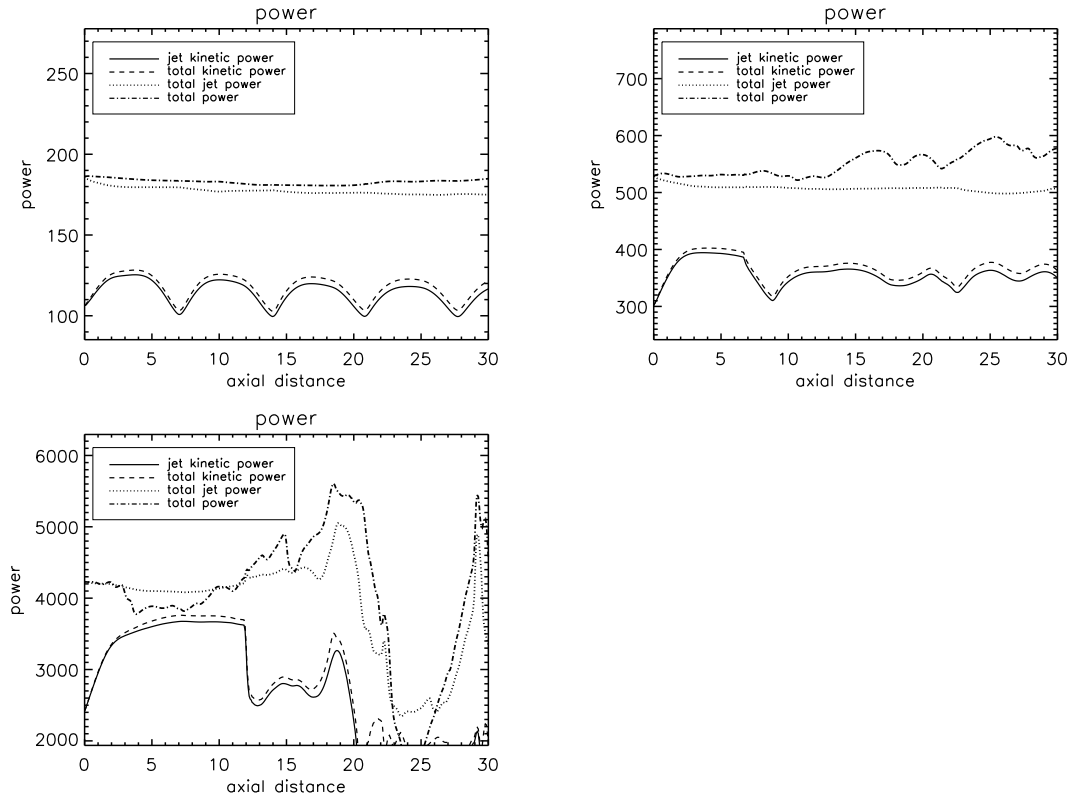


FIGURE 3.13: The integrated power over the entire circular cross-sections as a function of axial distance from the orifice boundary. A Mach 2 jet with density ratio $\eta = 0.1$ is taken, with over-pressure $\kappa = 2$ (top), $\kappa = 4$ (middle) and $\kappa = 16$ (lower panel). The time $t = 200$ corresponds to the end of the run.

We have created graphs that show the energy changes in the kinetic energy component of the jet and the total energy. Fig.3.13 shows this for three different over-pressures: $\kappa = 2, 4$ and 16 . The solid line in each panel indicates the power in the jet carried by kinetic energy. Thus, at this low Mach number, the kinetic energy is seen to oscillate smoothly between the diverging and converging sections of the jet. During the expansion phase of the jet, the thermal energy is converted into kinetic energy. This is then reversed when the jet then contracts. As seen from the diagrams, this process is very efficient.

The dashed line in each panel represents the total kinetic power the jet carries across the grid. We see there is a slight difference in kinetic power and total kinetic power, this is explained by the narrow sheath acting as a boundary

layer between the jet and the ambient medium.

As our flow is adiabatic, we know that the only loss of energy we can have is where mass flows out of the grid. Due to our use of staggered zones, we have minimised this energy loss. We also know from the definition of the work done by the jet, given by pdV , that we must account for this energy loss when considering the total energy of the jet. Therefore, the total power shown by the dotted and the dot-dashed line is the addition of kinetic energy and enthalpy in the flow. For $\kappa = 2$ we know that the jet converges to a steady state, and the total power is again higher due to energy being advected along the sheath.

Comparing the different energy diagrams for low and high over-pressures (see Fig.3.13), we see that for roughly the first 2.5 jet radii, all graphs follow a similar pattern as the main cause for energy change is the free expansion. The first notable difference occurs at the first shock, where for high over-pressures we know there is a Mach shock disk. We already know this decreases the velocity of the material that moves through it and that it does this by converting its kinetic energy into thermal energy. We also know that the Mach disk breaks the repeating shock pattern seen at low over-pressures. So it is surprising to see that for $\kappa = 4$, there is no overall significant energy loss from the jet shown by the dotted line, in fact, the energy remains quite steady, with fluctuations in total power being due to the vortices created through turbulence. This shows that the thick sheath of fast moving material surrounding the jet is protecting it from the changing 'effective pressure ratio' caused by turbulence. For $\kappa = 16$, we again see the beginning of the graph is dominated by the free expansion, however, we see a very high jet energy downstream coupled with a very high peak of total energy. The efficient energy transfer into the ambient medium is balanced by a reduction in the jet power upstream. This is then creating a 'feedback loop', whereas

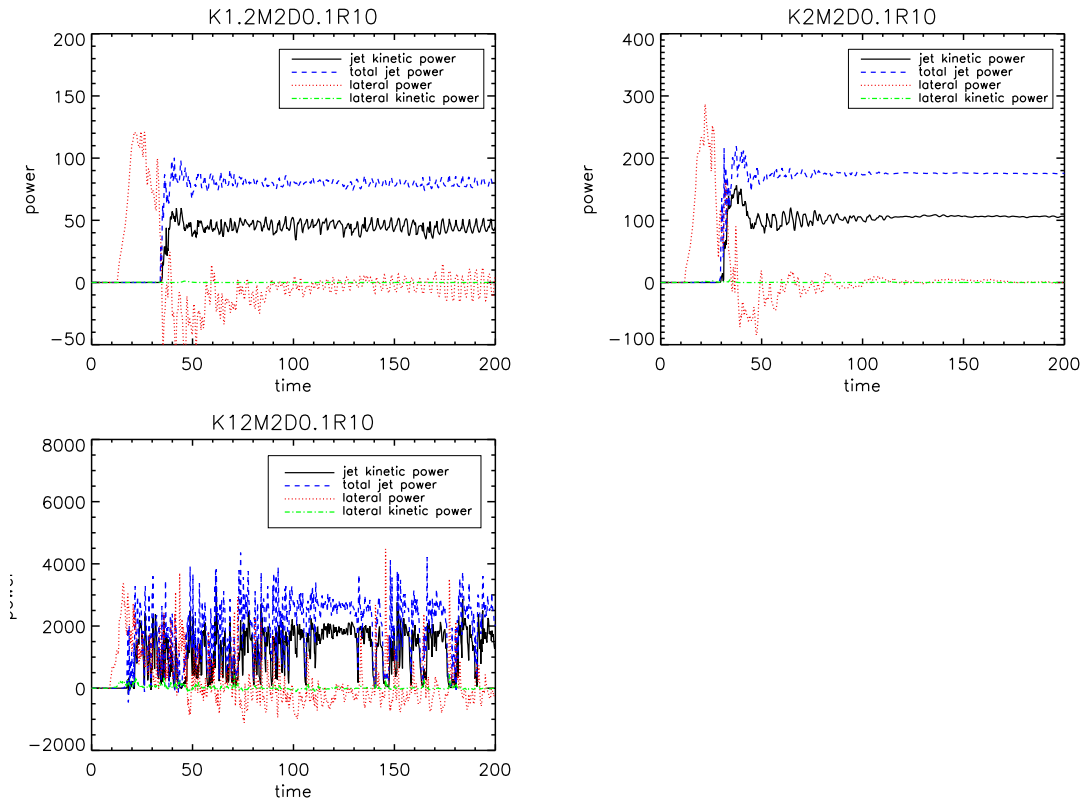


FIGURE 3.14: Evolution of the lateral and forward escape of energy for low density jets. The energy flux is out of a cylindrical surface, drawn with radius 180 zones and axial length 360 zones. Initially, the jet enters the grid and it takes ~ 30 time units to cross to the cylinder cap which is at 90% of the uniform grid length. These are the net power outflows in simulation units. The panel titles correspond to the pressure ratio K , the relative jet density D , and the ramp time allocated to the initial linear increase in jet velocity R .

the jet raises the pressure in the ambient medium, the 'effective pressure ratio' decreases, moving the stand off shock. Then, because the power of the flow upstream is decreased the 'effective pressure ratio' increases, moving the shock again. This then causes the large oscillations seen in Fig.3.10.

3.5.2 Lateral energy dispersion

Here we will look at how energy is dissipated laterally from the jet, completing our understanding of energy transfer. We want to see how the jet will effect the distant environment, we do this by finding the energy flux moving

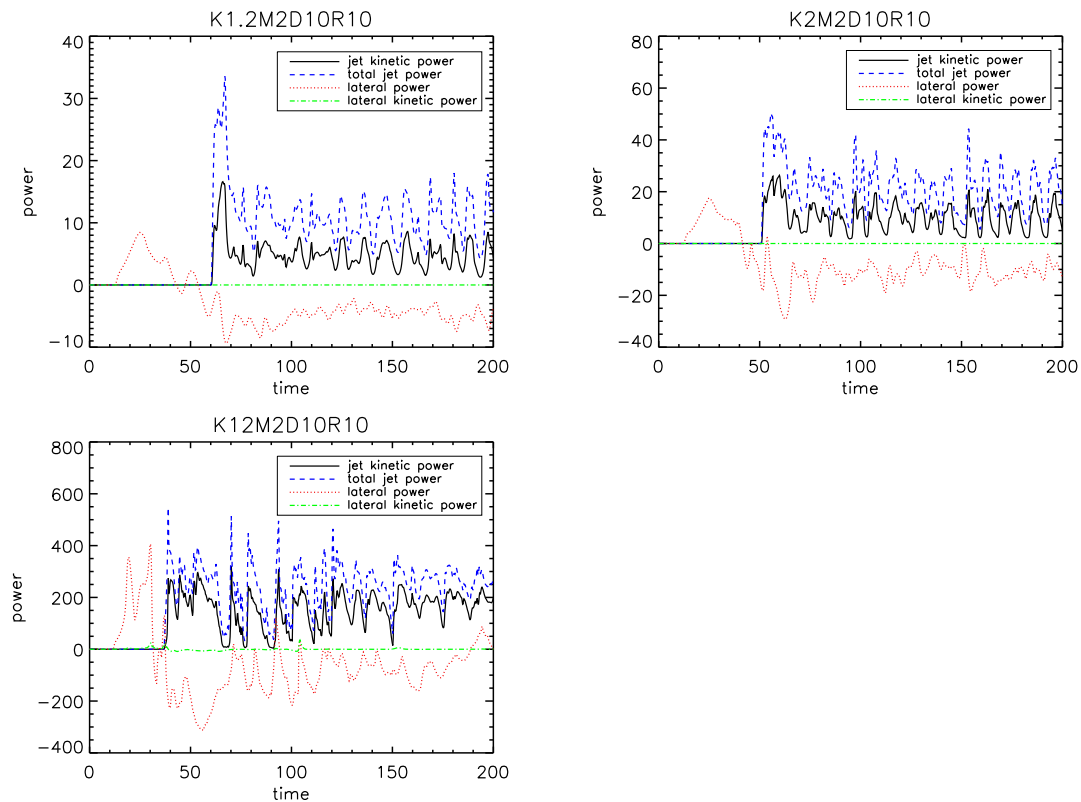


FIGURE 3.15: Evolution of the lateral and forward escape of energy for high density jets. The energy flux is out of a cylindrical surface, drawn with radius 180 zones and length 360 zones. Initially, the jet enters the grid and it takes ~ 30 time units to cross to the cylinder cap which is at 90% of the uniform grid length. These are the net power outflows in simulation units. The titles ensure the panels are correctly included with K corresponding to the pressure ratio, D to the relative jet density, and R to the time allocated to the initial linear increase in jet velocity.

through a cylinder of axial length 360 and radius 180 zones on the 400-200 standard Z-R domains; these are shown in Fig.3.14 and Fig.3.15.

We see that both flow patterns are capable of driving energy laterally out into the surroundings. It has been previously found that about 70% of the jet energy ends up as thermal energy in the ambient gas after the initial phase (Donohoe and Smith, 2016). This is very similar to our findings here when looking at the red line during the initial phase (up to roughly the first 40 time units) and comparing that to what we see in Fig.3.13. This is expected as the initial bow shock has to carve a path in the ambient medium and only injects a very small fraction of kinetic energy (shown by the green line).

From our graphs, we can also calculate the total amount of energy transferred laterally. We see that only for low over-pressures there is a net positive outflow of energy; only for $\kappa < 2.5$ and light jets. After the jet settles, time >100 , we then see small fluctuations in power where oscillations of $\sim 3.5\%$ are caused by the oscillating flow producing the screeching effect, meaning energy loss due to the produced sound waves. When looking at $\kappa > 6$ and light jets, we see a net negative in the flux of energy, therefore, the jet is taking in energy from its surroundings (see Fig.3.15). This is caused by the chaotic, turbulent nature of these flows; the turbulent jet disturbs the ambient gas and pulls it along. This then leaves a pocket that will be filled by the more distant lateral ambient material - causing the net negative energy transfer. We do note that there are significant fluctuations in the total jet power, with multiple positive spikes followed by periods of negative flux. This suggests that although the net flux is negative, it will provide little support to the far reaches of the ambient medium.

For heavy jets we can see the oscillations are much slower in frequency, however there is a greater negative inflow. This can be attributed to the fact a heavy, slow moving jet drags more ambient material along with its turbulent

vortices. Leaving a bigger pocket to be filled, thus there is a greater inflow of material.

For jets with a low density ratio and a low κ (shown in Fig.3.14), we notice the lateral flux experiences smooth oscillations about the zero line. However, these oscillations are also seen in the net lateral flux, implying a 'sloshing' of waves is present in the ambient medium. This could cause a shift in the stability of the jet, however, the power associated with these waves is comparatively small, meaning a small feedback effect is present but not enough to affect the stability of the jet.

Lateral waves are found only for intermediate over-pressures of the light jets, however, a comparatively small amount of energy is transferred this way. In contrast, the energy flux created by the motion of the turbulent vortexes reach 10% for the heavy jets. This could be related to the convection deduced from X-ray data (Kirkpatrick and McNamara, 2015; Hillel and Soker, 2017), which favour convection and mixing. On the other hand, many simulations yield high thermal energies and low kinetic/turbulent energy on large scales, suggesting that the convection in itself does not support an inward gas flow (Reynolds, Balbus, and Schekochihin, 2015; Weinberger et al., 2017).

3.6 The stand off distance

We define the shock stand off distance as the axial distance from the origin in which the first shock is located at the time of 200. As we know, a shock causes a sharp increase in pressure, we can easily find the first shock by looking along the axis and finding the increase in pressure. We also know that during the initial expansion phase of the jet, the pressure is constantly decreasing, so if we look for a pressure increase of 1% we can accurately determine the location of the first shock. However, an issue is introduced when we consider

that the shock is oscillating, and thus constantly moving. So we take a mean value and error for the last 10 time steps, these are the error bars seen in Fig.3.16.

Fig.3.16 displays the locations of the first three shocks, providing a visual interpretation of how the shock moves in relation to its over-pressure. As we are including the second and third shocks, we must account for sub-shocks that occur immediately after the initial shock. Therefore, we take a minimum distance of 40 zones before again searching for a rise in pressure.

The diamond shock pattern associated with the low over-pressures, leads to the steady movement of shock outwards, even up to the third shock. To better interpret these results, we have transferred our findings onto a log-log plot shown in Fig.3.17. On the graphs, we have incorporated two fitting lines. The initial one is represented by a dotted line, which essentially corresponds to a square root function, adjusted by a constant determined through trial and error. This confirms that the stand off distance is proportional to the initial over-pressure as discussed earlier (Eq.2.14). While this fit is almost perfect for the high pressure regime at low κ , this fit is not satisfactory. Consequently, we introduced our second fitting approach, represented by the dashed line. This approach involves a basic linear fit adjusted by a constant. Notably, the over-pressure at which the shocks shift to the alternate fitting method is denoted as $\kappa = 2.5$. This is the same kappa in which we saw the transition from the diamond flow pattern to the Mach shock disk. Because of this, we will divide the data into regions at the $\kappa = 2.5$ mark for the purpose of calculating the least squares fit. We generate the fits using IDL programme LINFIT in the form of $y = A + Bx$, calculating the error over the final 10 time units as the shock oscillates. The results of this can be seen in Table 3.2.

From this we can calculate the linear law describing $\kappa < 2.5$. We see that there is a fit of the form $y = 0.267 + 1.120x$ that can be converted to the power law

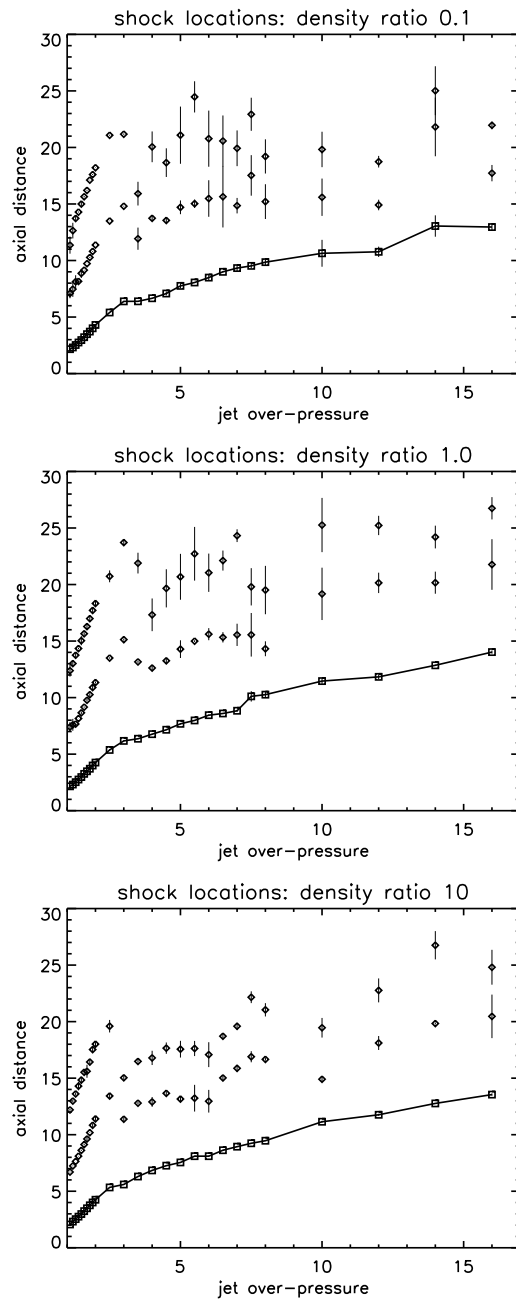


FIGURE 3.16: The shock front distances of the first three shocks along the jet axis as a function of the over-pressure, κ in units of the jet radius. Upper panel: Mach 2, density ratio $\eta = 0.1$. Middle panel: Mach 2, density ratio $\eta = 1$. Lower panel: Mach 2, density ratio $\eta = 10$.

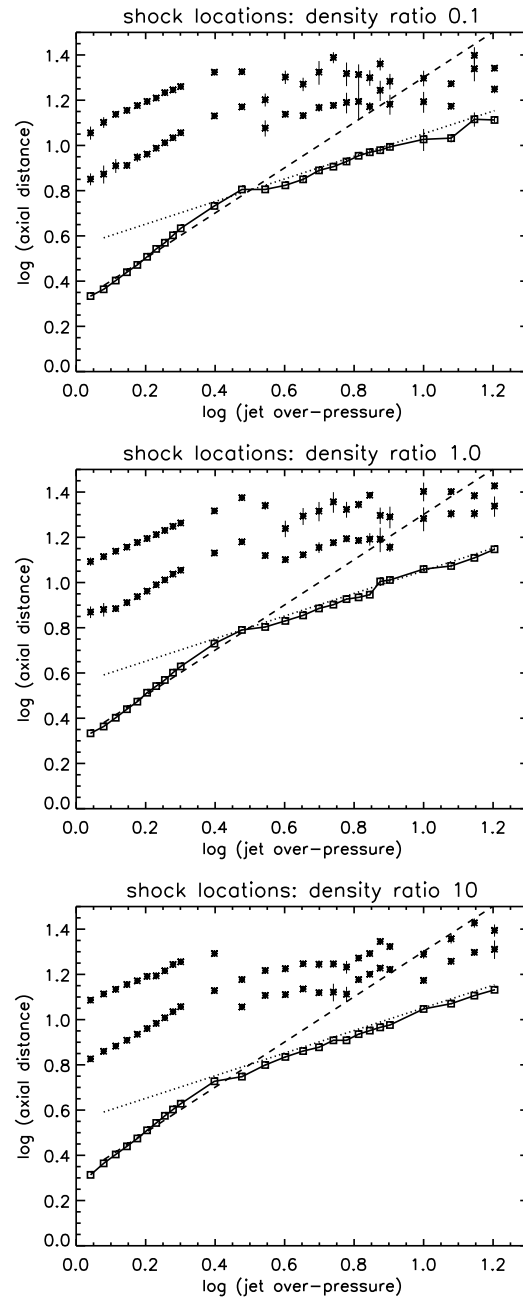


FIGURE 3.17: The logarithm of the shock distance of the first three shocks along the jet axis as a function of $\log \kappa$ in units of the jet radius. Upper panel: Mach 2, density ratio $\eta = 0.1$. Middle panel: Mach 2, density ratio $\eta = 1$. Lower panel: Mach 2, density ratio $\eta = 10$

TABLE 3.2: Least squares fits to log-log data in the linear form $y = A + Bx$ along with the sigma values generated by IDL programme LINFIT on using the root mean square values over the final 10 time units.

density ratio	shock number	κ range	y-intercept A	gradient B	y-intercept error σ	gradient error σ
$\eta = 0.1$	stand off	≤ 2.5	0.2607	1.2259	0.0004	0.0018
$\eta = 1$	stand off	≤ 2.5	0.2673	1.1973	0.0003	0.0017
$\eta = 10$	stand off	≤ 2.5	0.2673	1.1615	0.0002	0.0010
$\eta = 0.1$	second shock	≤ 2.5	0.7817	0.9053	0.0007	0.0023
$\eta = 1$	second shock	≤ 2.5	0.7831	0.8714	0.0012	0.0072
$\eta = 10$	second shock	≤ 2.5	0.7838	0.8714	0.0009	0.0072
$\eta = 0.1$	third shock	≤ 2.5	1.0601	0.6661	0.0015	0.0051
$\eta = 1$	third shock	≤ 2.5	1.0597	0.6653	0.0043	0.0210
$\eta = 10$	third shock	≤ 2.5	1.0610	0.6385	0.0027	0.0147
$\eta = 0.1$	stand off	> 2.5	0.6185	0.3903	0.0021	0.0044
$\eta = 1$	stand off	> 2.5	0.5286	0.5056	0.0028	0.0035
$\eta = 10$	stand off	> 2.5	0.5231	0.5078	1.1×10^{-6}	1.8×10^{-6}

$$D = 1.85\kappa^{1.20}.$$

We also calculate the power law describing the regime for $\kappa > 2.5$, which gives $X = 3.56\kappa^{1/2}$. The previously predicted square root behaviour has been shown, however, for light jets a flatter power law was needed. This makes sense when considering that the lighter jets were more heavily influenced by ambient pressure changes due to feedback from the oscillating shock.

For the second and third shocks, we see they are much more sporadic and do not fit into a power law (for high κ). This is expected as after the Mach shock disk the flow pattern becomes highly distorted and the shock fronts oscillate rapidly. Whereas for low κ , we see that a good approximation can be made for a linear increase. Because of this, we can look to quantify this for each shock seen in Fig.3.16 in the form of $D_i = a + b\kappa$ by simple subtraction. We thus find for the first shock:

$$D_1 = 1.81 + 2.43(\kappa - 1) \quad \eta = 0.1 \quad (3.2)$$

$$D_1 = 1.82 + 2.41(\kappa - 1) \quad \eta = 1.0 \quad (3.3)$$

$$D_1 = 1.82 + 2.41(\kappa - 1) \quad \eta = 10 \quad (3.4)$$

The distance to the next shock is then easily expressed:

$$D_2 - D_1 = 4.56 + 2.47(\kappa - 1) \quad \eta = 0.1 \quad (3.5)$$

$$D_2 - D_1 = 4.39 + 2.61(\kappa - 1) \quad \eta = 1.0 \quad (3.6)$$

$$D_2 - D_1 = 4.37 + 2.63(\kappa - 1) \quad \eta = 10 \quad (3.7)$$

The distance out to the third shock is:

$$D_3 - D_2 = 5.61 + 1.30(\kappa - 1) \quad \eta = 0.1 \quad (3.8)$$

$$D_3 - D_2 = 5.69 + 1.30(\kappa - 1) \quad \eta = 1.0 \quad (3.9)$$

$$D_3 - D_2 = 5.46 + 1.28(\kappa - 1) \quad \eta = 10 \quad (3.10)$$

Looking at the equations for the first shock (Eq 3.2, 3.3, 3.4), we see they are roughly equal across the different density ratios. Therefore, we have found linear equations for Mach 2 jets, with a $\kappa < 2.5$, describing the location of the first shock in terms of only its pressure ratio. It now seems to be possible to extract information about the jet source only by observing the distance between the first shock and the source. For $\kappa > 2.5$, the density ratio cannot be excluded due to feedback. With further study exploring a greater range of Mach numbers, pressure ratios and density ratios, you may also be able to

extract the Mach number and density ratio just by measuring the distance to the first shock.

3.7 Higher Mach numbers

Throughout this thesis, we have primarily focussed on the detailed analysis of Mach 2 jets, however, some time also went into developing results for higher Mach numbers, outlined in the abstract. Our findings show that higher Mach numbers follow a very similar pattern to those of Mach 2.

To determine the effect of the Mach number on the jet, we plot the stand off distance at varying Mach numbers with constant pressure and density ratios. We choose a density ratio of 10 to isolate the affect of the Mach number, as the higher density jets show more stability, as seen in the results for Mach 2. We see an almost linear relationship between Mach number and stand off distance (see Fig.3.18), which is expected as the Mach number should stretch the jet along the axis.

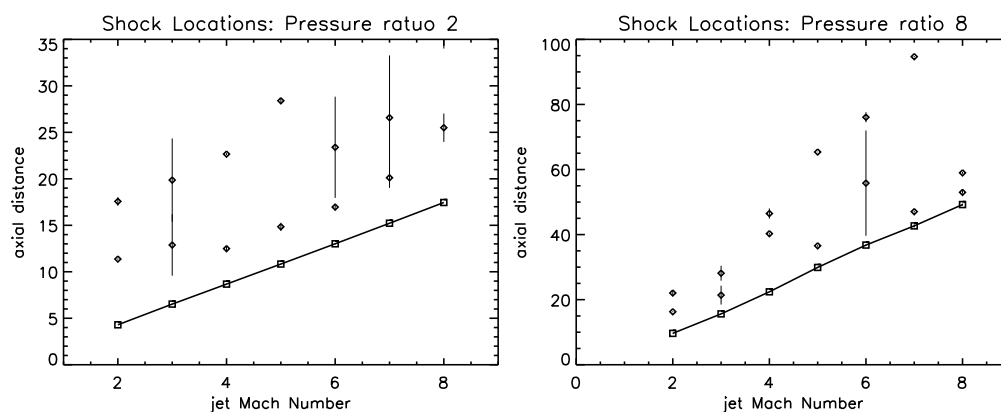


FIGURE 3.18: The distribution of the stand off distance with varying Mach number with constant $\kappa = 2$ (left), $\kappa = 8$ (right) and density ratio $\eta = 10$.

At higher Mach numbers we still see the three distinct flow patterns, however, the transition occurs at a different overpressure due to the effect of the Mach number.

The Mach 4 jets show that a diamond shock pattern dominates at over-pressures below 7, and a transformation to a Mach shock disk occurs between 7 and 8. For $\kappa = 2$, the Mach 4 jets have very similar structures with the length being scaled proportional to the Mach number which was expected (see Fig 3.18). These jets inject considerably more turbulence into the ambient medium. This, in-turn lowers the effective overpressure, which supports the diamond shock pattern and prolongs the transition to a Mach shock disk. This implies that as you increase Mach number you will have to simulate much greater over-pressures to see this transition.

A key point to note is that the feedback loop effect can have drastic effects on jet structure at higher Mach numbers. In extreme circumstances, shocks spreading from the unsteady jet can permanently raise the ambient pressure, causing a catastrophic collapse of the shock configuration (as shown in Fig.3.19 and Fig.3.20). We only see this result happen for Mach 8, most likely due to the extreme energy in the jet. We did not simulate higher than this but would expect this effect to have worsened. Unsurprisingly we did not see this effect for the higher density jets which showed increased stability. We leave further study and analysis of higher Mach numbers for future work.

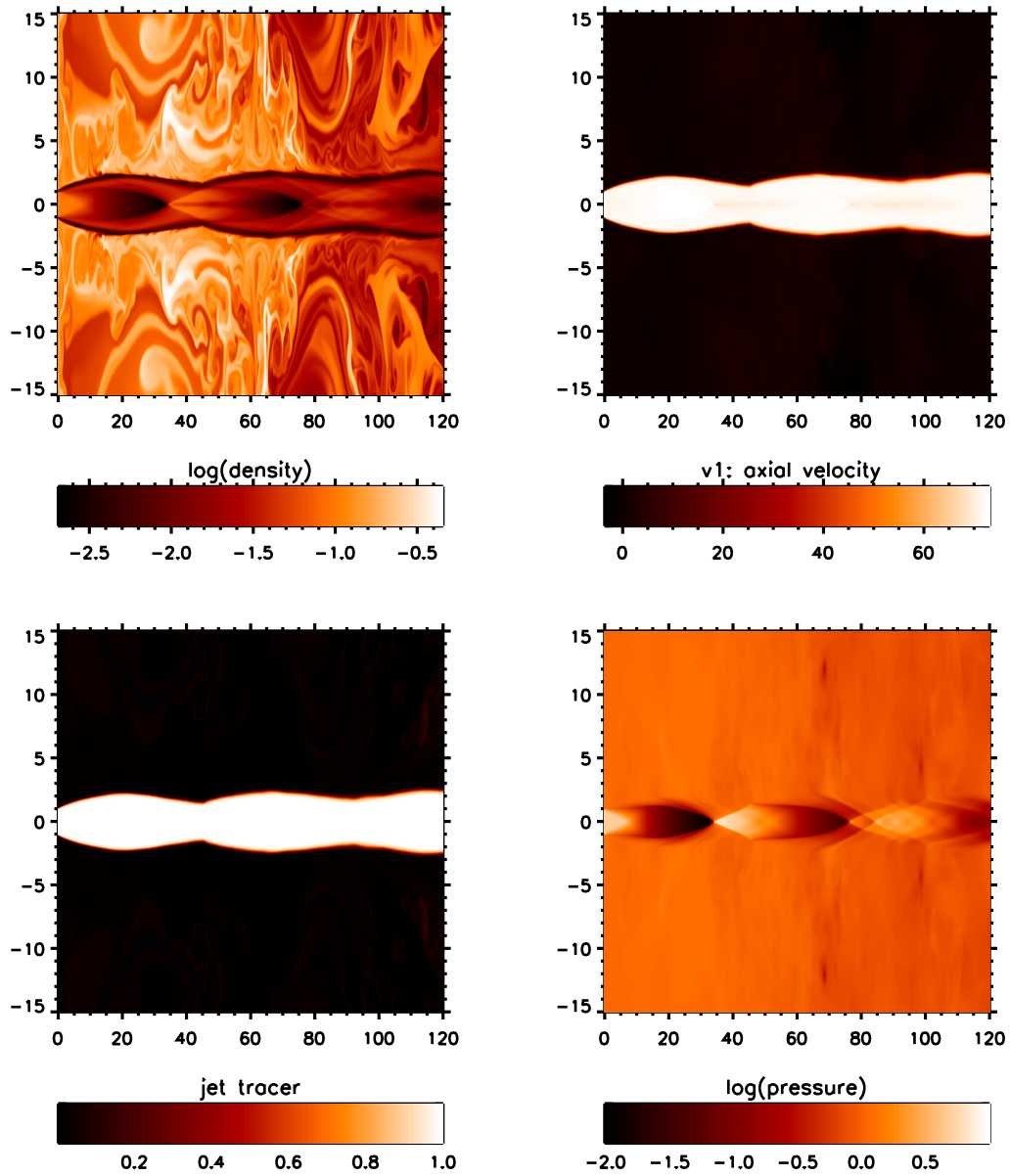


FIGURE 3.19: The distributions of physical parameters for a Mach 8 jet with over-pressure $\kappa = 8$ and density ratio $\eta = 0.1$. The time $t = 200$ corresponds to the end of the run. The length scale is in units of the jet radius. Upper-left panel: density, upper-right panel: axial velocity component, lower-left: tracer for jet gas, lower-right: pressure.

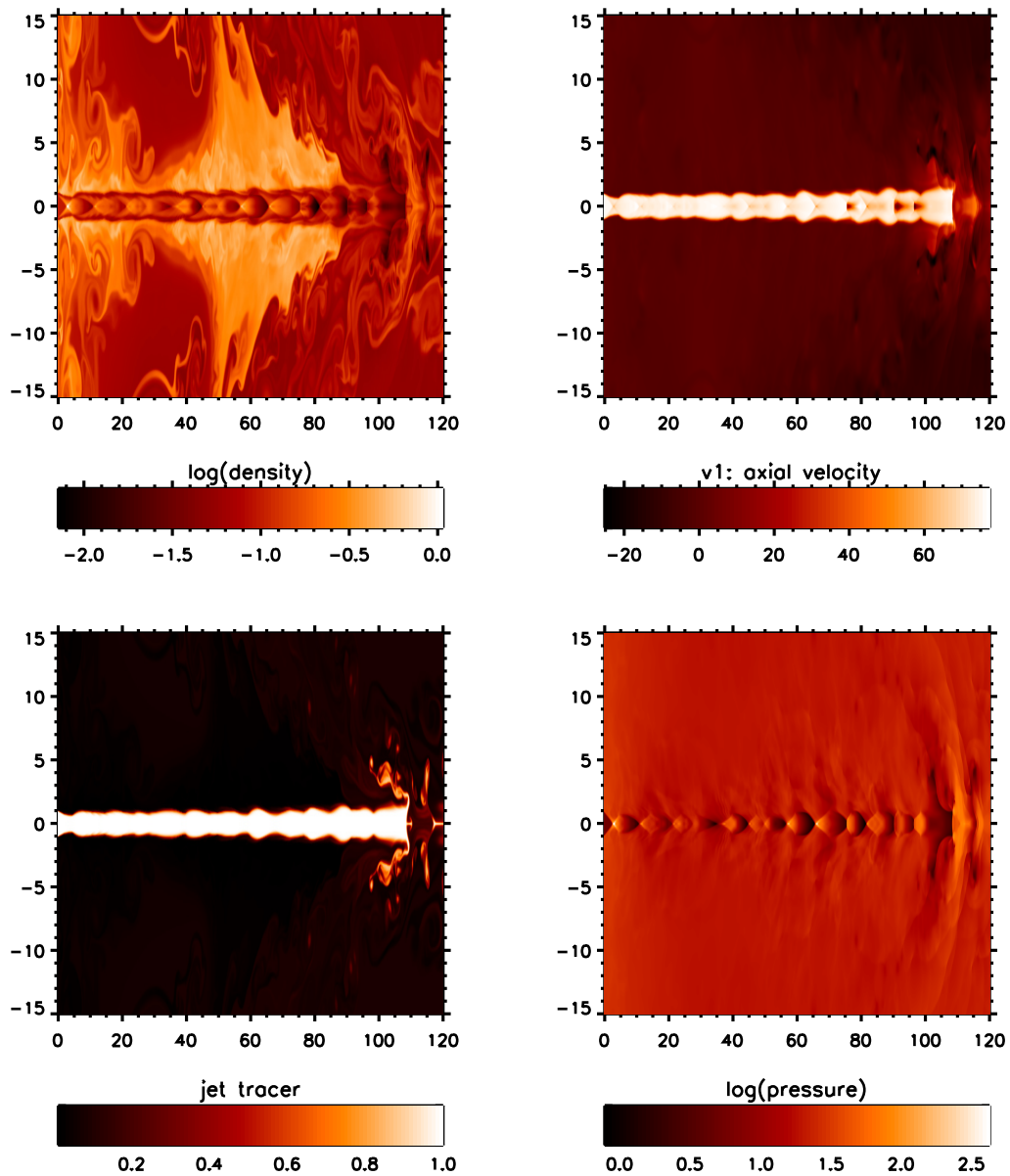


FIGURE 3.20: The distributions of physical parameters for a Mach 8 jet with over-pressure $\kappa = 9$ and density ratio $\eta = 0.1$. The time $t = 200$ corresponds to the end of the run. The length scale is in units of the jet radius. Upper-left panel: density, upper-right panel: axial velocity component, lower-left: tracer for jet gas, lower-right: pressure.

Chapter 4

Conclusions

Throughout this thesis, we have completed a comprehensive analysis of a simple supersonic hydrodynamic flow into an ambient medium. As this is the first analysis of its kind, we have primarily focused on the Mach number of two. After analysing over a range of different initial conditions, we have shown that:

1. High density jets generate quite steady channels and shock patterns with slow oscillations. Light jets also settle down except for high over-pressures that oscillate with high amplitude.
2. Three basic flow patterns are found. At low over-pressures, a diamond shock pattern that involves intersecting oblique shocks occurs. At high over-pressures, a normal Mach shock disc intercepts the oblique shocks at a triple point (a circle) due to the wide divergent-convergent structure.
3. At intermediate over-pressures, a series of Mach shock discs can occur downstream of the stand-off shock, while at high over-pressures a turbulent plume is predicted.
4. The oscillations drive shocks into the ambient medium that generate lateral sound waves. However, the major effect is to promote the advection of

ambient gas away from the nozzle and draw more material towards the jet axis.

After our findings, we can now better understand observed jets from a variety of man-made and astrophysical outflows, and structures they form.

At low over-pressures, we have shown that it is possible for the flow to form a stationary flow pattern but only out to the first shock. Subsequent shocks will require approximation. This low over-pressure regime follows a diamond shock pattern, present out to over-pressures of about 4.

Whereas at high over-pressures, a Mach shock disk is present and the flow follows Mach reflection. This in-turn leads to the significant oscillations of the shock, which depends on the jets density ratio, meaning we are not able to accurately represent its location.

We have plotted graphs showing the distance of the shock fronts from the origin, with efforts to account for the oscillations by using a mean of the shock position over multiple time units. For the low over-pressures with the diamond shock flow pattern, we have shown that the first will be located at about 1.82 -1.84 jet radii from the origin. The theory tells us that pressure signals will move through the jet with proportion to the Mach angle θ where $\sin \theta = 1/M$. This means that we can calculate that the pressure along the axis can only fall after a distance of $\sqrt{3} \sim 1.732$, which is consistent with our results.

Through the investigation of energy transport, it has been shown that a variety of jets will propagate sound waves far into the ambient medium. The sound waves generated are associated to what is known as jet screeching. We have shown that light jets are less stable leading to faster oscillations meaning a higher pitched screech will be heard. Despite the jet's ability to propagate sound waves far into the ambient medium, our study has shown that on a

more local scale, the turbulent vortices created by the jet pull ambient material along. This process leaves pockets where ambient material can flow in laterally, resulting in a net negative energy flux in some cases. It is important to note that along the axis the total energy flux is conserved by regular energy conversions between kinetic and thermal/enthalpy. This is shown in the middle panel of Fig. 3.14, where a small drop in power in the direction of the jet is balanced by the positive lateral flux.

We have identified a simple formula describing the location of the Mach shock disk (see Eq. 2.14). Rearranging this result to remove the Mach number gives:

$$D_1 = 1.38(\rho_{jet}v_{jet}^2 / p_{amb})^{1/2} \quad (4.1)$$

Thus we have deduced the location of shock depends on only two variables. These are the initial ram pressure at the nozzle and the ambient pressure. It now seems to be possible to extract information about the jet source only by observing the string of knots that it produces. With further study, you may also be able to extract the Mach number and pressure ratio from measuring this distance.

Throughout this thesis, we have excluded the effect from any external forces; however, these will affect the shock stability. For example cooling and chemistry will further decrease the stability of the shock, whereas implementation of a magnetic field could increase shock stability by providing a dampening force. It is also important to note we used a completely uniform ambient medium, whereas most astrophysical jets will have a pressure gradient in the ambient medium due to gravity.

We previously discussed that two distinct jet types exist for radio galaxies. We have produced a type of duality for low Mach number jets between edge-darkened and edge-brightened structures. We could say the formation of the

two types is due to a contrast in the parameters of the surrounding medium and the jets overpressure. We have shown for a pressure ratio > 4 we have created a plume that resembles what is seen in FR1 galaxies. Conversely, we have shown that for pressure ratios < 2 we can create bright stationary spots located away from the source resembling FR2 galaxies. However, as these jets will be affected by a vast array of forces we did not include, we cannot confirm this relationship, but the hope is further research will lead to this being confirmed.

Bibliography

- Adamson Jr, TC and James Arthur Nicholls (1959). "On the structure of jets from highly underexpanded nozzles into still air". In: *Journal of the Aerospace sciences* 26.1, pp. 16–24.
- Aithekar, Vijay (2019). "A Research Review Article on Journey of A Star: From Beginning to End". In: *International Journal of Trend in Scientific Research and Development*. URL: <https://api.semanticscholar.org/CorpusID:203387280>.
- Bashir, Musavir et al. (2020). "Wall Pressure Measurements Beneath the Supersonic Jets in an Abruptly Augmented Nozzle". In: URL: <https://api.semanticscholar.org/CorpusID:250602584>.
- Begelman, Mitchell C., Roger D. Blandford, and Martin J. Rees (1984). "Theory of extragalactic radio sources". In: *Rev. Mod. Phys.* 56 (2), pp. 255–351. DOI: [10.1103/RevModPhys.56.255](https://doi.org/10.1103/RevModPhys.56.255). URL: <https://link.aps.org/doi/10.1103/RevModPhys.56.255>.
- Blake, G. M. (Jan. 1972). "Fluid dynamic stability of double radio sources". In: 156, p. 67. DOI: [10.1093/mnras/156.1.67](https://doi.org/10.1093/mnras/156.1.67).
- Blandford, R. D. and M. J. Rees (Dec. 1974). "A "twin-exhaust" model for double radio sources." In: 169, pp. 395–415. DOI: [10.1093/mnras/169.3.395](https://doi.org/10.1093/mnras/169.3.395).
- Bridle, Alan H. et al. (Sept. 1994). "Deep VLA Imaging of Twelve Extended 3CR Quasars". In: 108, p. 766. DOI: [10.1086/117112](https://doi.org/10.1086/117112).
- Buckley F. I., Jr. (Jan. 1975). "Mach disk location in jets in co-flowing airstreams". In: *AIAA Journal* 13, p. 105. DOI: [10.2514/3.49638](https://doi.org/10.2514/3.49638).

- Buehrke, T., R. Mundt, and T. P. Ray (July 1988). "A detailed study of HH 34 and its associated jet." In: 200, pp. 99–119.
- Carlson, D. J. and C. H. Lewis (Apr. 1964). "Normal shock location in under-expanded gas and gas-particle jets". In: *AIAA Journal* 2.4, pp. 776–777. DOI: [10.2514/3.2409](https://doi.org/10.2514/3.2409).
- Chanson, Hubert (2004). "13 - Summary of basic hydraulic principles". In: *Hydraulics of Open Channel Flow (Second Edition)*. Ed. by Hubert Chanson. Second Edition. Oxford: Butterworth-Heinemann, pp. 249–252. ISBN: 978-0-7506-5978-9. DOI: <https://doi.org/10.1016/B978-075065978-9/50020-9>. URL: <https://www.sciencedirect.com/science/article/pii/B9780750659789500209>.
- Chatterjee, K et al. (Sept. 2019). "Accelerating AGN jets to parsec scales using general relativistic MHD simulations". In: *Monthly Notices of the Royal Astronomical Society* 490.2, pp. 2200–2218. ISSN: 0035-8711. DOI: [10.1093/mnras/stz2626](https://doi.org/10.1093/mnras/stz2626). eprint: <https://academic.oup.com/mnras/article-pdf/490/2/2200/32334152/stz2626.pdf>. URL: <https://doi.org/10.1093/mnras/stz2626>.
- Davidor, W. and S. S. Penner (Aug. 1971). "Shock standoff distances and Mach-disk diameters in underexpanded sonic jets". In: *AIAA Journal* 9.8, pp. 1651–1653. DOI: [10.2514/3.6410](https://doi.org/10.2514/3.6410).
- Derlopa, S. et al. (Apr. 2019). "High-velocity string of knots in the outburst of the planetary nebula Hb4". In: 484.3, pp. 3746–3754. DOI: [10.1093/mnras/stz193](https://doi.org/10.1093/mnras/stz193). arXiv: [1901.05767](https://arxiv.org/abs/1901.05767) [astro-ph.SR].
- Dionatos, Odysseas and Manuel Güdel (Jan. 2017). "Feedback of atomic jets from embedded protostars in NGC 1333". In: 597, A64, A64. DOI: [10.1051/0004-6361/201629179](https://doi.org/10.1051/0004-6361/201629179). arXiv: [1608.06131](https://arxiv.org/abs/1608.06131) [astro-ph.SR].
- Donohoe, J. and M. D. Smith (May 2016). "The physical structure of radio galaxies explored with three-dimensional simulations". In: 458, pp. 558–574. DOI: [10.1093/mnras/stw335](https://doi.org/10.1093/mnras/stw335). arXiv: [1601.08052](https://arxiv.org/abs/1601.08052).

- Dubois, Yohan et al. (Dec. 2010). "Jet-regulated cooling catastrophe". In: 409.3, pp. 985–1001. DOI: [10.1111/j.1365-2966.2010.17338.x](https://doi.org/10.1111/j.1365-2966.2010.17338.x). arXiv: [1004.1851](https://arxiv.org/abs/1004.1851) [astro-ph.CO].
- Ehlert, Kristian et al. (Apr. 2022). "Self-regulated AGN feedback of light jets in cool-core galaxy clusters". In: *arXiv e-prints*, arXiv:2204.01765, arXiv:2204.01765. arXiv: [2204.01765](https://arxiv.org/abs/2204.01765) [astro-ph.GA].
- Fabian, A. C. (Sept. 2012). "Observational Evidence of Active Galactic Nuclei Feedback". In: 50, pp. 455–489. DOI: [10.1146/annurev-astro-081811-125521](https://doi.org/10.1146/annurev-astro-081811-125521). arXiv: [1204.4114](https://arxiv.org/abs/1204.4114) [astro-ph.CO].
- Franquet, Erwin et al. (Aug. 2015). "Free underexpanded jets in a quiescent medium: A review". In: *Progress in Aerospace Sciences* 77, pp. 25–53. DOI: [10.1016/j.paerosci.2015.06.006](https://doi.org/10.1016/j.paerosci.2015.06.006).
- Franquet, Erwin et al. (2015). "Free underexpanded jets in a quiescent medium: A review". In: *Progress in Aerospace Sciences* 77, pp. 25–53. ISSN: 0376-0421. DOI: <https://doi.org/10.1016/j.paerosci.2015.06.006>. URL: <https://www.sciencedirect.com/science/article/pii/S0376042115000548>.
- Ghassemi, Majid and Azadeh Shahidian (2017). "Chapter 4 - Fluid Mechanics". In: *Nano and Bio Heat Transfer and Fluid Flow*. Ed. by Majid Ghassemi and Azadeh Shahidian. Oxford: Academic Press, pp. 57–87. ISBN: 978-0-12-803779-9. DOI: <https://doi.org/10.1016/B978-0-12-803779-9.00004-2>. URL: <https://www.sciencedirect.com/science/article/pii/B9780128037799000042>.
- Gómez, J. L. et al. (June 1997). "Hydrodynamical Models of Superluminal Sources". In: 482.1, pp. L33–L36. DOI: [10.1086/310671](https://doi.org/10.1086/310671).
- Hansen, C. J. et al. (Nov. 2008). "Water vapour jets inside the plume of gas leaving Enceladus". In: 456.7221, pp. 477–479. DOI: [10.1038/nature07542](https://doi.org/10.1038/nature07542).
- Hardee, P. E. (Nov. 1979). "On the configuration and propagation of jets in extragalactic radio sources." In: 234, pp. 47–55. DOI: [10.1086/157471](https://doi.org/10.1086/157471).

- H.E.S.S. Collaboration et al. (2018). “The population of TeV pulsar wind nebulae in the H.E.S.S. Galactic Plane Survey”. In: *A&A* 612, A2. DOI: [10.1051/0004-6361/201629377](https://doi.org/10.1051/0004-6361/201629377). URL: <https://doi.org/10.1051/0004-6361/201629377>.
- Hillel, Shlomi and Noam Soker (Mar. 2017). “Hitomi observations of Perseus support heating by mixing”. In: 466.1, pp. L39–L42. DOI: [10.1093/mnrasl/slw231](https://doi.org/10.1093/mnrasl/slw231). arXiv: [1608.07818](https://arxiv.org/abs/1608.07818) [astro-ph.GA].
- Irie, T. et al. (2003). “Characteristics of the mach disk in the underexpanded jet in which the back pressure continuously changes with time”. In: *Journal of Thermal Science* 12.2, pp. 132–137. DOI: [10.1007/s11630-003-0054-4](https://doi.org/10.1007/s11630-003-0054-4). URL: <https://doi.org/10.1007/s11630-003-0054-4>.
- Kellermann, K. I. (2002). “Tuning in to radio galaxies”. In: *Nature* 417.6886, pp. 224–224. DOI: [10.1038/417224a](https://doi.org/10.1038/417224a). URL: <https://doi.org/10.1038/417224a>.
- Kirkpatrick, C. C. and B. R. McNamara (Oct. 2015). “Hot outflows in galaxy clusters”. In: 452.4, pp. 4361–4376. DOI: [10.1093/mnras/stv1574](https://doi.org/10.1093/mnras/stv1574). arXiv: [1507.05973](https://arxiv.org/abs/1507.05973) [astro-ph.GA].
- Knee, L. B. G. and G. Sandell (Sept. 2000). “The molecular outflows in NGC 1333”. In: 361, pp. 671–684.
- Kwok, Sun (1988). “The Formation of Planetary Nebulae”. In: *Mass Outflows from Stars and Galactic Nuclei*. Ed. by Luciana Bianchi and Roberto Gilmozzi. Dordrecht: Springer Netherlands, pp. 123–136. ISBN: 978-94-009-2941-8.
- Liger-Belair, Gérard, Daniel Cordier, and Robert Georges (Sept. 2019). “Under-expanded supersonic CO₂ freezing jets during champagne cork popping”. In: *Science Advances* 5.9, eaav5528. DOI: [10.1126/sciadv.aav5528](https://doi.org/10.1126/sciadv.aav5528).
- Livio, Mario (Jan. 2000). “Jets in Planetary Nebulae”. In: *Asymmetrical Planetary Nebulae II: From Origins to Microstructures*. Ed. by J. H. Kastner, N. Soker, and S. Rappaport. Vol. 199. Astronomical Society of the Pacific Conference Series, p. 243.

- Martí, J. M., M. Perucho, and J. L. Gómez (Nov. 2016). “The Internal Structure of overpressured, Magnetized, Relativistic Jets”. In: 831.2, 163, p. 163. DOI: [10.3847/0004-637X/831/2/163](https://doi.org/10.3847/0004-637X/831/2/163). arXiv: 1609.00593 [astro-ph.HE].
- Massi, Fabrizio et al. (May 2022). “NIR spectroscopic survey of protostellar jets in the star forming region IC 1396N”. In: *arXiv e-prints*, arXiv:2205.09425, arXiv:2205.09425. arXiv: 2205.09425 [astro-ph.GA].
- Meyer, Eileen T. et al. (Apr. 2016). “An HST proper-motion study of the optical jet in 3C 264: Direct Evidence for the Internal Shock Model”. In: *AAS/High Energy Astrophysics Division #15*. Vol. 15. AAS/High Energy Astrophysics Division, 100.01, p. 100.01.
- Mignone, A. et al. (May 2007). “PLUTO: A Numerical Code for Computational Astrophysics”. In: 170.1, pp. 228–242. DOI: [10.1086/513316](https://doi.org/10.1086/513316). arXiv: [astro-ph/0701854](https://arxiv.org/abs/astro-ph/0701854) [astro-ph].
- Mizuno, Yosuke (2022). “GRMHD Simulations and Modeling for Jet Formation and Acceleration Region in AGNs”. In: *Universe* 8.2. ISSN: 2218-1997. DOI: [10.3390/universe8020085](https://doi.org/10.3390/universe8020085). URL: <https://www.mdpi.com/2218-1997/8/2/85>.
- Moya-Torregrosa, I. et al. (June 2021). “Magnetized relativistic jets and helical magnetic fields. I. Dynamics”. In: 650, A60, A60. DOI: [10.1051/0004-6361/202037898](https://doi.org/10.1051/0004-6361/202037898).
- Norman, M. L. et al. (Sept. 1982). “Structure and dynamics of supersonic jets.” In: 113, pp. 285–302.
- Ogden, Darcy E. et al. (Feb. 2008). “Numerical simulations of volcanic jets: Importance of vent overpressure”. In: *Journal of Geophysical Research (Solid Earth)* 113.B2, B02204, B02204. DOI: [10.1029/2007JB005133](https://doi.org/10.1029/2007JB005133).
- Palmer, Jennifer L. and Ronald K. Hanson (1998). “Application of Method of Characteristics to Underexpanded, Freejet Flows with Vibrational Nonequilibrium”. In: *AIAA Journal* 36.2, pp. 193–200. DOI: [10.2514/2.7501](https://doi.org/10.2514/2.7501). eprint:

- <https://doi.org/10.2514/2.7501>. URL: <https://doi.org/10.2514/2.7501>.
- Park, Jongho et al. (2021). “Jet Collimation and Acceleration in the Giant Radio Galaxy NGC 315”. In: *The Astrophysical Journal* 909.1, p. 76. DOI: [10.3847/1538-4357/abd6ee](https://doi.org/10.3847/1538-4357/abd6ee). URL: <https://dx.doi.org/10.3847/1538-4357/abd6ee>.
- Perley, R. A., A. G. Willis, and J. S. Scott (1979). “The structure of the radio jets in 3C449”. In: *Nature* 281.5731, pp. 437–442. DOI: [10.1038/281437a0](https://doi.org/10.1038/281437a0). URL: <https://doi.org/10.1038/281437a0>.
- Perlman, Eric S. et al. (Apr. 2001). “The Optical-Near-Infrared Spectrum of the M87 Jet from Hubble Space Telescope Observations”. In: 551.1, pp. 206–222. DOI: [10.1086/320052](https://doi.org/10.1086/320052). arXiv: [astro-ph/0012044](https://arxiv.org/abs/astro-ph/0012044) [astro-ph].
- Porth, Oliver and Serguei S. Komissarov (Sept. 2015). “Causality and stability of cosmic jets”. In: 452.2, pp. 1089–1104. DOI: [10.1093/mnras/stv1295](https://doi.org/10.1093/mnras/stv1295). arXiv: [1408.3318](https://arxiv.org/abs/1408.3318) [astro-ph.HE].
- Powell, A. (Dec. 1953). “On the Mechanism of Choked Jet Noise”. In: *Proceedings of the Physical Society B* 66.12, pp. 1039–1056. DOI: [10.1088/0370-1301/66/12/306](https://doi.org/10.1088/0370-1301/66/12/306).
- Rawlings, Steve and Matt J. Jarvis (Dec. 2004). “Evidence that powerful radio jets have a profound influence on the evolution of galaxies”. In: *Monthly Notices of the Royal Astronomical Society* 355.3, pp. L9–L12. ISSN: 0035-8711. DOI: [10.1111/j.1365-2966.2004.08234.x](https://doi.org/10.1111/j.1365-2966.2004.08234.x). eprint: <https://academic.oup.com/mnras/article-pdf/355/3/L9/18491180/355-3-L9.pdf>. URL: <https://doi.org/10.1111/j.1365-2966.2004.08234.x>.
- Reynolds, Christopher S., Steven A. Balbus, and Alexander A. Schekochihin (Dec. 2015). “Inefficient Driving of Bulk Turbulence By Active Galactic Nuclei in a Hydrodynamic Model of the Intracluster Medium”. In: 815.1, 41, p. 41. DOI: [10.1088/0004-637X/815/1/41](https://doi.org/10.1088/0004-637X/815/1/41). arXiv: [1511.03271](https://arxiv.org/abs/1511.03271) [astro-ph.HE].

- Sanders, R. H. (Mar. 1983). "The reconfinement of jets." In: 266, pp. 73–81.
DOI: [10.1086/160760](https://doi.org/10.1086/160760).
- Smith, Michael D. (2012). *Astrophysical Jets and Beams*. Cambridge Astrophysics. Cambridge University Press. DOI: [10.1017/CB09780511994562](https://doi.org/10.1017/CB09780511994562).
- Soker, Noam and Mario Livio (1994). "Disks and jets in planetary nebulae". In: *Astrophysical Journal, Part 1 (ISSN 0004-637X)*, vol. 421, no. 1, p. 219-224 421, pp. 219–224.
- Tam, C. K. W. (Jan. 1995). "Supersonic jet noise". In: *Annual Review of Fluid Mechanics* 27, pp. 17–43. DOI: [10.1146/annurev.fl.27.010195.000313](https://doi.org/10.1146/annurev.fl.27.010195.000313).
- Tanaka, Shuta J. and Fumio Takahara (2010). "A MODEL OF THE SPECTRAL EVOLUTION OF PULSAR WIND NEBULAE". In: *The Astrophysical Journal* 715.2, p. 1248. DOI: [10.1088/0004-637X/715/2/1248](https://doi.org/10.1088/0004-637X/715/2/1248). URL: <https://dx.doi.org/10.1088/0004-637X/715/2/1248>.
- Vincent, J. B. et al. (Nov. 2016). "Summer fireworks on comet 67P". In: 462, S184–S194. DOI: [10.1093/mnras/stw2409](https://doi.org/10.1093/mnras/stw2409). arXiv: [1609.07743](https://arxiv.org/abs/1609.07743) [astro-ph.EP].
- Waugh, J. et al. (Aug. 2009). "A jet production experiment using the high-repetition rate Astra laser". In: *Astrophysics and Space Science* 322, pp. 31–35. DOI: [10.1007/s10509-009-0036-4](https://doi.org/10.1007/s10509-009-0036-4).
- Weinberger, Rainer et al. (Oct. 2017). "Simulating the interaction of jets with the intracluster medium". In: 470.4, pp. 4530–4546. DOI: [10.1093/mnras/stx1409](https://doi.org/10.1093/mnras/stx1409). arXiv: [1703.09223](https://arxiv.org/abs/1703.09223) [astro-ph.GA].
- Young, David S. De (1991). "Astrophysical Jets". In: *Science* 252.5004, pp. 389–396. DOI: [10.1126/science.252.5004.389](https://doi.org/10.1126/science.252.5004.389). eprint: <https://www.science.org/doi/pdf/10.1126/science.252.5004.389>. URL: <https://www.science.org/doi/abs/10.1126/science.252.5004.389>.
- Zemskov, R. et al. (Jan. 2024). "Laboratory modeling of YSO jets collimation by a large-scale divergent interstellar magnetic field". In: 681, A37, A37. DOI: [10.1051/0004-6361/202245251](https://doi.org/10.1051/0004-6361/202245251).

Appendix A

Mach 2 Images

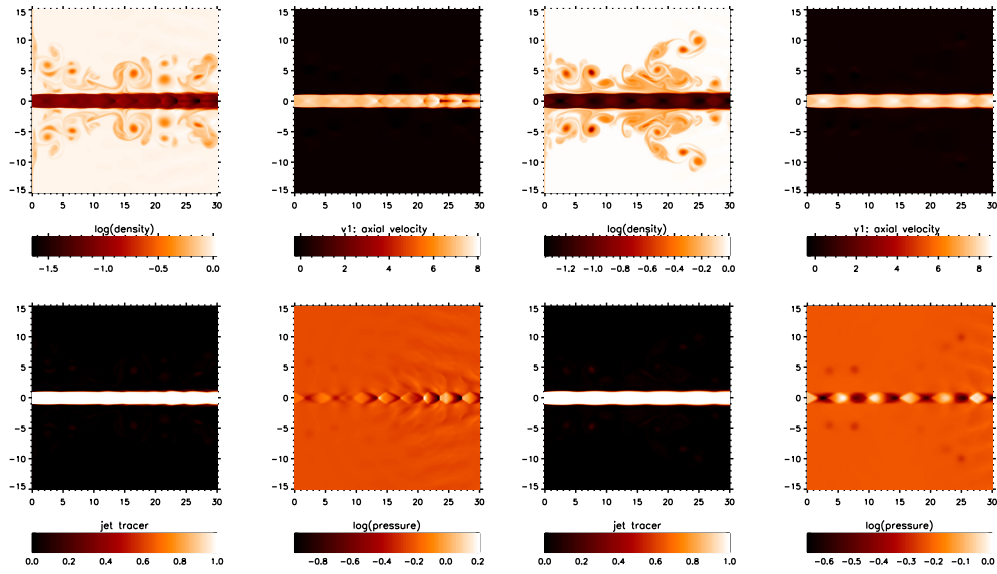


FIGURE A.1: Mach 2, over-pressure $\kappa = 1.2$ (left panel) $\kappa = 1.4$ (right panel) and density ratio $\eta = 0.1$.

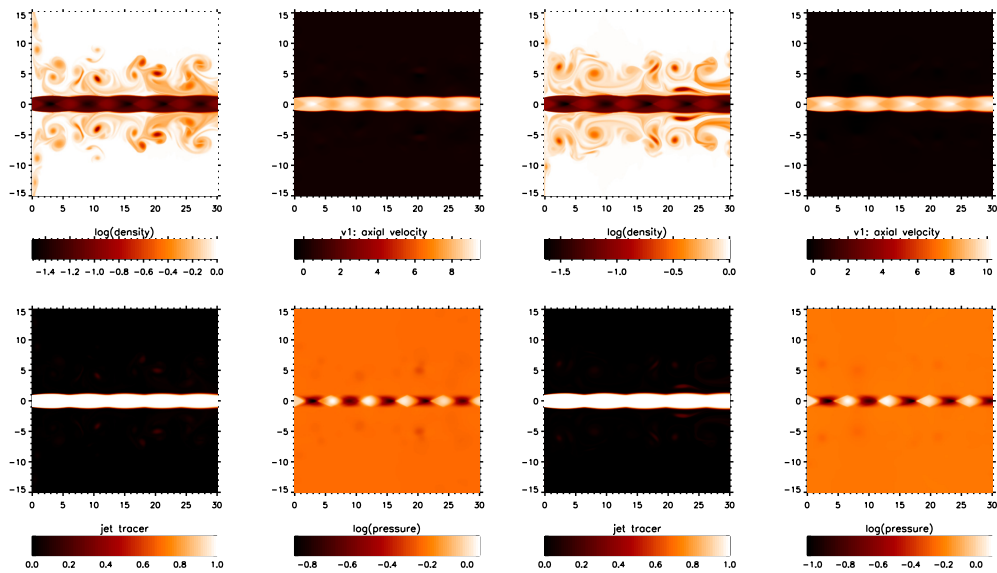


FIGURE A.2: Mach 2, over-pressure $\kappa = 1.6$ (left panel) $\kappa = 1.8$ (right panel) and density ratio $\eta = 0.1$.

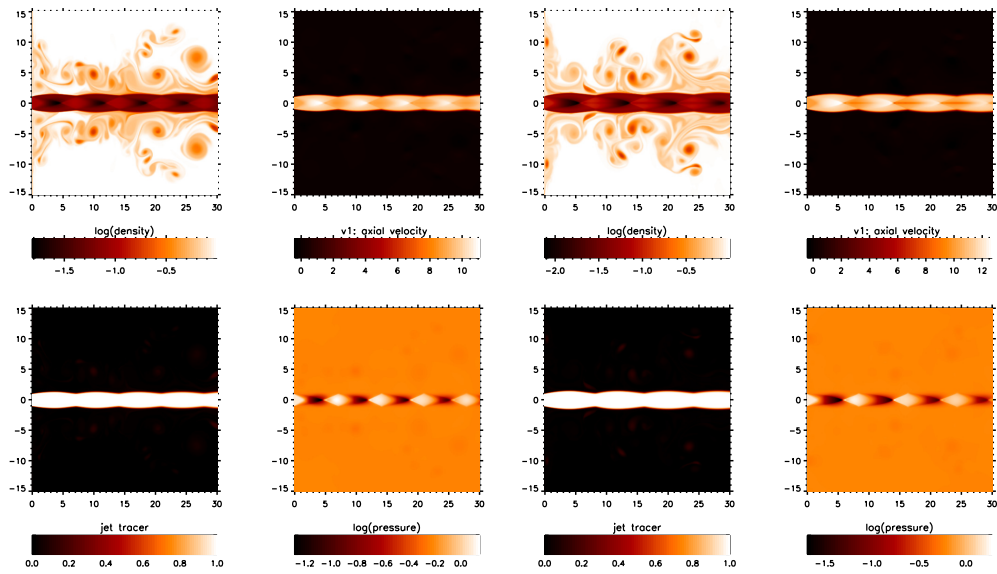


FIGURE A.3: Mach 2, over-pressure $\kappa = 2$ (left panel) $\kappa = 2.5$ (right panel) and density ratio $\eta = 0.1$.

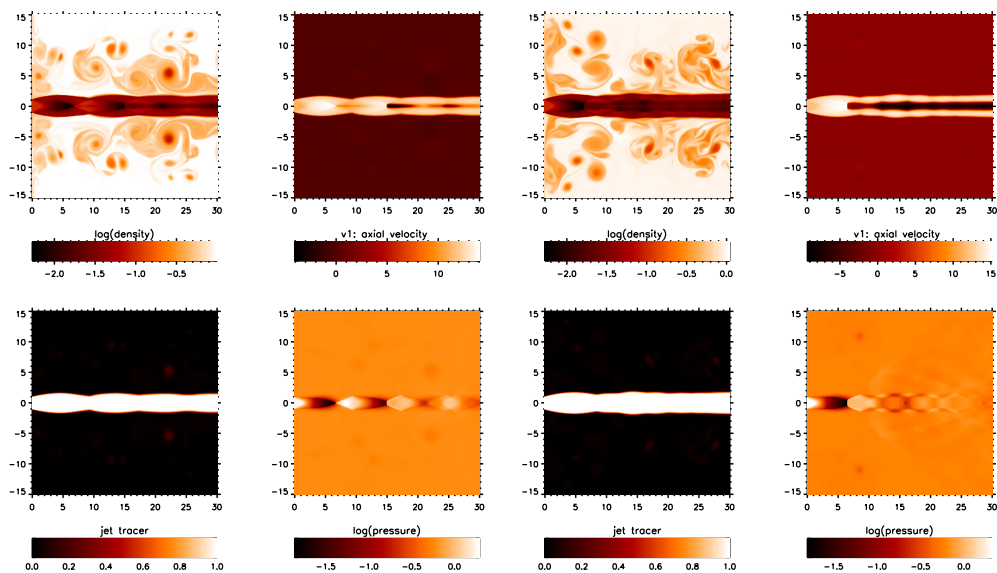


FIGURE A.4: Mach 2, over-pressure $\kappa = 3$ (left panel) $\kappa = 3.5$ (right panel) and density ratio $\eta = 0.1$.

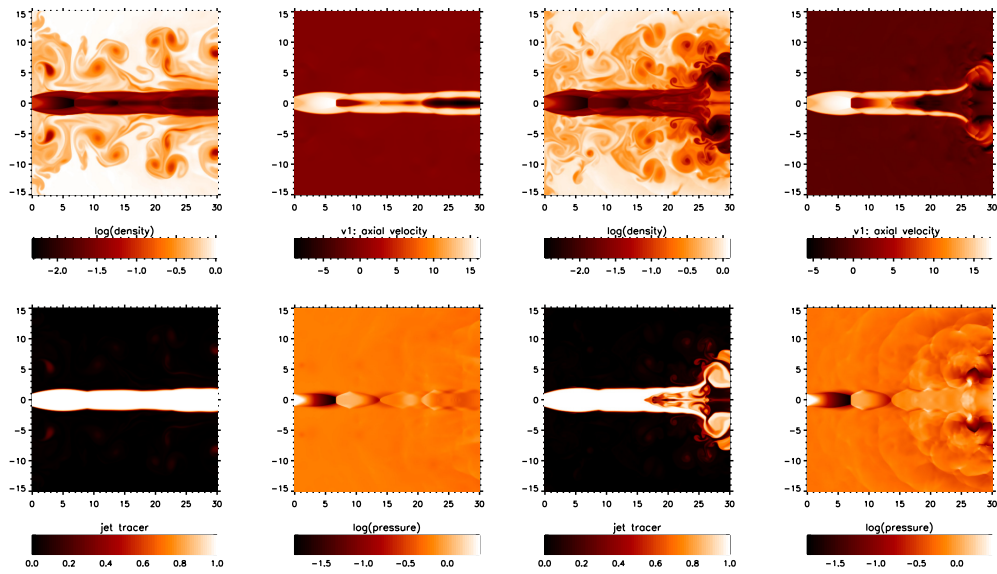


FIGURE A.5: Mach 2, over-pressure $\kappa = 4$ (left panel) $\kappa = 4.5$ (right panel) and density ratio $\eta = 0.1$.

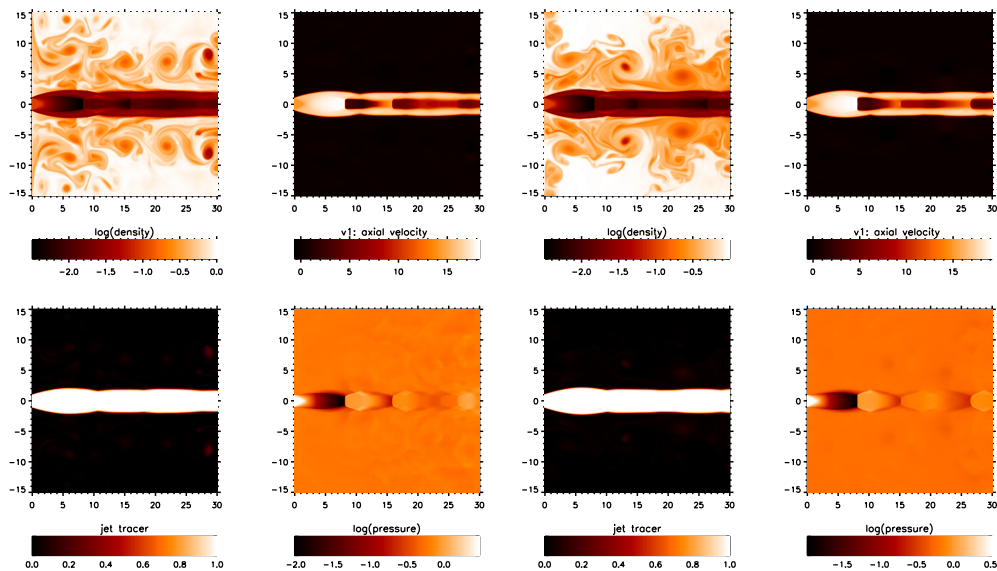


FIGURE A.6: Mach 2, over-pressure $\kappa = 5$ (left panel) $\kappa = 5.5$ (right panel) and density ratio $\eta = 0.1$.

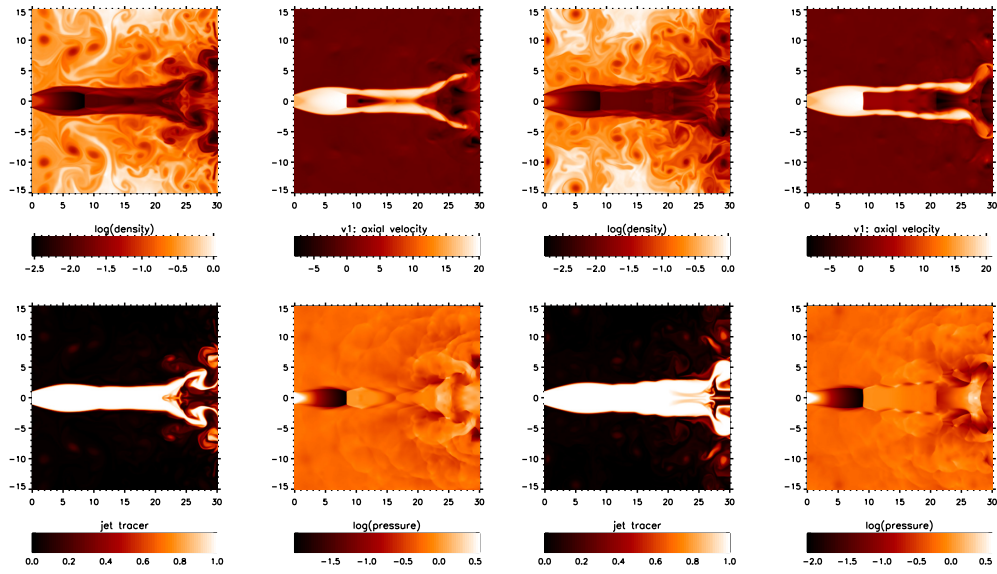


FIGURE A.7: Mach 2, over-pressure $\kappa = 6$ (left panel) $\kappa = 6.5$ (right panel) and density ratio $\eta = 0.1$.

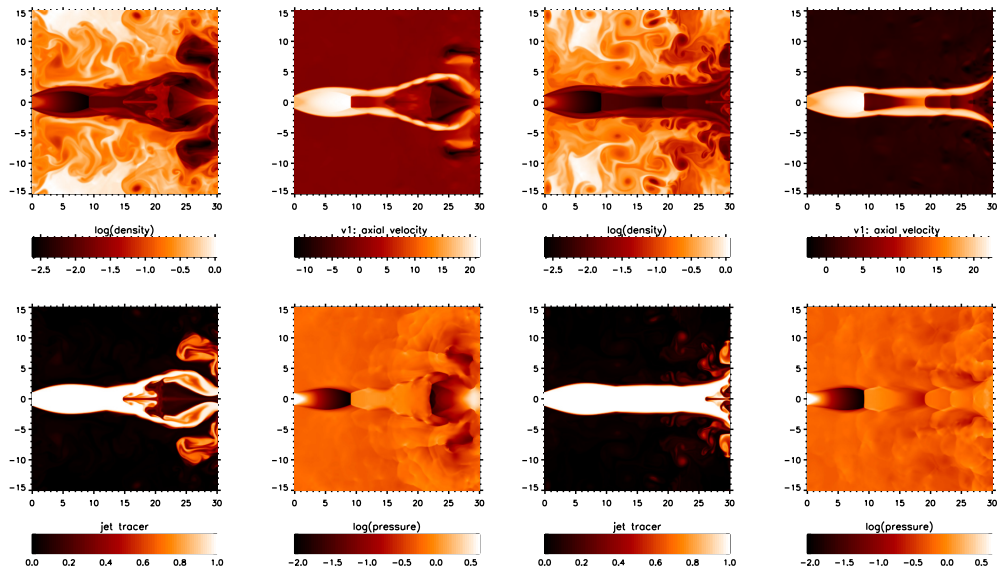


FIGURE A.8: Mach 2, over-pressure $\kappa = 7$ (left panel) $\kappa = 7.5$ (right panel) and density ratio $\eta = 0.1$.

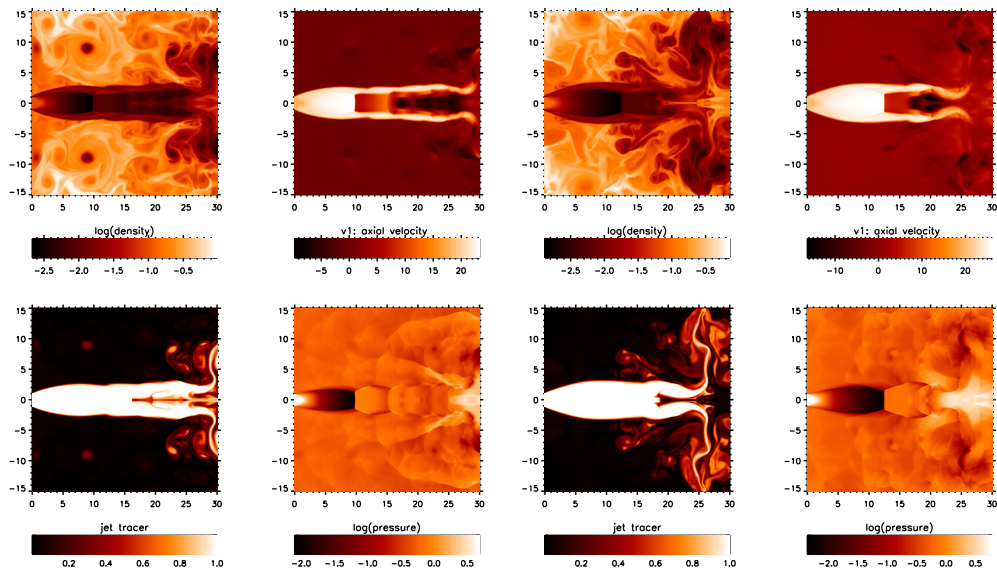


FIGURE A.9: Mach 2, over-pressure $\kappa = 8$ (left panel) $\kappa = 10$ (right panel) and density ratio $\eta = 0.1$.

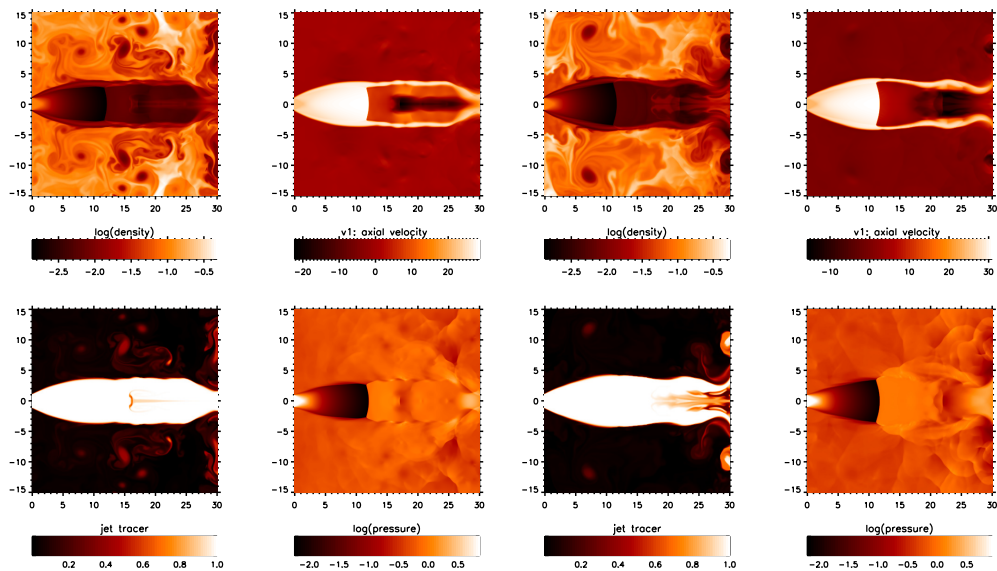


FIGURE A.10: Mach 2, over-pressure $\kappa = 12$ (left panel) $\kappa = 14$ (right panel) and density ratio $\eta = 0.1$.

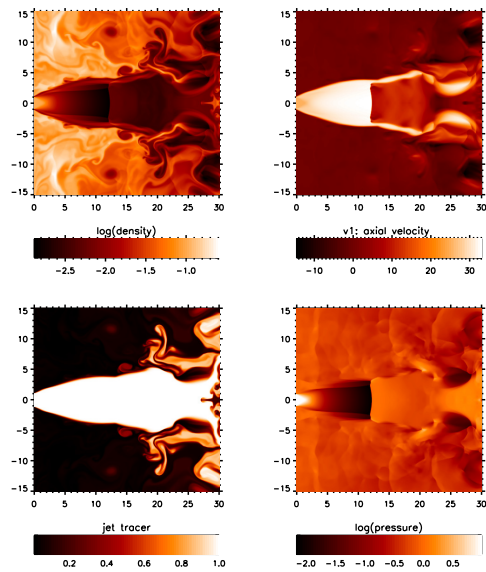


FIGURE A.11: Mach 2, over-pressure $\kappa = 16$ and density ratio $\eta = 0.1$.

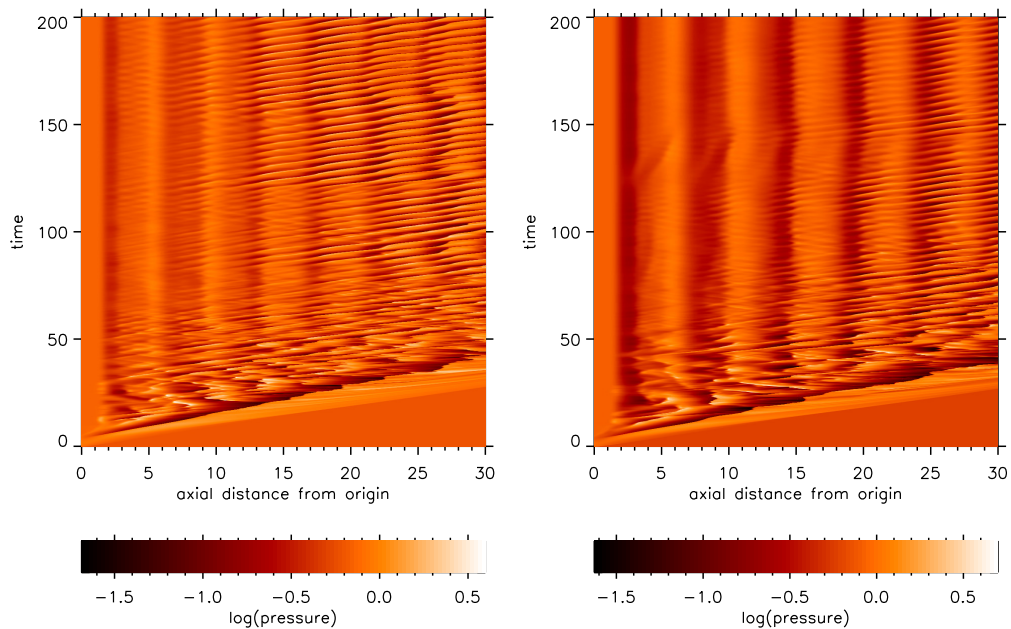


FIGURE A.12: Mach 2, over-pressure $\kappa = 1.2$ (left panel) $\kappa = 1.4$ (right panel) and density ratio $\eta = 0.1$.

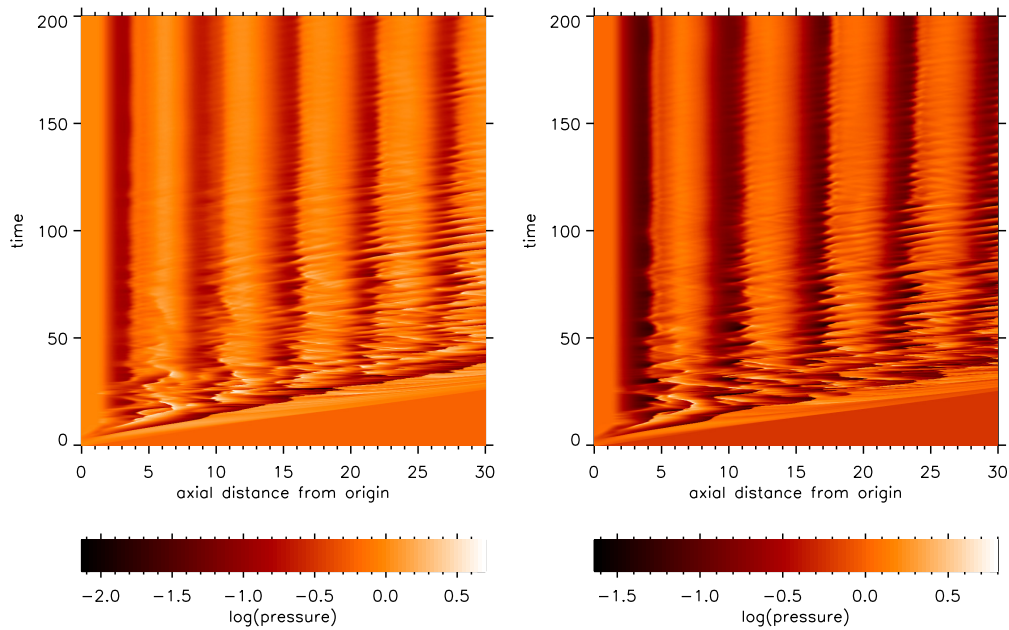


FIGURE A.13: Mach 2, over-pressure $\kappa = 1.6$ (left panel) $\kappa = 1.8$ (right panel) and density ratio $\eta = 0.1$.

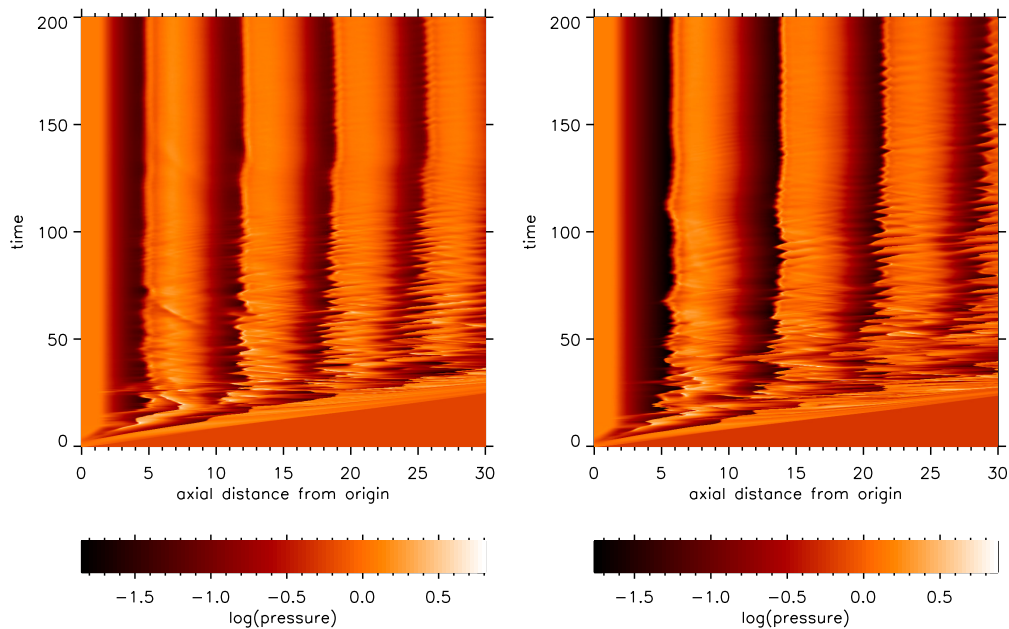


FIGURE A.14: Mach 2, over-pressure $\kappa = 2$ (left panel) $\kappa = 2.5$ (right panel) and density ratio $\eta = 0.1$.

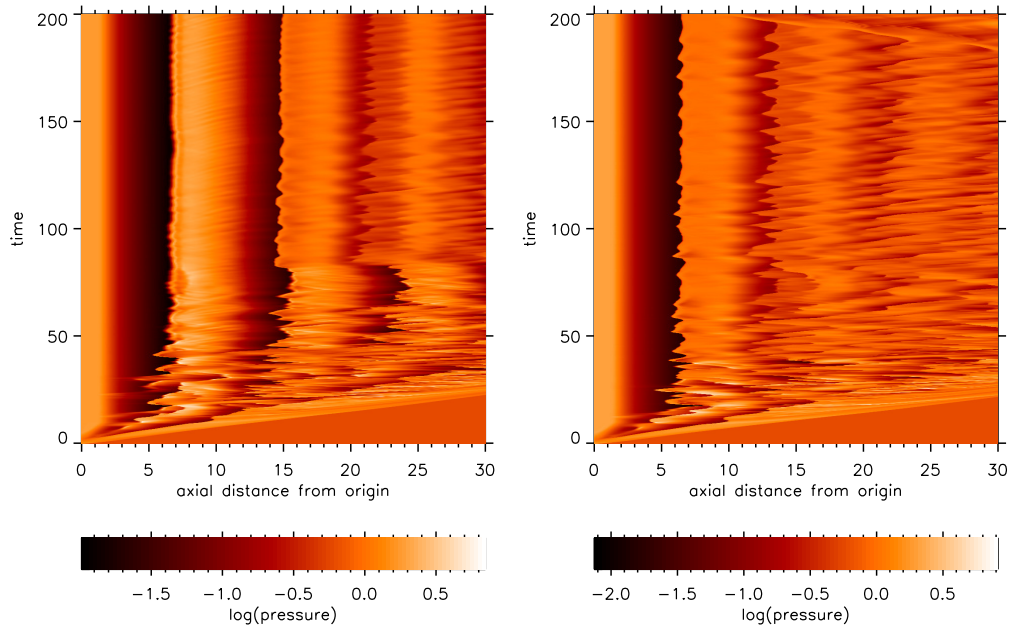


FIGURE A.15: Mach 2, over-pressure $\kappa = 3$ (left panel) $\kappa = 3.5$ (right panel) and density ratio $\eta = 0.1$.

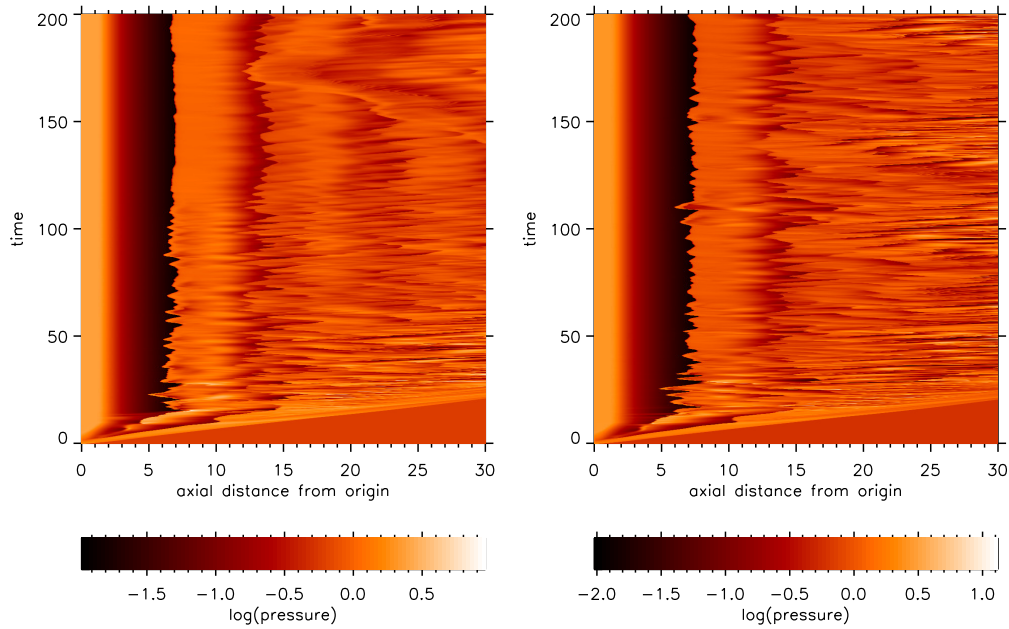


FIGURE A.16: Mach 2, over-pressure $\kappa = 4$ (left panel) $\kappa = 4.5$ (right panel) and density ratio $\eta = 0.1$.

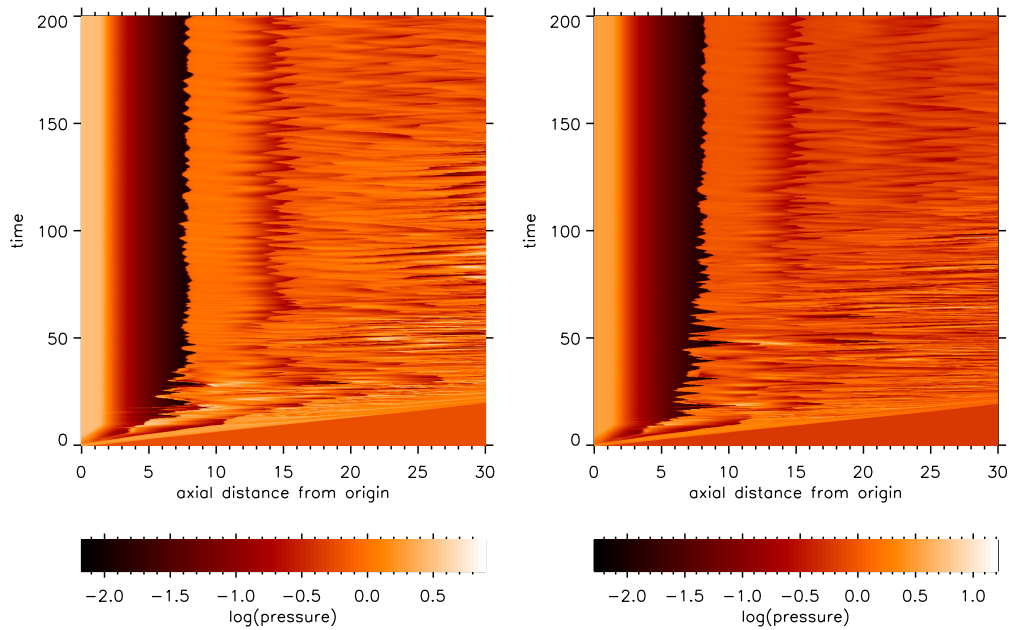


FIGURE A.17: Mach 2, over-pressure $\kappa = 5$ (left panel) $\kappa = 5.5$ (right panel) and density ratio $\eta = 0.1$.

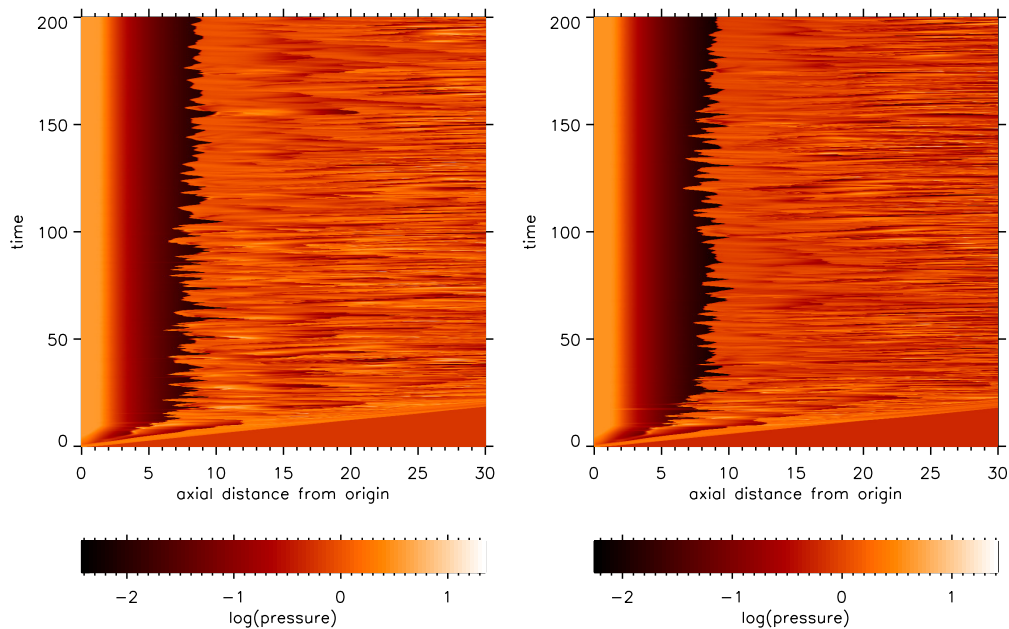


FIGURE A.18: Mach 2, over-pressure $\kappa = 6$ (left panel) $\kappa = 6.5$ (right panel) and density ratio $\eta = 0.1$.

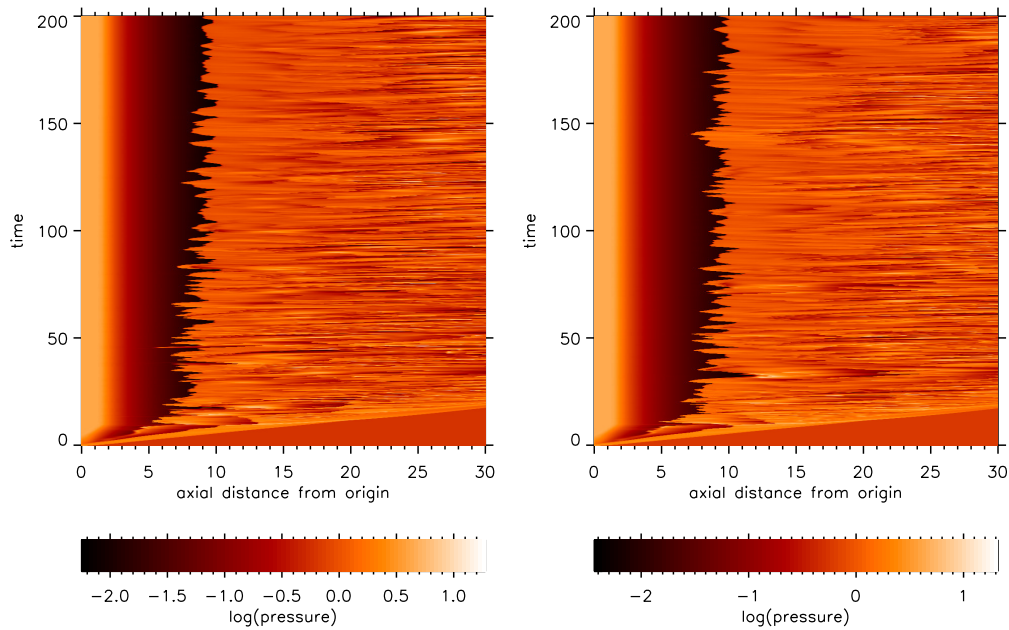


FIGURE A.19: Mach 2, over-pressure $\kappa = 7$ (left panel) $\kappa = 7.5$ (right panel) and density ratio $\eta = 0.1$.

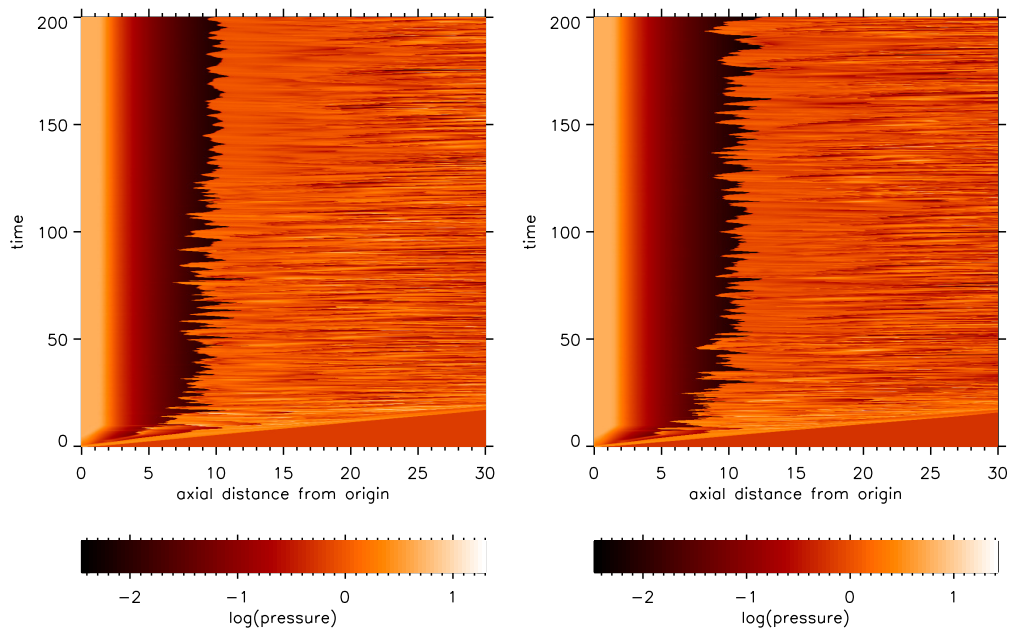


FIGURE A.20: Mach 2, over-pressure $\kappa = 8$ (left panel) $\kappa = 10$ (right panel) and density ratio $\eta = 0.1$.

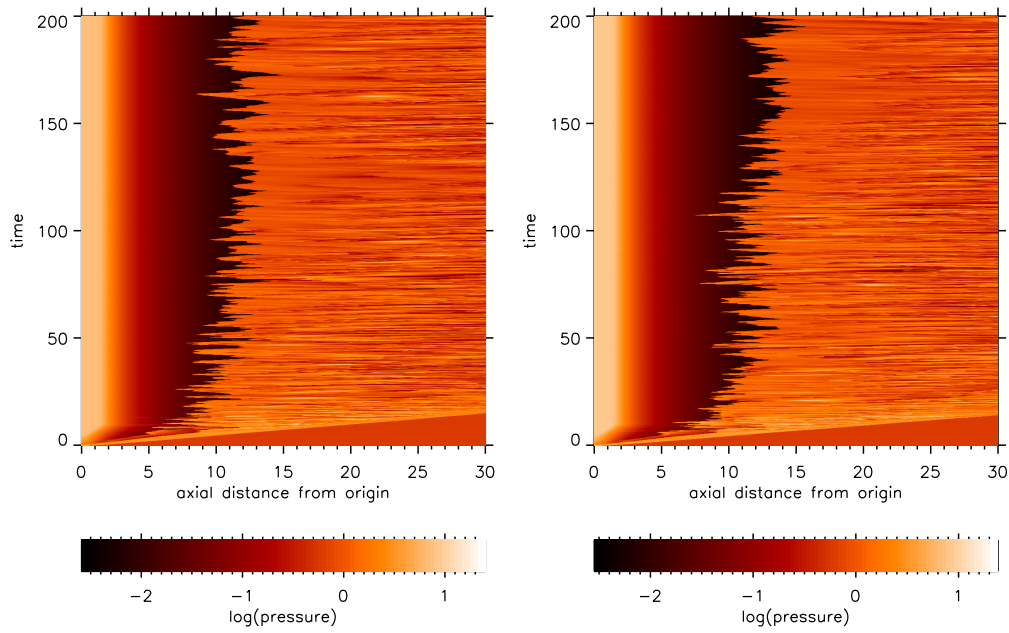


FIGURE A.21: Mach 2, over-pressure $\kappa = 12$ (left panel) $\kappa = 14$ (right panel) and density ratio $\eta = 0.1$.

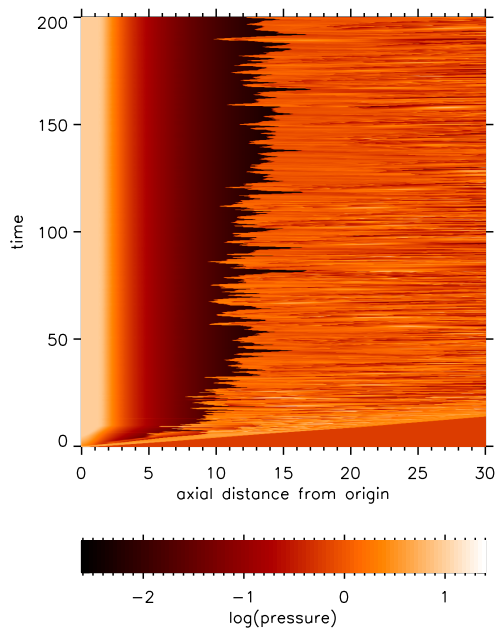


FIGURE A.22: Mach 2, over-pressure $\kappa = 16$ and density ratio $\eta = 0.1$.

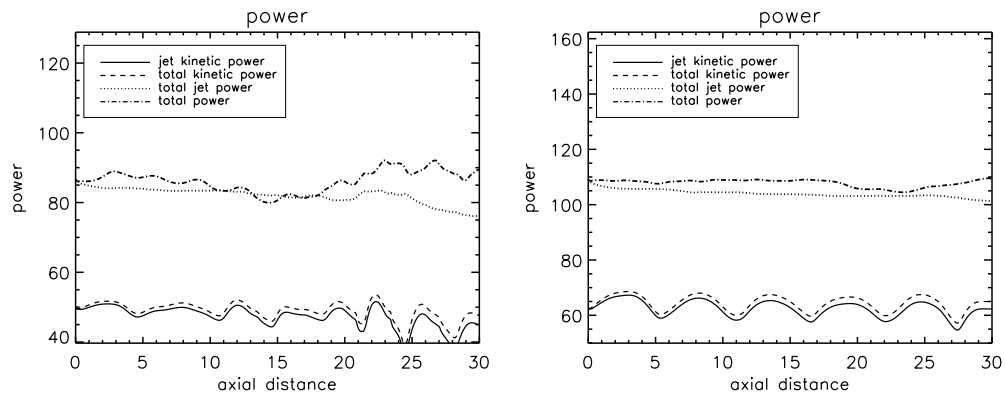


FIGURE A.23: Mach 2, over-pressure $\kappa = 1.2$ (left panel) $\kappa = 1.4$ (right panel) and density ratio $\eta = 0.1$.

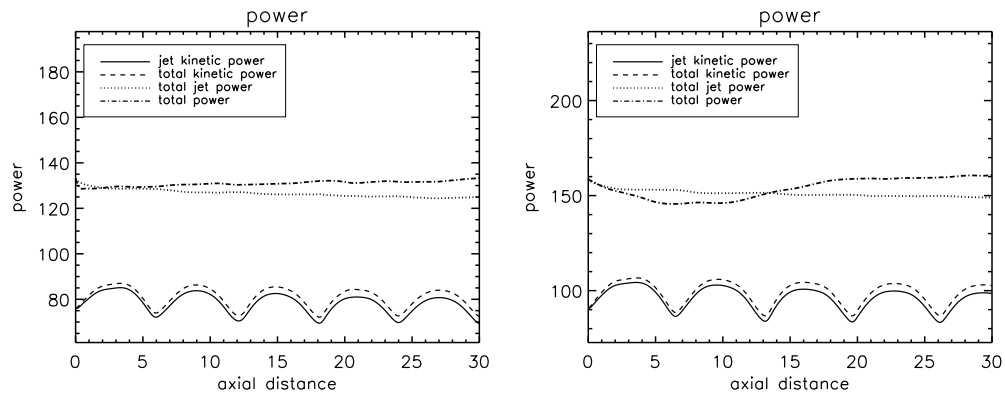


FIGURE A.24: Mach 2, over-pressure $\kappa = 1.6$ (left panel) $\kappa = 1.8$ (right panel) and density ratio $\eta = 0.1$.

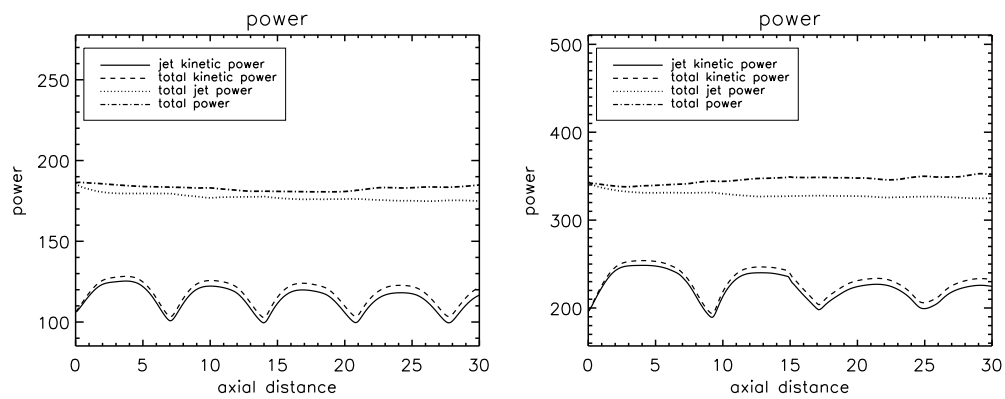


FIGURE A.25: Mach 2, over-pressure $\kappa = 2$ (left panel) $\kappa = 3$ (right panel) and density ratio $\eta = 0.1$.

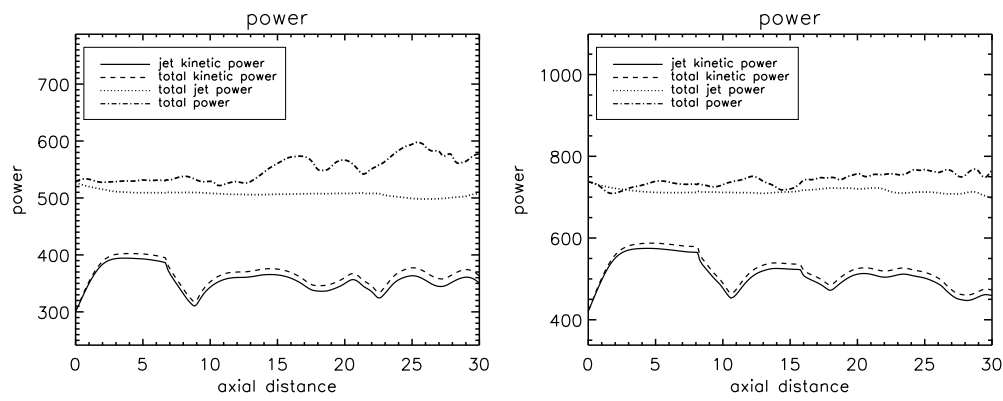


FIGURE A.26: Mach 2, over-pressure $\kappa = 4$ (left panel) $\kappa = 5$ (right panel) and density ratio $\eta = 0.1$.

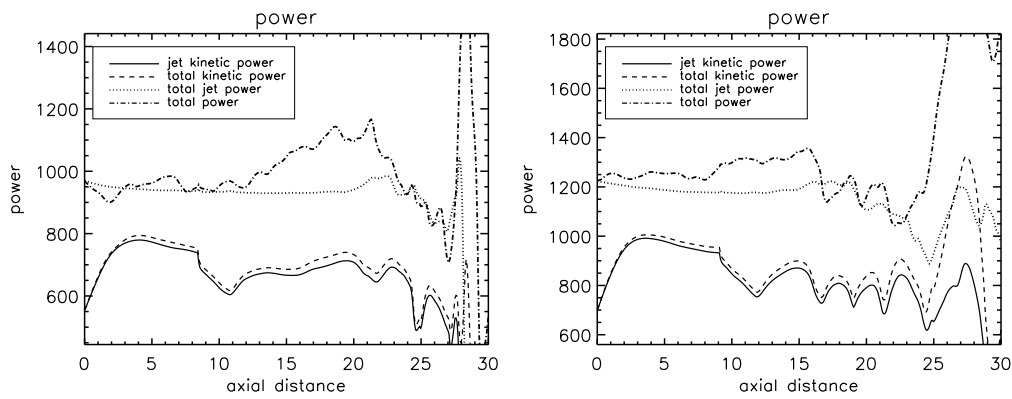


FIGURE A.27: Mach 2, over-pressure $\kappa = 6$ (left panel) $\kappa = 7$ (right panel) and density ratio $\eta = 0.1$.

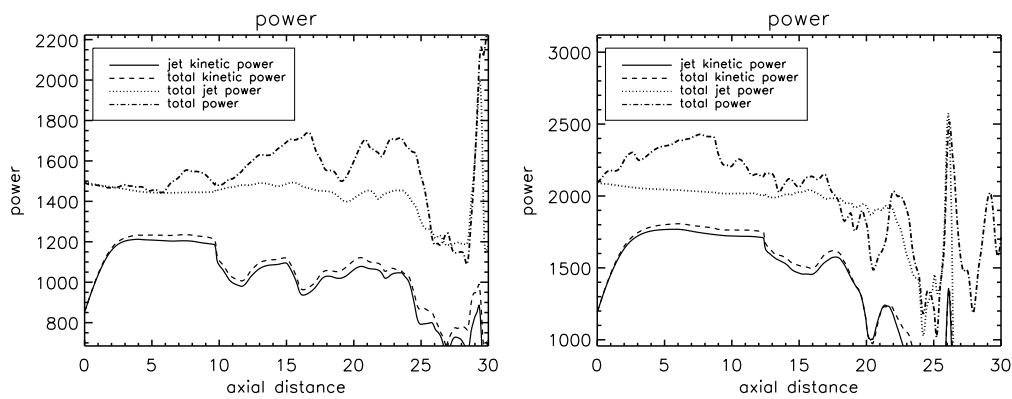


FIGURE A.28: Mach 2, over-pressure $\kappa = 8$ (left panel) $\kappa = 10$ (right panel) and density ratio $\eta = 0.1$.

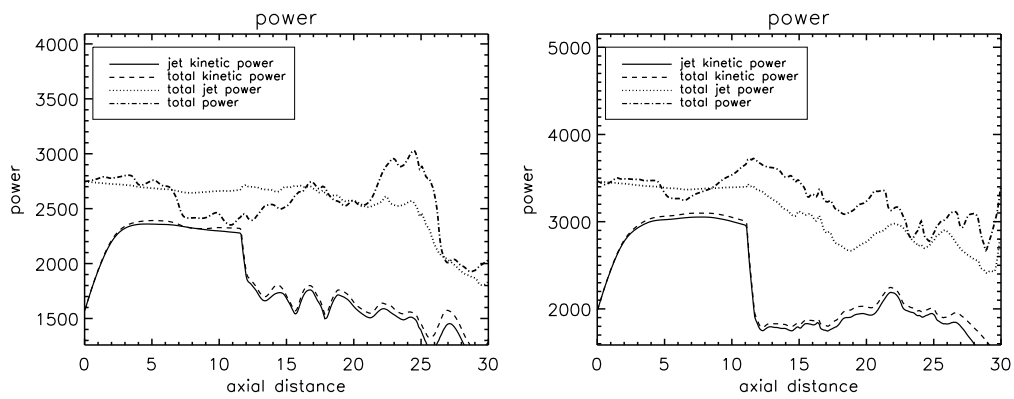


FIGURE A.29: Mach 2, over-pressure $\kappa = 12$ (left panel) $\kappa = 14$ (right panel) and density ratio $\eta = 0.1$.

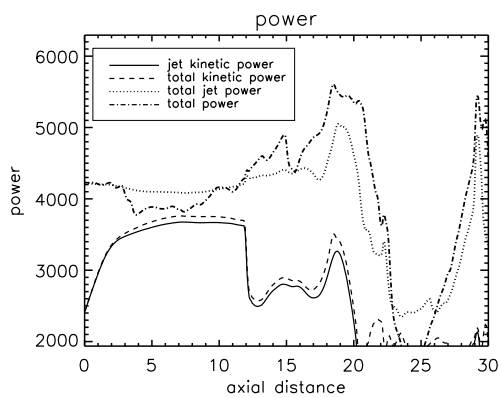


FIGURE A.30: Mach 2, over-pressure $\kappa = 16$ and density ratio $\eta = 0.1$.

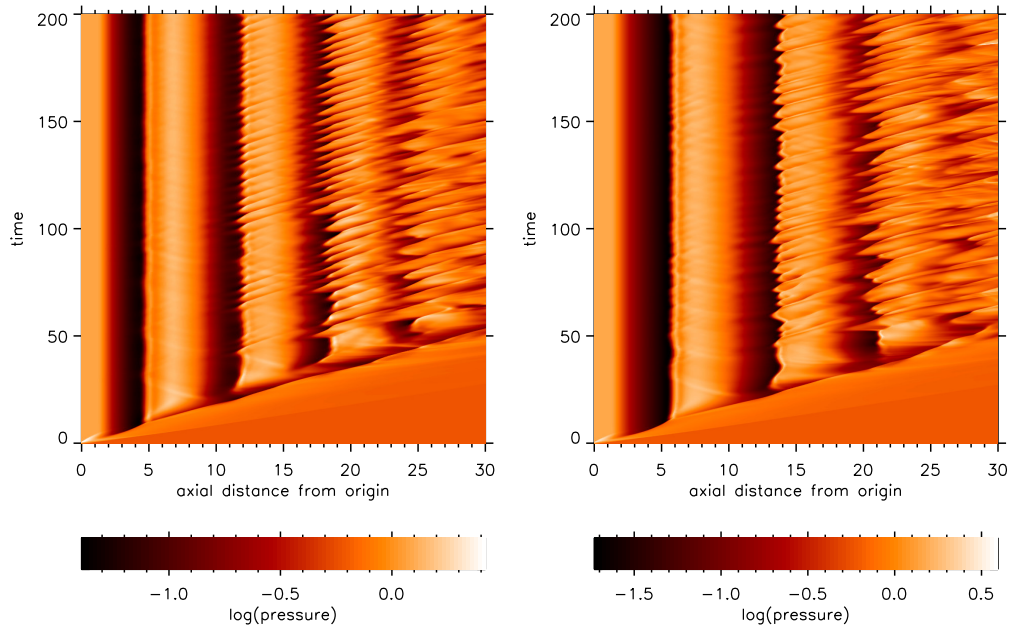


FIGURE A.31: Mach 2, over-pressure $\kappa = 2$ (left panel) $\kappa = 2.5$ (right panel) and density ratio $\eta = 10$.

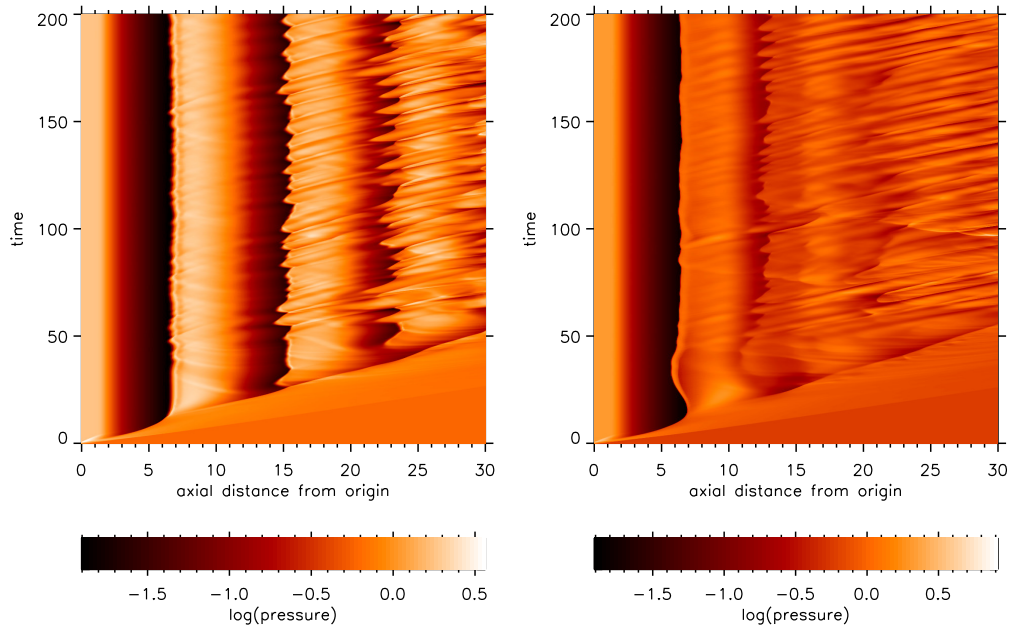


FIGURE A.32: Mach 2, over-pressure $\kappa = 3$ (left panel) $\kappa = 3.5$ (right panel) and density ratio $\eta = 10$.

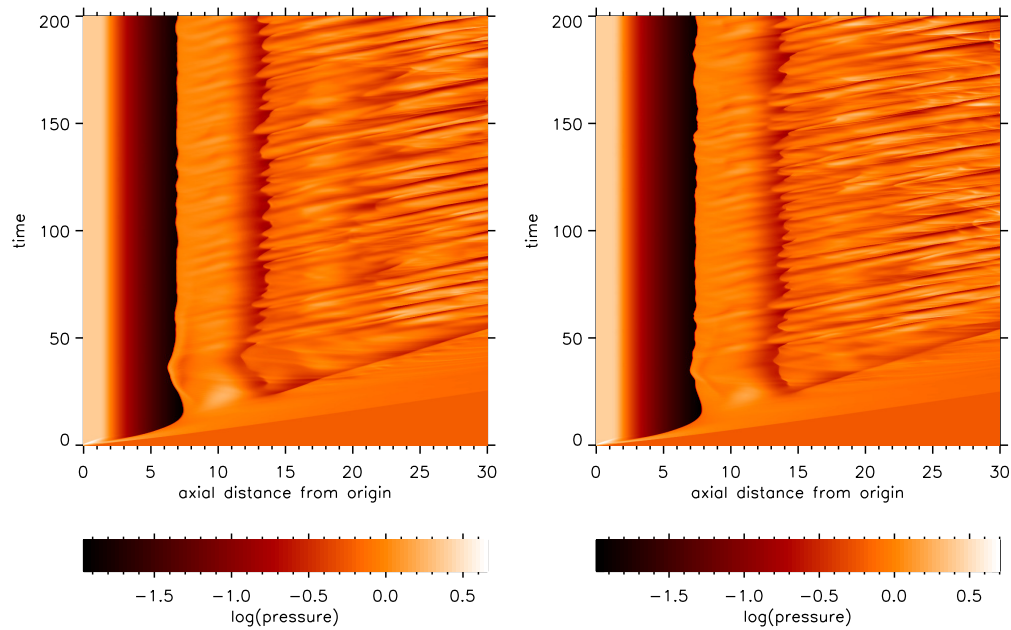


FIGURE A.33: Mach 2, over-pressure $\kappa = 4$ (left panel) $\kappa = 4.5$ (right panel) and density ratio $\eta = 10$.

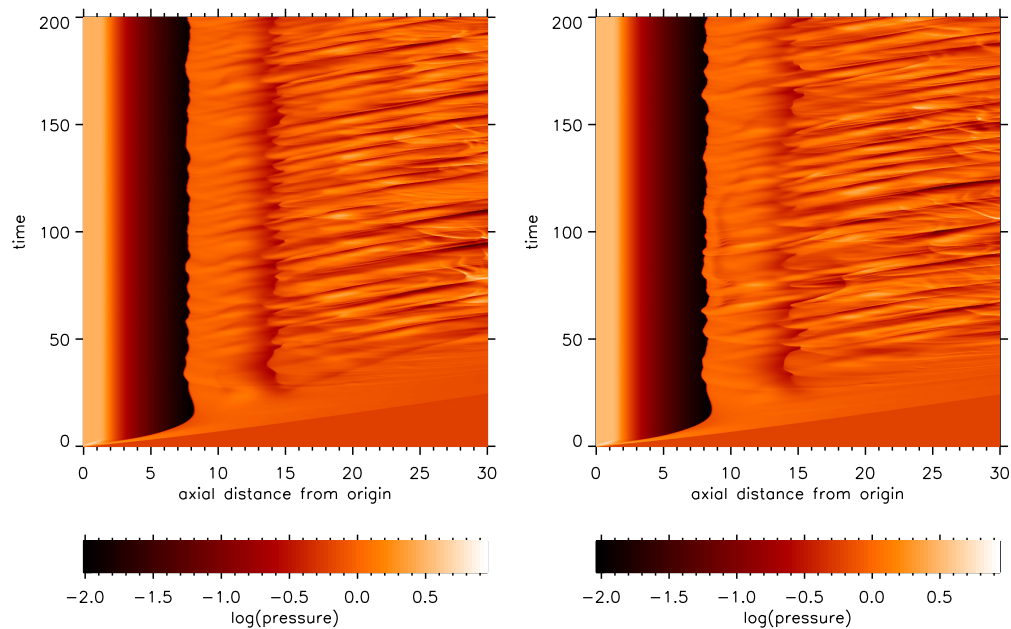


FIGURE A.34: Mach 2, over-pressure $\kappa = 5$ (left panel) $\kappa = 5.5$ (right panel) and density ratio $\eta = 10$.

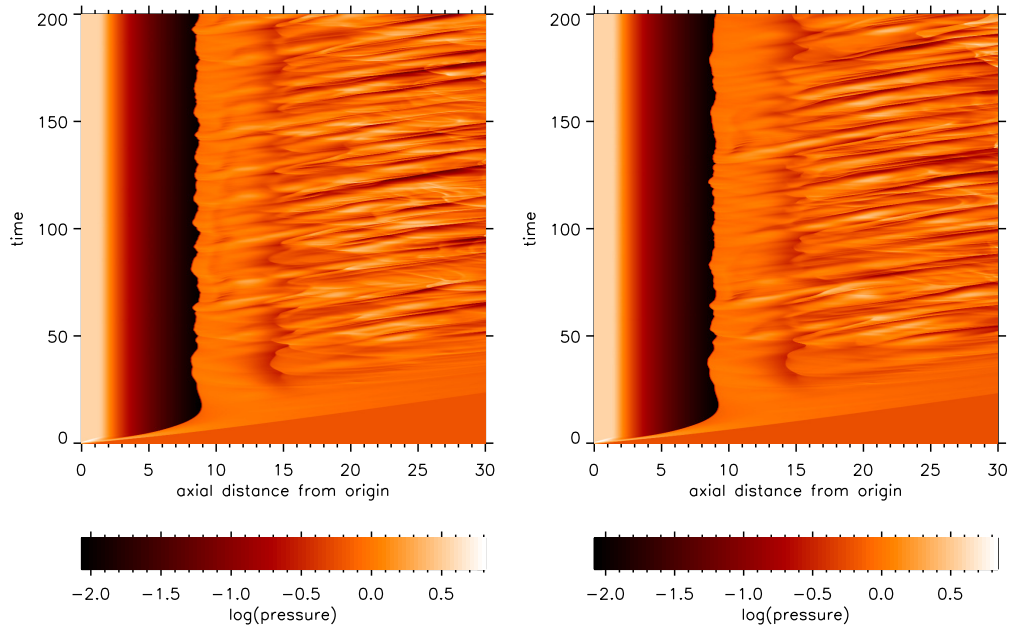


FIGURE A.35: Mach 2, over-pressure $\kappa = 6$ (left panel) $\kappa = 6.5$ (right panel) and density ratio $\eta = 10$.

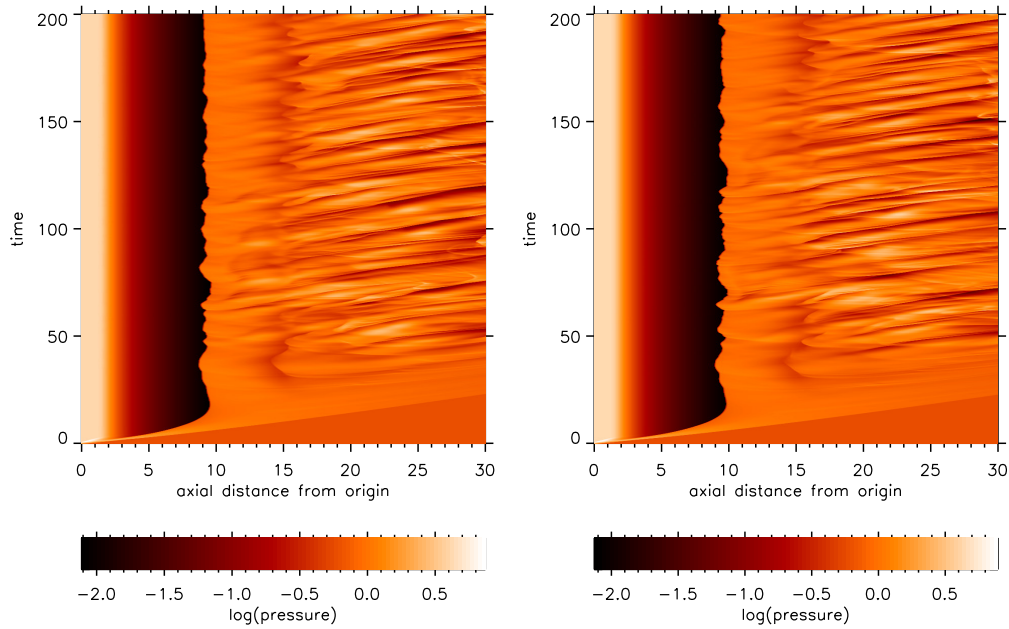


FIGURE A.36: Mach 2, over-pressure $\kappa = 7$ (left panel) $\kappa = 7.5$ (right panel) and density ratio $\eta = 10$.

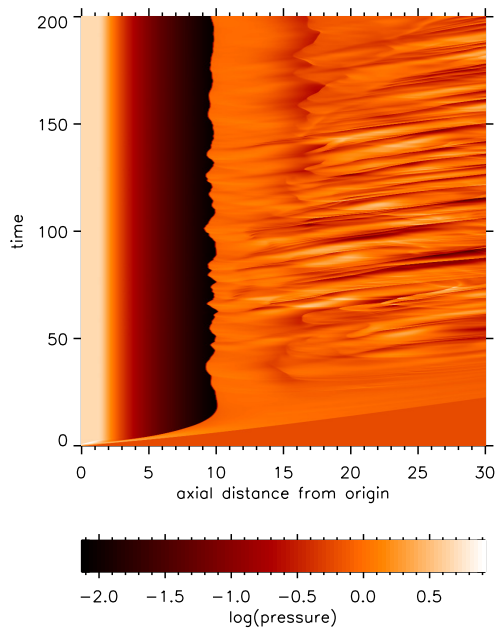


FIGURE A.37: Mach 2, over-pressure $\kappa = 8$ and density ratio $\eta = 10$.

Appendix B

Mach 4 Images

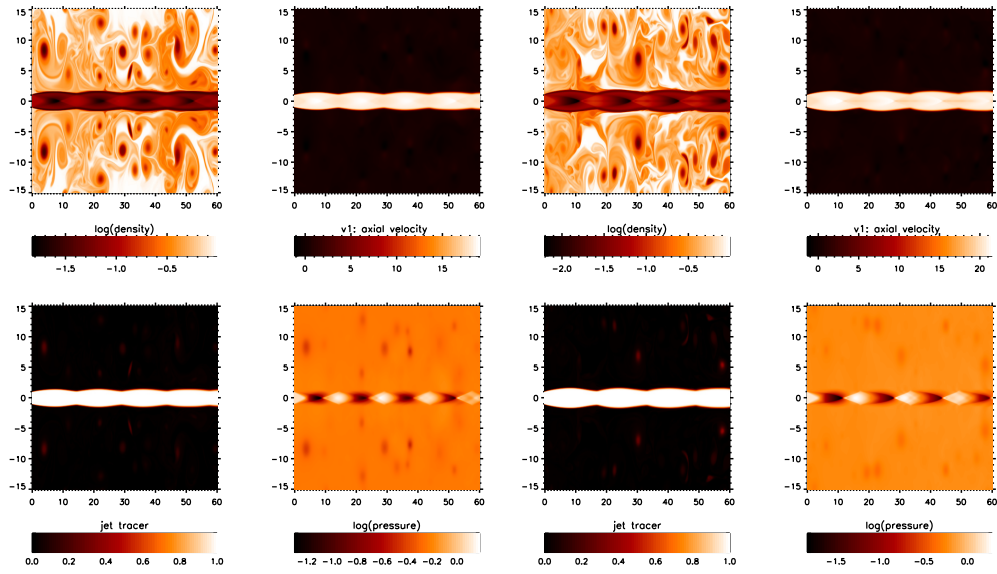


FIGURE B.1: Mach 4, over-pressure $\kappa = 2$ (left panel) $\kappa = 2.5$ (right panel) and density ratio $\eta = 0.1$.

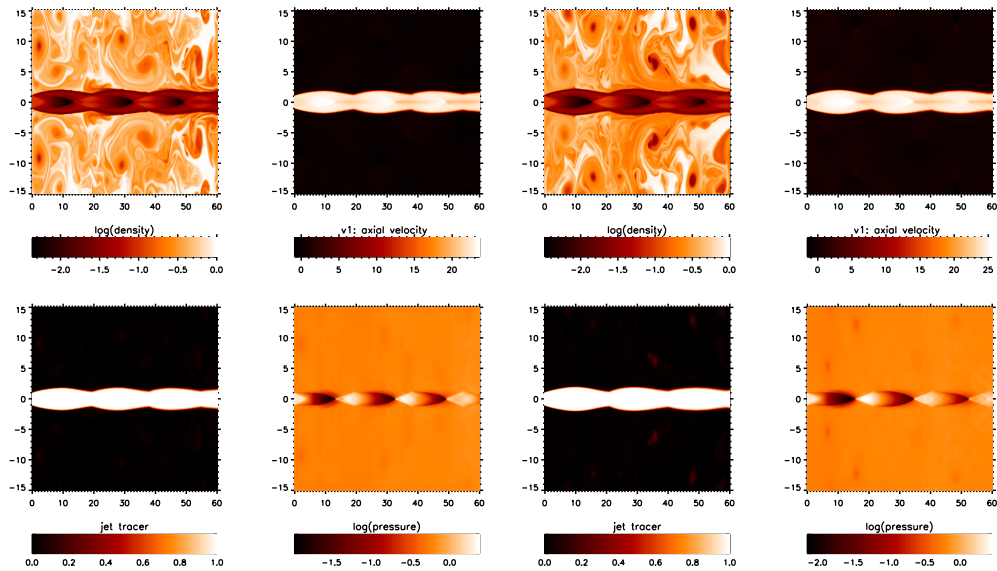


FIGURE B.2: Mach 4, over-pressure $\kappa = 3$ (left panel) $\kappa = 3.5$ (right panel) and density ratio $\eta = 0.1$.

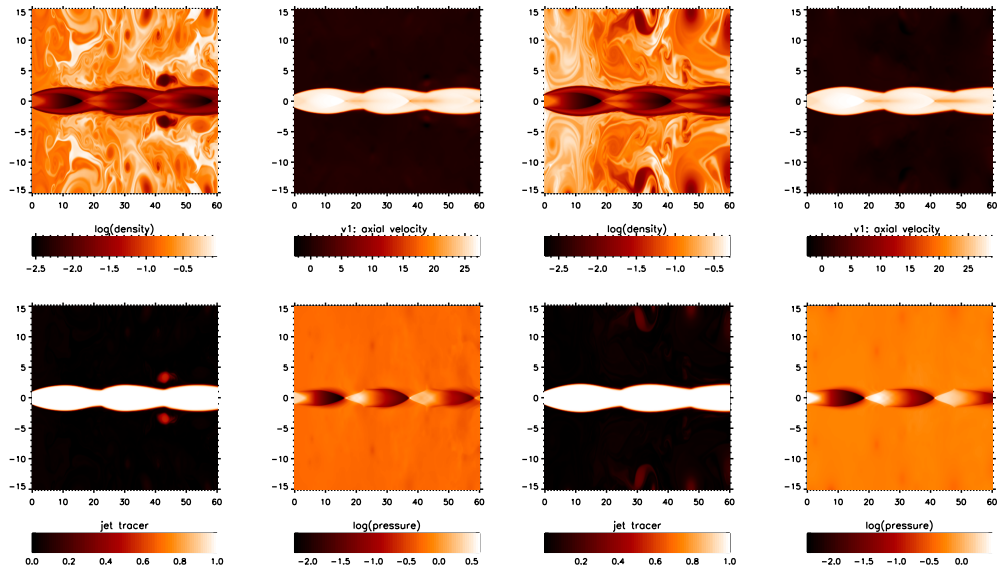


FIGURE B.3: Mach 4, over-pressure $\kappa = 4$ (left panel) $\kappa = 4.5$ (right panel) and density ratio $\eta = 0.1$.

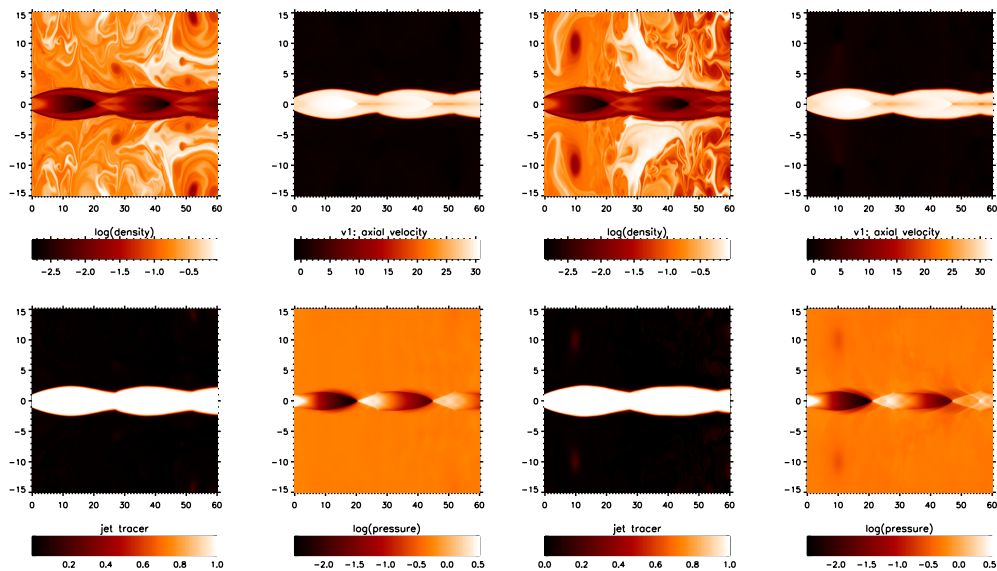


FIGURE B.4: Mach 4, over-pressure $\kappa = 5$ (left panel) $\kappa = 5.5$ (right panel) and density ratio $\eta = 0.1$.

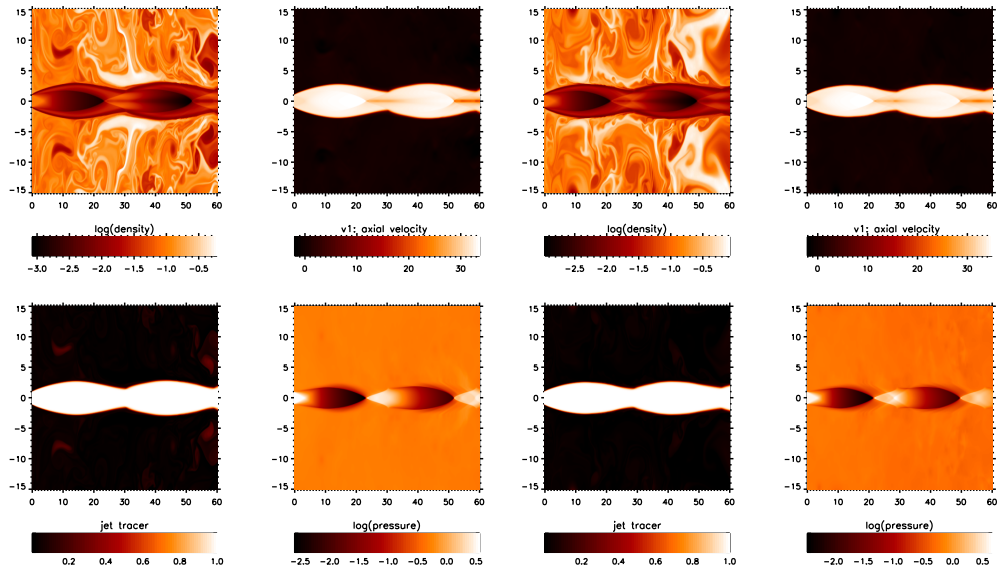


FIGURE B.5: Mach 4, over-pressure $\kappa = 6$ (left panel) $\kappa = 6.5$ (right panel) and density ratio $\eta = 0.1$.

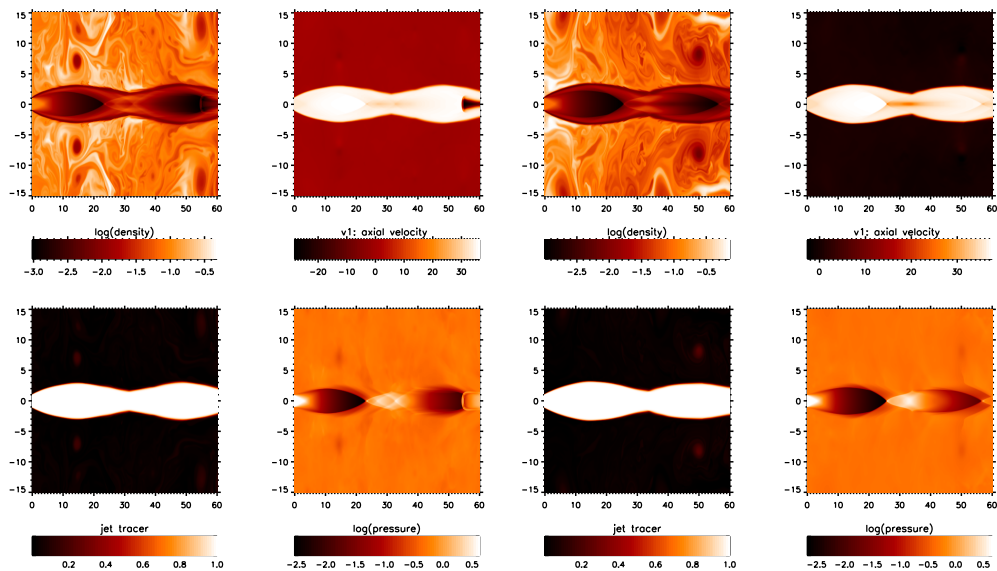


FIGURE B.6: Mach 4, over-pressure $\kappa = 7$ (left panel) $\kappa = 7.5$ (right panel) and density ratio $\eta = 0.1$.

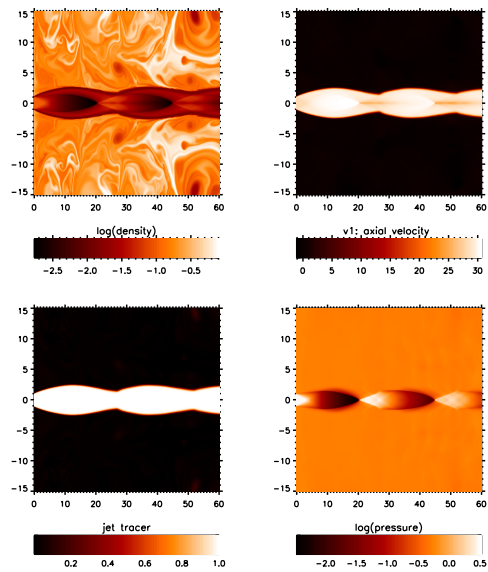


FIGURE B.7: Mach 4, over-pressure $\kappa = 8$ (and density ratio $\eta = 0.1$).

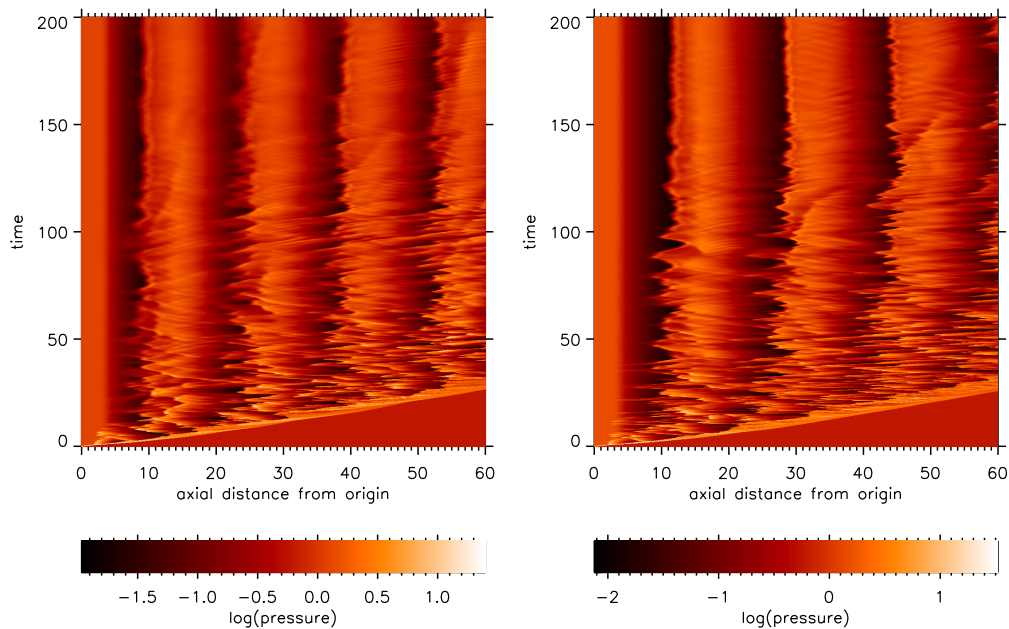


FIGURE B.8: Mach 4, over-pressure $\kappa = 2$ (left panel) $\kappa = 2.5$ (right panel) and density ratio $\eta = 0.1$.

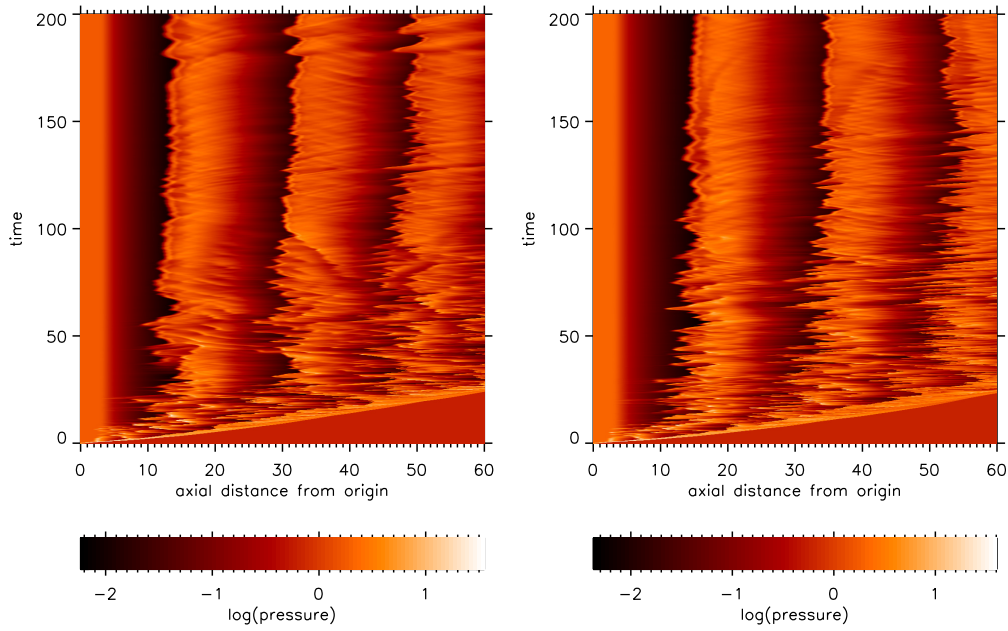


FIGURE B.9: Mach 4, over-pressure $\kappa = 3$ (left panel) $\kappa = 3.5$ (right panel) and density ratio $\eta = 0.1$.

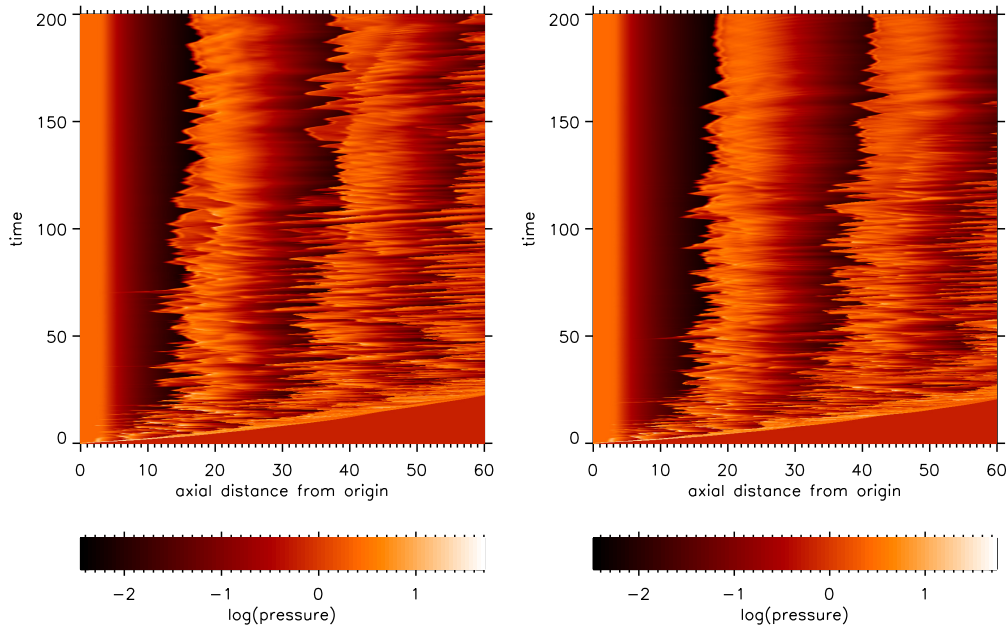


FIGURE B.10: Mach 4, over-pressure $\kappa = 4$ (left panel) $\kappa = 4.5$ (right panel) and density ratio $\eta = 0.1$.

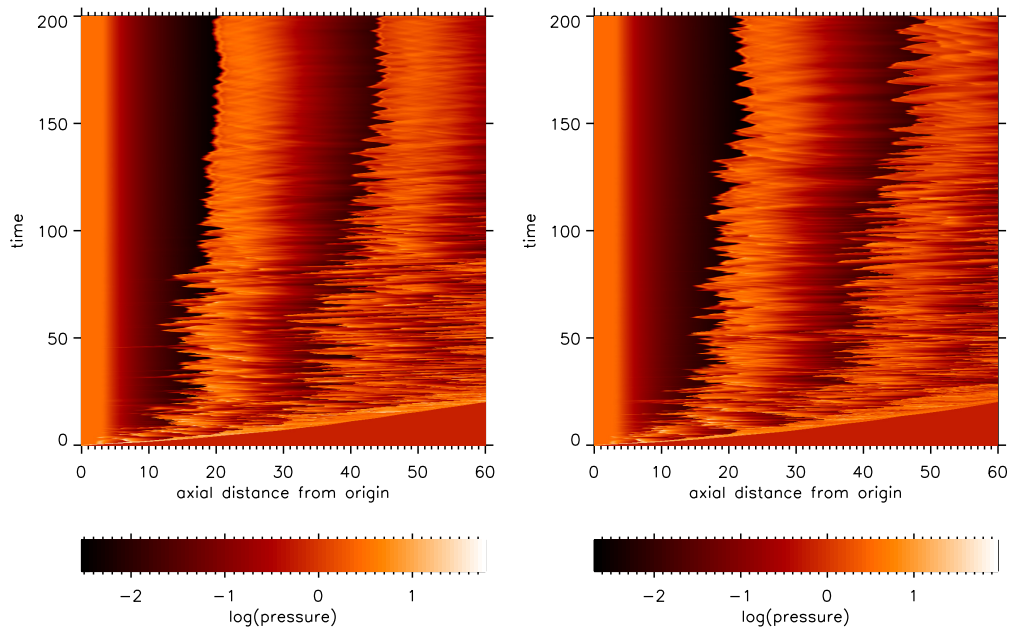


FIGURE B.11: Mach 4, over-pressure $\kappa = 5$ (left panel) $\kappa = 5.5$ (right panel) and density ratio $\eta = 0.1$.

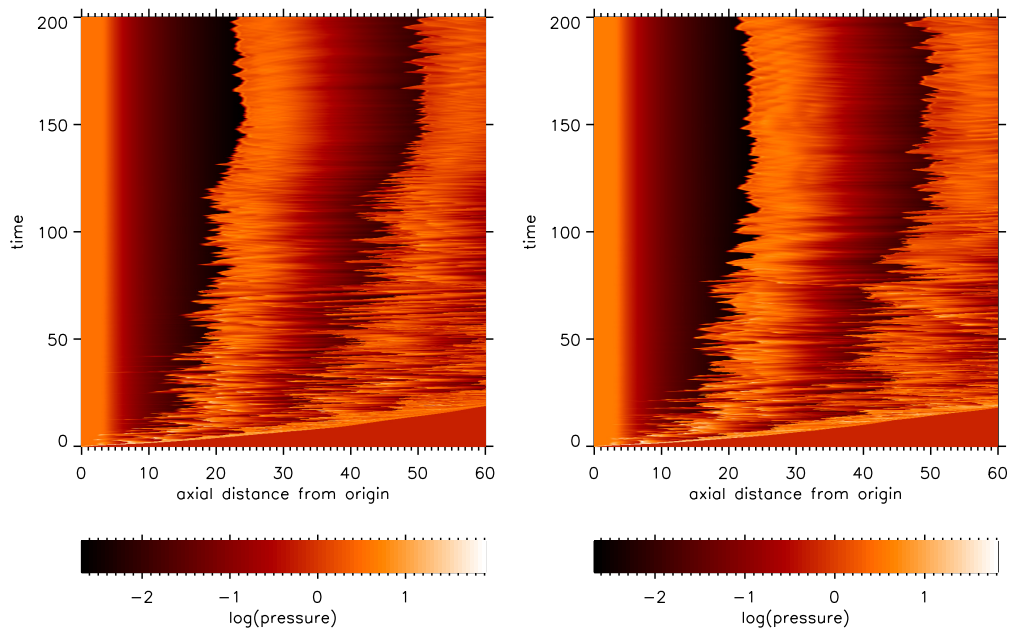


FIGURE B.12: Mach 4, over-pressure $\kappa = 6$ (left panel) $\kappa = 6.5$ (right panel) and density ratio $\eta = 0.1$.

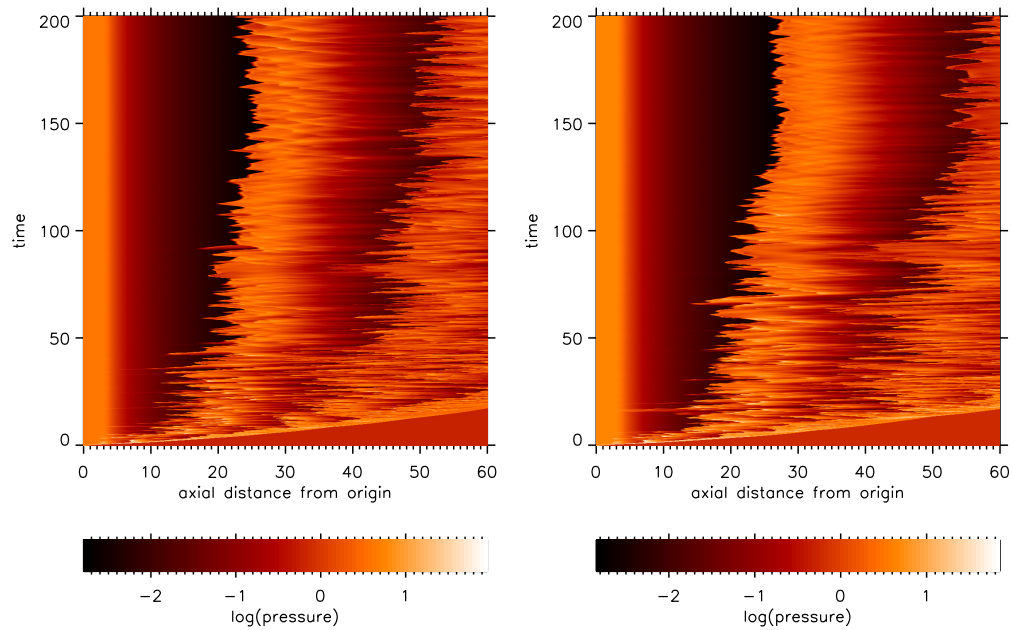


FIGURE B.13: Mach 4, over-pressure $\kappa = 7$ (left panel) $\kappa = 7.5$ (right panel) and density ratio $\eta = 0.1$.

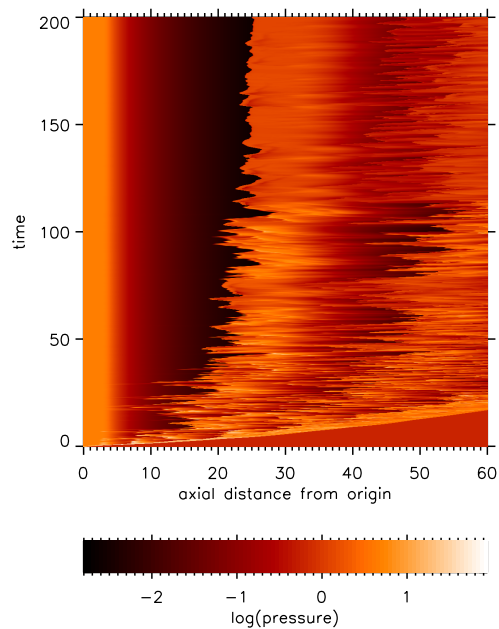


FIGURE B.14: Mach 4, over-pressure $\kappa = 8$ and density ratio $\eta = 0.1$.

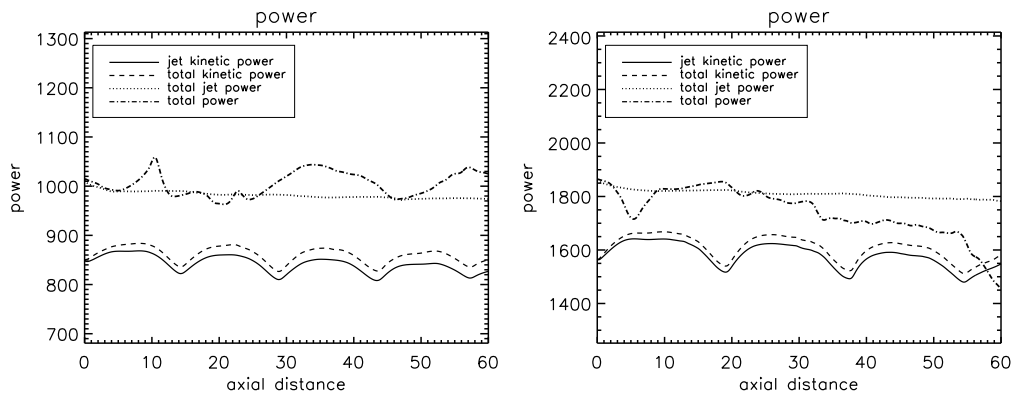


FIGURE B.15: Mach 4, over-pressure $\kappa = 2$ (left panel) $\kappa = 3$ (right panel) and density ratio $\eta = 0.1$.

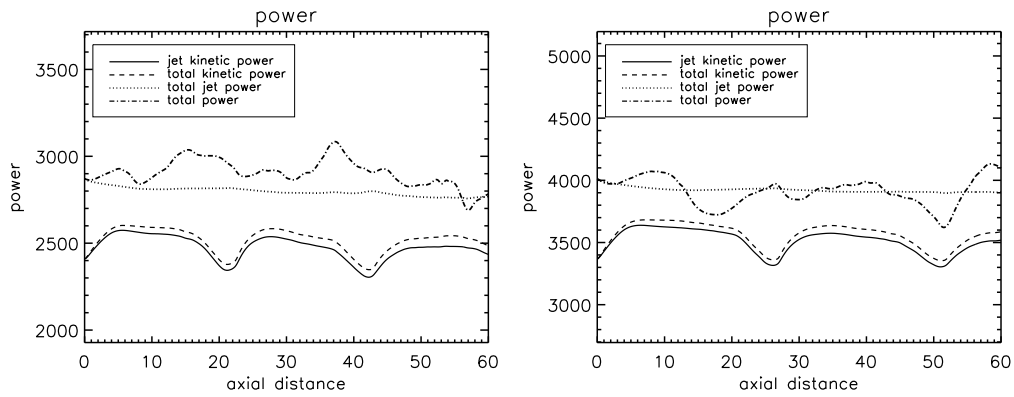


FIGURE B.16: Mach 4, over-pressure $\kappa = 4$ (left panel) $\kappa = 5$ (right panel) and density ratio $\eta = 0.1$.

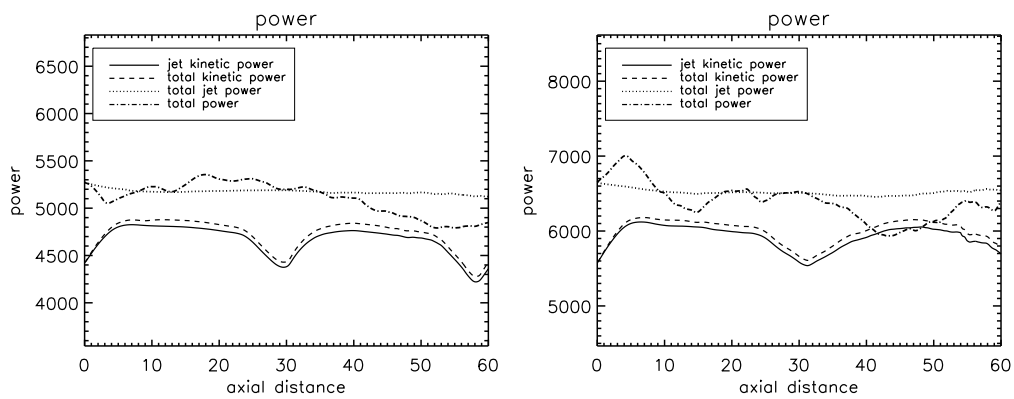


FIGURE B.17: Mach 4, over-pressure $\kappa = 6$ (left panel) $\kappa = 7$ (right panel) and density ratio $\eta = 0.1$.

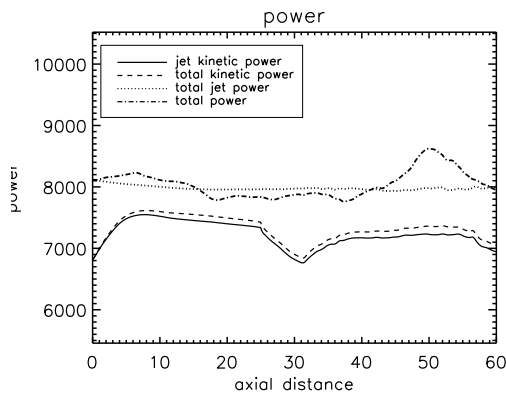


FIGURE B.18: Mach 4, over-pressure $\kappa = 8$ and density ratio $\eta = 0.1$.

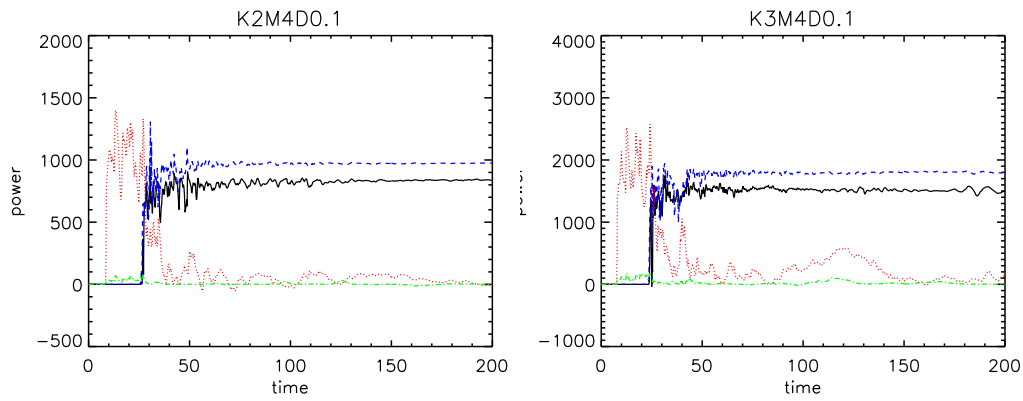


FIGURE B.19: Mach 4, over-pressure $\kappa = 2$ (left panel) $\kappa = 3$ (right panel) and density ratio $\eta = 0.1$.

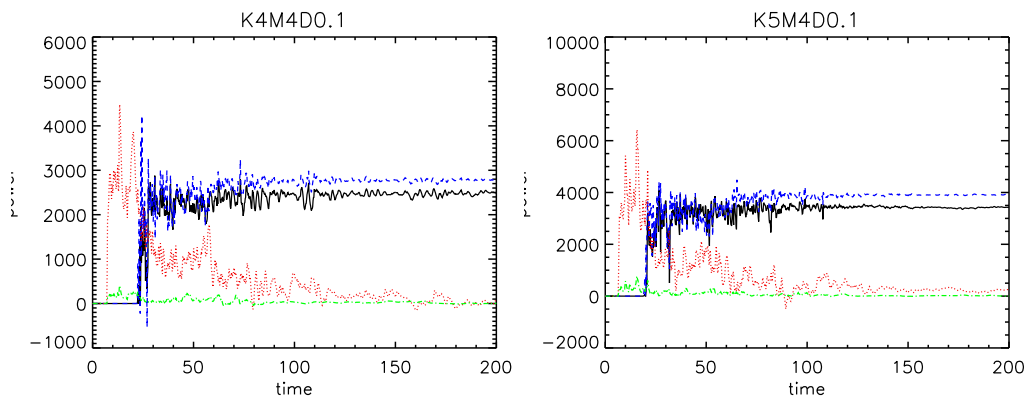


FIGURE B.20: Mach 4, over-pressure $\kappa = 4$ (left panel) $\kappa = 5$ (right panel) and density ratio $\eta = 0.1$.

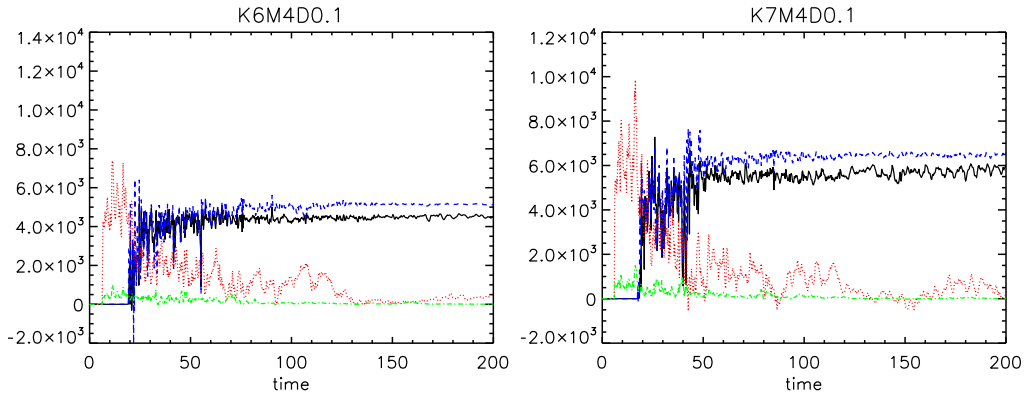


FIGURE B.21: Mach 4, over-pressure $\kappa = 6$ (left panel) $\kappa = 7$ (right panel) and density ratio $\eta = 0.1$.

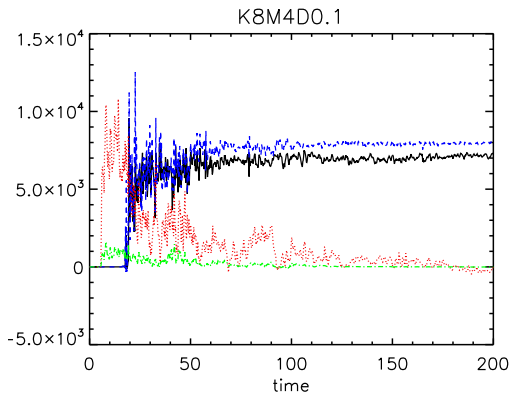


FIGURE B.22: Mach 4, over-pressure $\kappa = 8$ and density ratio $\eta = 0.1$.

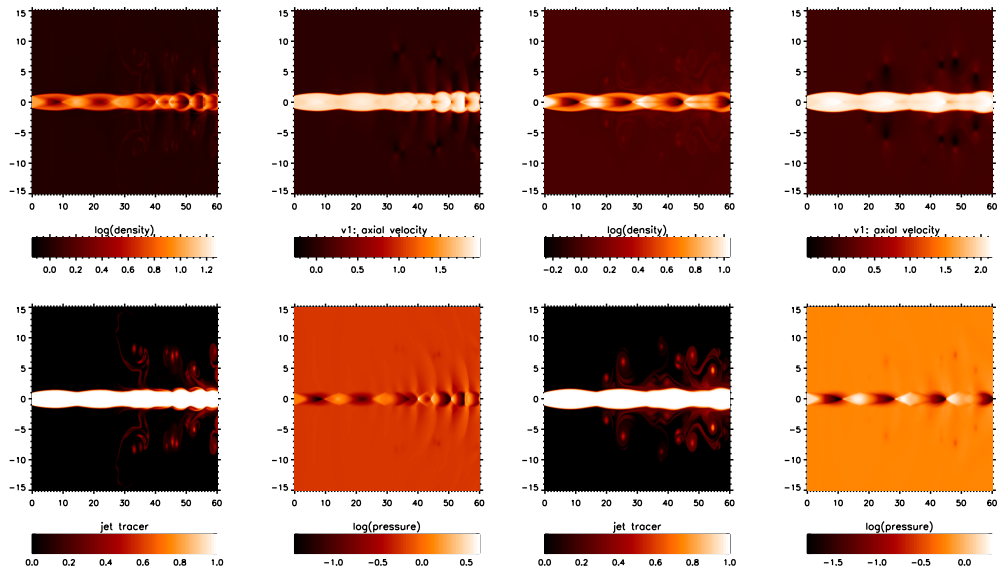


FIGURE B.23: Mach 4, over-pressure $\kappa = 2$ (left panel) $\kappa = 2.5$ (right panel) and density ratio $\eta = 10$.

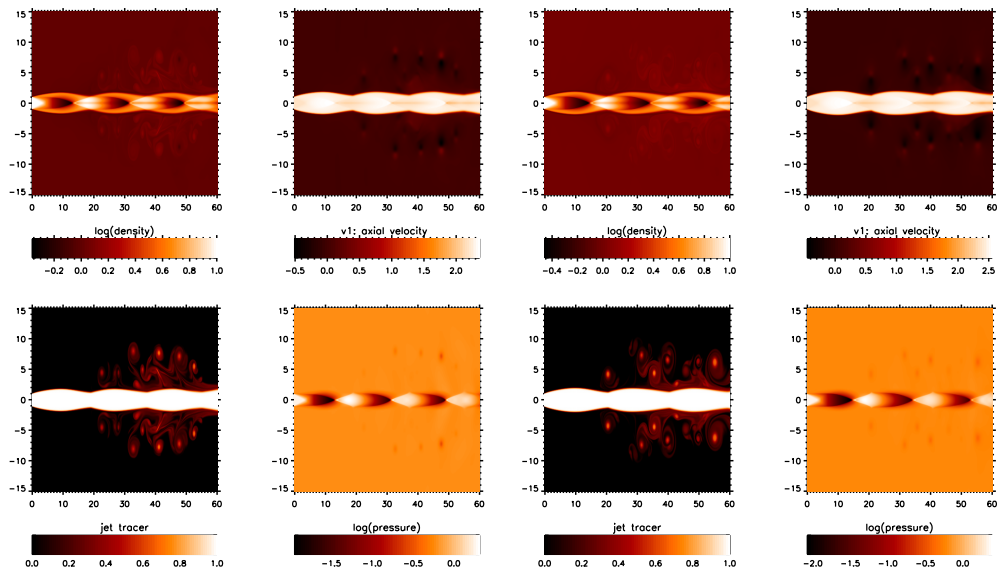


FIGURE B.24: Mach 4, over-pressure $\kappa = 3$ (left panel) $\kappa = 3.5$ (right panel) and density ratio $\eta = 10$.

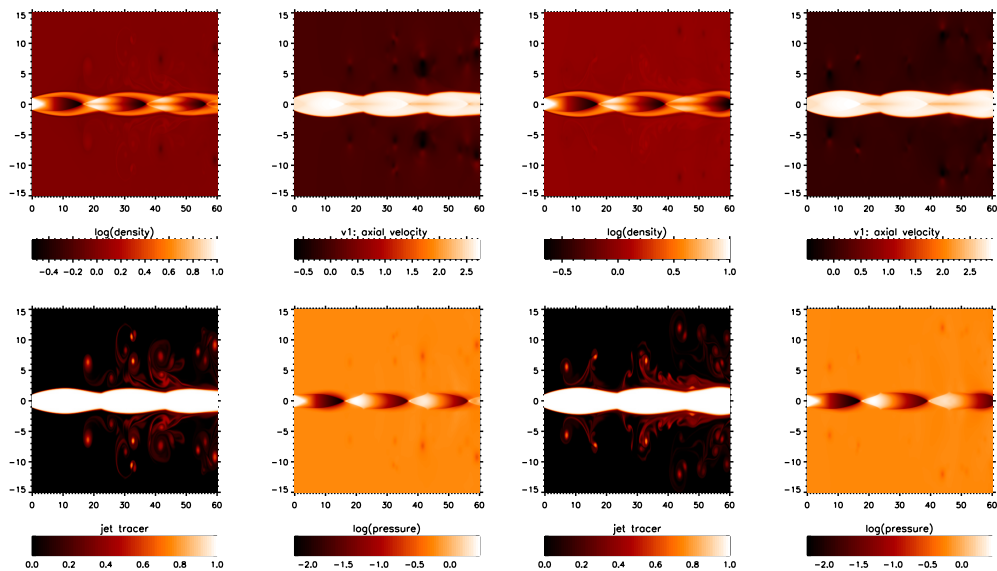


FIGURE B.25: Mach 4, over-pressure $\kappa = 4$ (left panel) $\kappa = 4.5$ (right panel) and density ratio $\eta = 10$.

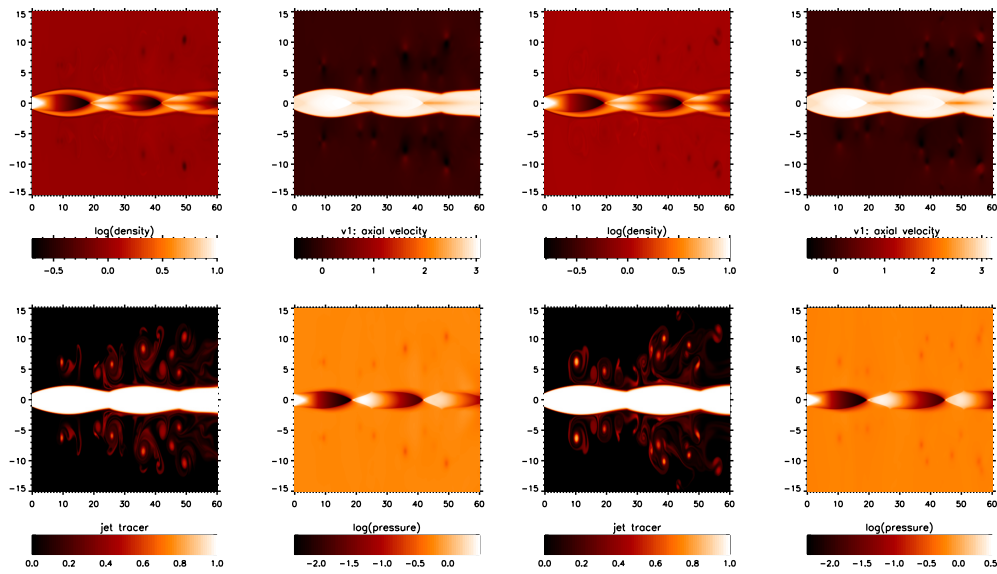


FIGURE B.26: Mach 4, over-pressure $\kappa = 5$ (left panel) $\kappa = 5.5$ (right panel) and density ratio $\eta = 10$.

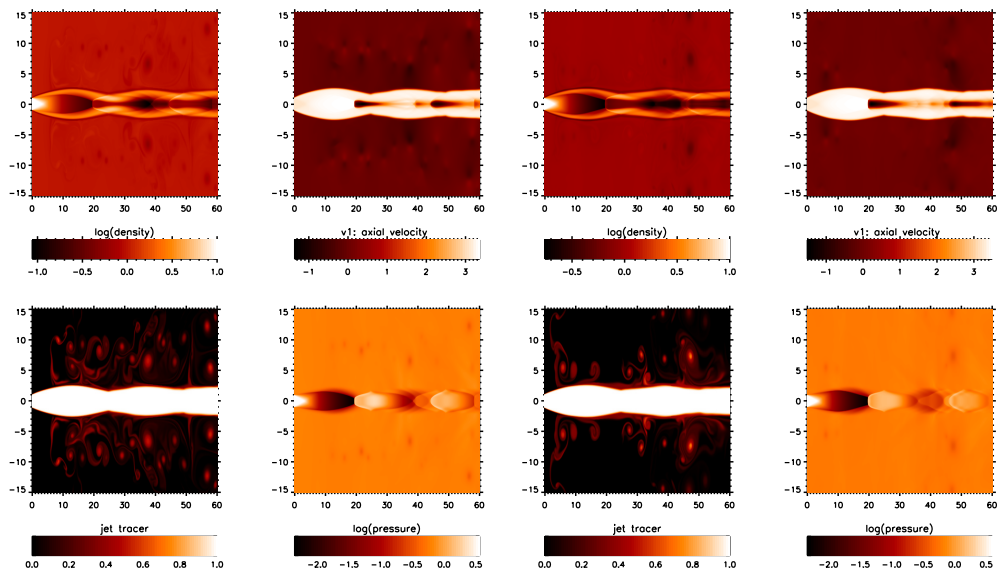


FIGURE B.27: Mach 4, over-pressure $\kappa = 6$ (left panel) $\kappa = 6.5$ (right panel) and density ratio $\eta = 10$.

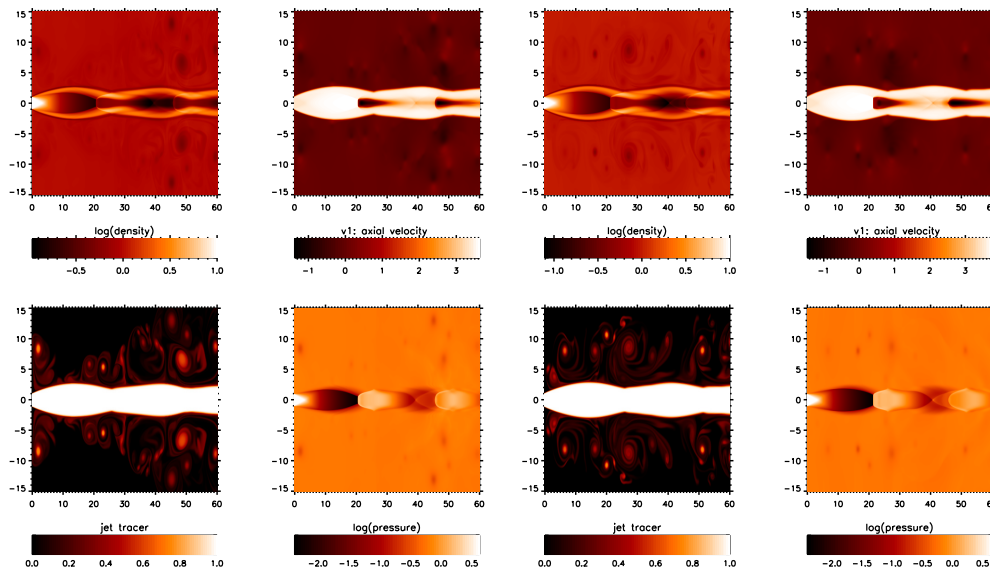


FIGURE B.28: Mach 4, over-pressure $\kappa = 7$ (left panel) $\kappa = 7.5$ (right panel) and density ratio $\eta = 10$.

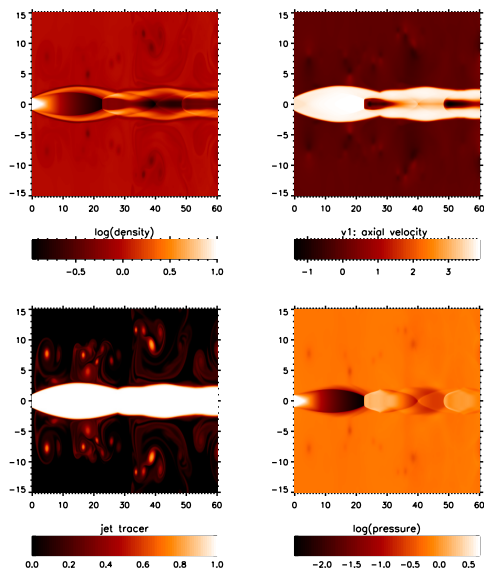


FIGURE B.29: Mach 4, over-pressure $\kappa = 8$ (and density ratio $\eta = 10$).

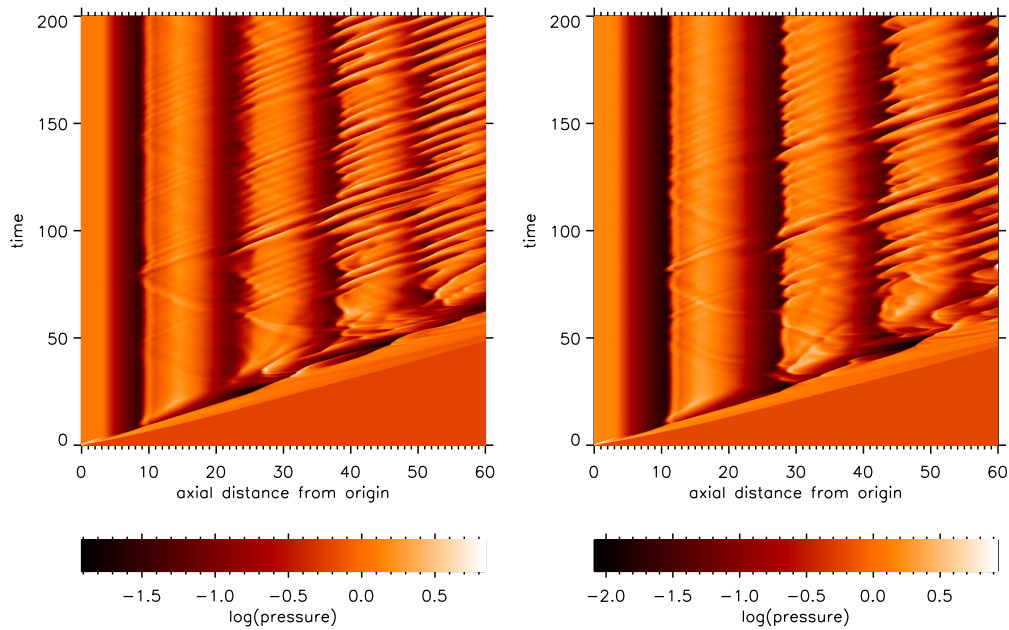


FIGURE B.30: Mach 4, over-pressure $\kappa = 2$ (left panel) $\kappa = 2.5$ (right panel) and density ratio $\eta = 10$.

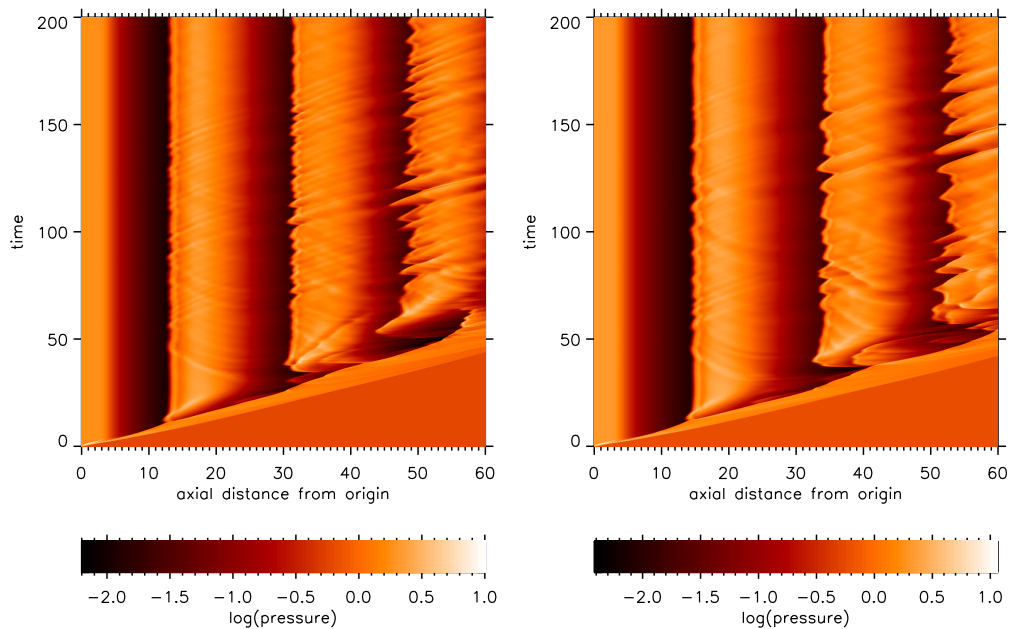


FIGURE B.31: Mach 4, over-pressure $\kappa = 3$ (left panel) $\kappa = 3.5$ (right panel) and density ratio $\eta = 10$.

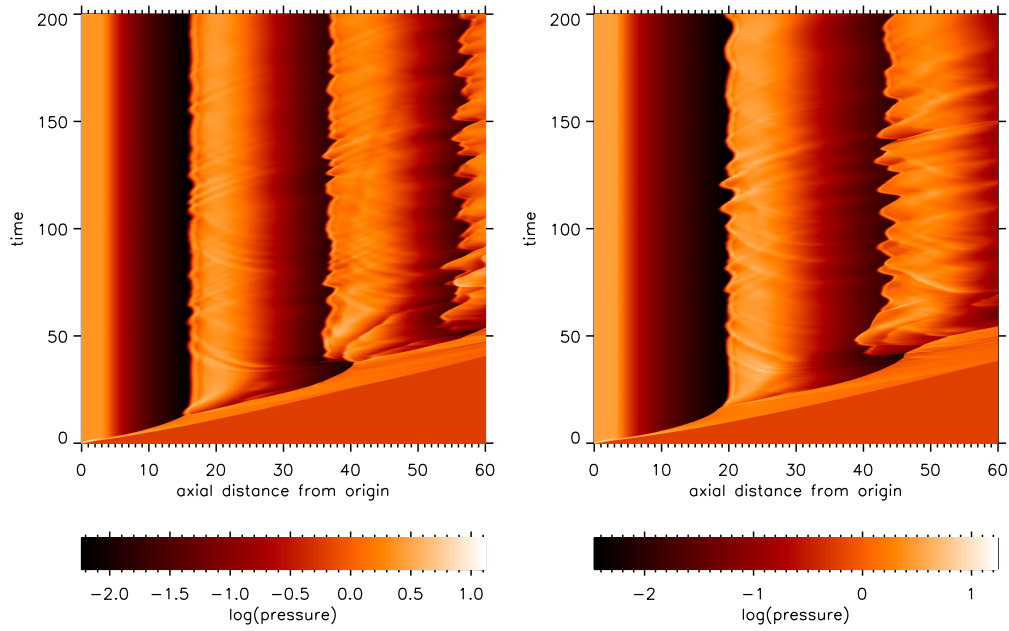


FIGURE B.32: Mach 4, over-pressure $\kappa = 4$ (left panel) $\kappa = 5$ (right panel) and density ratio $\eta = 10$.

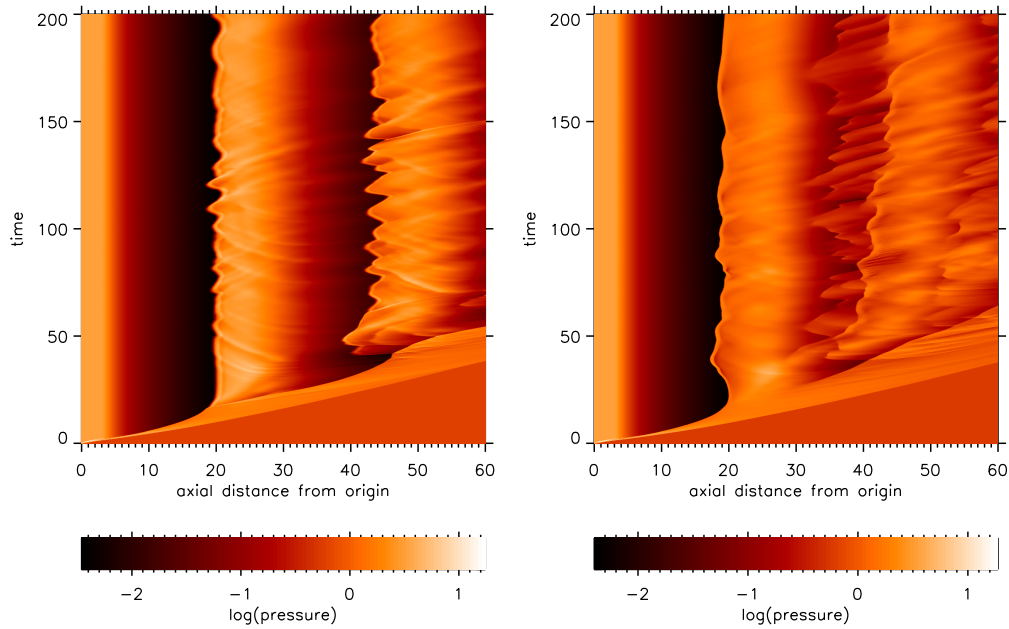


FIGURE B.33: Mach 4, over-pressure $\kappa = 5.5$ (left panel) $\kappa = 6$ (right panel) and density ratio $\eta = 10$.

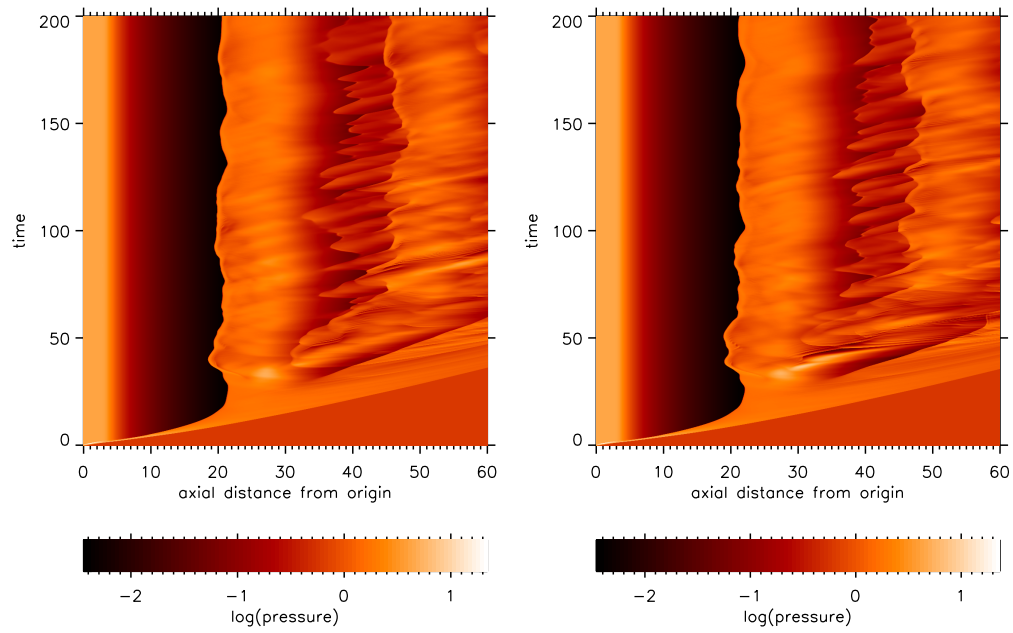


FIGURE B.34: Mach 4, over-pressure $\kappa = 7$ (left panel) $\kappa = 7.5$ (right panel) and density ratio $\eta = 10$.

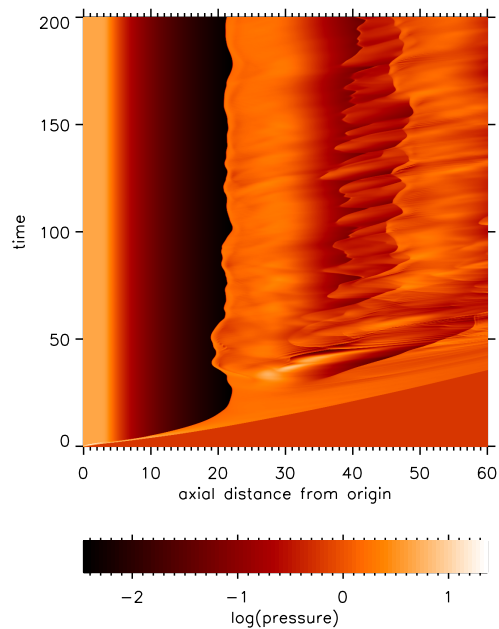


FIGURE B.35: Mach 4, over-pressure $\kappa = 8$ and density ratio $\eta = 10$.

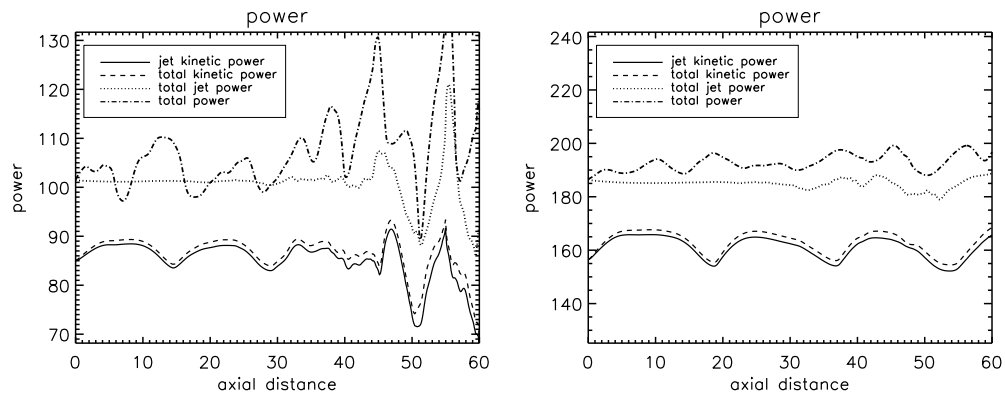


FIGURE B.36: Mach 4, over-pressure $\kappa = 2$ (left panel) $\kappa = 3$ (right panel) and density ratio $\eta = 10$.

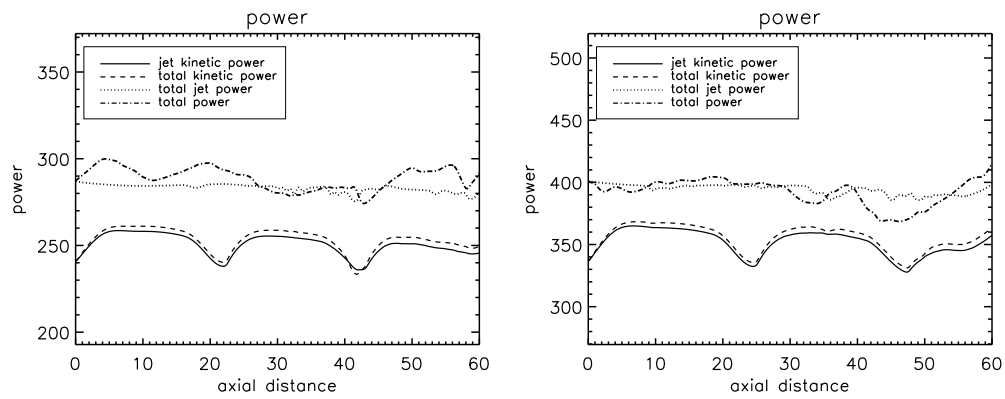


FIGURE B.37: Mach 4, over-pressure $\kappa = 4$ (left panel) $\kappa = 5$ (right panel) and density ratio $\eta = 10$.

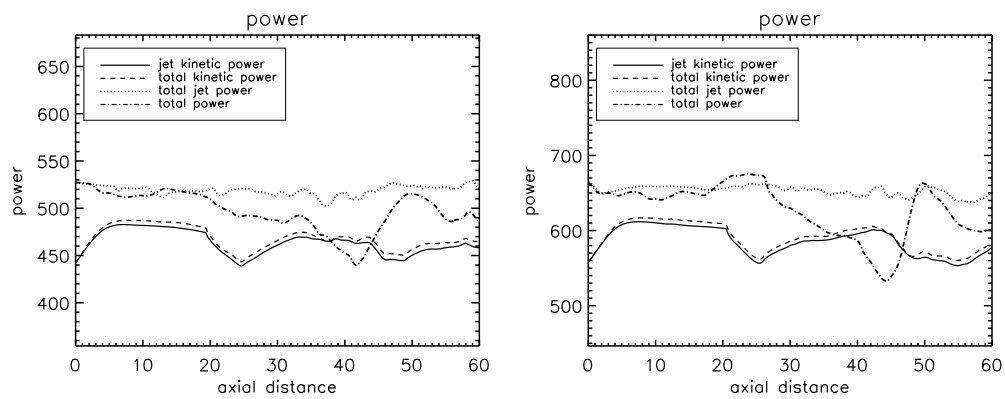


FIGURE B.38: Mach 4, over-pressure $\kappa = 6$ (left panel) $\kappa = 7$ (right panel) and density ratio $\eta = 10$.

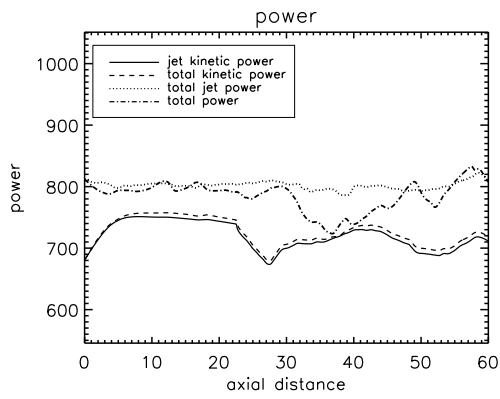


FIGURE B.39: Mach 4, over-pressure $\kappa = 8$ and density ratio $\eta = 10$.

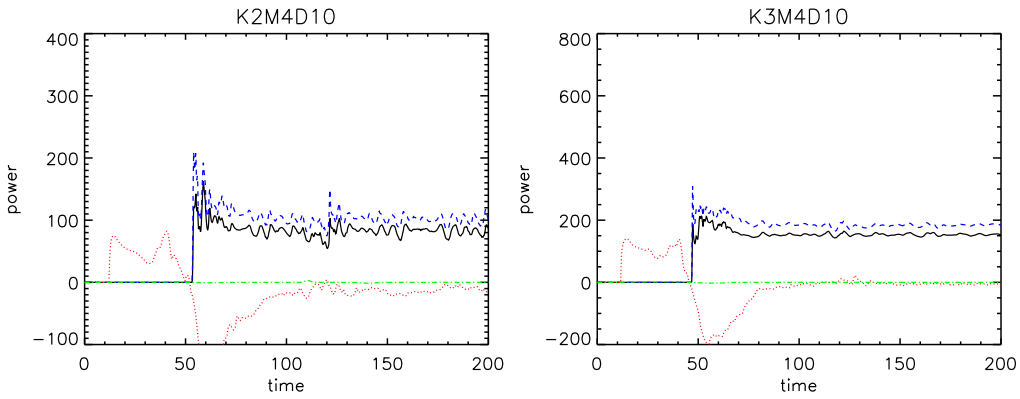


FIGURE B.40: Mach 4, over-pressure $\kappa = 2$ (left panel) $\kappa = 3$ (right panel) and density ratio $\eta = 10$.

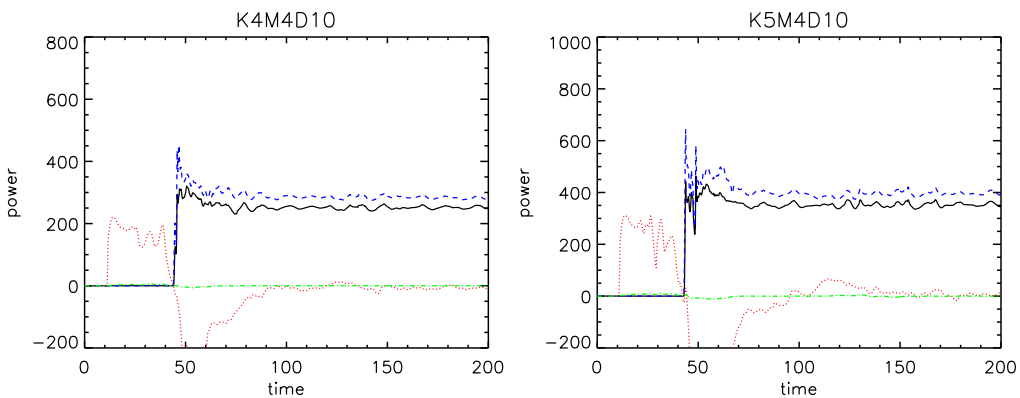


FIGURE B.41: Mach 4, over-pressure $\kappa = 4$ (left panel) $\kappa = 5$ (right panel) and density ratio $\eta = 10$.

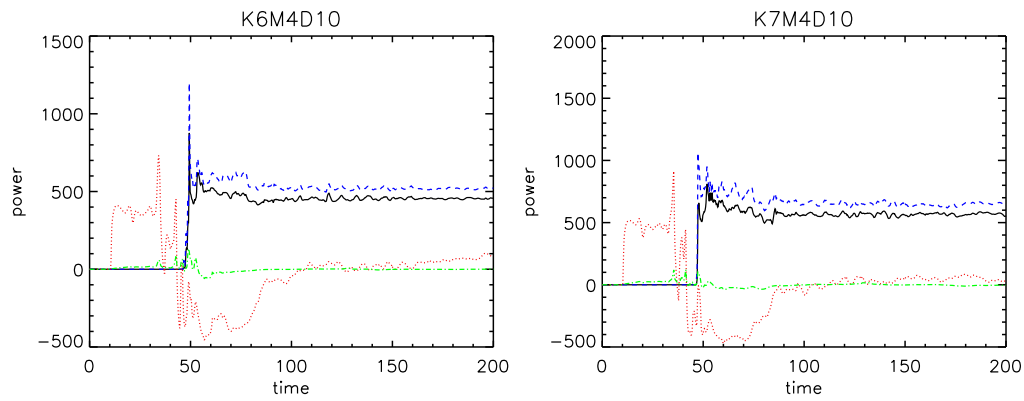


FIGURE B.42: Mach 4, over-pressure $\kappa = 6$ (left panel) $\kappa = 7$ (right panel) and density ratio $\eta = 10$.

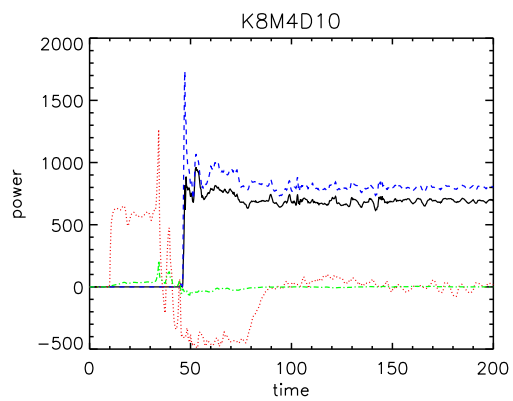


FIGURE B.43: Mach 4, over-pressure $\kappa = 8$ and density ratio $\eta = 10$.

Appendix C

Mach 6 Images

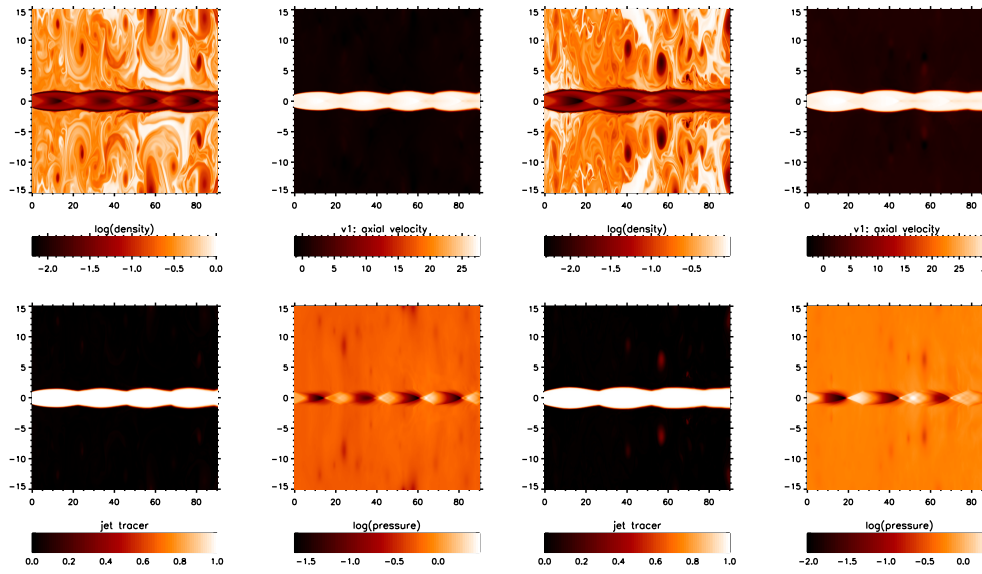


FIGURE C.1: Mach 6, over-pressure $\kappa = 2$ (left panel) $\kappa = 2.5$ (right panel) and density ratio $\eta = 0.1$.

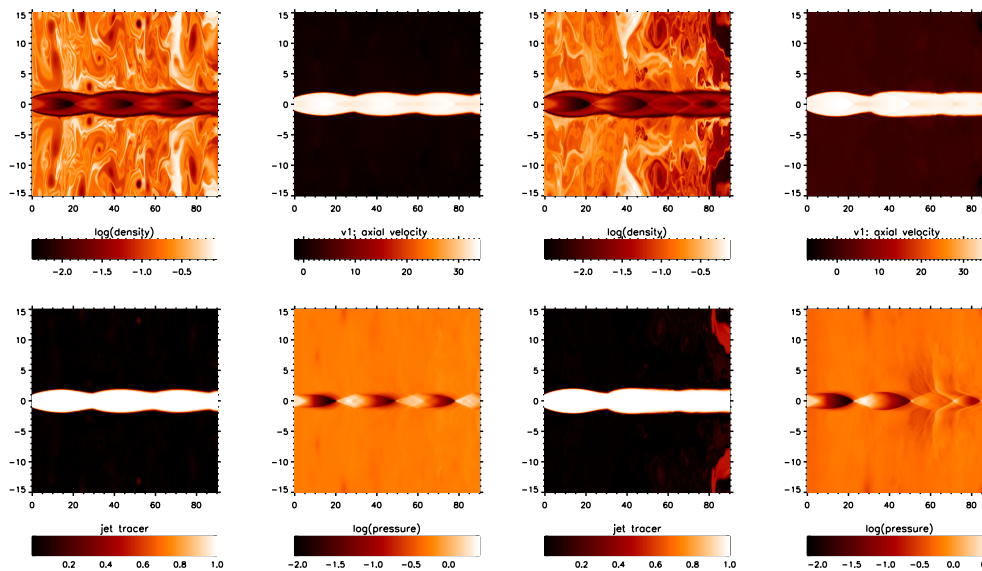


FIGURE C.2: Mach 6, over-pressure $\kappa = 3$ (left panel) $\kappa = 3.5$ (right panel) and density ratio $\eta = 0.1$.

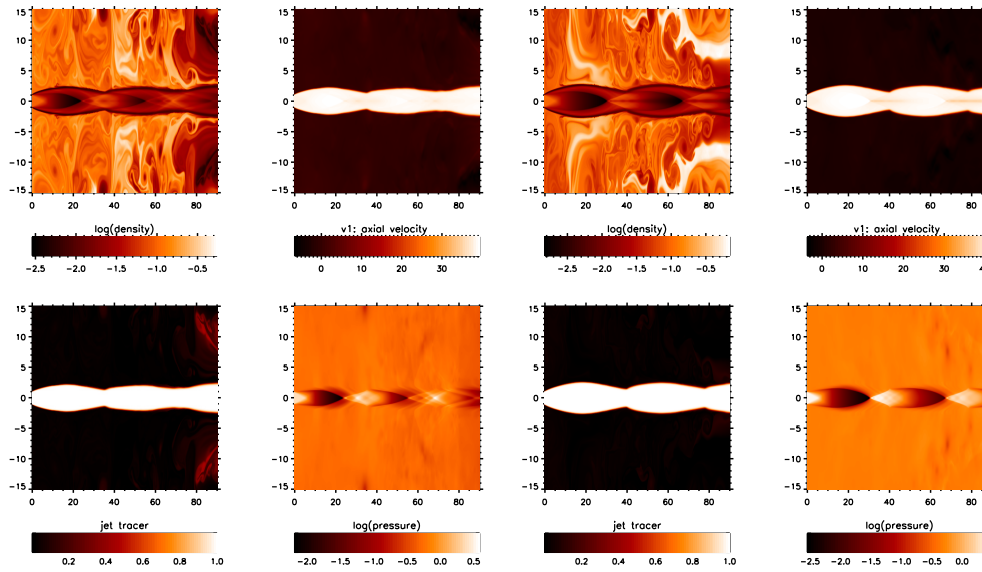


FIGURE C.3: Mach 6, over-pressure $\kappa = 4$ (left panel) $\kappa = 4.5$ (right panel) and density ratio $\eta = 0.1$.

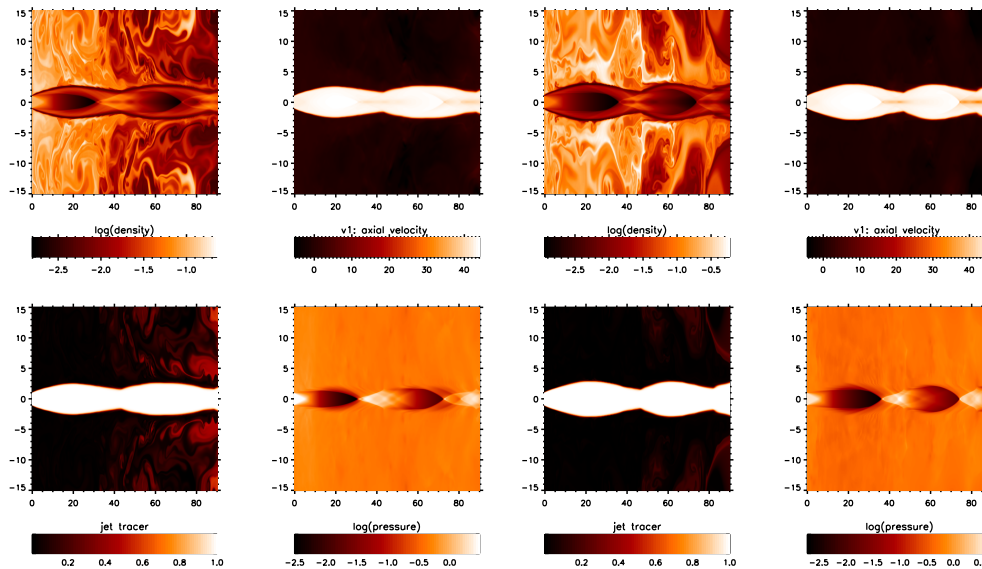


FIGURE C.4: Mach 6, over-pressure $\kappa = 5$ (left panel) $\kappa = 5.5$ (right panel) and density ratio $\eta = 0.1$.

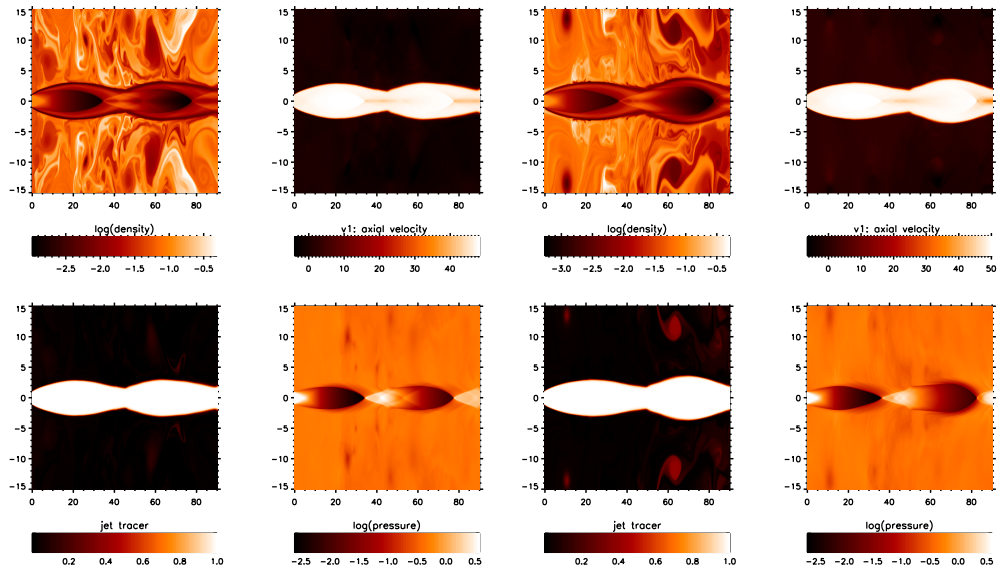


FIGURE C.5: Mach 6, over-pressure $\kappa = 6$ (left panel) $\kappa = 6.5$ (right panel) and density ratio $\eta = 0.1$.

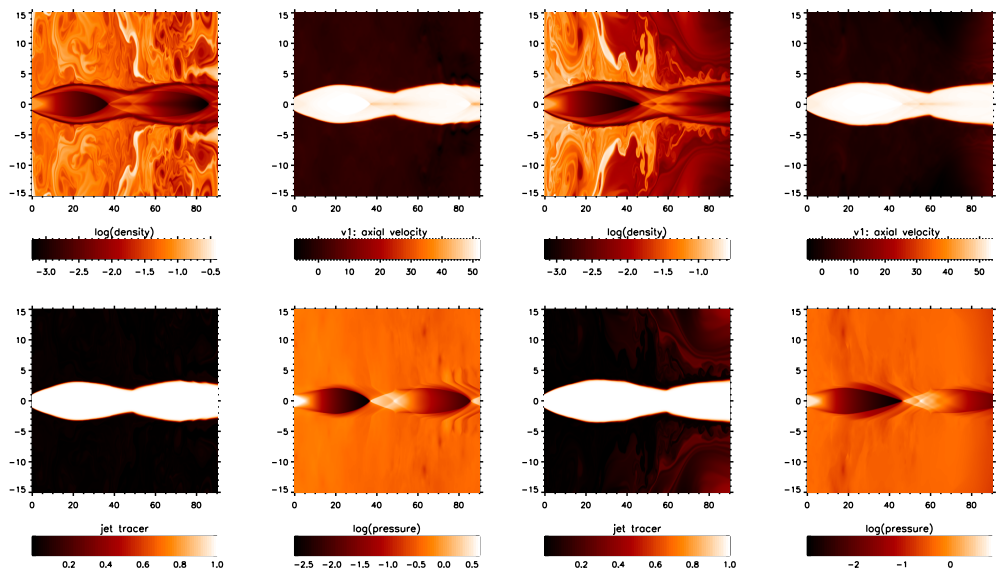


FIGURE C.6: Mach 6, over-pressure $\kappa = 7$ (left panel) $\kappa = 7.5$ (right panel) and density ratio $\eta = 0.1$.

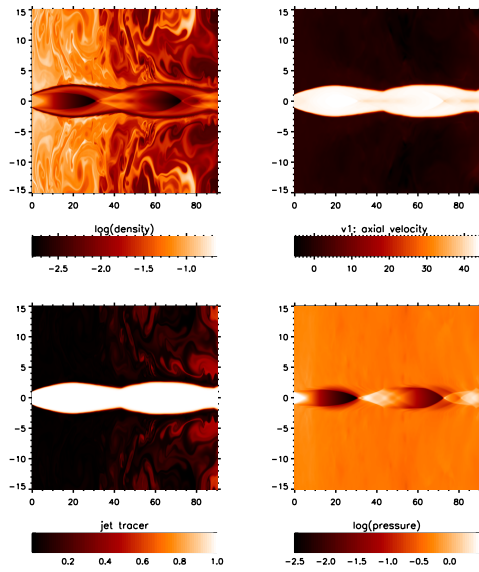


FIGURE C.7: Mach 6, over-pressure $\kappa = 8$ (and density ratio $\eta = 0.1$).

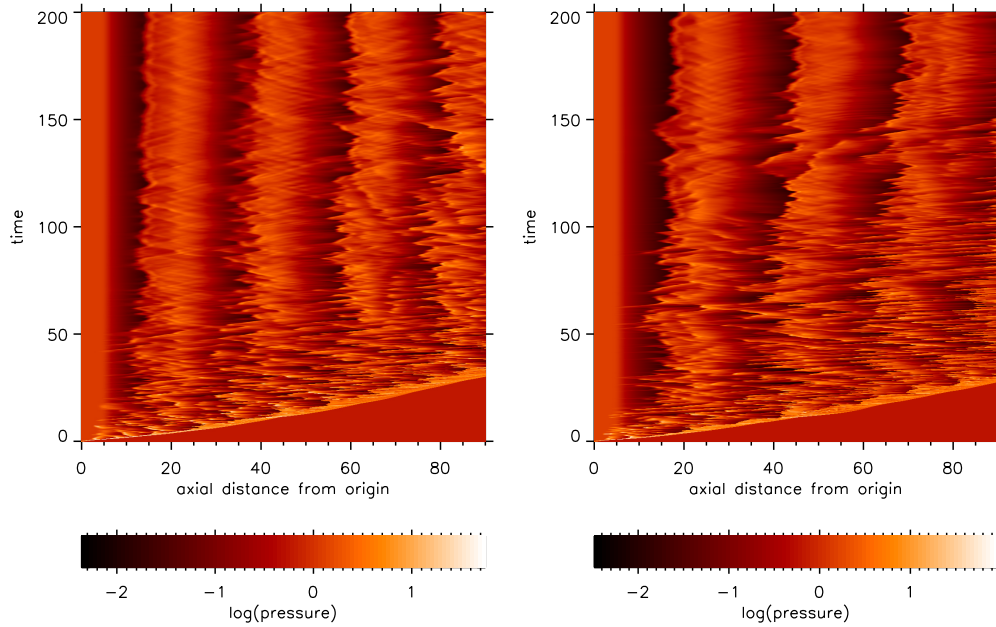


FIGURE C.8: Mach 6, over-pressure $\kappa = 2$ (left panel) $\kappa = 2.5$ (right panel) and density ratio $\eta = 0.1$.

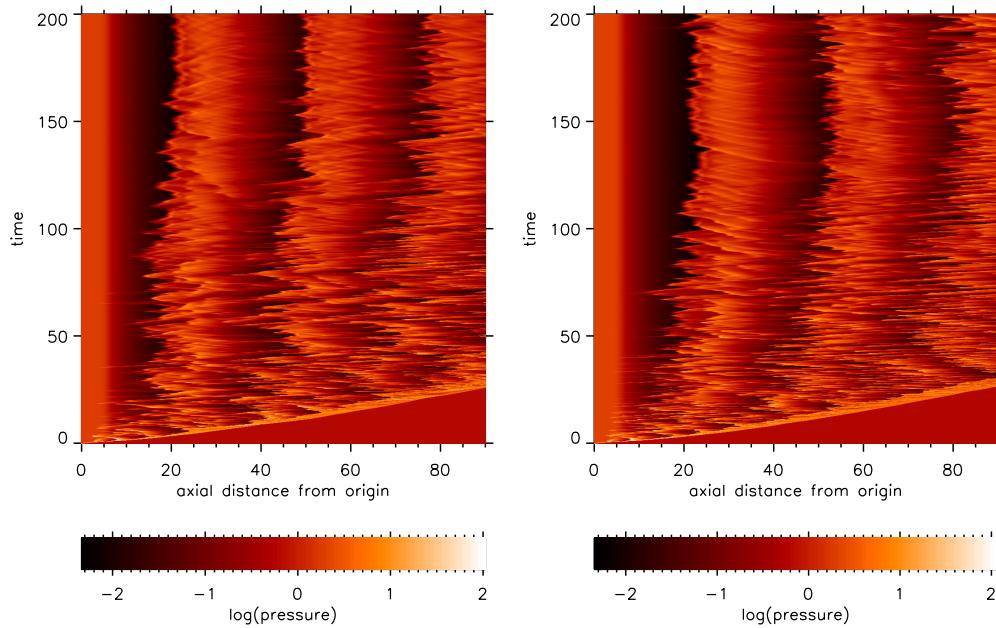


FIGURE C.9: Mach 6, over-pressure $\kappa = 3$ (left panel) $\kappa = 3.5$ (right panel) and density ratio $\eta = 0.1$.

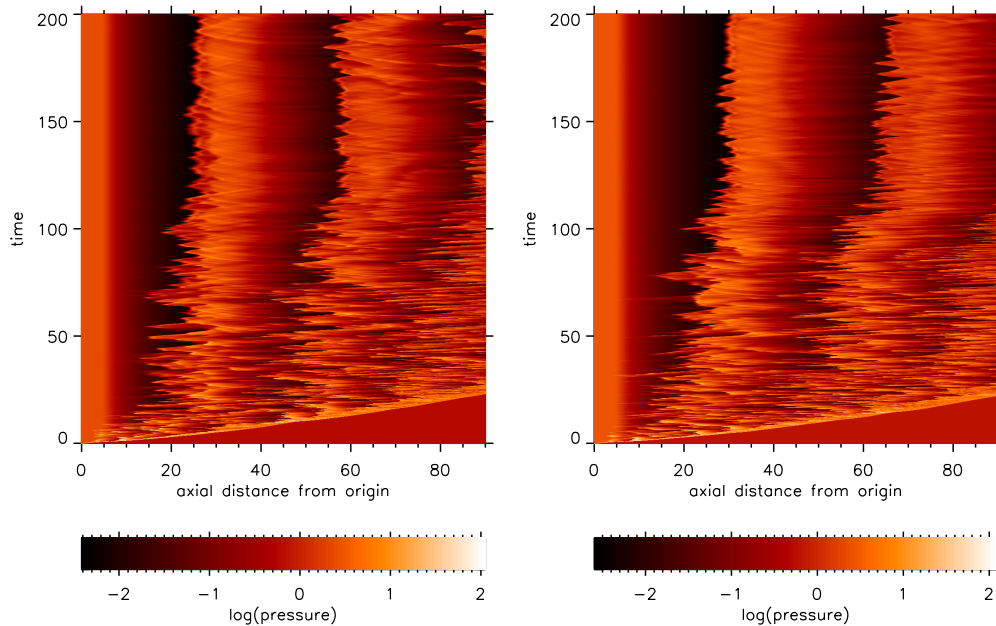


FIGURE C.10: Mach 6, over-pressure $\kappa = 4$ (left panel) $\kappa = 4.5$ (right panel) and density ratio $\eta = 0.1$.

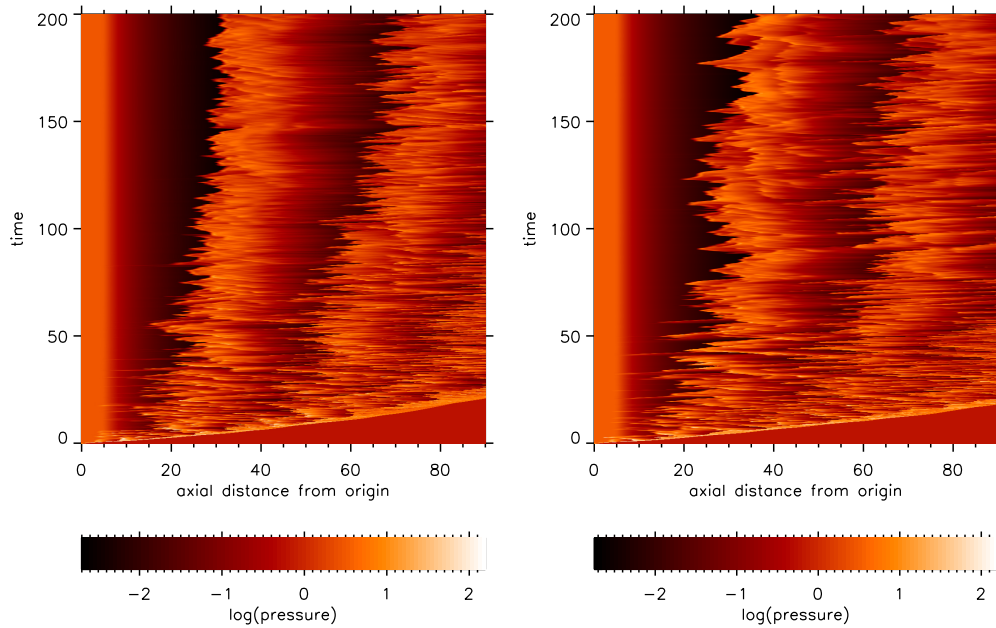


FIGURE C.11: Mach 6, over-pressure $\kappa = 5$ (left panel) $\kappa = 5.5$ (right panel) and density ratio $\eta = 0.1$.

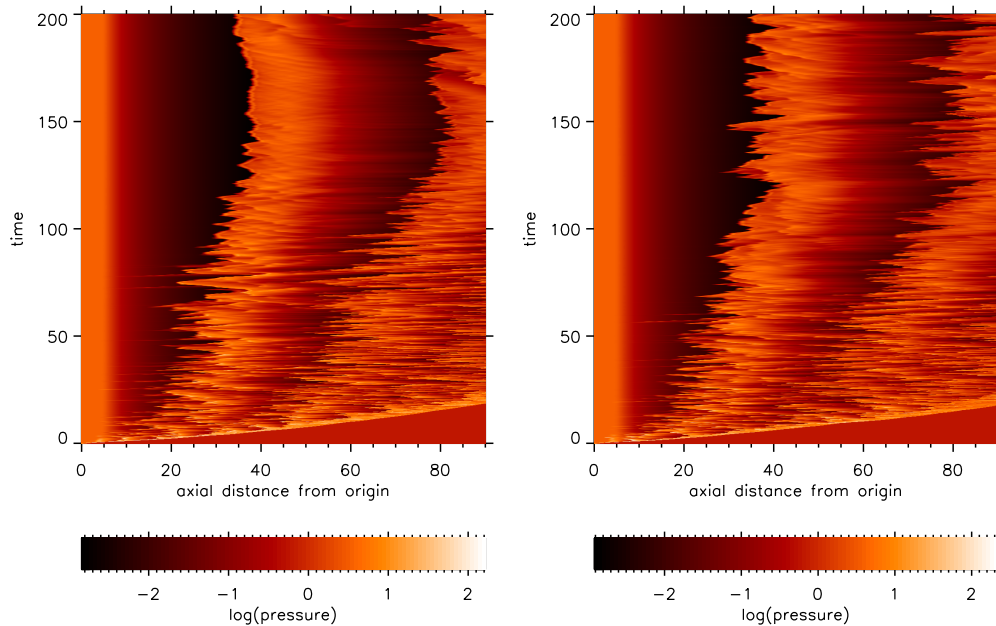


FIGURE C.12: Mach 6, over-pressure $\kappa = 6$ (left panel) $\kappa = 6.5$ (right panel) and density ratio $\eta = 0.1$.

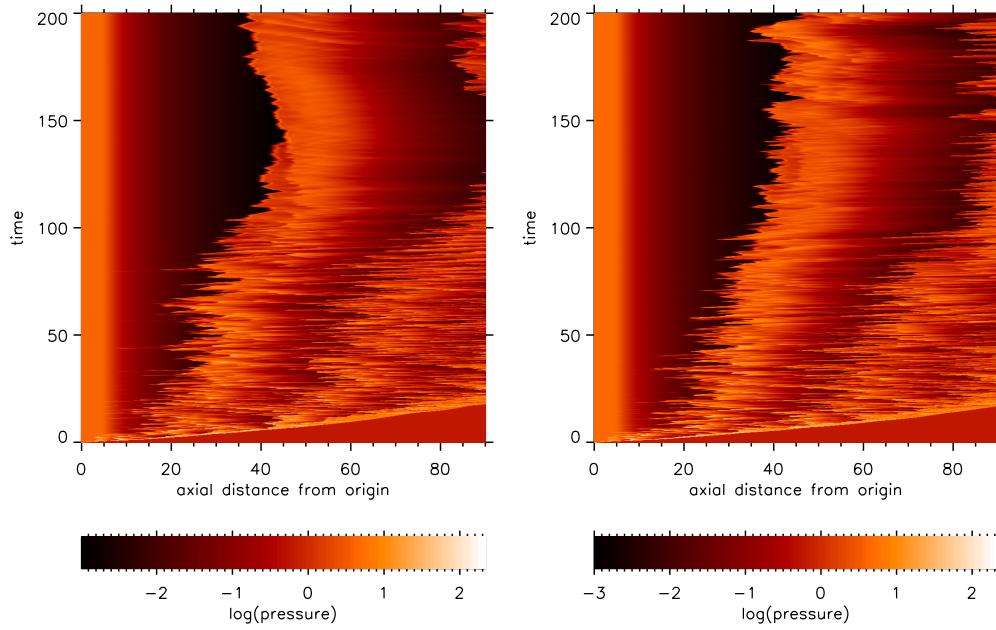


FIGURE C.13: Mach 6, over-pressure $\kappa = 7$ (left panel) $\kappa = 7.5$ (right panel) and density ratio $\eta = 0.1$.

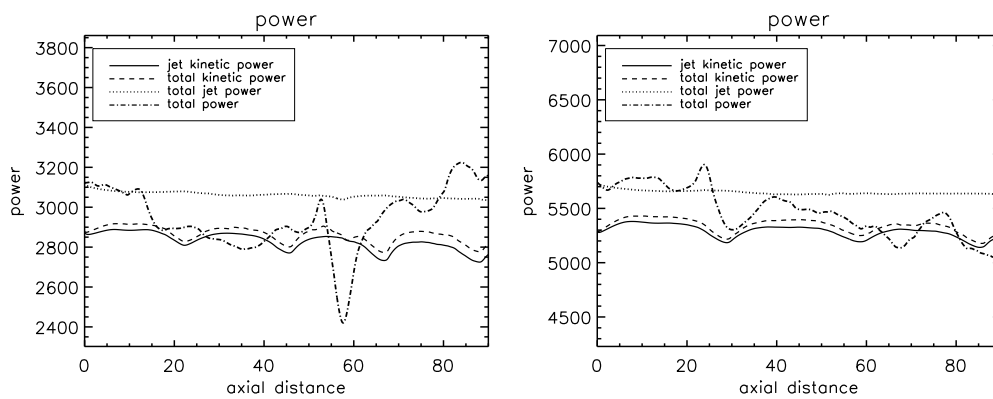


FIGURE C.14: Mach 6, over-pressure $\kappa = 2$ (left panel) $\kappa = 3$ (right panel) and density ratio $\eta = 0.1$.

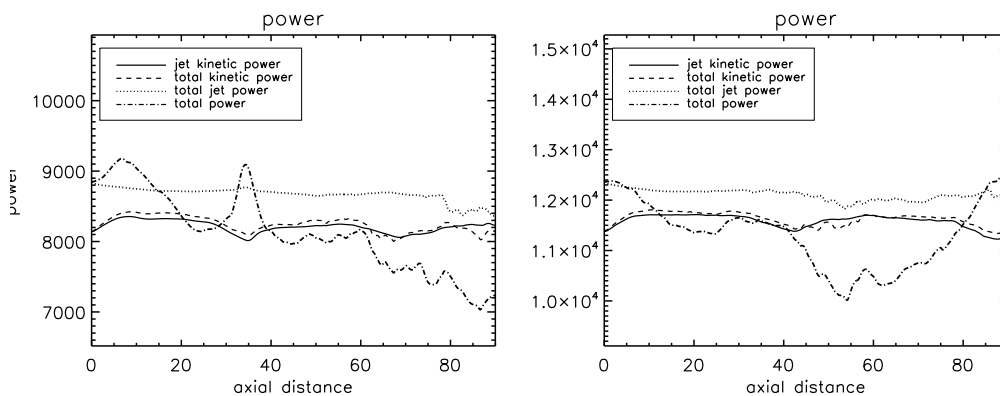


FIGURE C.15: Mach 6, over-pressure $\kappa = 4$ (left panel) $\kappa = 5$ (right panel) and density ratio $\eta = 0.1$.

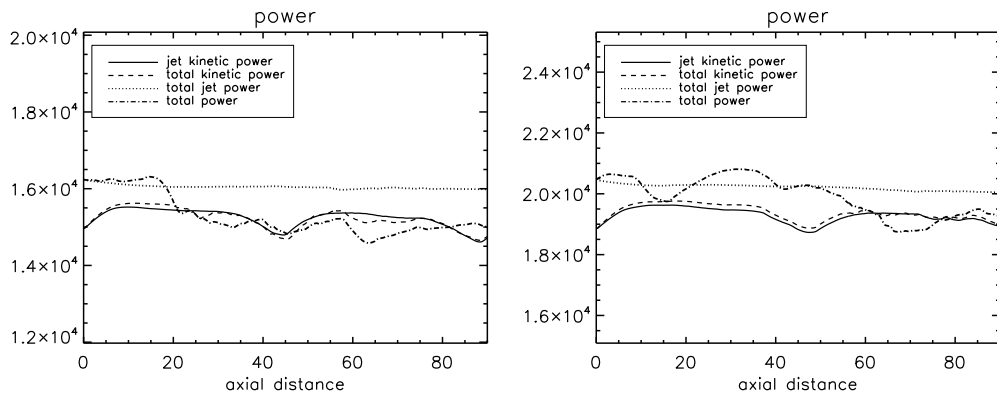


FIGURE C.16: Mach 6, over-pressure $\kappa = 6$ (left panel) $\kappa = 7$ (right panel) and density ratio $\eta = 0.1$.

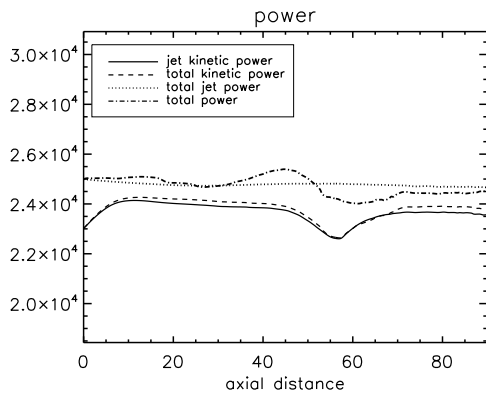


FIGURE C.17: Mach 6, over-pressure $\kappa = 8$ and density ratio $\eta = 0.1$.

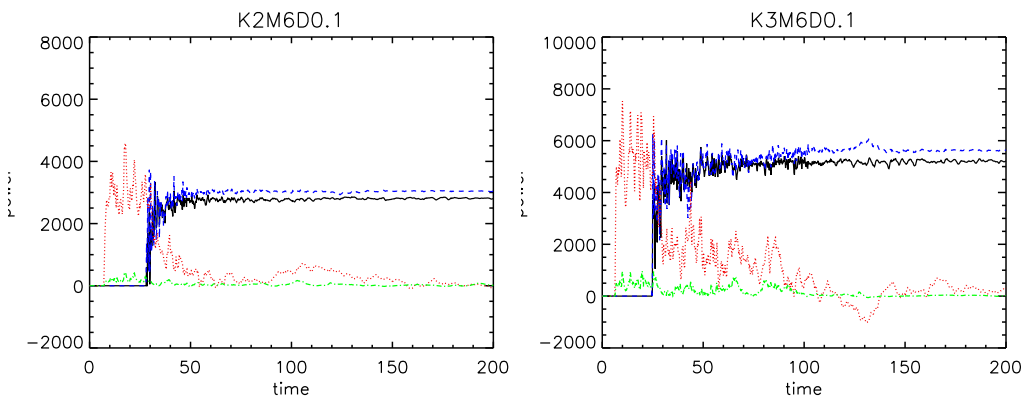


FIGURE C.18: Mach 6, over-pressure $\kappa = 2$ (left panel) $\kappa = 3$ (right panel) and density ratio $\eta = 0.1$.

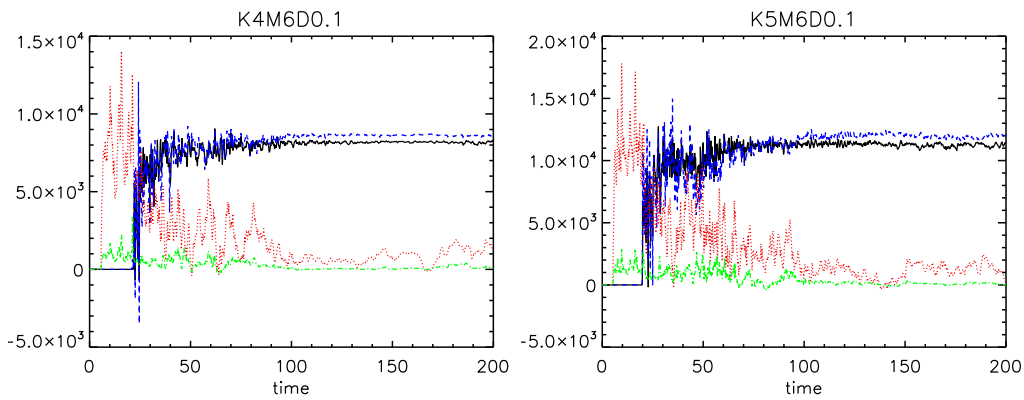


FIGURE C.19: Mach 6, over-pressure $\kappa = 4$ (left panel) $\kappa = 5$ (right panel) and density ratio $\eta = 0.1$.

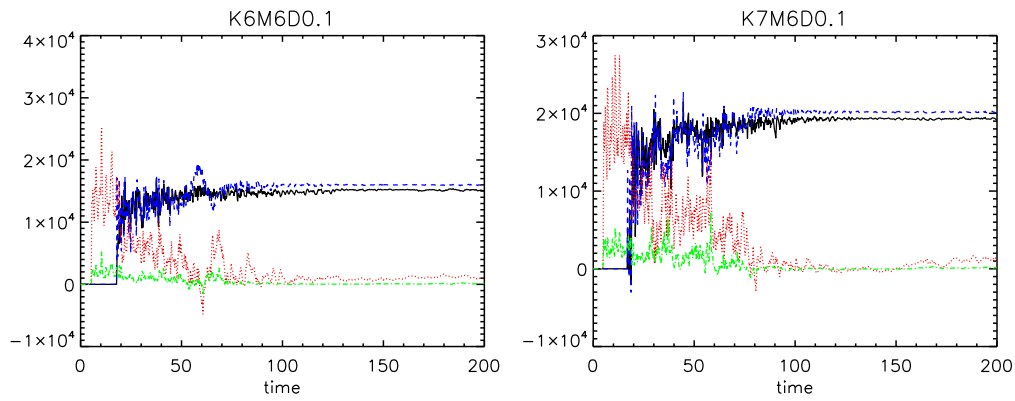


FIGURE C.20: Mach 6, over-pressure $\kappa = 6$ (left panel) $\kappa = 7$ (right panel) and density ratio $\eta = 0.1$.

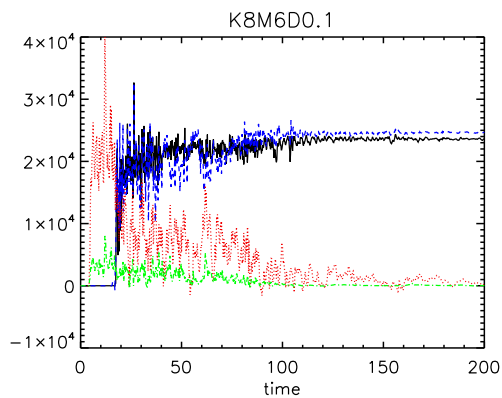


FIGURE C.21: Mach 6, over-pressure $\kappa = 8$ and density ratio $\eta = 0.1$.

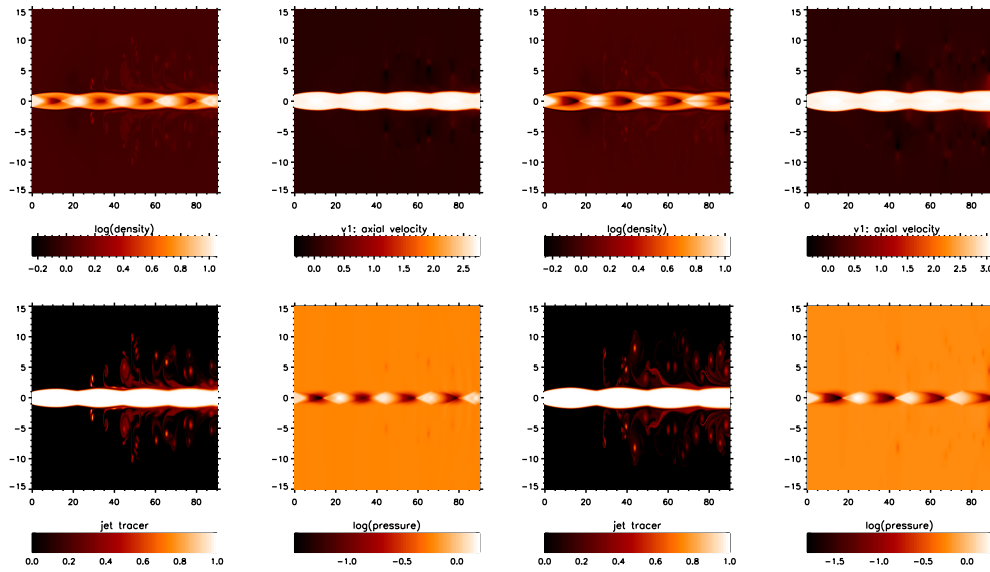


FIGURE C.22: Mach 6, over-pressure $\kappa = 2$ (left panel) $\kappa = 2.5$ (right panel) and density ratio $\eta = 10$.

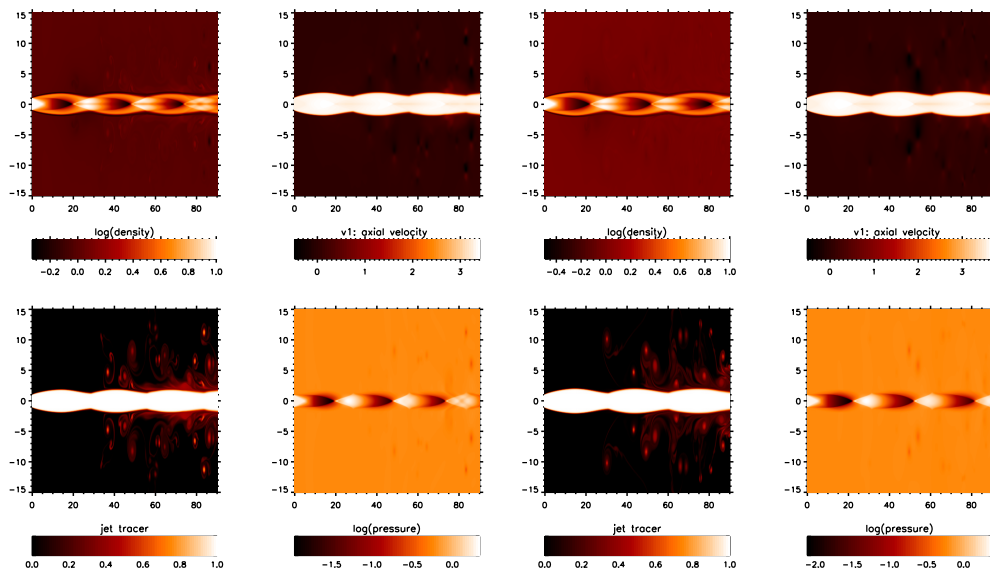


FIGURE C.23: Mach 6, over-pressure $\kappa = 3$ (left panel) $\kappa = 3.5$ (right panel) and density ratio $\eta = 10$.

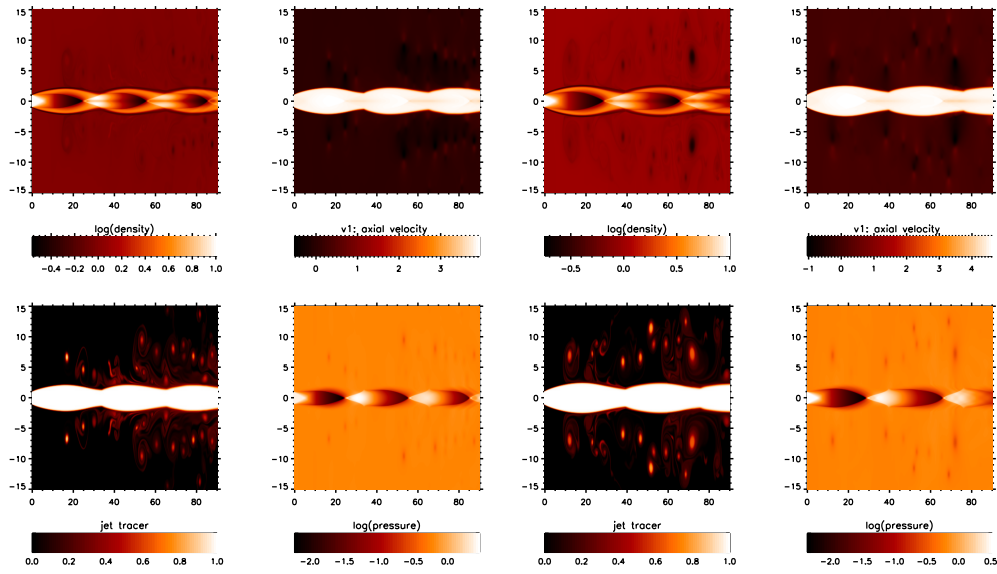


FIGURE C.24: Mach 6, over-pressure $\kappa = 4$ (left panel) $\kappa = 5.5$ (right panel) and density ratio $\eta = 10$.

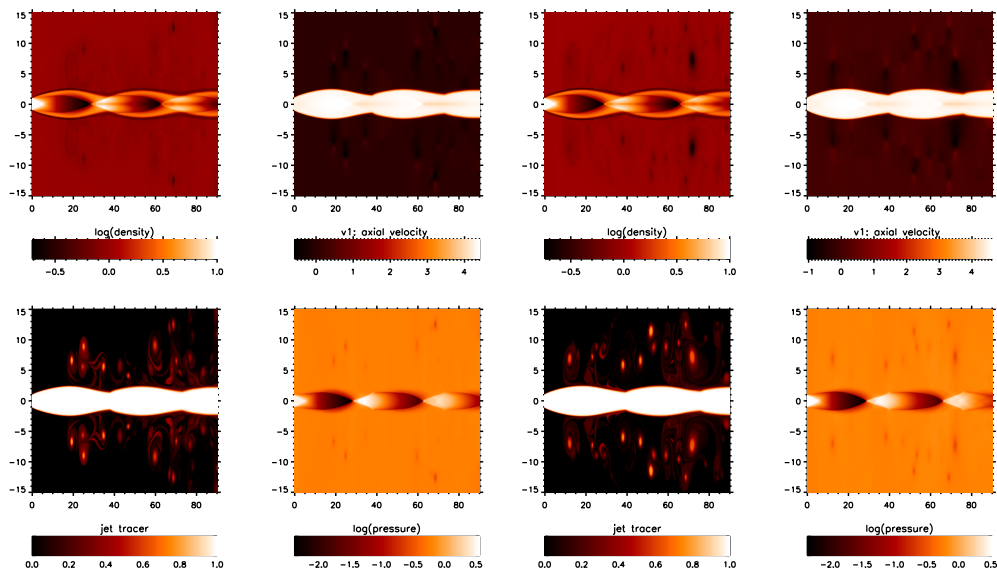


FIGURE C.25: Mach 6, over-pressure $\kappa = 5$ (left panel) $\kappa = 5.5$ (right panel) and density ratio $\eta = 10$.

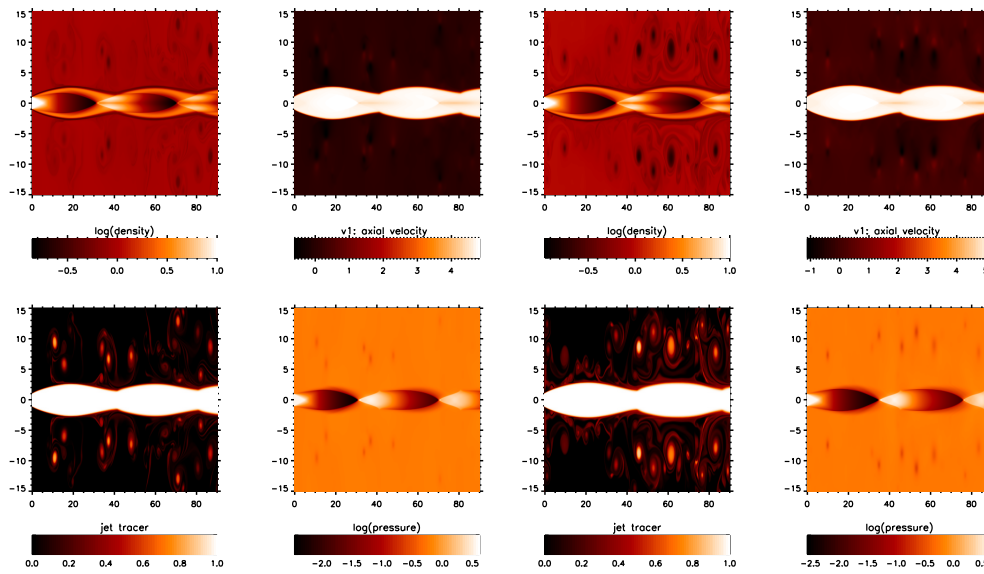


FIGURE C.26: Mach 6, over-pressure $\kappa = 6$ (left panel) $\kappa = 7$ (right panel) and density ratio $\eta = 10$.

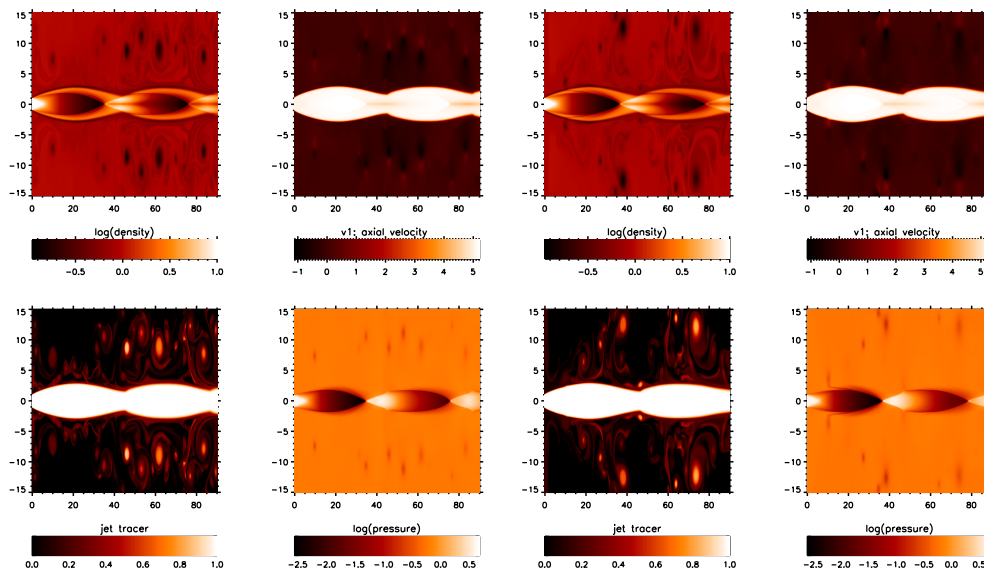


FIGURE C.27: Mach 6, over-pressure $\kappa = 7$ (left panel) $\kappa = 7.5$ (right panel) and density ratio $\eta = 10$.

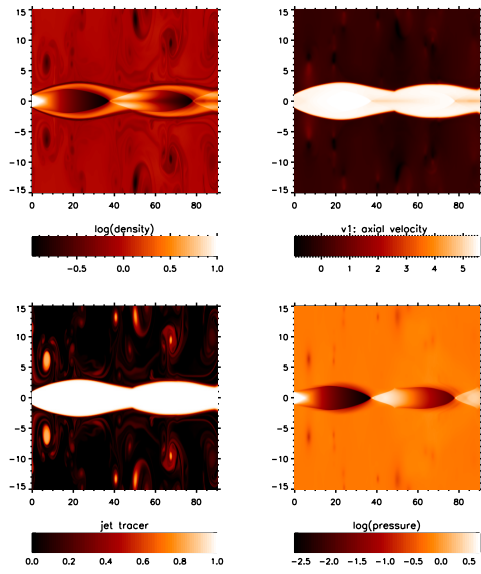


FIGURE C.28: Mach 4, over-pressure $\kappa = 8$ (and density ratio $\eta = 10$).

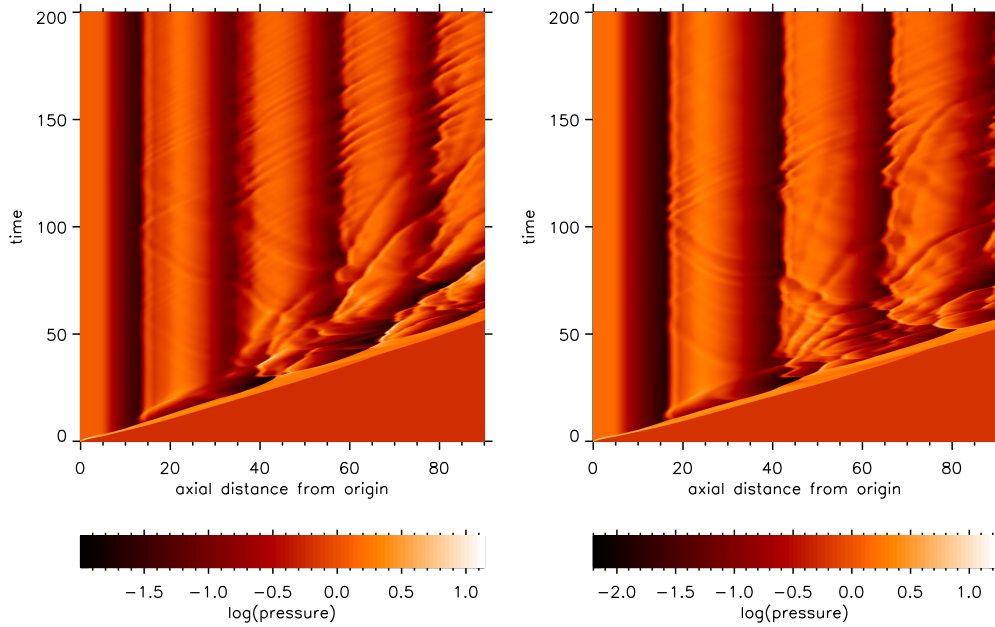


FIGURE C.29: Mach 4, over-pressure $\kappa = 2$ (left panel) $\kappa = 2.5$ (right panel) and density ratio $\eta = 10$.

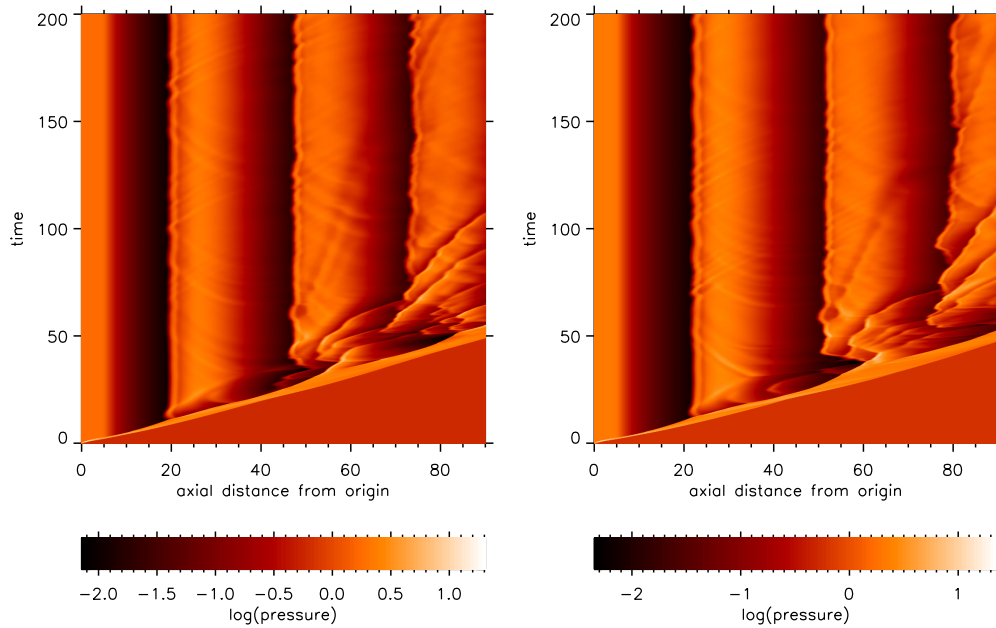


FIGURE C.30: Mach 6, over-pressure $\kappa = 3$ (left panel) $\kappa = 3.5$ (right panel) and density ratio $\eta = 10$.

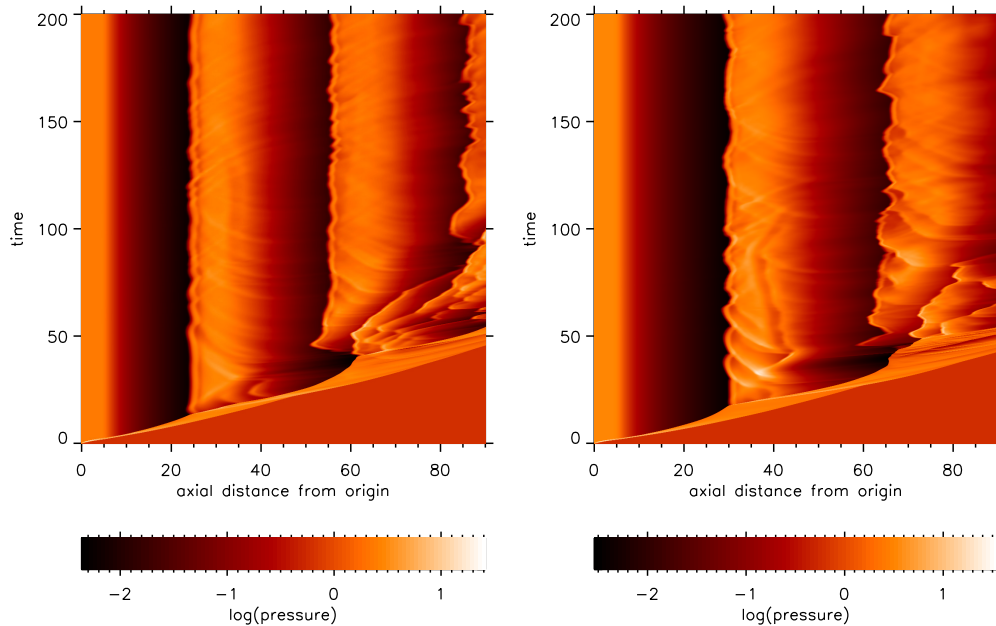


FIGURE C.31: Mach 6, over-pressure $\kappa = 4$ (left panel) $\kappa = 5.5$ (right panel) and density ratio $\eta = 10$.

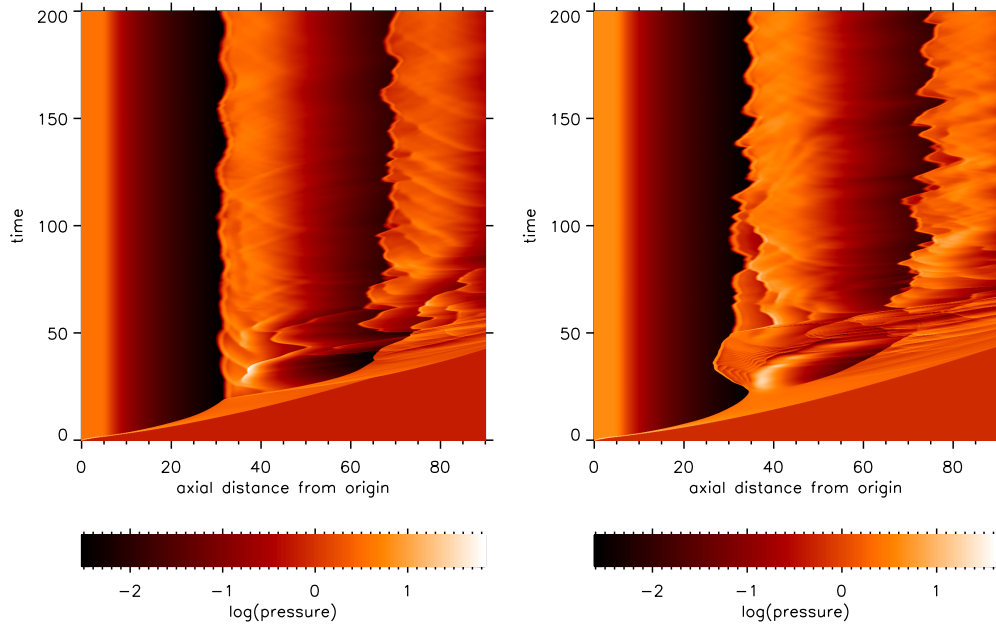


FIGURE C.32: Mach 6, over-pressure $\kappa = 6$ (left panel) $\kappa = 7$ (right panel) and density ratio $\eta = 10$.

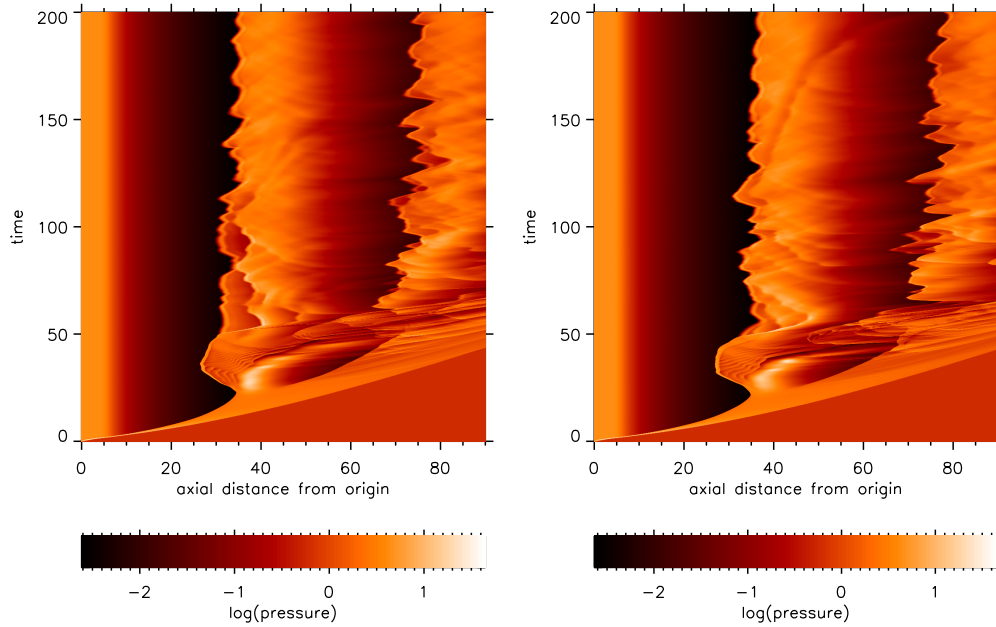


FIGURE C.33: Mach 6, over-pressure $\kappa = 7$ (left panel) $\kappa = 7.5$ (right panel) and density ratio $\eta = 10$.

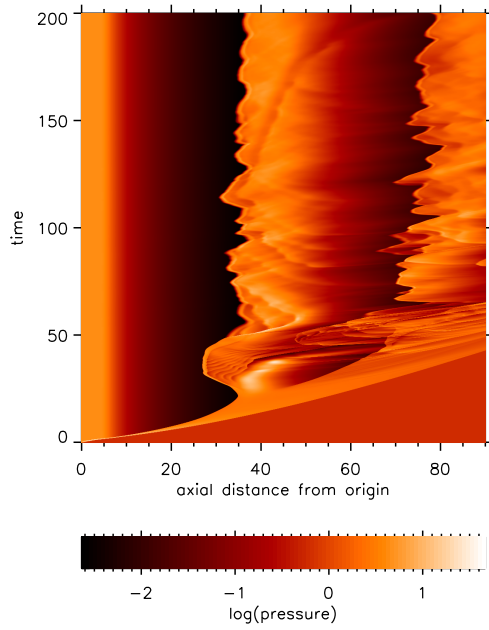


FIGURE C.34: Mach 4, over-pressure $\kappa = 8$ and density ratio $\eta = 10$.

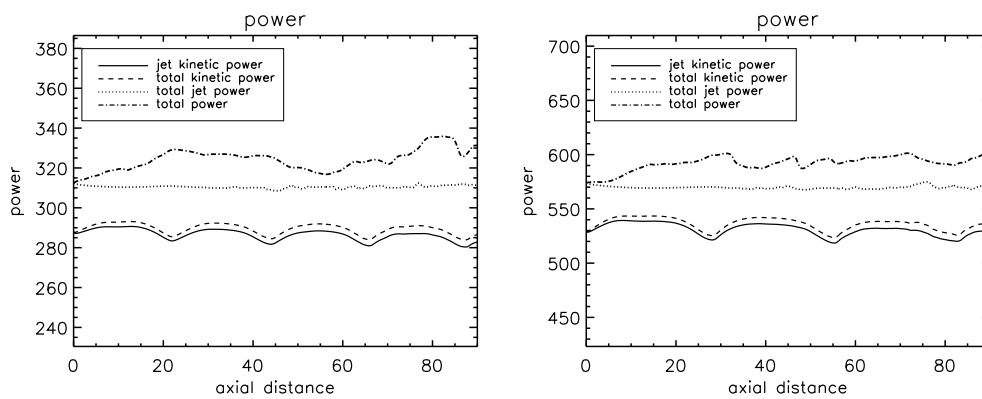


FIGURE C.35: Mach 6, over-pressure $\kappa = 2$ (left panel) $\kappa = 3$ (right panel) and density ratio $\eta = 10$.

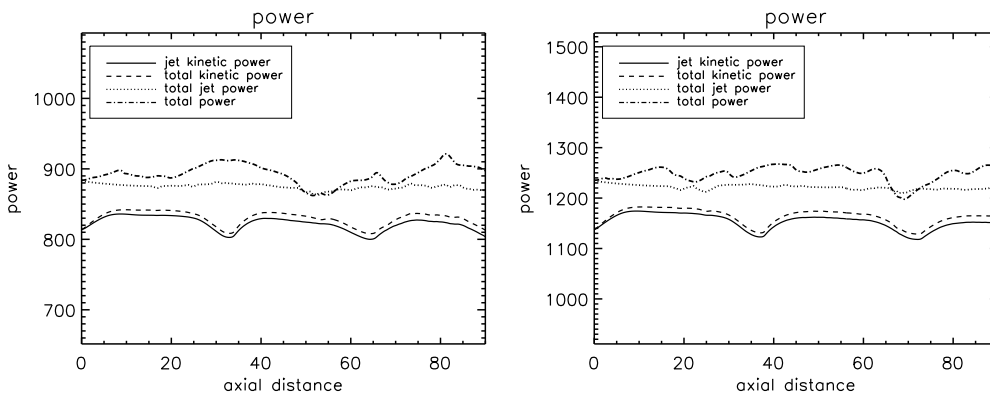


FIGURE C.36: Mach 6, over-pressure $\kappa = 4$ (left panel) $\kappa = 5$ (right panel) and density ratio $\eta = 10$.

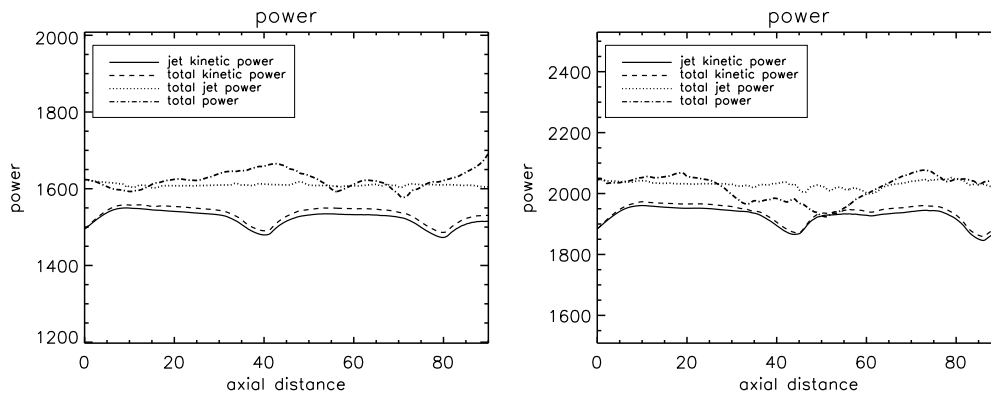


FIGURE C.37: Mach 6, over-pressure $\kappa = 6$ (left panel) $\kappa = 7$ (right panel) and density ratio $\eta = 10$.

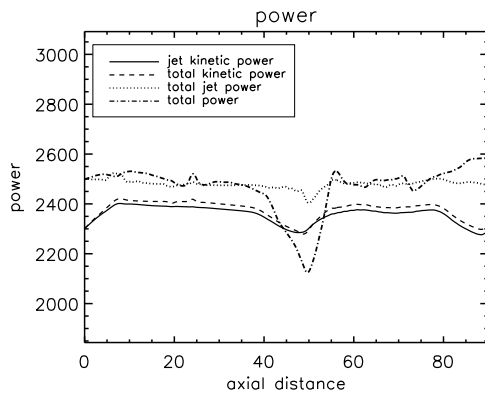


FIGURE C.38: Mach 6, over-pressure $\kappa = 8$ and density ratio $\eta = 10$.

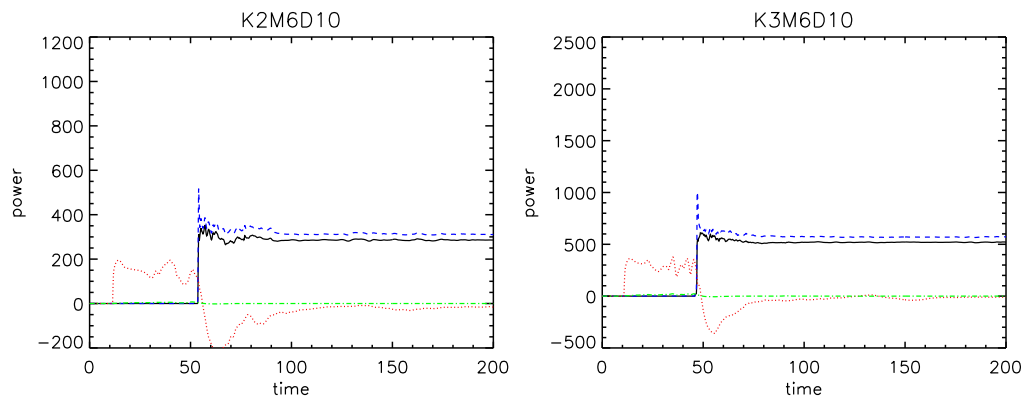


FIGURE C.39: Mach 6, over-pressure $\kappa = 2$ (left panel) $\kappa = 3$ (right panel) and density ratio $\eta = 10$.

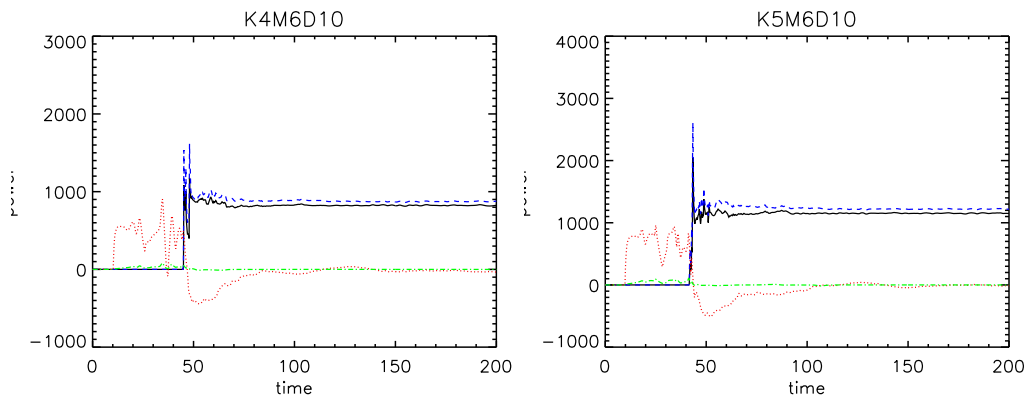


FIGURE C.40: Mach 6, over-pressure $\kappa = 4$ (left panel) $\kappa = 5$ (right panel) and density ratio $\eta = 10$.

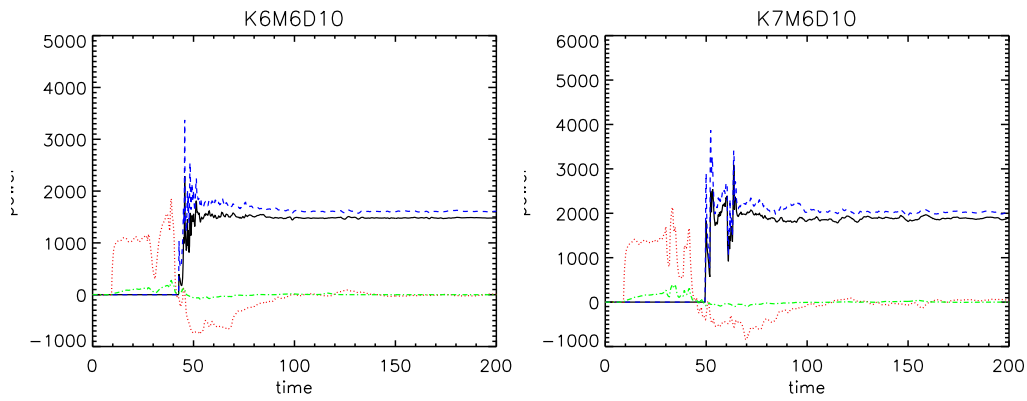


FIGURE C.41: Mach 6, over-pressure $\kappa = 6$ (left panel) $\kappa = 7$ (right panel) and density ratio $\eta = 10$.

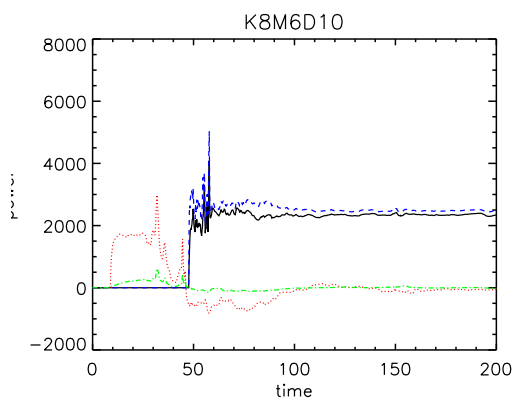


FIGURE C.42: Mach 6, over-pressure $\kappa = 8$ and density ratio $\eta = 10$.

Appendix D

Mach 8 Images

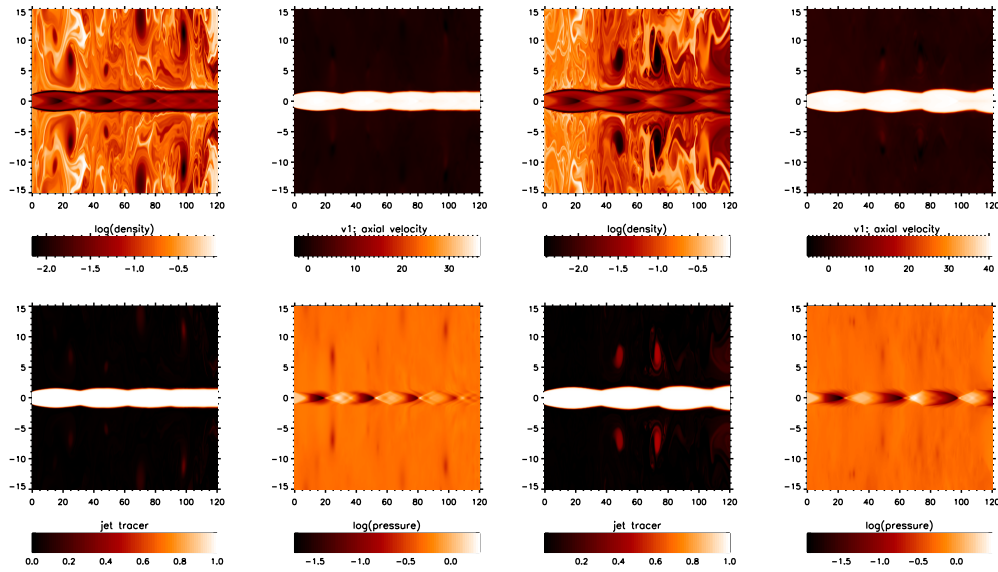


FIGURE D.1: Mach 8, over-pressure $\kappa = 2$ (left panel) $\kappa = 2.5$ (right panel) and density ratio $\eta = 0.1$.

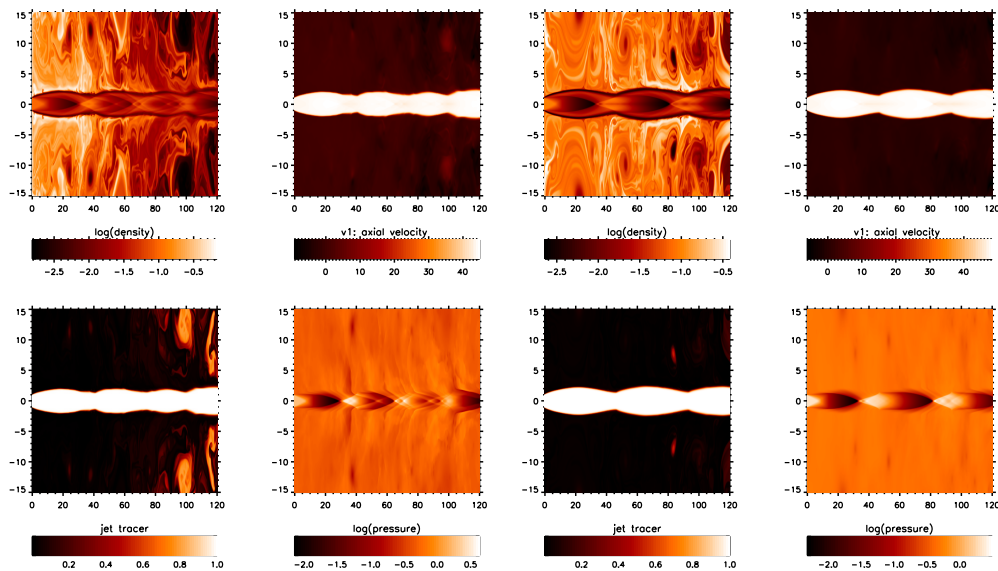


FIGURE D.2: Mach 8, over-pressure $\kappa = 3$ (left panel) $\kappa = 3.5$ (right panel) and density ratio $\eta = 0.1$.

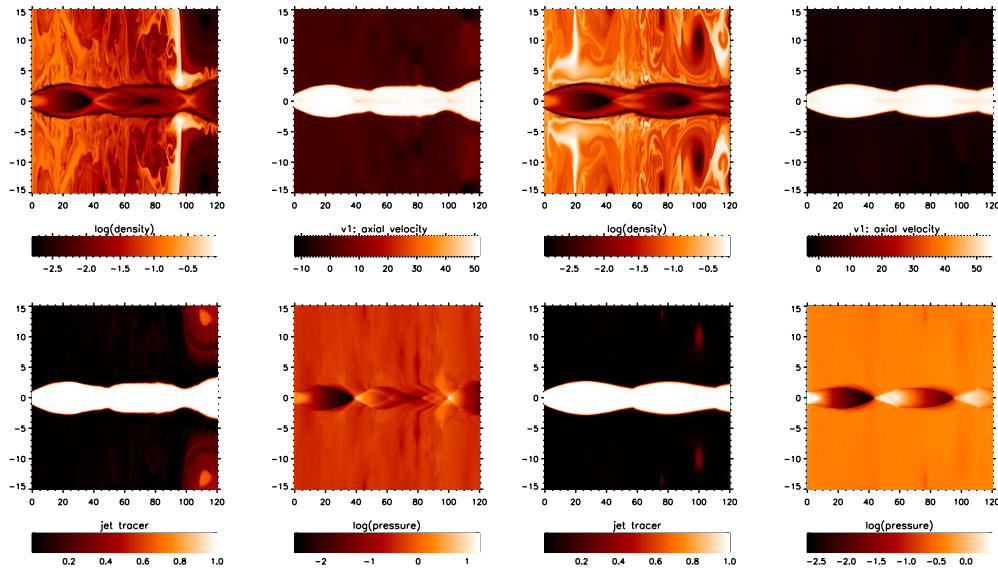


FIGURE D.3: Mach 8, over-pressure $\kappa = 4$ (left panel) $\kappa = 4.5$ (right panel) and density ratio $\eta = 0.1$.

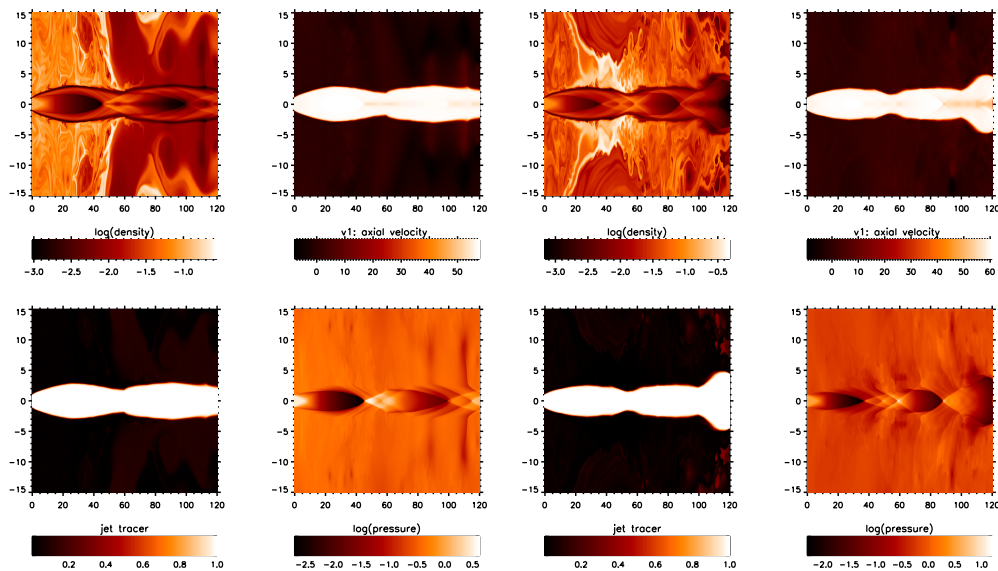


FIGURE D.4: Mach 8, over-pressure $\kappa = 5$ (left panel) $\kappa = 5.5$ (right panel) and density ratio $\eta = 0.1$.

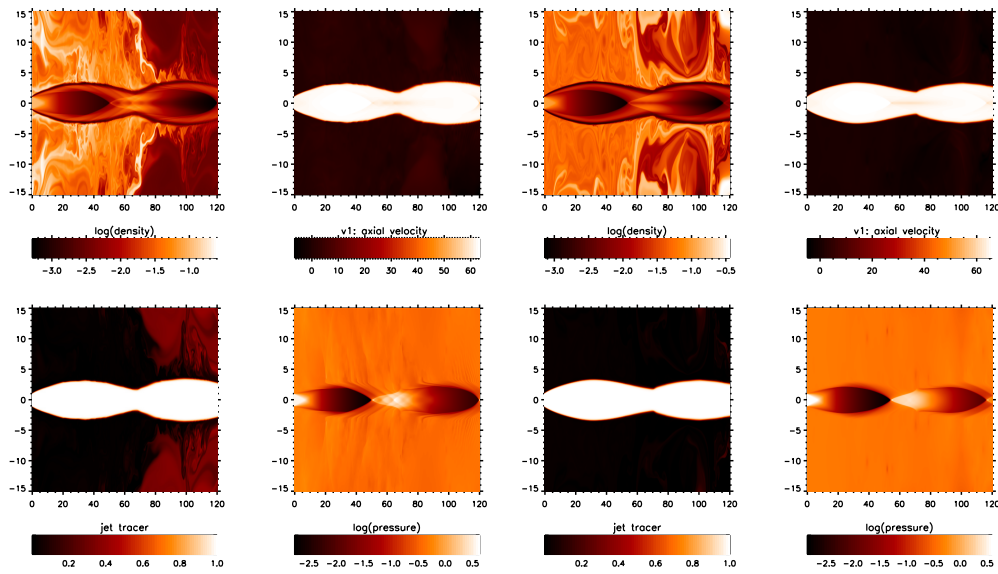


FIGURE D.5: Mach 8 , over-pressure $\kappa = 6$ (left panel) $\kappa = 6.5$ (right panel) and density ratio $\eta = 0.1$.

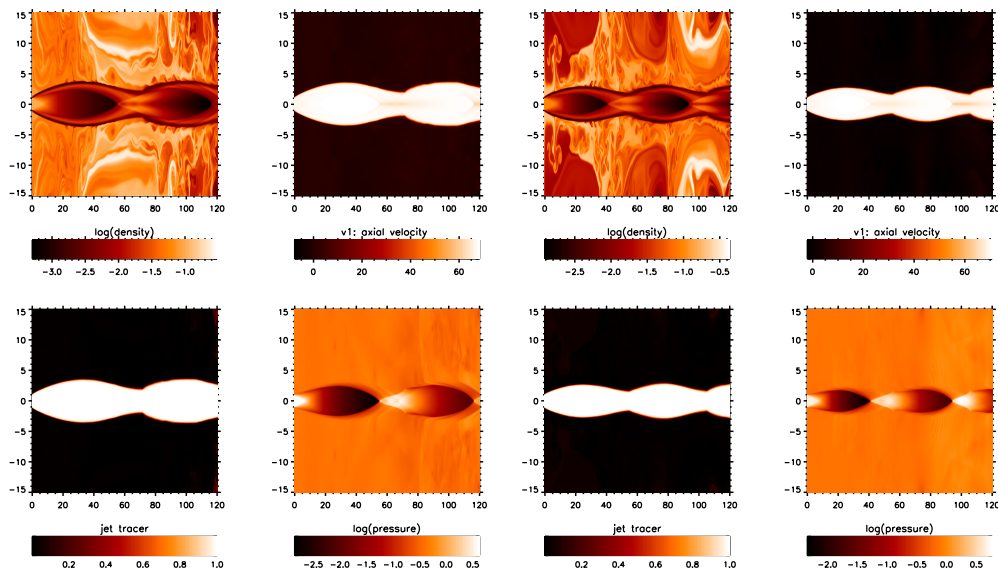


FIGURE D.6: Mach 8, over-pressure $\kappa = 7$ (left panel) $\kappa = 7.5$ (right panel) and density ratio $\eta = 0.1$.

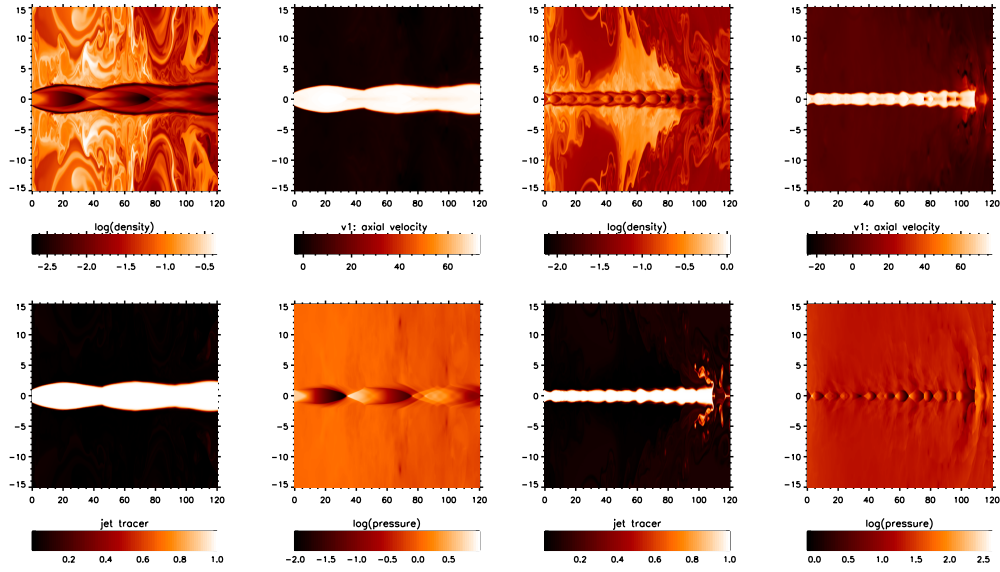


FIGURE D.7: Mach 8, over-pressure $\kappa = 8$ (left panel) $\kappa = 9$ (right panel) density ratio $\eta = 0.1$.

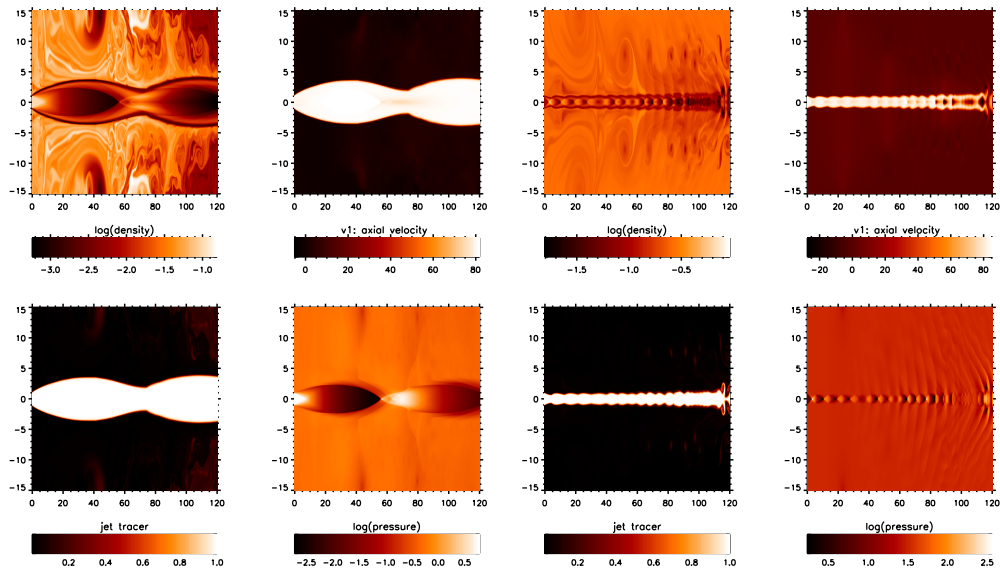


FIGURE D.8: Mach 8, over-pressure $\kappa = 10$ (left panel) $\kappa = 11$ (right panel) density ratio $\eta = 0.1$.

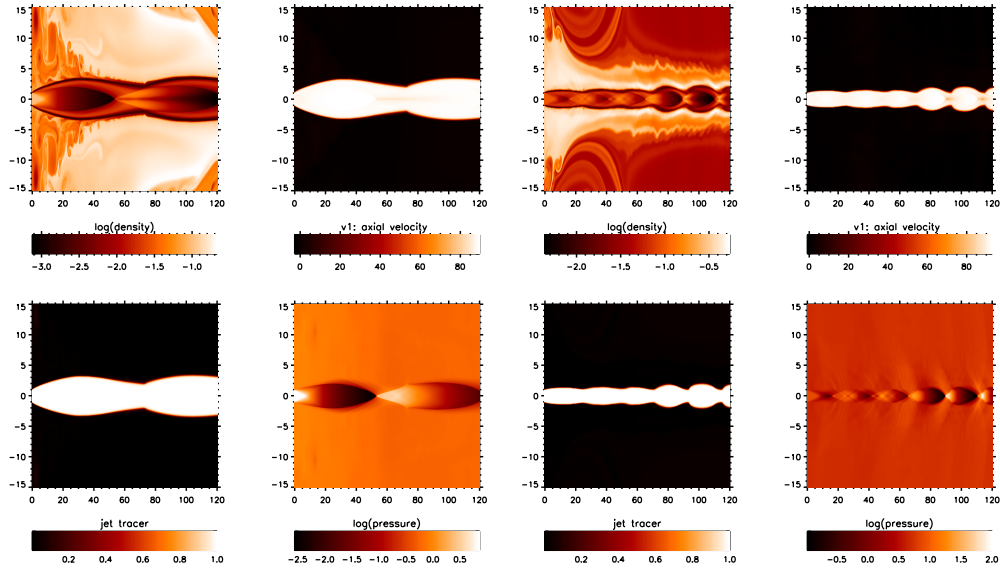


FIGURE D.9: Mach 8, over-pressure $\kappa = 12$ (left panel) $\kappa = 13$ (right panel) density ratio $\eta = 0.1$.

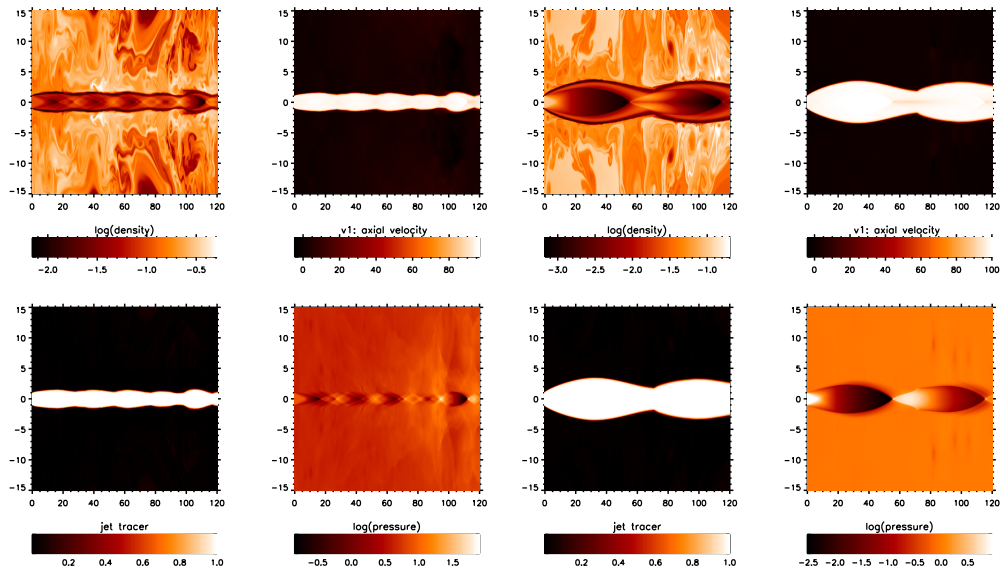


FIGURE D.10: Mach 8, over-pressure $\kappa = 14$ (left panel) $\kappa = 15$ (right panel) density ratio $\eta = 0.1$.

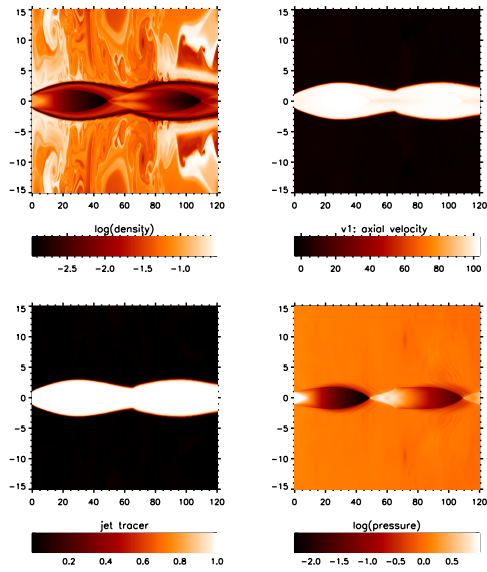


FIGURE D.11: Mach 8, over-pressure $\kappa = 16$ and density ratio $\eta = 0.1$.

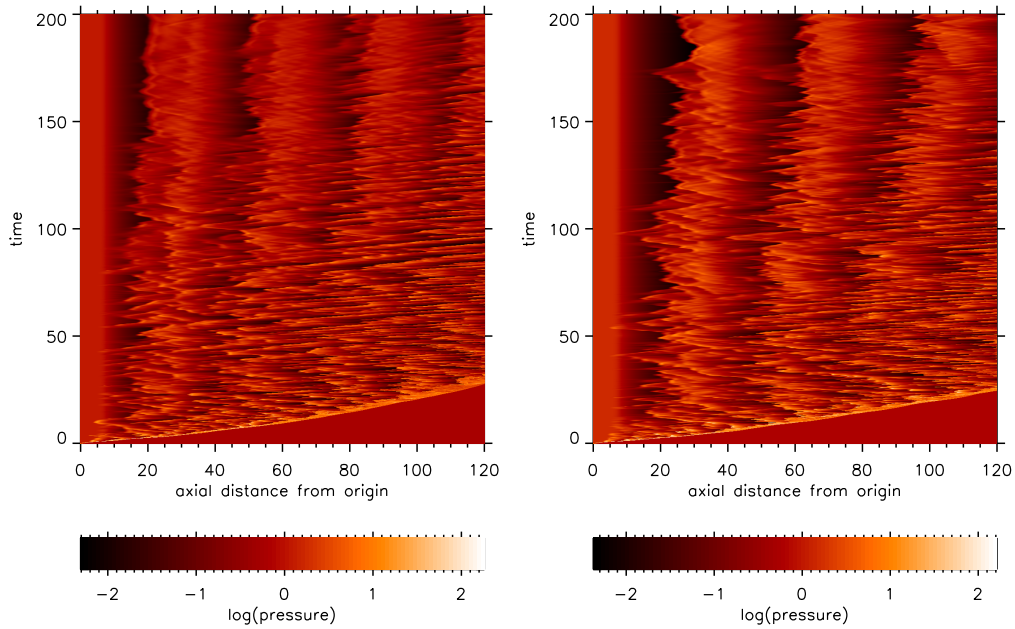


FIGURE D.12: Mach 8, over-pressure $\kappa = 2$ (left panel) $\kappa = 2.5$ (right panel) and density ratio $\eta = 0.1$.

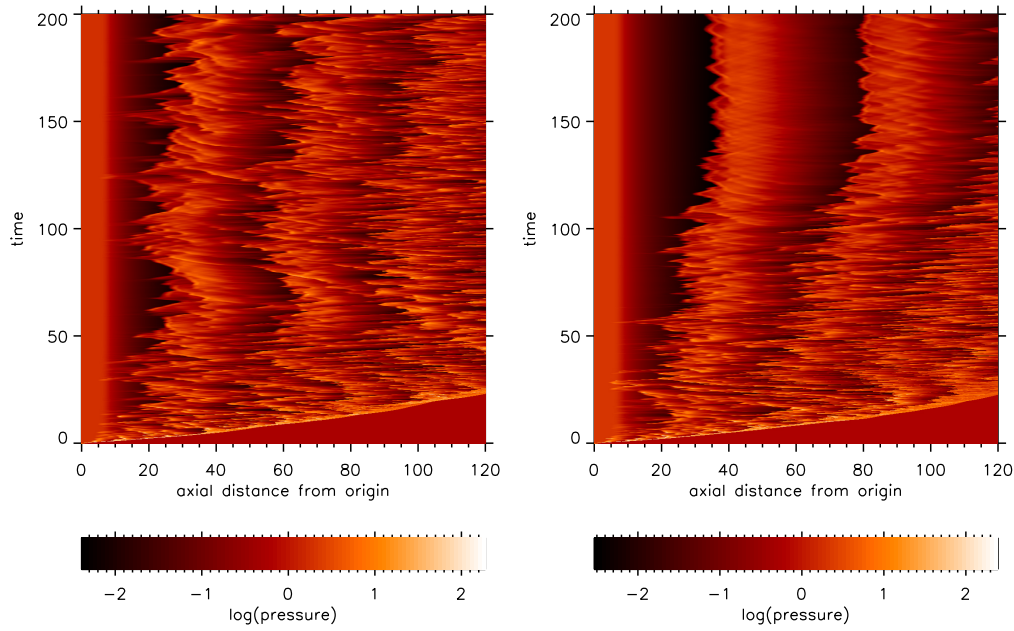


FIGURE D.13: Mach 8, over-pressure $\kappa = 3$ (left panel) $\kappa = 3.5$ (right panel) and density ratio $\eta = 0.1$.

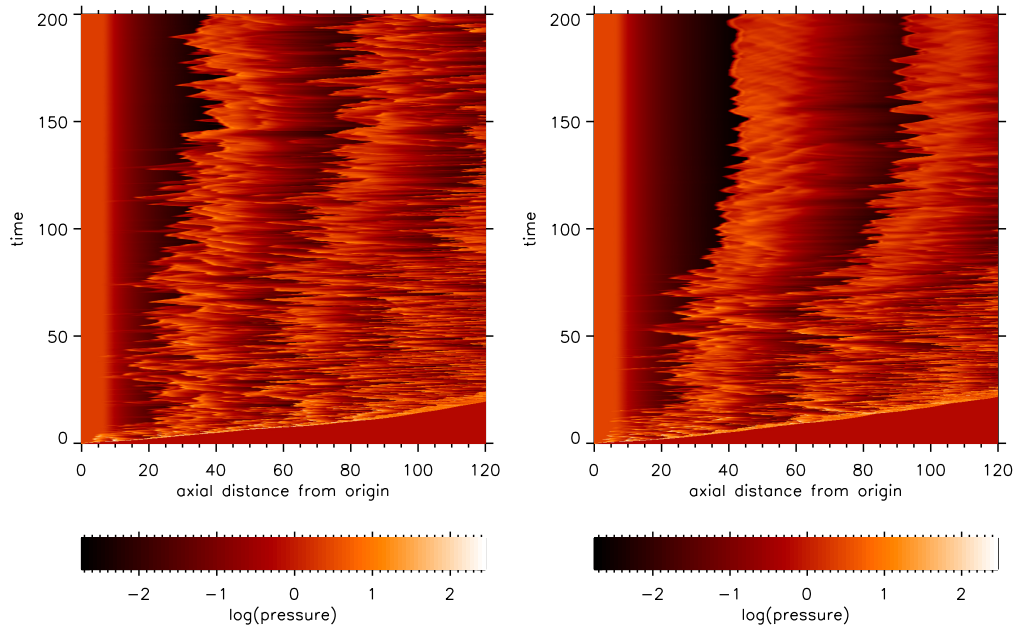


FIGURE D.14: Mach 8, over-pressure $\kappa = 4$ (left panel) $\kappa = 4.5$ (right panel) and density ratio $\eta = 0.1$.

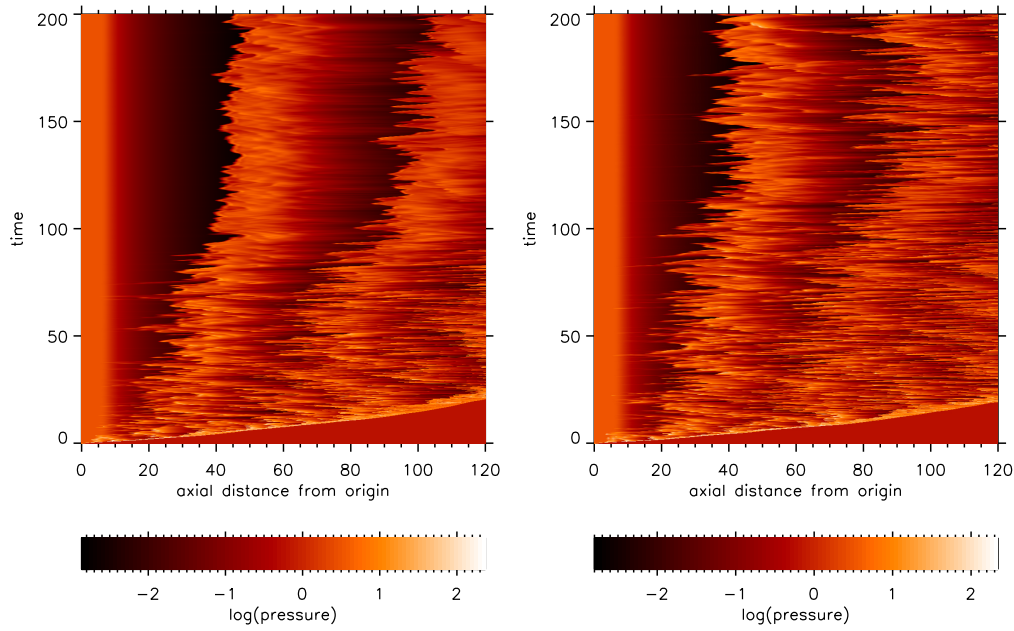


FIGURE D.15: Mach 8, over-pressure $\kappa = 5$ (left panel) $\kappa = 5.5$ (right panel) and density ratio $\eta = 0.1$.

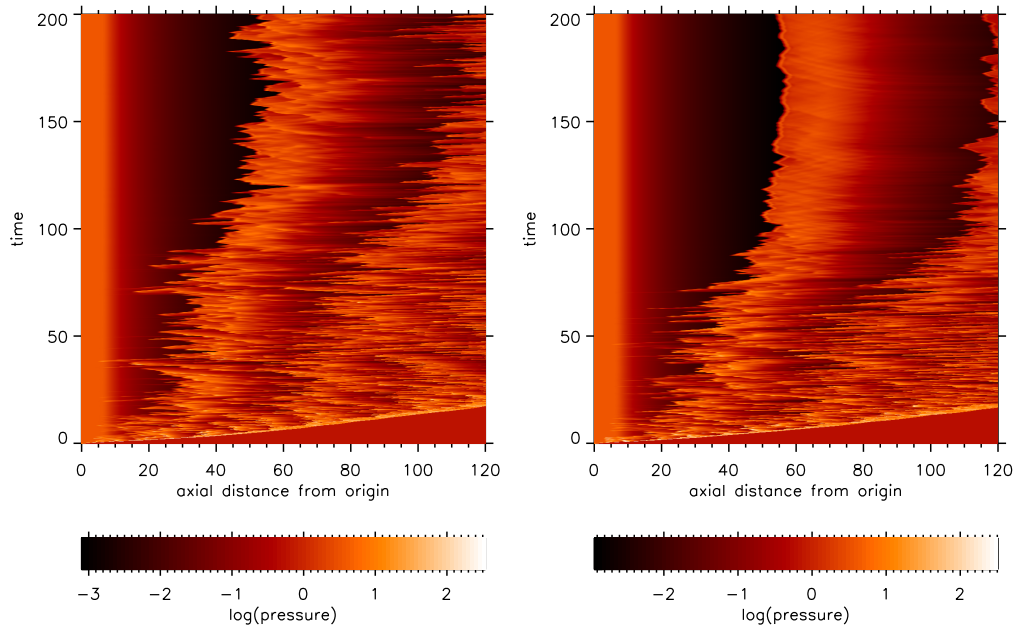


FIGURE D.16: Mach 8, over-pressure $\kappa = 6$ (left panel) $\kappa = 6.5$ (right panel) and density ratio $\eta = 0.1$.

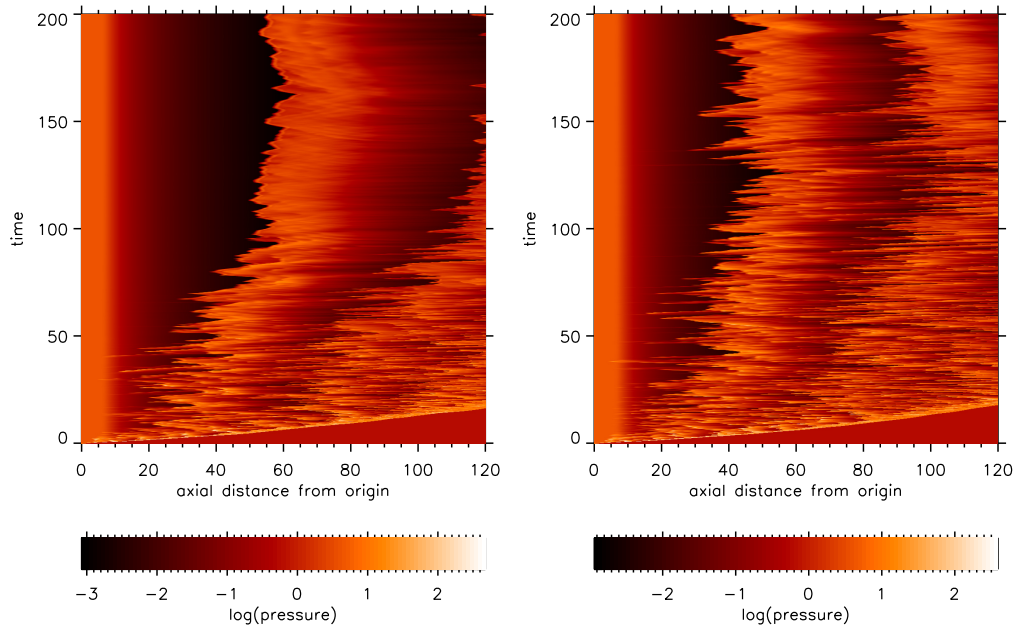


FIGURE D.17: Mach 8, over-pressure $\kappa = 7$ (left panel) $\kappa = 7.5$ (right panel) and density ratio $\eta = 0.1$.

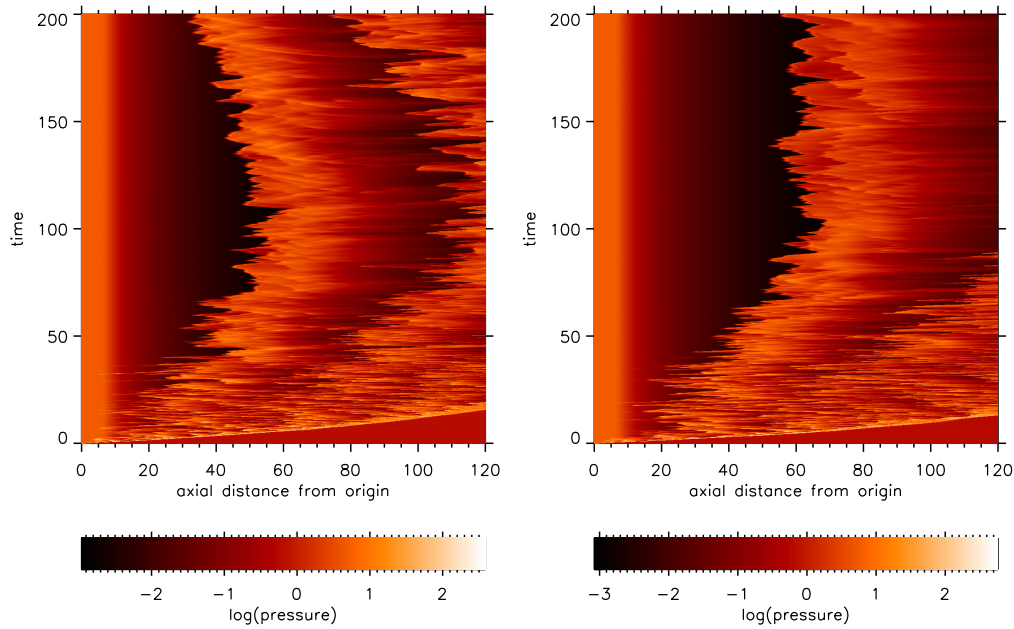


FIGURE D.18: Mach 8, over-pressure $\kappa = 8$ (left panel) $\kappa = 10$ (right panel) and density ratio $\eta = 0.1$.

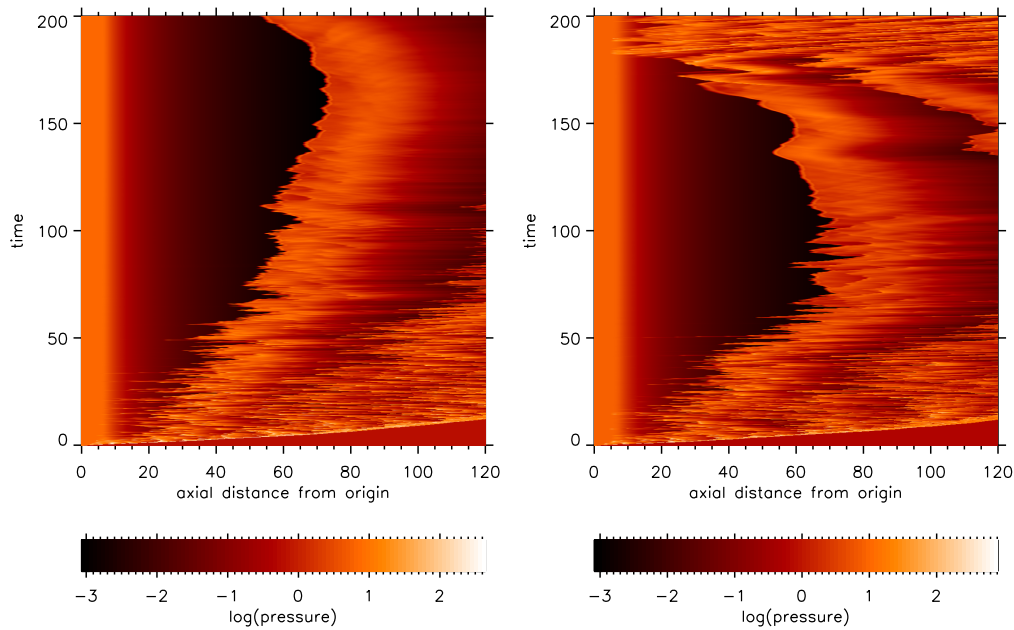


FIGURE D.19: Mach 8, over-pressure $\kappa = 12$ (left panel) $\kappa = 14$ (right panel) and density ratio $\eta = 0.1$.

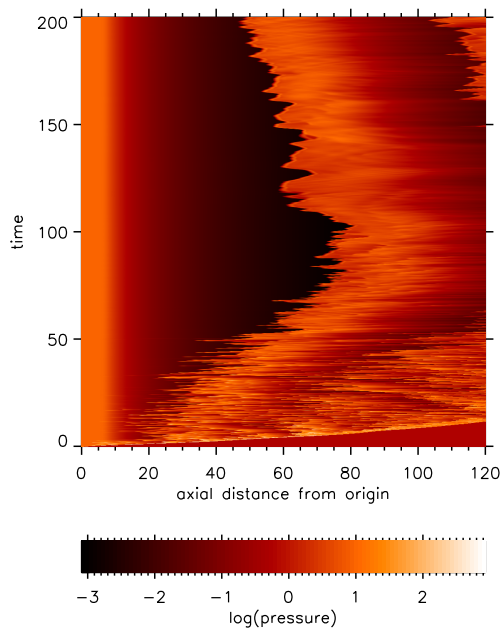


FIGURE D.20: Mach 8, over-pressure $\kappa = 16$ and density ratio $\eta = 0.1$.

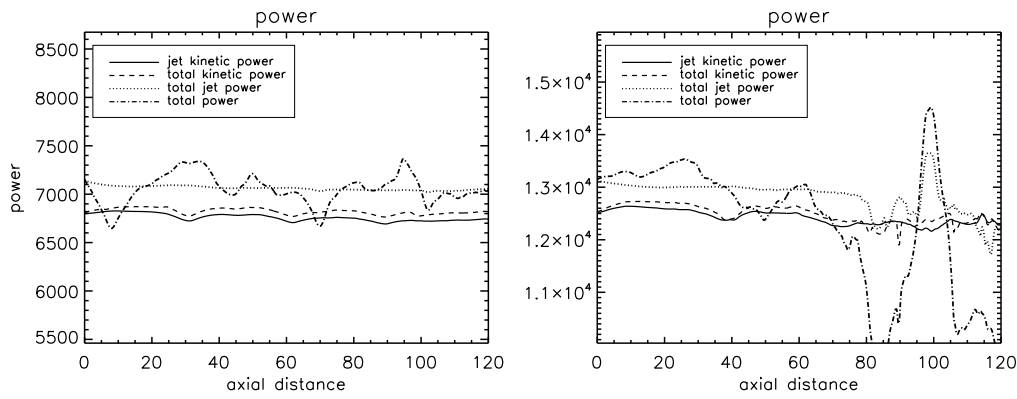


FIGURE D.21: Mach 8, over-pressure $\kappa = 2$ (left panel) $\kappa = 3$ (right panel) and density ratio $\eta = 0.1$.

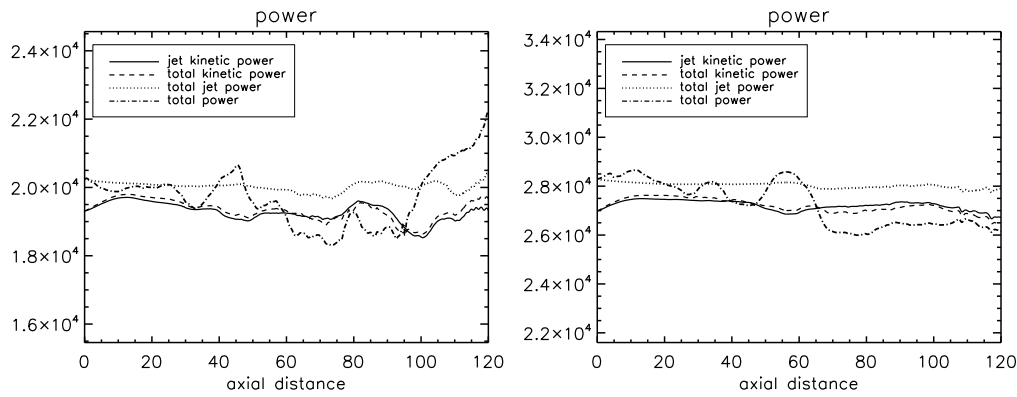


FIGURE D.22: Mach 8, over-pressure $\kappa = 4$ (left panel) $\kappa = 5$ (right panel) and density ratio $\eta = 0.1$.

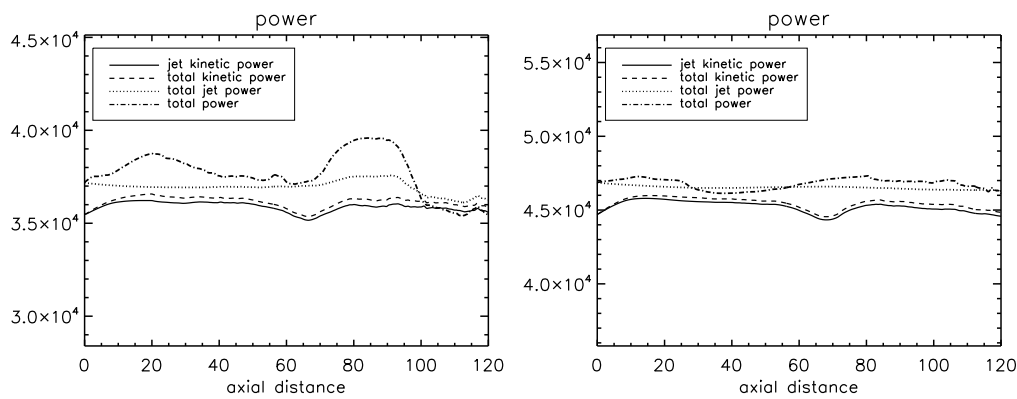


FIGURE D.23: Mach 8, over-pressure $\kappa = 6$ (left panel) $\kappa = 7$ (right panel) and density ratio $\eta = 0.1$.

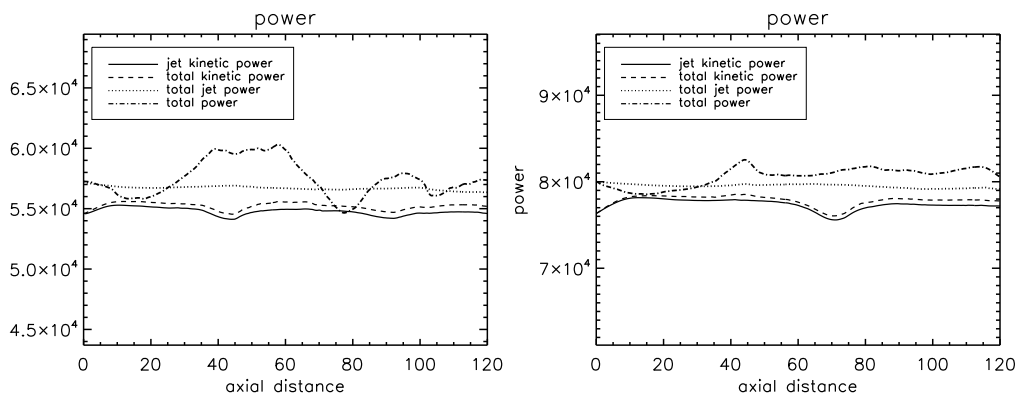


FIGURE D.24: Mach 8, over-pressure $\kappa = 8$ (left panel) $\kappa = 10$ (right panel) and density ratio $\eta = 0.1$.

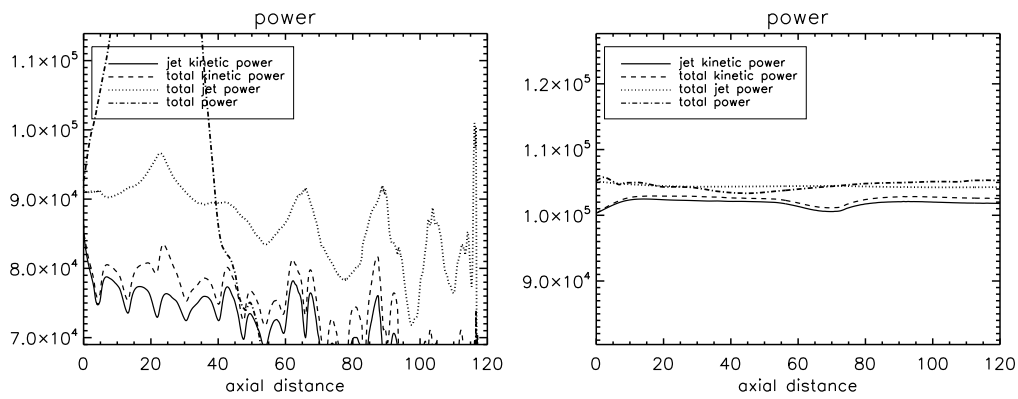


FIGURE D.25: Mach 8, over-pressure $\kappa = 11$ (left panel) $\kappa = 12$ (right panel) and density ratio $\eta = 0.1$.

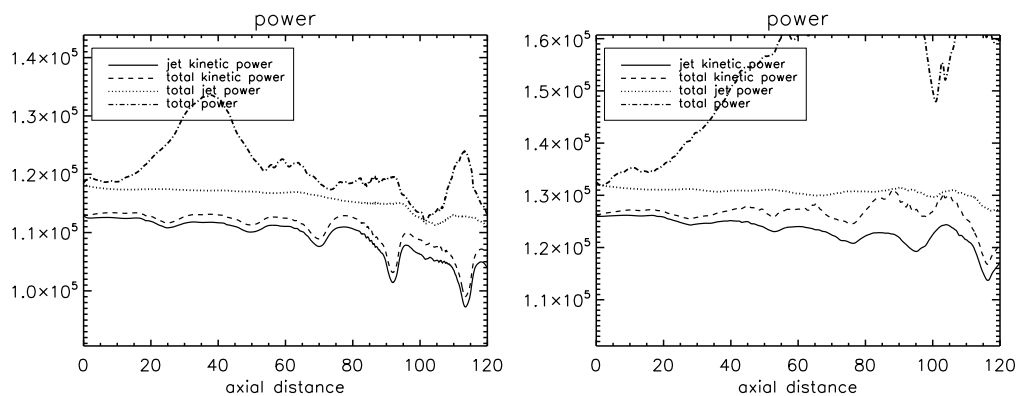


FIGURE D.26: Mach 8, over-pressure $\kappa = 13$ (left panel) $\kappa = 14$ (right panel) and density ratio $\eta = 0.1$.

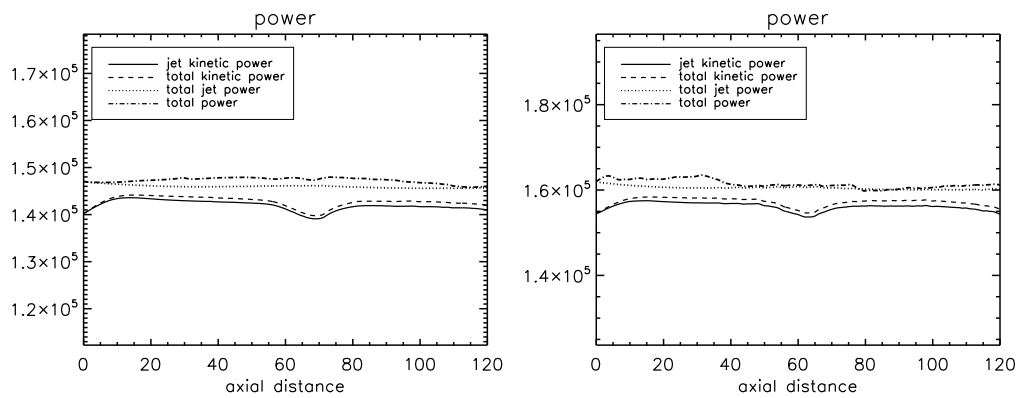


FIGURE D.27: Mach 8, over-pressure $\kappa = 15$ (left panel) $\kappa = 16$ (right panel) and density ratio $\eta = 0.1$.

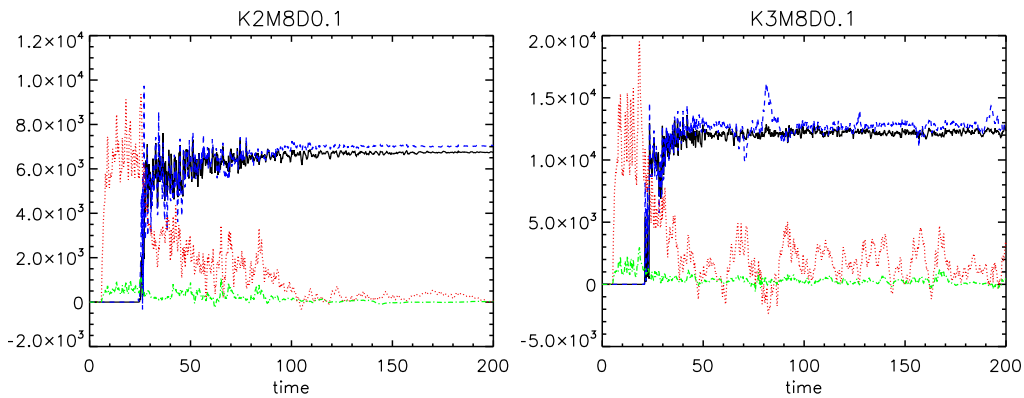


FIGURE D.28: Mach 8 , over-pressure $\kappa = 2$ (left panel) $\kappa = 3$ (right panel) and density ratio $\eta = 0.1$.

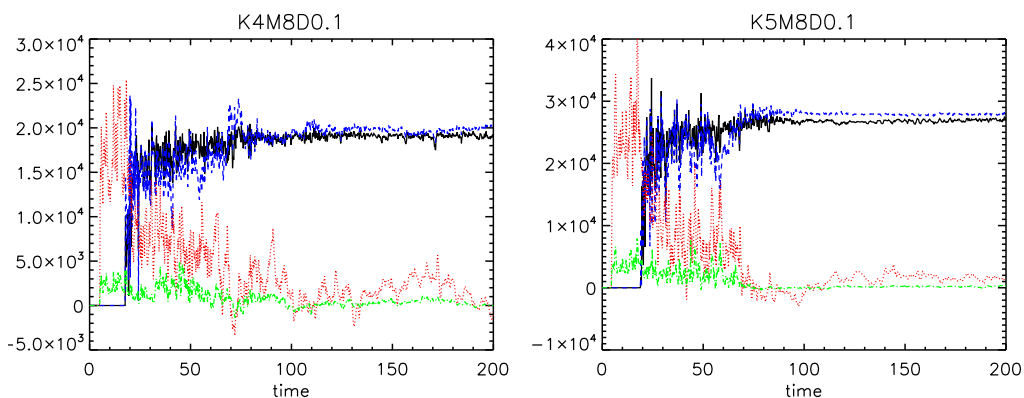


FIGURE D.29: Mach 8 , over-pressure $\kappa = 4$ (left panel) $\kappa = 5$ (right panel) and density ratio $\eta = 0.1$.

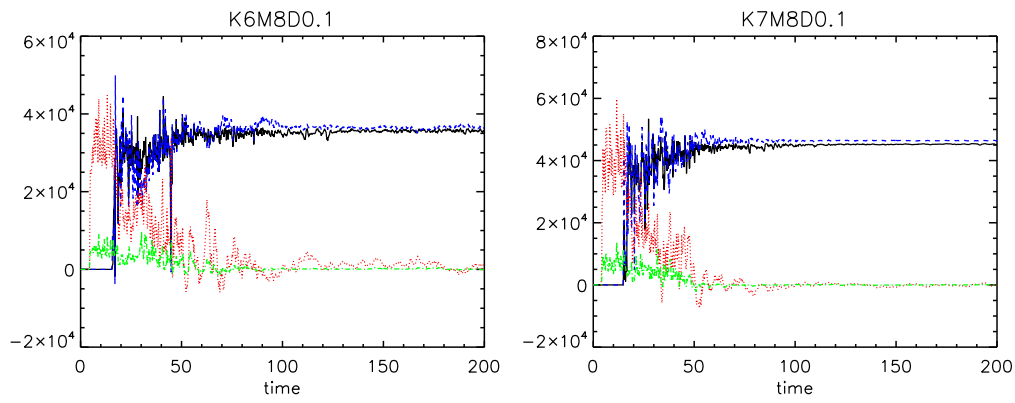


FIGURE D.30: Mach 8 , over-pressure $\kappa = 6$ (left panel) $\kappa = 7$ (right panel) and density ratio $\eta = 0.1$.

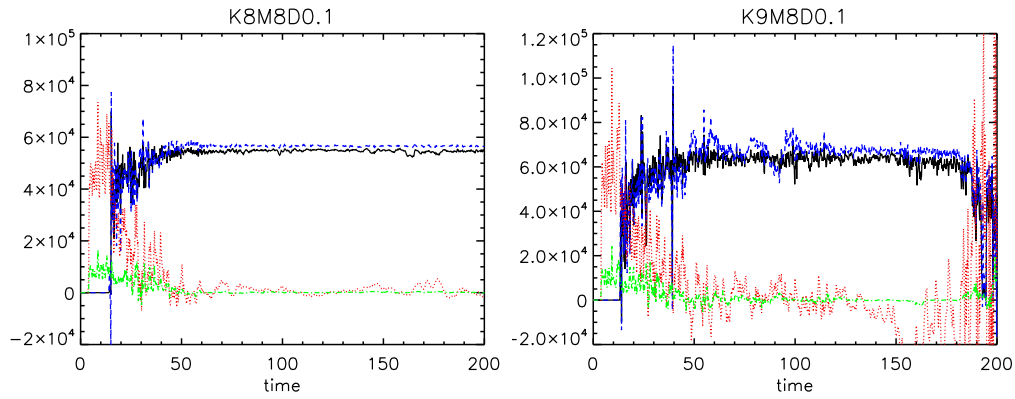


FIGURE D.31: Mach 8 , over-pressure $\kappa = 8$ (left panel) $\kappa = 9$ (right panel) and density ratio $\eta = 0.1$.

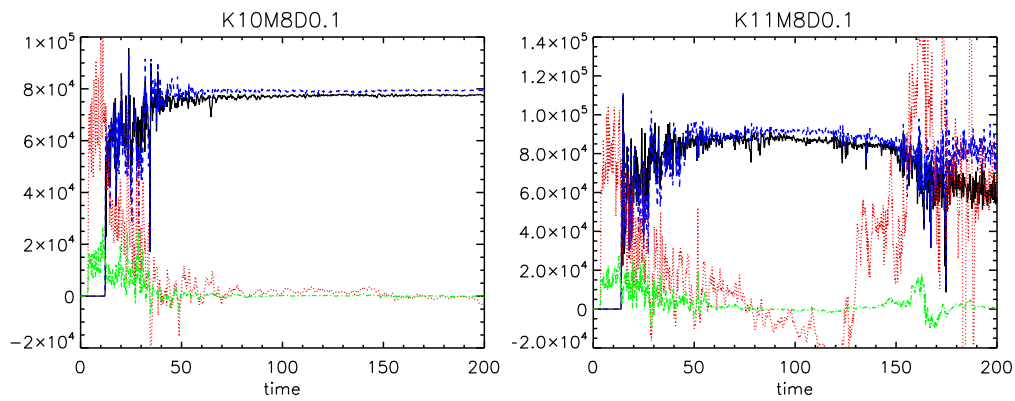


FIGURE D.32: Mach 8 , over-pressure $\kappa = 10$ (left panel) $\kappa = 11$ (right panel) and density ratio $\eta = 0.1$.

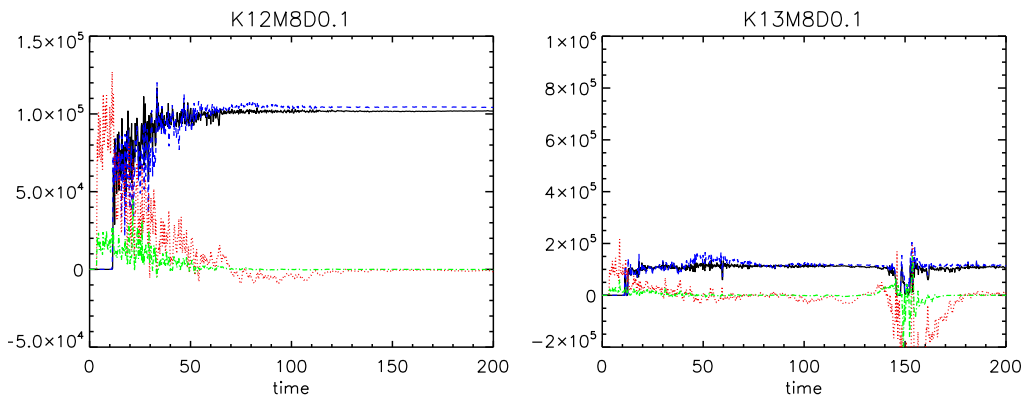


FIGURE D.33: Mach 8 , over-pressure $\kappa = 12$ (left panel) $\kappa = 13$ (right panel) and density ratio $\eta = 0.1$.

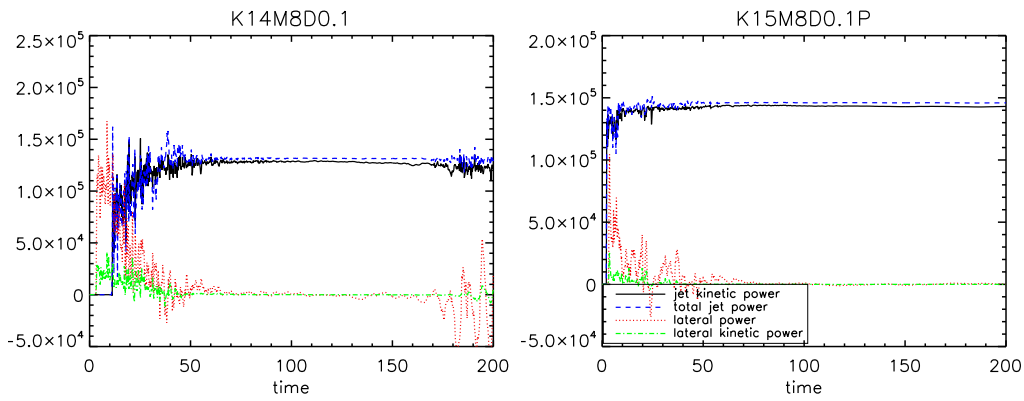


FIGURE D.34: Mach 8 , over-pressure $\kappa = 14$ (left panel) $\kappa = 15$ (right panel) and density ratio $\eta = 0.1$.

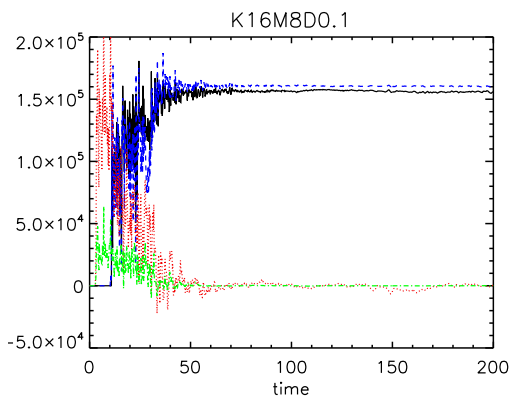


FIGURE D.35: Mach 8 , over-pressure $\kappa = 16$ and density ratio $\eta = 0.1$.

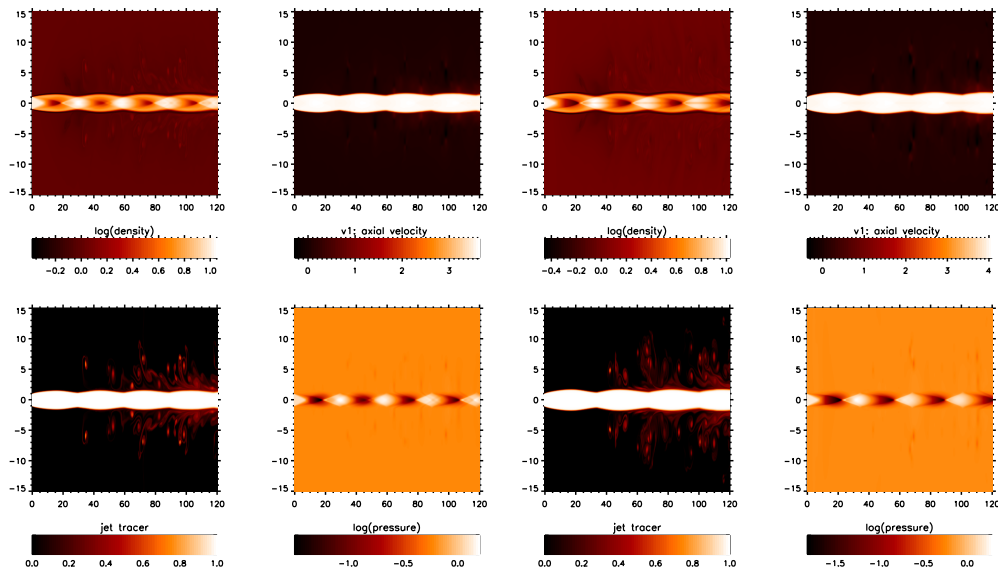


FIGURE D.36: Mach 8 , over-pressure $\kappa = 2$ (left panel) $\kappa = 2.5$ (right panel) and density ratio $\eta = 10$.

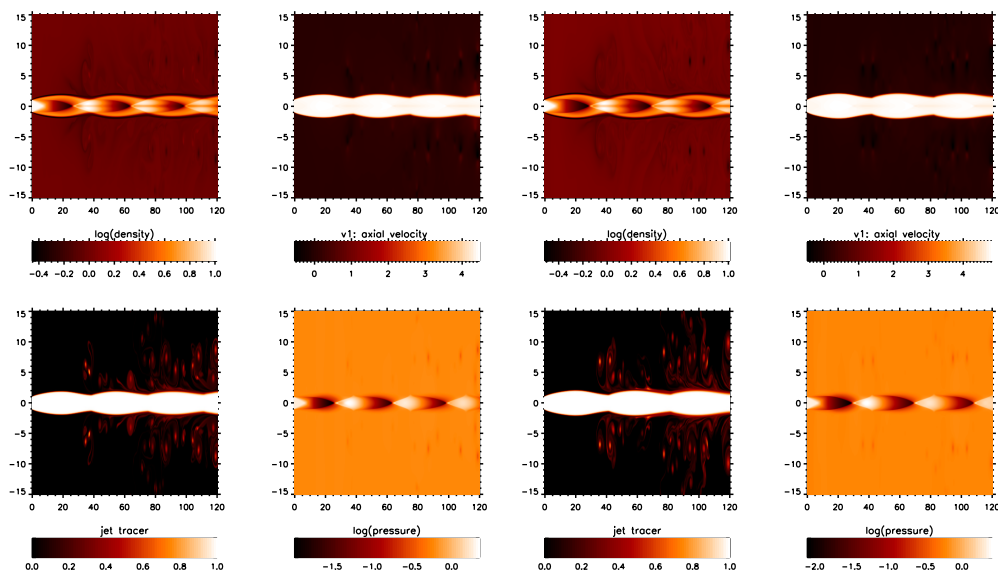


FIGURE D.37: Mach 8 , over-pressure $\kappa = 3$ (left panel) $\kappa = 3.5$ (right panel) and density ratio $\eta = 10$.

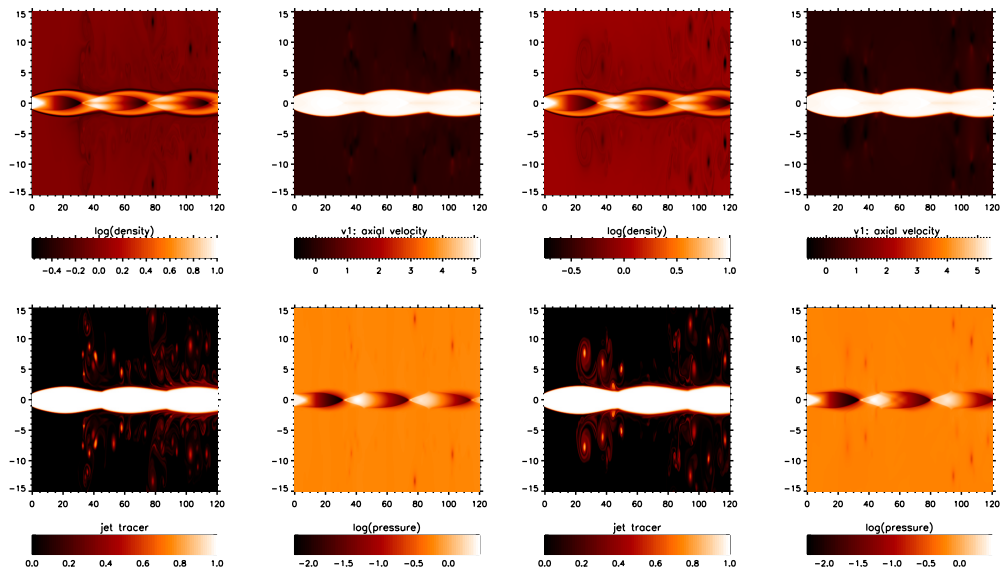


FIGURE D.38: Mach 8 , over-pressure $\kappa = 4$ (left panel) $\kappa = 4.5$ (right panel) and density ratio $\eta = 10$.

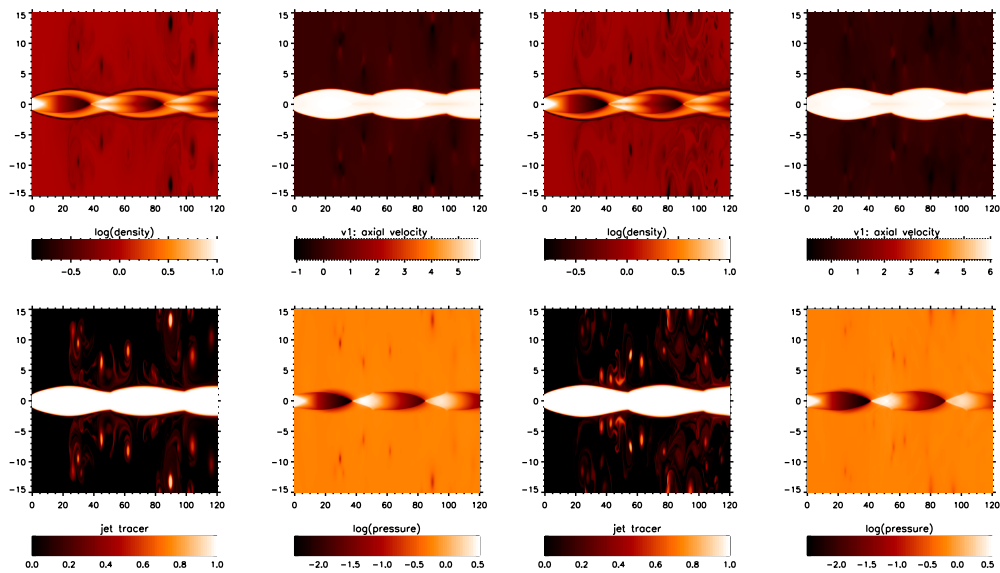


FIGURE D.39: Mach 8 , over-pressure $\kappa = 5$ (left panel) $\kappa = 5.5$ (right panel) and density ratio $\eta = 10$.

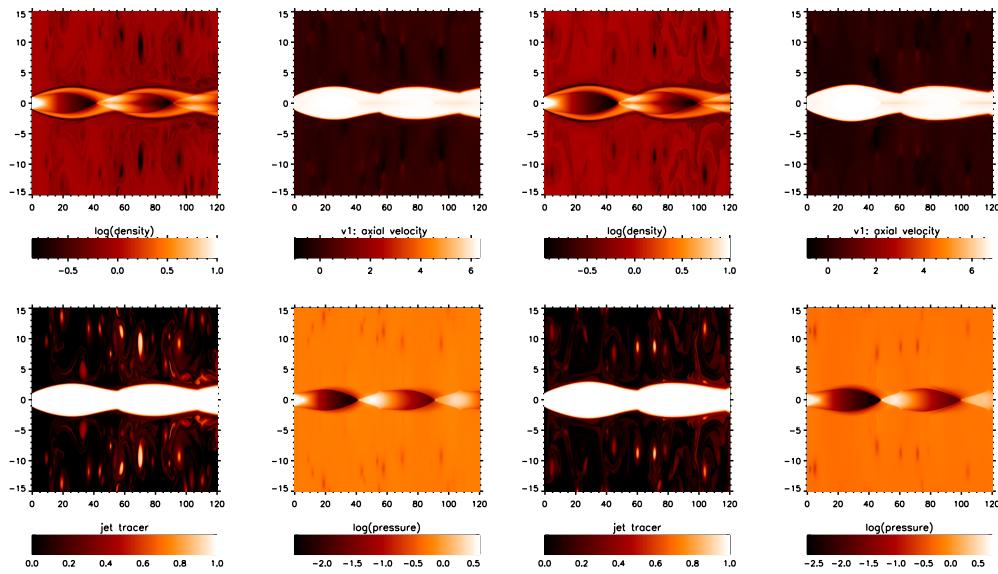


FIGURE D.40: Mach 8 , over-pressure $\kappa = 6$ (left panel) $\kappa = 7$ (right panel) and density ratio $\eta = 10$.

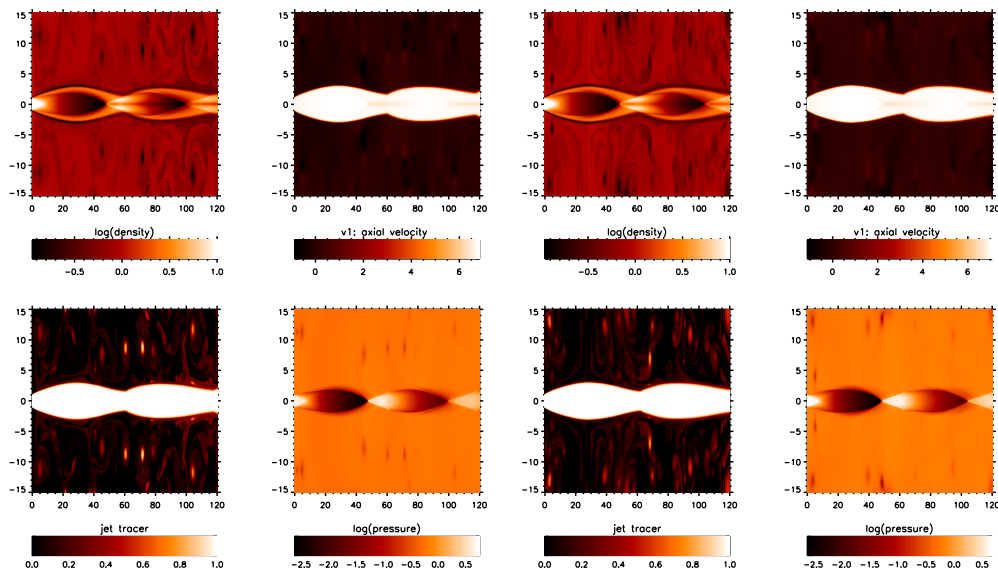


FIGURE D.41: Mach 8 , over-pressure $\kappa = 7$ (left panel) $\kappa = 7.5$ (right panel) and density ratio $\eta = 10$.

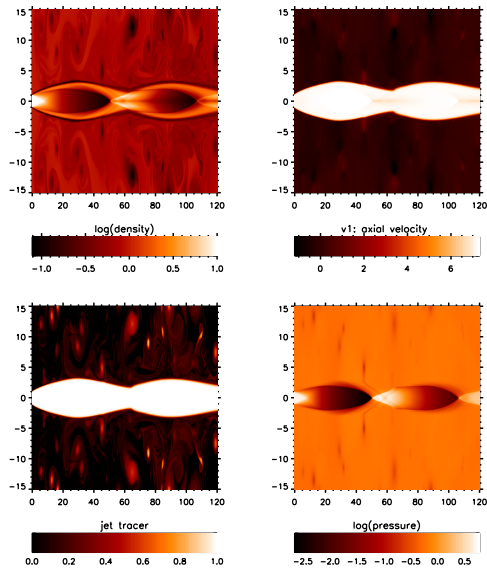


FIGURE D.42: Mach 8, over-pressure $\kappa = 8$ (and density ratio $\eta = 10$).

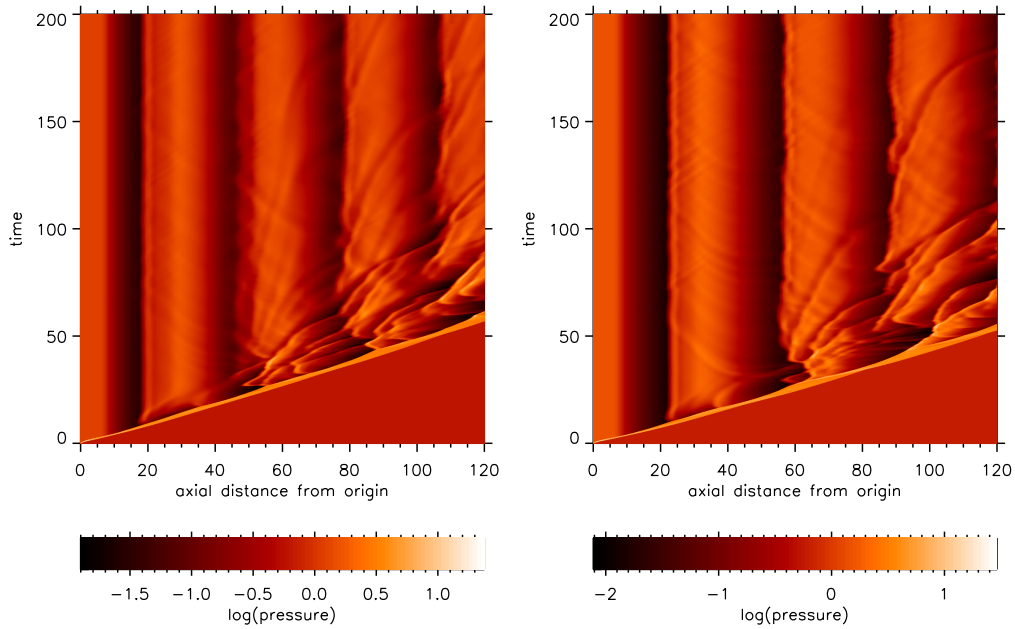


FIGURE D.43: Mach 8, over-pressure $\kappa = 2$ (left panel) $\kappa = 2.5$ (right panel) and density ratio $\eta = 10$.

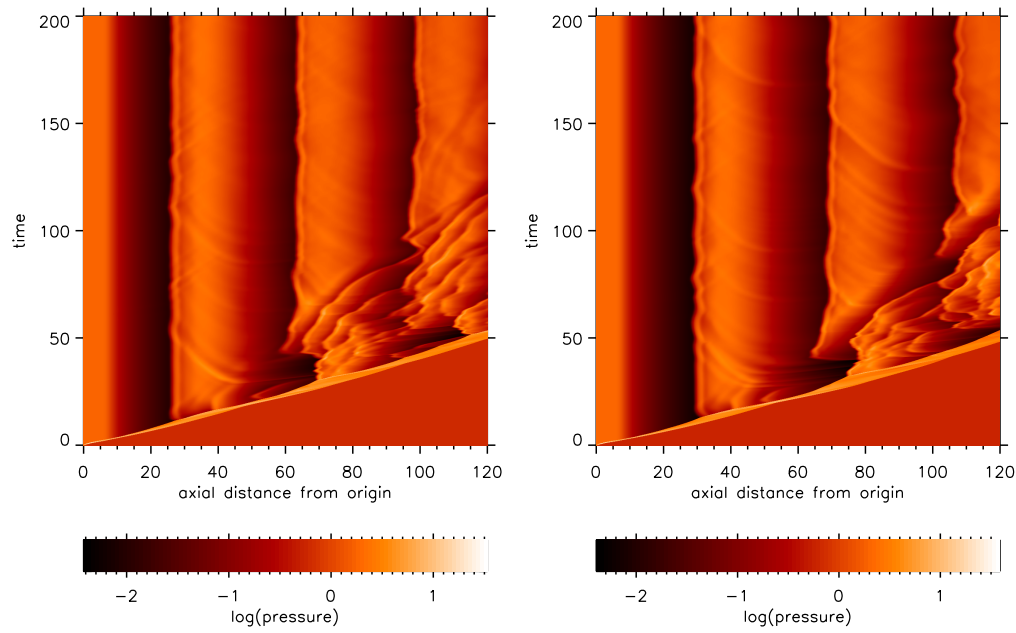


FIGURE D.44: Mach 8 , over-pressure $\kappa = 3$ (left panel) $\kappa = 3.5$ (right panel) and density ratio $\eta = 10$.

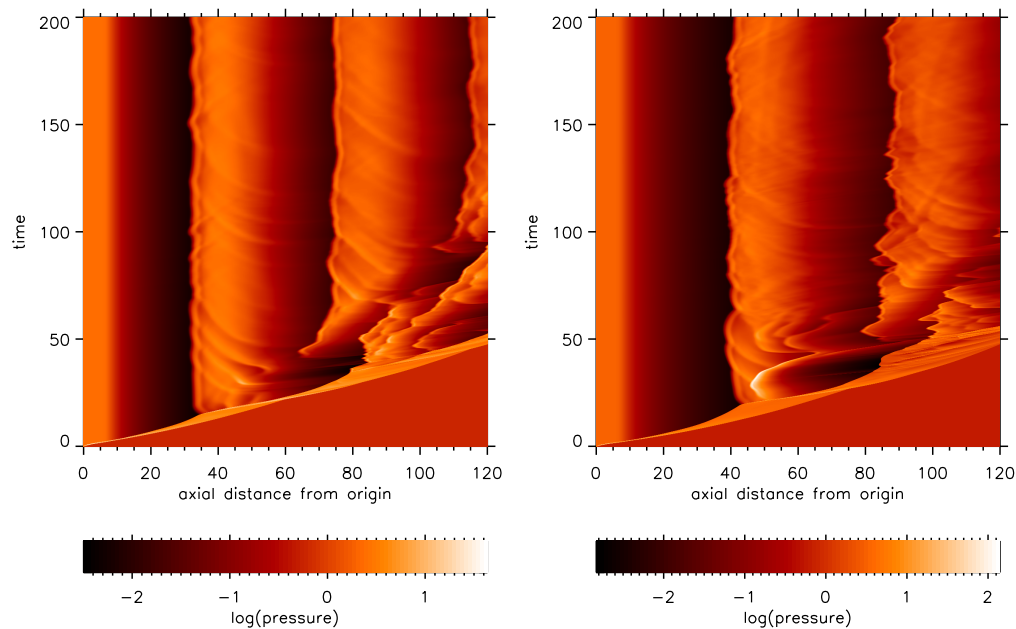


FIGURE D.45: Mach 8 , over-pressure $\kappa = 4$ (left panel) $\kappa = 5.5$ (right panel) and density ratio $\eta = 10$.

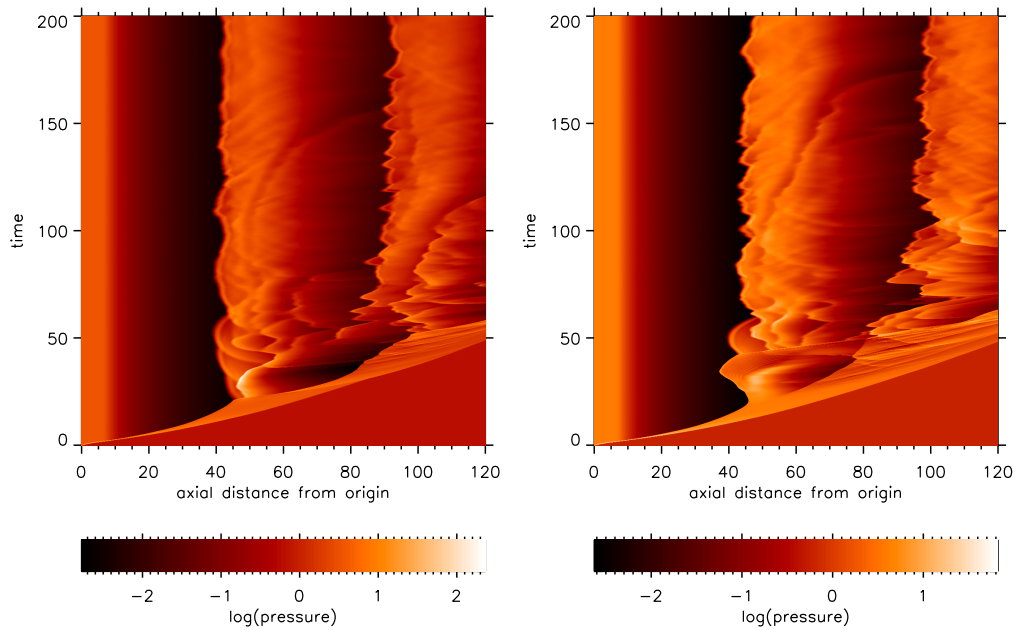


FIGURE D.46: Mach 8 , over-pressure $\kappa = 6$ (left panel) $\kappa = 7$ (right panel) and density ratio $\eta = 10$.

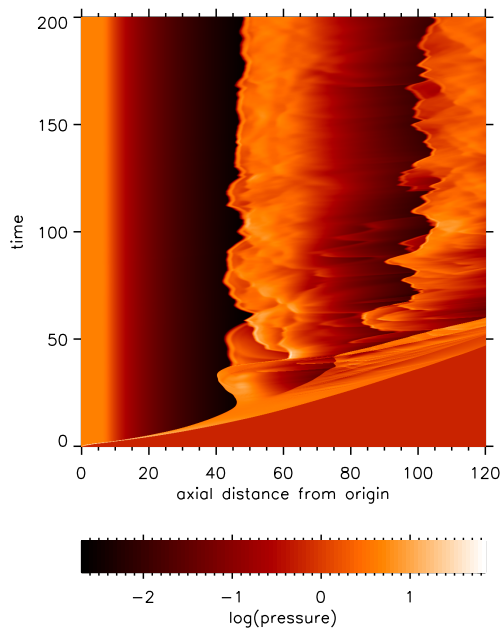


FIGURE D.47: Mach 4, over-pressure $\kappa = 7.5$ and density ratio $\eta = 10$.

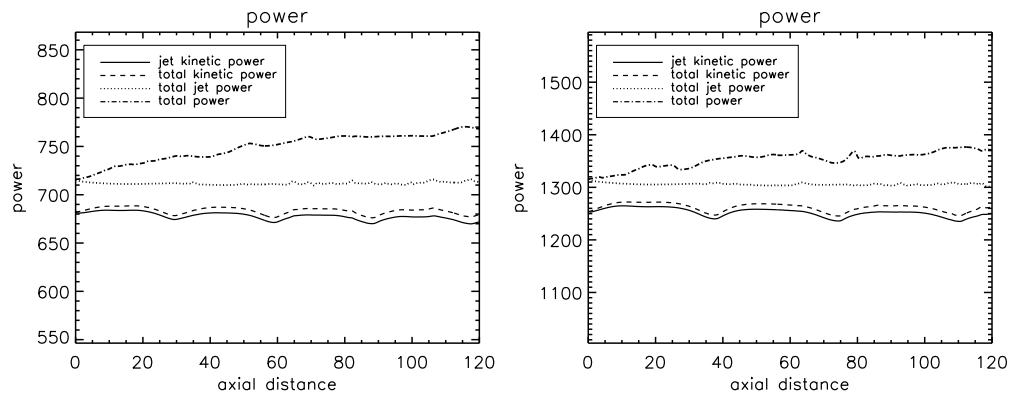


FIGURE D.48: Mach 8 , over-pressure $\kappa = 2$ (left panel) $\kappa = 3$ (right panel) and density ratio $\eta = 10$.

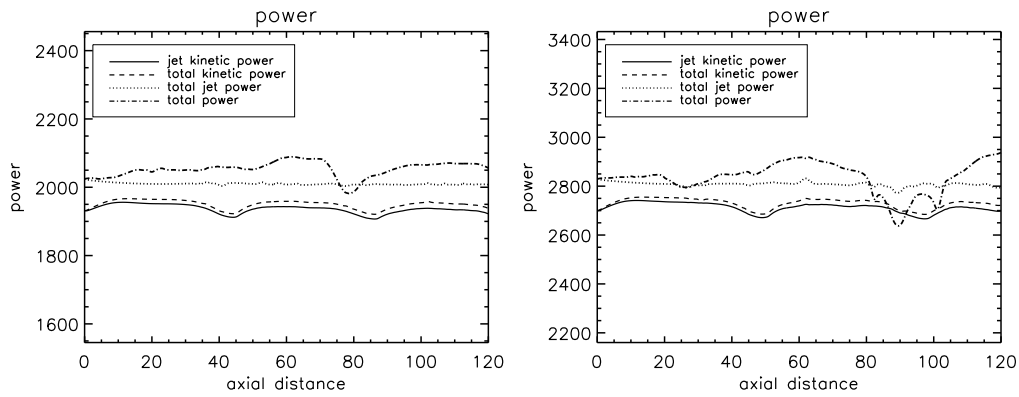


FIGURE D.49: Mach 8 , over-pressure $\kappa = 4$ (left panel) $\kappa = 5$ (right panel) and density ratio $\eta = 10$.

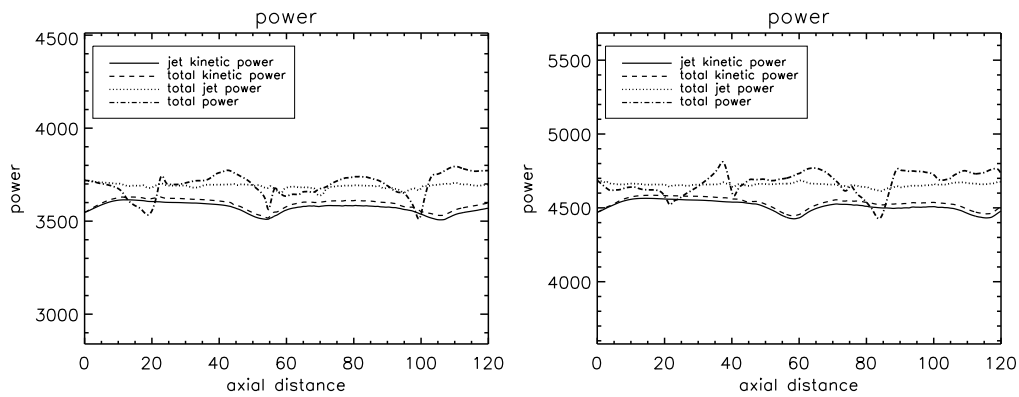


FIGURE D.50: Mach 8 , over-pressure $\kappa = 6$ (left panel) $\kappa = 7$ (right panel) and density ratio $\eta = 10$.

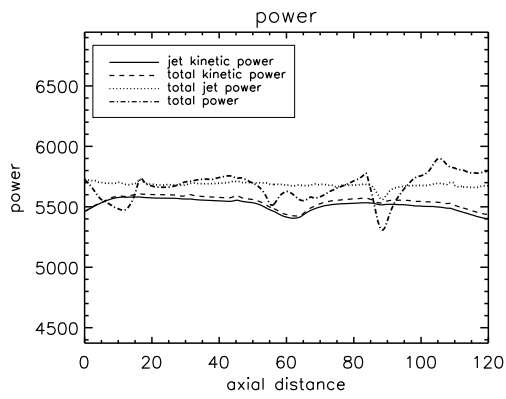


FIGURE D.51: Mach 8 , over-pressure $\kappa = 8$ and density ratio $\eta = 10$.

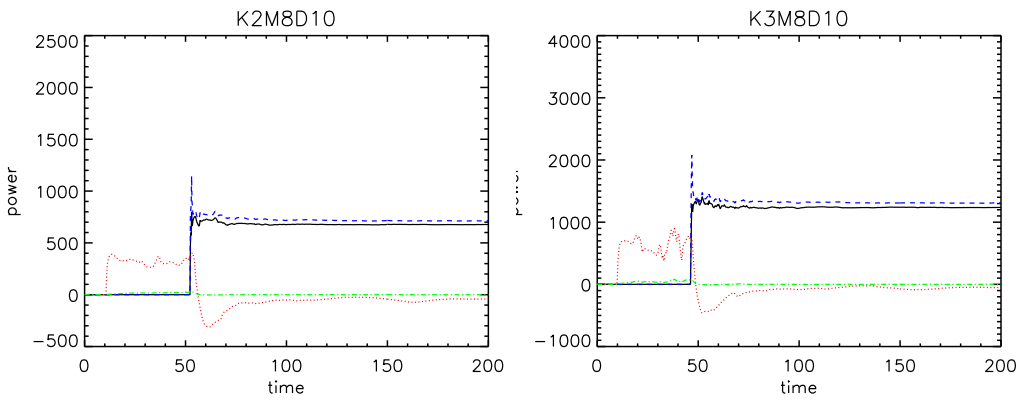


FIGURE D.52: Mach 8 , over-pressure $\kappa = 2$ (left panel) $\kappa = 3$ (right panel) and density ratio $\eta = 10$.

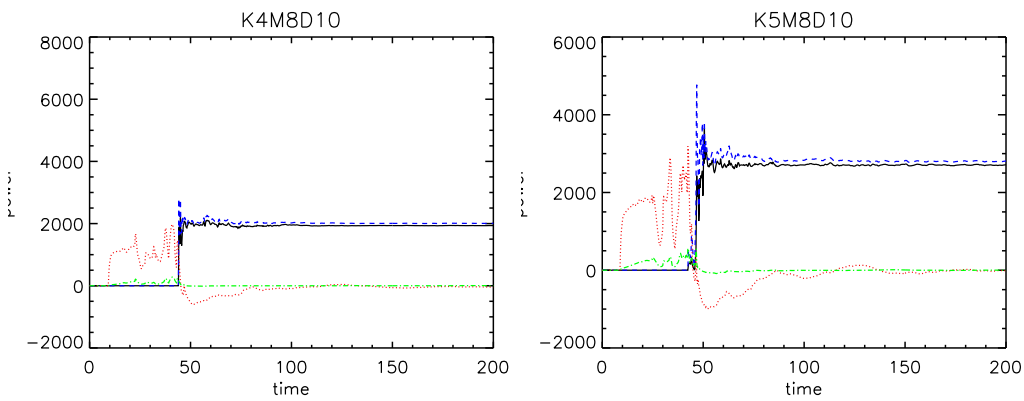


FIGURE D.53: Mach 8 , over-pressure $\kappa = 4$ (left panel) $\kappa = 5$ (right panel) and density ratio $\eta = 10$.

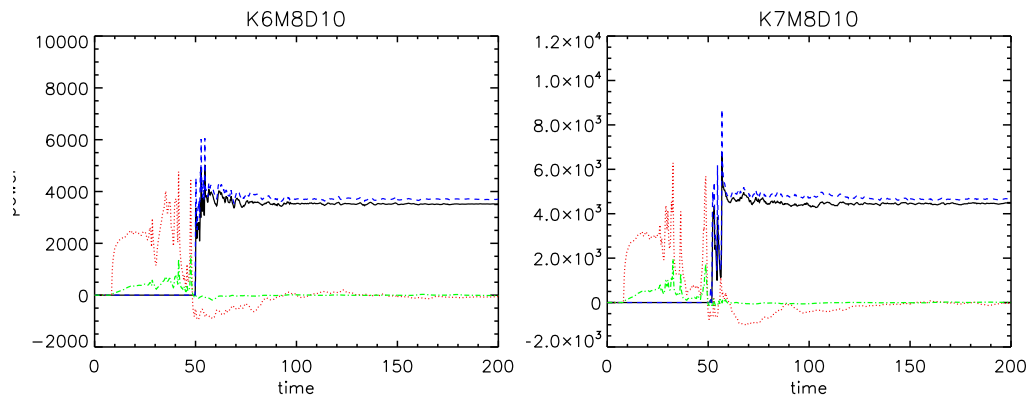


FIGURE D.54: Mach 8 , over-pressure $\kappa = 6$ (left panel) $\kappa = 7$ (right panel) and density ratio $\eta = 10$.

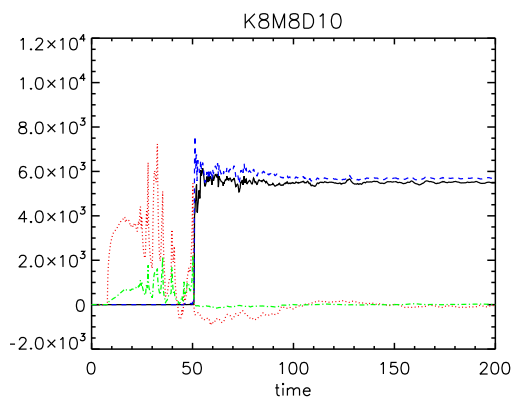


FIGURE D.55: Mach 8 , over-pressure $\kappa = 8$ and density ratio $\eta = 10$.

Appendix E

Pluto.ini

[Grid]

X1-grid	2	0.0	200	u	15.0	100	s	65.0
X2-grid	2	0.0	400	u	30.0	200	s	130.0
X3-grid	1	0.0	1	u	1.0			

[Chombo Refinement]

Levels	4
Ref_ratio	2 2 2 2 2
Regrid_interval	2 2 2 2
Refine_thresh	0.3
Tag_buffer_size	3
Block_factor	4
Max_grid_size	32
Fill_ratio	0.75

[Time]

CFL	0.4
-----	-----

```
CFL_max_var    1.1
tstop          60.1
first_dt       1.e-6
```

```
[Solver]
```

```
Solver         hllc
```

```
[Boundary]
```

```
X1-beg         reflective
X1-end         outflow
X2-beg         userdef
X2-end         outflow
X3-beg         outflow
X3-end         outflow
```

```
[Uniform Grid Output]
```

```
uservar        0
dbl            0.2 -1  single_file
flt           -1.0 -1  single_file
vtk           -1.0 -1  single_file
tab           -1.0 -1
png           -1.0 -1
ppm           -1.0 -1
log            -1.0
analysis      -1.0 -1
```

[Chombo HDF5 output]

Checkpoint_interval -1.0 0

Plot_interval 1.0 0

[Parameters]

D_RATIO 0.1

P_RATIO 2.0

MACH 2.0

R_JET 1.0

THETA_R 0.174533

F_PULSE 0.2

OM_PULSE 12.5664

F_SHEAR 0.

RAMPTIME 10.0

OM_JAWS 0.314159265

Appendix F

init.c

```
include "pluto.h"

/* ***** */
void Init (double *us, double x1, double x2, double x3)
/*
 *
 *
 *
***** */
{
    g_gamma = 5./3.;

    us[RHO] = 1.0;
    us[VX1] = 0.0;
    us[VX2] = 0.0;
    us[VX3] = 0.0;
    us[PRS] = 1.0/g_gamma;
    us[TRC] = 0.0;
```

```
}
```

```
/* ***** */
void InitDomain (Data *d, Grid *grid)
/*!
 * Assign initial condition by looping over the computational domain.
 * Called after the usual Init() function to assign initial conditions
 * on primitive variables.
 * Value assigned here will overwrite those prescribed during Init().
 *
 *
 ***** */
{
}
```

```
/* ***** */
void Analysis (const Data *d, Grid *grid)
/*
 *
 *
 ***** */
{

}
```

```
/* ***** */
void UserDefBoundary (const Data *d, RBox *box, int side, Grid *grid)
/*!
 * Assign user-defined boundary conditions.
 *
```

```

* \param [in,out] d pointer to the PLUTO data structure containing
*
* cell-centered primitive quantities (d->Vc) and
*
* staggered magnetic fields (d->Vs, when used) to
*
* be filled.
*
* \param [in] box pointer to a RBox structure containing the lower
*
* and upper indices of the ghost zone-centers/nodes
*
* or edges at which data values should be assigned.
*
* \param [in] side specifies the boundary side where ghost zones need
*
* to be filled. It can assume the following
*
* pre-definite values: X1_BEG, X1_END,
*
*                          X2_BEG, X2_END,
*
*                          X3_BEG, X3_END.
*
* The special value side == 0 is used to control
*
* a region inside the computational domain.
*
* \param [in] grid pointer to an array of Grid structures.
*
*
* ***** */
{
  int    i, j, k;
  double *R;
  real   pjet, djet, vjet,rjet,thetar,ompulse,fpulse,fshear;
  real   scrh,rampt,vjeta,omjaws,thetamax;

  scrh = 1.0/(g_gamma - 1.0);

  R = grid->xgc[IDIR];

```

```

pjet      = g_inputParam[P_RATIO]/g_gamma;
djet      = g_inputParam[D_RATIO];
rjet      = g_inputParam[R_JET];
thetamax  = g_inputParam[THETA_R];
ompulse   = g_inputParam[OM_PULSE];
omjaws    = g_inputParam[OM_JAWS];
rampt     = g_inputParam[RAMPTIME];
fpulse    = g_inputParam[F_PULSE]* sin(ompulse*g_time);
thetar    = thetamax* cos(omjaws*g_time);
    vjeta  = g_inputParam[MACH]*(1.-fpulse)*sqrt(g_gamma*pjet/djet);
if (g_time <= rampt ) {
    vjet = vjeta*g_time/rampt;
} else {
    vjet = vjeta;
}
fshear = g_inputParam[F_SHEAR];

if (side == X2_BEG){

    X2_BEG_LOOP(k,j,i){

        if (R[i] <= 1.) {
            d->Vc[RHO][k][j][i] = djet;
            d->Vc[VX1][k][j][i] = vjet*sin(thetar*R[i]/rjet)*(1.-fshear*cos(1.5708*R[i]
            d->Vc[VX2][k][j][i] = vjet*cos(thetar*R[i]/rjet)*(1.-fshear*cos(1.5708*R[i]
            d->Vc[PRS][k][j][i] = pjet;
            d->Vc[TRC][k][j][i] = 1.0;
        } else {
            d->Vc[RHO][k][j][i] = d->Vc[RHO][k][2*JBEG - j - 1][i];

```

```
d->Vc[VX1][k][j][i] = d->Vc[VX1][k][2*JBEG - j - 1][i];
d->Vc[VX2][k][j][i] = -d->Vc[VX2][k][2*JBEG - j - 1][i];
d->Vc[PRS][k][j][i] = d->Vc[PRS][k][2*JBEG - j - 1][i];
d->Vc[TRC][k][j][i] = d->Vc[TRC][k][2*JBEG - j - 1][i];
}
}
}
}
```

Appendix G

Definitions.h

```
#define PHYSICS HD
#define DIMENSIONS 2
#define COMPONENTS 2
#define GEOMETRY CYLINDRICAL
#define BODY_FORCE NO
#define FORCED_TURB NO
#define COOLING NO
#define RECONSTRUCTION LINEAR
#define TIME_STEPPING HANCOCK
#define DIMENSIONAL_SPLITTING YES
#define NTRACER 1
#define USER_DEF_PARAMETERS 10

/* -- physics dependent declarations -- */

#define EOS IDEAL
#define ENTROPY_SWITCH NO
#define THERMAL_CONDUCTION NO
#define VISCOSITY NO
#define ROTATING_FRAME NO
```

```
/* -- user-defined parameters (labels) -- */

#define D_RATIO 0
#define P_RATIO 1
#define MACH 2
#define R_JET 3
#define THETA_R 4
#define F_PULSE 5
#define OM_PULSE 6
#define F_SHEAR 7
#define RAMPTIME 8
#define OM_JAWS 9

/* [Beg] user-defined constants (do not change this line) */

#define SHOCK_FLATTENING MULTID
#define CHAR_LIMITING YES
#define LIMITER VANLEER_LIM

/* [End] user-defined constants (do not change this line) */
```